Annual Report
Jahresbericht

2006

WALTHER–MEISSNER–INSTITUT
für Tieftemperaturforschung
Bayerische Akademie der Wissenschaften

Contact:

Prof. Dr. Rudolf Gross
Walther–Meißner–Institut für Tieftemperaturforschung
Bayerische Akademie der Wissenschaften
and
Lehrstuhl für Technische Physik – E23
Technische Universität München

Address:

Walther–Meißner–Str. 8	Phone:	+49 – (0)89 289 14201
D - 85748 Garching	Fax:	+49 – (0)89 289 14206
GERMANY	e–mail:	Rudolf.Gross@wmi.badw.de
	WWW–address:	http://www.wmi.badw.de

Secretary's Office and Administration:

Emel Dönertas	Phone:	+49 – (0)89 289 14205
	Fax:	+49 – (0)89 289 14206
	e–mail:	Emel.Doenertas@wmi.badw.de
Tina Pinkert	Phone:	+49 – (0)89 289 14202
	Fax:	+49 – (0)89 289 14206
	e–mail:	Tina.Pinkert@wmi.badw.de

Preface

The Walther–Meißner–Institute for Low Temperature Research (WMI) can look back on a very successful year 2006. In particular, the WMI was participating in the ***Excellence Initiative*** of the German federal and state governments, which aims to both promote top-level research and improve the quality of German universities and research institutions, and was significantly contributing to the success of the Cluster of Excellence ***Nanosystems Initiative Munich – NIM*** (coordinator: J. P. Kotthaus). NIM was installed by the German Science Foundation (DFG) effective in November 2006. The WMI is involved in three different research areas: project area A – Single Electron and Spin Systems (R. Gross, S.T.B. Gönnenwein), project area C – Quantum Information Nanosystems (R. Gross, A. Marx), and project area F – Nanoanalytics and Enabling Techniques (B.A. Hermann). We are convinced that NIM will stimulate our research activities in the field of nanosciences, further foster the fruitful collaboration in the Munich area in this important research field, and help to promote the career of young scientists.

Beside the success in the Excellence Initiative, also the various other research projects of WMI have been successfully continued in 2006 and promising new projects could be started. In particular, the research work within the Cooperative Research Center (SFB) 631 on ***Solid-State Quantum Information Processing: Physical Concepts and Materials Aspects*** (coordinator: R. Gross), which has been installed by the German Science Foundation in July 2003, has been very fruitful and brought major breakthroughs (see `http://www.wmi.badw-muenchen.de/SFB631` and reports below). In 2006, the first progress report and the application for the next four-year funding period of SFB 631 have been prepared and submitted to the German Science Foundation. Similarly successful was the work within the Research Unit FOR 538 on ***High Temperature Superconductivity*** (coordinator: R. Hackl), which has been installed by the German Science Foundation in April 2004 (see `http://www.wmi.badw-muenchen.de/FG538` and reports below). The FOR 538 has been reviewed by the DFG in November 2006 and received an excellent grading. Due to the big success of the Research Unit the number of projects has been extended from 7 to 9 to further strengthen our research program. The WMI is also conducting a large research project on ***New Functional Thin Film Systems Based on Artificial Heterostructures of Transition Metal Oxides*** within the Priority Programme 1157 of the DFG on ***Integrated Electroceramic Functional Systems***. This project has been evaluated very positively and extended on the same level for a further two-year period. Furthermore, the WMI also submitted a proposal for a project on ***Spin injection, spin transport and controllable ferromagnetism in transition metal doped ZnO*** within the new DFG Priority Programme 1285 on ***Semiconductor Spin Electronics*** (R. Gross, S.B.T. Gönnenwein, M. Opel). The more than 60 proposals submitted for this six-year priority program have been evaluated in December 2006 and our proposal has been recommended for funding. There are further smaller national and international projects that are listed in the section on "Research Projects and Cooperations" in this report.

The year 2006 not only brought very good progress in our research projects, but also important improvements of the technological infrastructure of the WMI. Despite the tight financial situation several new experimental facilities could be developed and installed during the last year. For example, a new ultra-low temperature system has been developed and fabricated at the WMI. This system, which has been set up in the basement of WMI, is specially designed for spectroscopy and time domain measurements on solid-state quantum information systems and allows low-noise experiments up to 40 GHz and down to 20 mK. For the testing of superconducting microwave circuits a crygenic wafer probing station with up to four probing tips for frequencies up to 20 GHz and temperatures down to 4 K has been installed. For combined optical and magnetotransport experiments on magnetic thin films and spintronic devices a 7 T

split-coil magnet with optical access has been set up on a vibration insulated optical table. Further important new experimental facilities are a diamond anvil cell for Raman experiments ($p < 200\,\text{kbar}$, $T > 1.7\,\text{K}$) and a dilution refrigerator combined with a vector magnet system ($B_{\parallel} < 1,5\,\text{T}$, $B_{\perp} < 0.33\,\text{T}$, $T > 20\,\text{mK}$). The former is very interesting for the study of quantum phase transition, the latter for the investigation of the interplay of different ordering phenomena in layered organic conductors.

All together, our research activities and our efforts to improve the technological infrastructure and experimental facilities of WMI have been highly successful in 2006. This is demonstrated by a large number of scientific papers in high quality journals, invited presentations at national and international conferences as well as seminar talks and colloquia. The staff of WMI was still growing in 2006 due to the increasing number of PhD and diploma/master students. Throughout 2006, an average of 13 scientific staff members, 19 members of the administrative and technical staff, 16 doctorate candidates, more than 25 diploma/master students as well as a large number of short and long–term guests belonged to the institute. The high level of scientific productivity of WMI strongly profits from the collaborative atmosphere, the commitment and high motivation of its research and technical staff and the support of various funding agencies. In particular, we acknowledge the financial support from the Bavarian Academy of Sciences, the German Science Foundation, the Bavarian Ministry for Science and Arts, the BMBF and the EU. Although WMI again had to suffer a cut-back of its annual total budget by more than 15% in 2006, we could keep the high level of our research program by the very successful acquisition of additional research money from various funding agencies. However, there is no doubt that on the long term similar cut-backs will significantly affect the technical infrastructure of WMI and, in turn, its competitiveness in acquiring external research projects.

The Annual Report 2006 gives an overview on the scientific results of the WMI obtained in many cases within joint national and international research projects and in close collaboration with international guests. The report is intended to provide an overview on our work to our friends and partners in research and industry and thereby to intensify our numerous collaborations. In order to be useful also for our numerous international partners the report is written in English.

I finally would like to thank all the colleagues, guests, students, post–docs and cooperating partners, who contributed to the success of our work within the last year, and last but not least all our friends and sponsors for their interest, trust and continuous support.

Rudolf Gross

Garching, December 2006

The majority of the WMI group members (October 2006)

Contents

The Walther–Meißner–Institute

The Walther–Meißner–Institute for Low Temperature Research (WMI) is operated by the Commission for Low Temperature Research of the Bavarian Academy of Sciences and Humanities (BAdW). The Commissions (Research Groups) of the Academy are set up in order to carry out long–term projects, which are too ambitious for the lifetime or capacity of any single researcher, or which require the collaboration of specialists in various disciplines. At present, the Bavarian Academy of Sciences and Humanities consists of 36 Commissions with more than 300 employees.

The WMI also is the host institute of the chair for Technical Physics (E 23) of the Technical University of Munich (TUM) with the director of the WMI being ordinarius at the Faculty of Physics of TUM. Furthermore, since 2004 the WMI hosts a new scanning probe division with the head of this division being professor at the Ludwig-Maximilians-University of Munich (LMU) and also member of the Center for Nano Science (CeNS) of the LMU. In this way a tight collaboration has been established between research groups of both Munich universities joining technological and human resources in the fields of experimental and theoretical solid-state and condensed matter physics, low temperature techniques, materials science as well as thin film and nanotechnology. Finally, the WMI supplies liquid helium to more than 20 research groups at both Munich universities and provides the technological basis for low temperature research.

The research activities of the Walther–Meißner–Institute are focused on low temperature solid-state and condensed matter physics (see reports below). The research program is devoted to both **fundamental** and **applied research** and also addresses **materials science, thin film and nanotechnology** aspects. With respect to **basic research** the main focus of the WMI is on

- superconductivity and superfluidity,
- magnetism and spin transport,
- quantum phenomena in mesoscopic systems and nanostructures,
- self-organization of molecules on surfaces,
- and the general properties of metallic systems at low and very low temperatures.

The WMI also conducts **applied research** in the fields of

- solid-state quantum information processing systems,
- superconducting and spintronic devices,
- oxide electronics,
- multi-functional and multiferroic materials,
- and the development of low and ultra low temperature systems and techniques.

With respect to **materials science, thin film and nanotechnology** the research program is focused on

- the synthesis of superconducting and magnetic materials,
- the single crystal growth of oxide materials,
- the thin film technology of complex oxide heterostructures including multi-functional and multiferroic material systems,
- the fabrication of superconducting, magnetic, and hybrid nanostructures,
- and the growth of self-organized molecular ad-layers.

The WMI also develops and operates systems and techniques for low and ultra–low temperature experiments. A recent development are dry mK-systems that can be operated without liquid helium by using a pulse-tube refrigerator for precooling. Meanwhile, these systems have been successfully commercialized by the company VeriCold Technologies GmbH at Ismaning, Germany. As further typical examples we mention a nuclear demagnetization cryostat for temperature down to below 100 μK, or very flexible dilution refrigerator inserts for temperatures down to about 20 mK fitting into a 2 inch bore. These systems have been engineered and fabricated at the WMI. Within the last years, several dilution refrigerators have been provided to other research groups for various low temperature experiments. The WMI also operates a helium liquifier with a capacity of more than 150.000 liters per year and supplies both Munich universities with liquid helium. To optimize the transfer of liquid helium into transport containers the WMI has developed a pumping system for liquid helium that is commercialized in collaboration with a company.

The individual research groups of WMI offer a wide range of attractive research opportunities for diploma (graduate) students, PhD students and postdoctoral fellows. The WMI is equipped with state of the art facilities for the preparation and characterization of superconducting and magnetic materials as well as for various low and ultra–low temperature experiments. The main experimental and technological resources of WMI are listed in the following.

Materials Preparation and Fabrication of Nanostructures

- Laser Molecular Beam Epitaxy system for oxide heterostructures (equipped with in–situ RHEED, AFM/STM system, atomic oxygen source, laser heating system, metallization)
- UHV magnetron sputtering systems for metals (e.g. Nb, Al, NiPd, ...)
- magnetron sputtering system for oxide heteroepitaxy (equipped with four sputtering guns and an oxygen ion gun)
- ion beam sputtering system
- UHV metallization system (equipped with e–gun and thermal evaporators)
- reactive ion etching (RIE) system, Plasmalab 80 Plus with ICP plasma source, Oxford Instruments Plasma Technology
- ion beam etching (IBE) system equipped with a LN_2 cooled sample holder
- polishing machine for substrate preparation
- ultrasonic bonding machine
- 50 m^2 class 1000 clean room facility
- optical lithography (Süss maskaligner MJB 3 and projection lithography)
- electron beam lithography (based on Philips XL 30 SFEG scanning electron microscope and Raith Elphy Plus lithography system including a laser stage)
- four-mirror image furnace for crystal growth

Characterization

- 2–circle x–ray diffractometer (Bruker D8 Advance, sample temperature up to 1 600°C)
- high resolution 4–circle x–ray diffractometer (Bruker D8 Discover)
- scanning electron microscope with EDX analysis
- UHV room temperature AFM/STM system
- 2048 u high resolution mass spectrometer (Fa. Pfeiffer, cross beam ion source, SEM)

- Low Energy Electron Diffraction (SPECTA-LEED, Fa. Omicron)
- two Raman spectroscopy systems (1.5 to 300 K, in-situ sample preparation)
- SQUID magnetometer (Quantum Design, 1.5 to 700 K, up to 7 Tesla)
- several high field magnet systems (up to 17 Tesla) with variable temperature inserts
- 7 Tesla split coil magnet systems with optical access and variable temperature insert
- experimental set–ups for the measurement of noise including low noise SQUID amplifiers and signal analyzers
- high-frequency network analyzer (up to 40 GHz) and various microwave components (sources, mixers, circulators, attenuators) for the determination of high frequency parameters
- high-frequency cryogenic probing station (up to 20 GHz, $T > 4$ K)

Low temperature systems and techniques

- 5 K-Scanning Tunneling Microscope (low temperature STM, Fa. Omicron)
- several ^{3}He/^{4}He dilution refrigerator inserts for temperatures down to 10 mK
- "dry" mK-cooler based on a dilution refrigerator with pulse-tube precooling
- ultra–low temperature facility for temperatures down to below 100 μK based on a nuclear demagnetization cryostat
- experimental set–ups for the measurement of specific heat, magnetization, thermal expansion as well as electrical and thermal transport properties as a function of temperature, magnetic field and pressure

Solid-State Quantum Information Processing: Funding proposal for second period of SFB 631 has been submitted

R. Gross [1]

The Collaborative Research Center 631 (SFB 631) on ***Solid-State Quantum Information Processing: Physical Concepts and Materials Aspects*** (coordinator: R. Gross) plays a key role in the research program of WMI (see reports below). It was installed by the German Science Foundation in July 2003. In 2006, the first progress report and the application for the next four-year funding period of SFB 631 have been prepared and submitted to the German Science Foundation. The review meeting will take place in February 2007. In the first funding period the research work within SFB 631 was very fruitful and already brought major breakthroughs in several areas. The success of SFB 631 not only is demonstrated by a large number of scientific publications in high quality journals (see `http://www.wmi.badw-muenchen.de/SFB631`), but also by a large number of scientific honors and awards (> 20) given to members of SFB 631 and by in total 9 appointments of young scientists to professor positions. The fact that 9 junior scientists of SFB 631 could receive full and associate professor positions within the first funding period documents the quality, relevance, and attractiveness of the research work of SFB 631. Fortunately, at the same time SFB 631 could attract a large number of young scientists, providing an excellent replacement of the principal investigators having accepted professor positions at other universities. In general, since the start of SFB 631 in July 2003 the research field of solid-state quantum information processing without any doubt has gained strongly increasing importance both nationally and internationally. This is documented by a large number of new chairs and professor positions dedicated to this field, a still growing number of national and international workshops and conferences, as well as the founding of new research facilities and centers of competence. Most national and foreign funding agencies have started programs and increased funding in the research field of SFB 631 and related areas.

Solid-state quantum information systems will be a central research activity of WMI also in the coming years and WMI will play a key role in further promoting SFB 631. For the next funding period the key scientific goal of SFB 631 stays unchanged: It aims at the general understanding and development of the physical concepts, materials aspects, and technological foundations of ***solid-state quantum information processing (SQIP)***. This interdisciplinary research field has the potential to revolutionize many areas of science and technology. It deals with the coherent dynamics of solid-state quantum systems and has the daring vision to be able to process and communicate information on the basis of quantum mechanical principles. To realize this vision, SFB 631 aims at the clarification of the key physical questions and technological problems related to SQIP: How can we realize solid-state based quantum bits (qubits – the quantum mechanical generalizations of the classical bits in classical information processing) with sufficiently long decoherence time? How can we effectively control, manipulate and read-out these qubits? What are the optimum concepts for controlling decoherence? How can we couple solid-state qubits to complex systems? Which are the key materials aspects and technological problems to be solved for the successful implementation of SQIP? How can we transfer qubit states to photons to generate an interface between solid-state quantum processors and quantum communication systems? To clarify these questions in a fundamental and comprehensive way, SFB 631 joins research activities from quantum information theory, experimental and theoretical solid-state physics, quantum optics, materials science, nanotechnology and electrical engineering. The objective is to achieve a profound understanding of the physics, technology,

[1] This work is supported by the DFG through the Cooperative Research Center 631.

and materials aspects of SQIP by applying state of the art experimental and theoretical methods in a coordinated interdisciplinary research effort. Particular goals are to design and implement solid-state qubits with long coherence time, to learn how to efficiently control, manipulate and read-out the qubits, to couple them to complex systems as well as to develop theoretical tools for modeling the dynamics of driven, damped qubits in different experimental systems. In the long term, the quantum properties of the solid-state qubits, namely the possibility to form superpositions of different quantum states and to entangle several qubits, form the basis for new, completely secure communication methods like quantum cryptography and quantum teleportation. SQIP also holds the promise of immense computing power far beyond the capabilities of classical computers. Finally, it is closely linked to a variety of emerging quantum technologies such as quantum sensors, quantum standards, or quantum measuring systems.

The particular research focus of WMI within SFB 631 is on the fabrication and detailed understanding of superconducting quantum information systems. Our successful work on superconducting qubits within SFB 631 was based on the fruitful collaboration with the theory groups at the LMU (Marquardt, Wilhelm, Solano, von Delft) and the University of Augsburg (Hänggi, Kohler). Part of our experimental work was performed in close collaboration with NTT Basic Research Laboratories (Takayanagi, Semba). Among our key results achieved in SFB 631 are the identification of the weak and strong coupling regimes in superconducting circuit-QED as well as the development of the fabrication technology for Al based superconducting flux qubits and the measuring techniques required for the study of their quantum coherent dynamics. Moreover, we have fabricated so-called π Josephson junctions with ferromagnetic interlayers. By the first observation of macroscopic quantum tunneling and level quantization in these junctions we could directly demonstrate the quantum behavior of these junctions and thus their applicability in so-called quiet qubits. Furthermore, we could study the phase coherent dynamics of superconducting three-Josephson-junction flux qubits both in the frequency and time domain. The qubit state has been detected using a dc SQUID method with resistive or capacitive bias, thereby allowing to deliberately design the electromagnetic environment of one and the same qubit. We found that the phase coherence time of the flux qubits is limited by energy relaxation at the degeneracy point and rapidly falls off moving away from this point due to $1/f$-noise. We also found non-random beatings in the Ramsey and spin echo decay traces of flux qubits. As suggested by numerical simulations, the beatings are most likely caused by the resonant interaction of the qubit with one or a few two-level fluctuators.

In a joint activity between experimental and theory groups we also could make important contributions to the field of superconducting circuit quantum electrodynamics (circuit-QED), the circuit analogue of optical cavity-QED. This very interesting and prospering new field in SQIP was emerging from the successful experimental implementation of quantum-optical ideas into superconducting solid-state circuits. In the field of quantum optics a large toolbox for manipulating quantum information has been developed during the past decades. While the basic ideas exist, the challenge now consists in transferring them to superconducting solid-state systems, e.g. to the domain of microwave photons traveling along superconducting transmission lines and interacting with superconducting circuitry, taking into account the different parameter regimes and limitations such as decoherence processes. Even more than that, this novel physical implementation may allow for completely new concepts to be developed.

The field of superconducting circuit-QED is given increasing attention in SFB 631 by a new project conducted by WMI and is expected to receive growing importance for other kinds of solid-state qubits. In our preliminary work we already proposed a source for single microwave photons and a homodyne tomography detection scheme based on superconducting quantum

circuits. Furthermore, a scheme for the highly efficient generation of microwave photon pairs in a superconducting transmission line resonator coupled to a superconducting circuit on a chip has been proposed and analyzed. Experiments that implement part of the required microwave elements (e.g. a hybrid ring acting as beam splitter, transmission lines, resonators) already have been started at WMI and are planned to be continued in the next funding period of SFB 631.

Highlights and perspectives in high-T_c research: A midterm report of the Research Unit FOR 538

R. Hackl [1]

20 years of research into high-T_c superconducting cuprates provided us with new fascinating physics and painstaking efforts to disentangle intrinsic from generic properties. Needless to say that the understanding of the various phenomena, in particular the explanation of superconductivity is far from being complete. To make further progress joint efforts became more and more promising. Among the various efforts worldwide there are two initiatives fostering a relatively close collaboration: the Canadian Institute of Advanced Research (CIAR) and the DFG Research Unit (Forschergruppe FOR 538) *Doping Dependence of Phase Transitions and Ordering Phenomena in Copper-Oxygen Superconductors*.

The Research Unit with seven experimental and theoretical groups and the WMI as coordinating institution was launched in February 2004. One may wonder what kind of new information could be added after 20 years of worldwide effort. However, the last years brought enormous progress in instrumentation, theoretical methodology, and sample preparation. Just as an example, the electronic mean free path at low temperature reaches now the micrometer range in the quarternary oxide $YBa_2Cu_3O_{6+x}$. Not surprisingly, quite unexpected results are being collected since then.

In addition, the Research Unit follows a quite unique approach and tries to combine the results of several methods on the very same sample, not as usual on a material system. In this way, a quantitative simultaneous analysis really tells us something about the intrinsic properties and facilitates the isolation of material-specific ones. On such a basis, the microscopic and phenomenological theoretical approaches have a much better chance to carve out the mechanism of superconductivity.

In the period 2004-2006, 47 papers were published by FOR 538 including 11 publications in Nature, Science, and Physical Review Letters. Two articles appeared in or are accepted for publication in Review of Modern Physics. In the same time period the principal investigators were invited to 99 topical presentations at international conferences. Among the topics studied, the following results can be considered particular highlights:

- Numerical schemes to calculate the ground-state properties and one-particle spectral functions of the Hubbard and t-J models have advanced considerably. The results compare very favorably with experimental observations. By developing and implementing novel, systematic cluster approximation methods Hanke's group at the University of Würzburg has contributed substantially [1].

- Detailed studies of the momentum, temperature, and dopant dependence of the dressing of the charge carriers by angle-resolved photoemission spectroscopy (ARPES) studies have uncovered key evidence of strong interactions between spin excitations and charge carriers. Many of the developments originate in the work of the group at the Leibniz Institute of Solid State and Materials Research (IFW) in Dresden [2]. In particular, this group pioneered the use of circularly polarized light to determine the parity of the pairing boson [3].

- Optical ellipsometry measurements pioneered by Bernhard's group at the University of Fribourg (Switzerland) now continuously cover a spectral range from about 5 meV to

[1] This work is supported by the DFG through the Research Unit FOR538.

6.5 eV. Measurements of the in-plane and out-of-plane optical conductivities using this method [4] have revealed a detailed picture of spectral weight shifts associated with the superconducting state and with the pseudogap state, with incisive implications for kinetic energy-driven pairing mechanisms.

- Evidence of a "universal" spin excitation spectrum common to all families of high-temperature superconductors has emerged from recent neutron scattering measurements, with Keimer's group at the Max-Planck Institute for Solid State Research in Stuttgart and at the new neutron source "Heinz Maier-Leibnitz" in Garching contributing at the cutting edge [5]. By working on large arrays of fully untwinned crystals, this group has also reported the first detailed characterization of the in-plane anisotropy of the spin excitations, which allows an in-depth comparison with the predictions of stripe theories [6].

- Universal low-energy excitations in the sub-THz range have been observed in $La_{2-x}Sr_2CuO_4$ and $YBa_2Cu_3O_{6+x}$ by electronic Raman scattering experiments in the group at the WMI reflecting fluctuations of the charge and spin superstructure (see contribution "Interrelation of ordering and superconductivity in cuprates" in this Report) [7].

- Controlled substitution of magnetic and nonmagnetic impurities has been used to pinpoint the origin of various anomalies in the cuprates. The results can be viewed as a magnetic analog of the isotope effect. Prominent examples include joint work by the groups in Dresden, Stuttgart and Munich (Erb) on the modification of spin excitations and electron self-energy effects by Zn substitution [8], and the observation of an enhancement of the pseudogap by Ni substitution in Bernhard's group [9]. Hanke's group has recently developed new numerical concepts for a systematic understanding of impurity effects in the cuprates.

- The demonstration of high-level ARPES experiments on $YBa_2Cu_3O_{6+x}$ by the IFW group in Dresden [10] has opened up the possibility to carry out detailed neutron and ARPES experiments on the same samples, and to analyze data from these momentum-resolved spin and charge spectroscopies in terms of quantitative theoretical models. A joint effort by the Dresden, Stuttgart, and Würzburg groups has generated very promising results.

- The preparation of high quality single crystals of $Nd_{2-x}Ce_2CuO_4$ and $Pr_{2-x}Ce_2CuO_4$ (see contribution "Sampling of the phase diagram of the cuprate superconductors") in the complete accessible range facilitates now systematic studies in the entire phase diagram. Preliminary ARPES, ellipsometry, and Raman results are promising, and the crystals are big enough even for inelastic neutron scattering experiments.

This list and important results published by other groups demonstrate that the unique interplay of spin, charge, and lattice degrees of freedom will be in the main focus of future research to explain the cuprates. To this end and in order to further strengthen the Research Unit for the second funding period proposed recently, three new groups are supposed to join. Among those the two additional theory projects not only improve the balance between the now 6 experimental and 3 theoretical projects but also bring in exactly the required expertise to better understand the competition between different interactions and phases in the strong- and the weak-coupling limits.

The potential importance of electron-phonon interactions for the pairing mechanism has been highlighted by theoretical work [11] as well as ARPES [12], neutron scattering [13] and scanning tunneling spectroscopy [14] experiments. The Research Unit recognizes the scientific interest in electron-phonon interactions in strongly correlated systems, and the importance of

resolving the relative contributions of magnetic and electron-phonon interactions to the electron self-energy in the cuprates. We have hence invited Carsten Honerkamp at the University of Würzburg to join. He and his group pioneered a renormalization-group scheme that allows a controlled, systematic treatment of the electron-phonon and electron-electron interaction on equal footing for weak and intermediate coupling [15].

Recent theoretical advances have led to the first reliable prediction of the spin dynamics of striped phases [18]. The results allow a detailed comparison with neutron scattering data. Matthias Vojta and his group at the University of Cologne, who are leading contributors to this work and the first to calculate the magnetic excitations of fluctuating stripe arrays [19], have joined the Research Unit for the renewal.

Finally, thermodynamic and transport data on the boundary between superconducting and antiferromagnetic phases in $YBa_2Cu_3O_{6+x}$ have recently been reported by a Canadian research group , utilizing in part a newly developed "room-temperature annealing" protocol [20]. The Research Unit will pursue this and an alternative approach. Specifically, we will apply multiple experimental probes to ultra-pure Ca-substituted $Y_{1-y}Ca_yBa_2Cu_3O_{6+x}$ single crystals supplied by Erb's group at the WMI and analyze the results in close cooperation. The transport and NMR group of the IFW headed by B. Büchner will join the Research Unit and complement the arsenal of experimental probes available to resolve important issues such as stripe order. In this context the application of magnetic fields and pressure is an important diagnostic tool [21] and will be implemented by the groups in Dresden and Munich.

The evaluation meeting of the renewal on November 15, 2006 can be considered very promising. Given the unanimous positive vote of the referees we hope - after final approval by the DFG - to receive funding for another three years starting in February 2007.

References

[1] M. Aichhorn *et al.*, Phys. Rev. B **74**, 024508 (2006); C. Dahnken *et al.*, Phys. Rev. B **70**, 245110 2004.
[2] A.A. Kordyuk *et al.*, Phys. Rev. Lett. **92**, 257006 (2004), A.A. Kordyuk *et al.*, Phys. Rev. Lett. **97**, 017002 (2006).
[3] S.V. Borisenko *et al.*, Phys. Rev. Lett. **96**, 067001 (2006).
[4] A.V. Boris *et al.*, Science **304**, 708 (2004).
[5] S. Pailhès *et al.*, Phys. Rev. Lett. **93**, 167001 (2004).
[6] V. Hinkov *et al.*, Nature (London) **430**, 650 (2004).
[7] L. Tassini *et al.*, Phys. Rev. Lett. **95**, 117002 (2005); R. Hackl *et al.*, in *Adv. in Solid State Phys.* **45**, edited by B. Kramer (Springer, Berlin, 2005), p. 227.
[8] V.B. Zabolotnyy *et al.*, Phys. Rev. Lett. **96**, 037003 (2006).
[9] A.V. Pimenov *et al.*, Phys. Rev. Lett. **94**, 227003 (2005).
[10] A.S.Borisenko *et al.*, Phys. Rev. Lett. **96**, 117004 (2006).
[11] Z.B. Huang *et al.*, Phys. Rev. B **68** 220507(R) (2003); A.S. Mishchenko and N. Nagaosa, Phys. Rev. Lett. **93**, 036402 (2004); T.P. Devereaux *el al.*, Phys. Rev. Lett. **93**, 117004 (2004).
[12] A. Lanzara *el al.*, Nature (London) **412**, 510 (2001); T. Cuk *el al.*, Phys. Rev. Lett. **93**, 117003 (2004).
[13] D. Reznik *et al.*, Nature (London) **440**, 1170 (2006).
[14] J. Lee *et al.*, Nature **442**, 546 (2006).
[15] H.C. Fu, C. Honerkamp, and D.H. Lee, Europhys. Lett. **75**, 146 (2006).
[16] T. Keller *et al.*, Phys. Rev. Lett. **96**, 225501 (2006).
[17] S.P. Bayrakci *et al.*, Science **312**, 1926 (2006).
[18] G. Uhrig, K.P. Schmidt, and M. Grüninger, Phys. Rev. Lett. **93**, 267003 (2004); M. Vojta and T. Ulbricht, Phys. Rev. Lett. **93**, 127002 (2004).
[19] M. Vojta, T. Vojta, and R.K. Kaul, cond-mat/0510448.
[20] R. Liang *el al.*, Physica C **383**, 1 (2002); A. Hosseini *et al.*, Phys. Rev. Lett. **93**, 107003 (2004); R. Liang *et al.*, Phys. Rev. Lett. **94**, 117001 (2005); M. Sutherland *et al.*, Phys. Rev. Lett. **94**, 147004 (2005); N. Doiron-Leyraud *et al.*, cond-mat/0606645.
[21] B. Lake *et al.*, Nature (London) **415**, 299 (2002); B. Lake *et al.*, Nature Mater. **4**, 658 (2005); B. Simovič *et al.*, Europhys. Lett. **66**, 722 (2004).

Response and relaxation in unconventional superconductors

Dietrich Einzel and Ludwig Klam

Introduction

We consider quite generally the impurity–limited transport and relaxation properties of unconventional superconductors in view of an applicability to hole–doped cuprate superconductors. It is well established, that the pairing correlations in cuprate superconductors are *unconventional* in the sense that the Fermi surface average of the gap function $\Delta_{\mathbf{p}}$ vanishes, i. e. $\langle\Delta_{\mathbf{p}}\rangle_{\rm FS} \equiv 0$. As a special form of the gap anisotropy we consider the case of B_{1g} gap symmetry, $\Delta_{\mathbf{p}} = \Delta_0(T)\cos(2\phi)$. Note that the nodal structure of such a gap function implies, that the thermal excitations of the system, the Bogoliubov quasiparticles (BQP), which have an excitation spectrum of the usual form $E_{\mathbf{p}} = [\xi_{\mathbf{p}}^2 + \Delta_{\mathbf{p}}^2]^{1/2}$, can be created at arbitrary small energies $E_{\mathbf{p}}$ (nodal quasiparticles). This is reflected in the form of the BQP density of states $N_{\rm S}$ varying as $N_{\rm S}/N_0 = E_{\mathbf{p}}/\Delta_0$ at low energy in the clean limit. Here N_0 is the electronic density of states at the Fermi surface for one spin projection. The statistical properties of the excitation gas can conveniently be described by the thermal Fermi distribution $\nu_{\mathbf{p}} = [\exp(E_{\mathbf{p}}/k_{\rm B}T) + 1]^{-1}$. Collisions of the BQP with impurities are treated within the t-matrix approximation, which is limited here to the case s–wave scattering. In that case, the relevant scattering parameters are the impurity concentration n_i and the s–wave scattering phase shift δ_0, giving rise to a normal state scattering rate $\tau_{\rm N}^{-1} = (2n_i/\pi\hbar N_0)\sin^2\delta_0$. The description thus allows to treat the cases of weak scattering (Born limit, $\delta_0 \to 0$) and strong scattering (unitary limit $\delta_0 \to \pi/2$) on the same footing.

The resonant impurity scattering model

In the presence of impurities, the BQP energy gets renormalized through the impurity self–energy Σ_e via $\tilde{E}_{\mathbf{p}} = E_{\mathbf{p}} + \Sigma_e(\tilde{E_{\mathbf{p}}})$, with Σ_e evaluated within the self–consistent t–matrix approximation [1]

$$\Sigma_e(\tilde{E}_{\mathbf{p}}) \;=\; \frac{i\hbar}{2\tau_{\rm N}}\;\frac{D(\tilde{E}_{\mathbf{p}})}{\cos^2\delta_0 + \sin^2\delta_0 D^2(\tilde{E}_{\mathbf{p}})} \tag{1}$$

Here, the complex function $D(\tilde{E}_{\mathbf{p}}) = \langle\tilde{E}_{\mathbf{p}}/[\tilde{E}_{\mathbf{p}}^2 - \Delta_{\mathbf{p}}^2]^{1/2}\rangle_{\rm FS}$ extends the density of states of the superconductor $N_{\rm S}(E_{\mathbf{p}})/N_0 = \Re D(\tilde{E}_{\mathbf{p}})$ to include impurity effects. From the impurity self energy we obtain the elastic scattering rate [2]

$$\frac{1}{\tau_{\mathbf{p}}^{\rm S}} \;=\; \frac{2}{\hbar}\Im\Sigma_e(\tilde{E}_{\mathbf{p}}) = \frac{\Re D(\tilde{E}_{\mathbf{p}})}{\tau_{\rm N}}\frac{\cos^2\delta_0 + \sin^2\delta_0|D(\tilde{E}_{\mathbf{p}})|^2}{|\cos^2\delta_0 + \sin^2\delta_0 D^2(\tilde{E}_{\mathbf{p}})|^2} \tag{2}$$

The explicit form for $1/\tau_{\mathbf{p}}^{\rm S}$ becomes particularly simple at high energies and in the limit $E_{\mathbf{p}} \to 0$, where the full self–consistent treatment of the renormalization $\tilde{E}_{\mathbf{k}}$ is necessary ($\Sigma_0'' \equiv \Im\Sigma_e(0)$) [3]:

$$\frac{\xi_{\mathbf{p}}}{E_{\mathbf{p}}}\tau_{\mathbf{p}}^{\rm s} = \begin{cases} \Theta(E_{\mathbf{p}} - \Delta_{\mathbf{p}})\frac{\tau_{\rm N}}{\Re D(\tilde{E}_{\mathbf{p}})}\left[\cos^2\delta_0 + \sin^2\delta_0|D(E_{\mathbf{p}})|^2\right] & ;\; E_{\mathbf{p}} > \Sigma_0'' \\ \frac{\hbar}{2}\Sigma_0''^2/\left[\Sigma_0''^2 + \Delta_{\mathbf{p}}^2\right]^{3/2} & ;\; E_{\mathbf{p}} \to 0 \end{cases} \tag{3}$$

Response theory

In order to test the response and transport properties of a superconducting system, one has to apply external perturbation potentials, which can be classified in the following way:

$$\delta\xi_{\mathbf{k}}^{\mathrm{ext}} \;=\; e\Phi - \frac{e}{c}\mathbf{v}_{\mathbf{k}}\cdot\mathbf{A} + m\{\mathbf{M}_{\mathbf{k}}^{-1}\}_{ij} r_0 A_i^I A_j^S + \left[p_i V_{\mathbf{k}j} - \frac{\mathbf{p}\cdot\mathbf{V}_{\mathbf{k}}}{d}\delta_{ij}\right]\delta u_{ij} = \sum_a a_{\mathbf{k}}\delta\xi_a \qquad (4)$$

The first and second term in (4) describe the coupling of the electronic system to the electromagnetic scalar (Φ) and vector ($\mathbf{A}$) potential, respectively. The third term represents the electronic coupling to a typical Raman scattering process, with an incoming photon of energy $\hbar\omega_I$, momentum $\hbar\mathbf{k}_I$ and polarization along $\mathbf{A}^I$, and a scattered photon with energy $\hbar\omega_S$, momentum $\hbar\mathbf{k}_S$ and polarization along $\mathbf{A}^S$ leaving the sample. This process couples, for example, to electronic excitations near the Fermi surface with energy transfer $\hbar\omega = \hbar\omega_I - \hbar\omega_S$ and momentum transfer $\hbar\mathbf{q} = \hbar\mathbf{k}_I - \hbar\mathbf{k}_S$, and is describable by a $\mathbf{k}$–dependent so–called Raman tensor $\boldsymbol{\gamma}_{\mathbf{k}}$, which we have approximated in Eq. (4) by the inverse effective mass tensor $\{\mathbf{M}_{\mathbf{k}}^{-1}\}_{\mu\nu} = \partial^2\xi_{\mathbf{k}}/\hbar^2\partial k_\mu\partial k_\nu$. In (4) $r_0 = e^2/mc^2$ denotes the Thompson radius. The fourth term in (4) represents the electronic coupling to the lattice strain field δu_{ij}, which leads to a dissipative response of the electronic stress tensor and hence to the attenuation of ultrasound. In (4) $\mathbf{V}_{\mathbf{k}} = \partial E_{\mathbf{k}}/\hbar\partial\mathbf{k} = (\xi_{\mathbf{k}}/E_{\mathbf{k}})\mathbf{v}_{\mathbf{k}}$ is the group velocity of the BQP and d the dimension of the system. The r.h.s. of Eq. (4) generalizes the $\mathbf{k}$–space structure of the perturbation potentials by introducing a $\mathbf{k}$–dependent so–called vertex function $a_{\mathbf{k}}$, together with a collection of fictive potentials $\delta\xi_a$, related to each vertex. In this spirit, the vertex function $a_{\mathbf{k}}$ is related to the specific experiment (electromagnetic response, Raman response and relaxation, sound attenuation) under consideration. In the Raman case one has $a_{\mathbf{k}} = \gamma_{\mathbf{k}} = \hat{\mathbf{e}}_I\cdot\boldsymbol{\gamma}_{\mathbf{k}}\cdot\hat{\mathbf{e}}_S$ with $\hat{\mathbf{e}}_{I,S}$ the unit vectors in the direction of $\mathbf{A}_{I,S}$ and $\delta\xi_\gamma = r_0|\mathbf{A}_I||\mathbf{A}_S|$. In the case of sound attenuation one may write $a_{\mathbf{k}} = \hat{\mathbf{q}}\cdot\boldsymbol{\sigma}_{\mathbf{k}}\cdot\hat{\mathbf{u}}$ with the definitions $p_i V_{\mathbf{k}j} - \mathbf{p}\cdot\mathbf{V}_{\mathbf{k}}\delta_{ij}/d = p_{\mathrm{F}} v_{\mathrm{F}}(\xi_{\mathbf{k}}/E_{\mathbf{k}})\sigma_{\mathbf{k}ij}$ and $\delta\xi_\sigma = \omega|\mathbf{q}||\mathbf{u}|$. It is interesting to note, that in quasi–2–d systems the vertex functions $a_{\mathbf{k}}$ for Raman scattering and sound attenuation coincide in case of B_{1g}– ($a_{\mathbf{k}} = \cos(2\phi)$) and B_{2g}– ($a_{\mathbf{k}} = \sin(2\phi)$) symmetry. These Raman polarizations can be shown to correspond to the attenuation of *transverse* sound, i. e. $\hat{\mathbf{q}}\perp\hat{\mathbf{u}}$, if $\mathbf{q}$ is oriented parallel (B_{2g}–symmetry) to the crystal (a–) axis, or is tilted by 45^o (B_{1g}–symmetry) from it. [4]. In the homogeneous limit $\mathbf{q}\to 0$ the response and transport properties can be clearly separated into a condensate and a BQP contribution. In the case of electronic Raman scattering, the condensate contributes to what is referred to as the *pair–breaking Raman effect*, which has been extensively discussed in the literature [5, 6]. In contrast, the condensate does not contribute to dissipative processes like, for example, the sound attenuation.

Response and homogeneous quasiparticle relaxation

In what follows we shall therefore concentrate on the BQP contribution (normal component in the spirit of a two–fluid description) to the response, transport and relaxation properties. Restricting our consideration to the case of Raman scattering and sound attenuation, the vertex $a_{\mathbf{k}}$ has positive parity, i. e. $a_{-\mathbf{k}} = a_{\mathbf{k}}$. In this case, one may define a macroscopic BQP density via

$$\delta n_a^Q = \sum_{\mathbf{p}\sigma} a_{\mathbf{p}}(\xi_{\mathbf{p}}/E_{\mathbf{p}})\delta\nu_{\mathbf{p}}\ , \qquad (5)$$

with $\delta\nu_{\mathbf{p}}$ the deviation of the BQP distribution function from equilibrium. Special cases include then the BQP Raman response function δn_γ^Q and the stress tensor response function $\hat{\mathbf{q}}\cdot\boldsymbol{\Pi}^Q\cdot\hat{\mathbf{u}}$.

Here $\mathbf{\Pi}^Q$ denotes the BQP stress tensor and the unit vectors in the direction of propagation ($\hat{\mathbf{q}}$) and polarization ($\hat{\mathbf{u}}$) emerge from the standard representation of the strain tensor $\delta u_{ij} \propto q_i u_j$ [4]. In the homogeneous limit $\mathbf{q} \to 0$ the dynamics of the BQP system is entirely governed by relaxation processes on time scales set forth by a vertex–dependent BQP relaxation time τ^Q_{aa}. Assuming the fictive potentials $\delta\xi_a$ to vary as $\propto \exp(i\mathbf{q}\cdot\mathbf{r} - i\omega t)$, these relaxation processes obey a set of general equations for each vertex $a_{\mathbf{k}}$

$$\omega \delta n^Q_a = -i \left[\delta n^Q_a - \delta n^{Q\ \mathrm{loc}}_a \right] / \tau^Q_{aa} \quad , \tag{6}$$

which describe the relaxation of the BQP density back to its local equilibrium value $\delta n^{Q\ \mathrm{loc}}_a = \chi^{Q\ \mathrm{loc}}_{aa} \delta\xi_a$ where $\chi^{Q\ \mathrm{loc}}_{aa} = \sum_{\mathbf{p}\sigma} a^2_{\mathbf{p}} (\xi^2_{\mathbf{p}}/E^2_{\mathbf{p}})(-\partial\nu_{\mathbf{p}}/\partial E_{\mathbf{p}})$. Eq. (6) represents a straightforward generalization of the problem of intrinsic BQP density relaxation [7], which can be obtained from (6) in the special case $a_{\mathbf{p}} \equiv 1$. The decay of the BQP density δn^Q_1 occurs then as a consequence of the fact that the number of Bogoliubov quasiparticles is not a conserved quantity. Since the quasiparticle number is conserved in the normal state, the BQP density relaxation time τ^Q_{11} must diverge in the limit as $T \to T_c^-$ [7]. Eq. (6) originates from the homogeneous limit of a BQP Boltzmann equation for the nonequilibrium BQP distribution function $\delta\nu_{\mathbf{p}}$ [8], in which the collision integral is approximated such that it preserves the number conservation law in the normal state [8]. The general solution of Eq. (6) can be written in terms of a homogeneous BQP response function $\chi^Q_{aa}(\omega)$, generalized to the case of a vertex function $a_{\mathbf{k}}$ different from a constant:

$$\delta n^Q_{aa}(\omega) = \chi^Q_{aa}(\omega)\delta\xi_a(\omega) \ ; \ \chi^Q_{aa}(\omega) = \chi^{Q\ \mathrm{loc}}_{aa} / [1 - i\omega\tau^Q_{aa}] \tag{7}$$

Eq. (7) describes the general connection between response and relaxation of the BQP system in the homogeneous limit for a given vertex $a_{\mathbf{k}}$.

Transport properties

The transport parameter T^Q_{aa}, related to τ^Q_{aa}, can be defined in the usual way:

$$T^Q_{aa} = \Im[\chi^Q_{aa}(\omega)/\omega] \stackrel{\omega\to 0}{\to} \chi^{Q\ \mathrm{loc}}_{aa} \tau^Q_{aa} \tag{8}$$

After a lengthy calculation, the details of which can be found in ref. [9], we obtain the following result for T^Q_{aa} the BQP relaxation time τ^Q_{aa} at $\omega \to 0$:

$$T^Q_{aa} = \chi^{Q\ \mathrm{loc}}_{aa} \tau^Q_{aa} \stackrel{\omega\to 0}{=} \sum_{\mathbf{p}\sigma} a^2_{\mathbf{p}} \frac{\xi^2_{\mathbf{p}}}{E^2_{\mathbf{p}}} \left(-\frac{\partial\nu_{\mathbf{p}}}{\partial E_{\mathbf{p}}} \right) \tau^S_{\mathbf{p}} + \left[\sum_{\mathbf{p}\sigma} a_{\mathbf{p}} \frac{\xi^2_{\mathbf{p}}}{E^2_{\mathbf{p}}} \left(-\frac{\partial\nu_{\mathbf{p}}}{\partial E_{\mathbf{p}}} \right) \right]^2 / \sum_{\mathbf{p}\sigma} \frac{\Delta^2_{\mathbf{p}}}{E^2_{\mathbf{p}}} \left(-\frac{\partial\nu_{\mathbf{p}}}{\partial E_{\mathbf{p}}} \right) \frac{1}{\tau^S_{\mathbf{p}}} \tag{9}$$

As already mentioned, the case $a_{\mathbf{p}} = 1$ describes the phenomenon of intrinsic BQP relaxation and the associated BQP density relaxation time τ^Q_{11} is seen to diverge in the limit $T \to T_c^-$, thus reflecting the number conservation law in the normal state. On the other hand, the second term in Eq. (9) vanishes identically for vertices obeying $\langle a_{\mathbf{p}} \rangle_{\mathrm{FS}} \equiv 0$ and T^Q_{aa} has the usual form of a transport parameter related to the vertex $a_{\mathbf{k}}$. In what follows, we wish to restrict our considerations to the latter case and rewrite the transport parameter T^Q_{aa} in the following form, in which the dependence on temperature and scattering phase shift becomes particularly clear [10]:

$$T^Q_{aa}(T) = T^N_{aa} \left\{ C_{aa} + (1 - C_{aa}) \left[\sin^2\delta_0 Y^{aa}_1(T) + \cos^2\delta_0 Y^{aa}_3(T) \right] \right\} \tag{10}$$

In (10) T_{aa}^N denotes the normal state limit of T_{aa}^Q. Eq. (11) represents an interpolation procedure for the temperature dependence of the transport parameter T_{aa}^Q, which uses the fact, expressed in Eq. (3), that at high BQP energies the BQP relaxation time $\tau_{\mathbf{k}}^S$ does not need to be evaluated self–consistently. This gives rise to the definition of a set of generalized Yosida functions of the form

$$Y_n^{aa}(T) = \frac{1}{\langle a_{\mathbf{p}}^2 \rangle_{\mathrm{FS}}} \left\langle 2a_{\mathbf{p}}^2 \int_{\Delta_{\mathbf{p}}}^{\infty} \frac{dE_{\mathbf{p}} \sqrt{E_{\mathbf{p}}^2 - \Delta_{\mathbf{p}}^2}}{E_{\mathbf{p}}} \left(-\frac{\partial \nu_{\mathbf{p}}}{\partial E_{\mathbf{p}}} \right) \frac{|D(E_{\mathbf{p}})|^{3-n}}{\Re D(E_{\mathbf{p}})} \right\rangle_{\mathrm{FS}} \quad ; \tag{11}$$

which describe the temperature dependence of T_{aa}^Q. On the other hand, an inspection of (3) shows, that in the limit $E_{\mathbf{k}} \to 0$ the elastic relaxation time $\tau_{\mathbf{k}}^s$ tends to a *finite value* in the unitary limit, which reflects the fact, that there exists an impurity band originating from resonant pair–breaking processes, described by the t–matrix. This leads to a low–temperature offset in the temperature dependence of T_{aa}^Q, which is described by the dimensionless parameter [11]

$$C_{aa} = \frac{\hbar}{2\tau_{\mathrm{N}}} \frac{1}{\langle a_{\mathbf{p}}^2 \rangle_{\mathrm{FS}}} \left\langle a_{\mathbf{p}}^2 \Sigma_0''^2 / \left[\Sigma_0''^2 + \Delta_{\mathbf{p}}^2 \right]^{3/2} \right\rangle_{\mathrm{FS}} \tag{12}$$

The description of the transport parameter T_{aa}^Q becomes *exact* at $T = 0$ and represents a very accurate approximation just below the transition temperature. For intermediate temperatures, Eq. (10) represents a physically quite transparent temperature interpolation scheme, which, however, is meaningful only as long as the generalized Yosida functions Y_n^{aa} vanish in the low temperature limit $T \to 0$. We turn now to an evaluation of Eq. (10) in the low temperature limit. In the limits of unitary ($\delta_0 \to \pi/2$) and Born ($\delta_0 \to 0$) scattering, we obtain for not too large values of Σ_0''/Δ_0:

$$\lim_{T\to 0} \frac{T_{aa}^{\mathrm{Q}}}{2\langle a_{\mathbf{p}}^2 \rangle_{\mathrm{FS}}} \overset{\delta_0 \to \pi/2}{=} \frac{N_{\mathrm{F}}\hbar}{\pi\Delta_0} \cdot \begin{cases} \left(\frac{\Sigma_0''}{\Delta_0}\right)^2 \ln \frac{4\Delta_0}{\Sigma_0''} & ; \ \mathrm{B}_{1g} \\ 1 & ; \ \mathrm{B}_{2g} \end{cases} \quad ; \quad \lim_{T\to 0} \frac{T_{aa}^{\mathrm{Q}}}{2\langle a_{\mathbf{p}}^2 \rangle_{\mathrm{FS}}} \overset{\delta_0 \to 0}{=} \begin{cases} 0 & ; \ \mathrm{B}_{1g} \\ \frac{N_{\mathrm{F}}\hbar}{\pi\Delta_0} & ; \ \mathrm{B}_{2g} \end{cases} \tag{13}$$

This important result shows an amazing qualitative difference between the B_{1g} and the B_{2g} polarization: in the B_{1g} case, the transport parameter depends on the parameters n_i and δ_0, characterizing the impurity scattering, whereas in the B_{2g} case it does not. This behavior of the zero temperature transport properties in the B_{2g} case occurs also in the case of electronic conductivity [3], the electronic thermal conductivity [13], the (electron–phonon interaction induced) sound attenuation [12] and has been termed *universal transport* [3]. For the case of Raman scattering, this result has first been derived for the unitary limit in ref. [14].

We consider finally the temperature dependence of T_{aa}^Q in the low temperature limit, where an analytical treatment is possible. Using the expansion of $D(x) = x[1 + i(2/\pi)\ln(x/4)]$ for $x = E_{\mathbf{k}}/\Delta_0 \ll 1$, one obtains in the B_{1g} case

$$\lim_{T\to 0} Y_1(T) = 4 \left(\frac{k_{\mathrm{B}}T}{\Delta_0}\right)^4 \left[b_{10} - b_{11} \ln\left(\frac{2\Delta_0}{k_{\mathrm{B}}T}\right) + b_{12} \ln^2\left(\frac{2\Delta_0}{k_{\mathrm{B}}T}\right) \right] \ ; \ \lim_{T\to 0} Y_3(T) = \frac{1}{12} \left(\frac{\pi k_{\mathrm{B}}T}{\Delta_0}\right)^2 \tag{14}$$

and in the B_{2g} case

$$\lim_{T\to 0} Y_1(T) = 4 \left(\frac{k_{\mathrm{B}}T}{\Delta_0}\right)^2 \left[b_{20} - b_{21} \ln\left(\frac{2\Delta_0}{k_{\mathrm{B}}T}\right) + b_{22} \ln^2\left(\frac{2\Delta_0}{k_{\mathrm{B}}T}\right) \right] \ ; \ \lim_{T\to 0} Y_3(T) = 1 \tag{15}$$

Here we have defined the coefficients $b_{k0} = a_{k0} + 4a_{k2}/\pi^2$, $b_{k1} = 8a_{k1}/\pi^2$, $b_{k2} = 4a_{k0}/\pi^2$, $k = 1, 2$ and $a_{k\mu} = \int_0^\infty dv v^{6-2k} \ln^\mu v / \cosh^2 v$ [15]. Clearly, the theory predicts a temperature–independent result for T_{aa}^Q in the B_{2g} case in the Born scattering limit. This was actually the

motivation for Pethick and Pines [1] to apply the t–matrix to the description of transport in heavy Fermion superconductors, since the experiments showed transport parameters vanishing at low T instead of staying constant below T_c.

Conclusion

In summary, we have demonstrated, how the response and transport properties of unconventional superconductors are linked together in a very simple way, if the long wavelength limit $\mathbf{q} \to 0$ is taken. We could also show, that for quasi–2–d systems the Raman scattering intensity is closely related to the transport of momentum (stress tensor) in the BQP system. An exception forms the A_{1g} Raman intensity, which has no analogue in the momentum current response. Moreover, since a constant contributes to the A_{1g}–Raman vertex, we can no longer expect the last term in Eq. (9) to vanish and we thus predict, that the BQP relaxation time diverges in the limit $T \to T_c^-$ for A_{1g} symmetry. A closer investigation of this fact will be subject to a forthcoming publication [16].

References

[1] C. J. Pethick and D. Pines, Phys. Rev. Lett. **57**, 118 (1986); P. Hirschfeld, D. Vollhardt, and P. Wölfle, Solid State Commun. **59**, 111 (1986).
[2] B. Arfi and C. J. Pethick, Phys. Rev. **B 38**, 2312 (1988).
[3] P. A. Lee, Phys. Rev. Lett. **71**, 1887 (1993).
[4] J. Moreno and P. Coleman, Phys. Rev. **B 53**, R2995 (1996).
[5] D. Einzel and R. Hackl, J. Raman Spectroscopy **27**, 307 (1996).
[6] T. P. Devereaux and A. P. Kampf, Int. J. of Modern Physics B **11**, 2093 (1997).
[7] P. Wölfle and D. Einzel, J. Low Temp. Phys. **23**, 39 (1978).
[8] D. Einzel and P. Wölfle, J. Low Temp. Phys. **32**, 19 (1978).
[9] Ludwig Klam, Diploma thesis, TU München (2006).
[10] D. Einzel and J. M. Parpia, Phys. Rev. **B 72**, 214518 (2005).
[11] In the Born limit ($\delta_0 \to 0$) there is a simple relation between Σ_0'' and the normal state lifetime τ_N, namely $\Sigma_0'' = 4\Delta_0 \exp(-\pi\tau_N\Delta_0/\hbar)$. In the unitary limit, on the other hand, one has to solve the transcendental equation $a^2 \ln(4/a) = \pi\hbar/4\tau_N\Delta_0$ for $a = \Sigma_0''/\Delta_0 \ll 1$ in order to relate Σ_0'' to τ_N.
[12] M. B. Walker, M. F. Smith and K. V. Samockhin, Phys. Rev. **B 65**, 014517 (2001).
[13] M. J. Graf, S.–K. Yip, J. A. Sausls, and D. Rainer, Phys. Rev. **B 53**, 15147 (1996).
[14] W. C. Wu and J. P. Carbotte, Phys. Rev. **B 57**, R5614 (1998); for a review see ref. [6].
[15] It is quite surprising, that the low–T behavior of $Y_1^{aa}(T)$ is close to the power laws $T^{3.5}$ in the B_{1g}– and $T^{1.5}$ in the B_{2g}–case, as predicted by Moreno and Coleman [4].
[16] D. Einzel and L. Klam, *to be published* (2007).

Electromagnetic and Raman response in unconventional superconductors

Dietrich Einzel and Ludwig Klam

Introduction

We consider quite generally both the collisionless electromagnetic response and the electronic Raman response of unconventional superconductors in view of an applicability to hole–doped cuprate superconductors. Traditionally, the collisionless response of superconductors is treated close to the homogeneous limit $\mathbf{q} \to 0$, with $\mathbf{q}$ the wavenumber of the external perturbation potentials [1]. In this contribution, the description will be generalized to arbitrary wavenumbers $\mathbf{q}$, with the only restriction that a separation of the various response kernels into particle–hole symmetric and asymmetric contributions still makes sense. The Bogoliubov quasiparticle (BQP) excitation spectrum is of the usual form $E_{\mathbf{k}} = [\xi_{\mathbf{k}}^2 + \Delta_{\mathbf{k}}^2]^{1/2}$ (with $\xi_{\mathbf{k}} = \epsilon_{\mathbf{k}} - \mu$ the normal state energy measured relative to the Fermi energy) and dominates the statistical properties of the excitation gas in terms of the thermal Fermi distribution $\nu_{\mathbf{k}} = [\exp(E_{\mathbf{k}}/k_{\rm B}T) + 1]^{-1}$. In global thermodynamic equilibrium, the superconductor is described by a diagonal momentum distribution function $n_{\mathbf{k}} = \langle \hat{c}_{\mathbf{k}\sigma}^\dagger \hat{c}_{\mathbf{k}\sigma} \rangle = u_{\mathbf{k}}^2 \nu_{\mathbf{k}} + v_{\mathbf{k}}^2 [1 - \nu_{\mathbf{k}}]$, with the BCS coherence factors $u_{\mathbf{k}}^2 = \frac{1}{2}(1 + \xi_{\mathbf{k}}/E_{\mathbf{k}})$ and $v_{\mathbf{k}}^2 = 1 - u_{\mathbf{k}}^2$. The pair formation, which sets in spontaneously below the transition temperature $T_{\rm c}$ as a consequence of an attractive pairing interaction $\Gamma_{\mathbf{kp}}$, is described in global equilibrium by the (singlet) pair amplitude $g_{\mathbf{k}} = \langle \hat{c}_{-\mathbf{k}\uparrow} \hat{c}_{\mathbf{k}\downarrow} \rangle = u_{\mathbf{k}} v_{\mathbf{k}} [1 - 2\nu_{\mathbf{k}}] = -\theta_{\mathbf{k}} \Delta_{\mathbf{k}}$, with $\theta_{\mathbf{k}} = \tanh(E_{\mathbf{k}}/2k_{\rm B}T)/2E_{\mathbf{k}}$. The energy gap $\Delta_{\mathbf{k}}$ of the superconductor is determined from the self–consistency equation $\Delta_{\mathbf{k}} = \sum_{\mathbf{p}} \Gamma_{\mathbf{kp}} g_{\mathbf{p}}$. In what follows, we will assume *unconventional* spin singlet pairing correlations, with a gap function $\Delta_{\mathbf{k}} = \Delta_0(T) \cos(2\phi)$ of d–wave (B_{1g}–) symmetry, which vanishes, when integrated over the Fermi surface, i. e. $\langle \Delta_{\mathbf{p}} \rangle_{\rm FS} \equiv 0$.

Response formalism

In order to test the response properties of a superconducting system, one has to apply external perturbation potentials, which can be classified in the following way:

$$\delta\xi_{\mathbf{k}}^{\rm ext} = e\Phi - \frac{e}{c}\mathbf{v}_{\mathbf{k}} \cdot \mathbf{A} + \{\boldsymbol{\gamma}_{\mathbf{k}}\}_{ij} r_0 A_i^I A_j^S \tag{1}$$

The first and second term on the r.h.s. of (1) describe the coupling of the electronic system to the electromagnetic scalar (Φ) and vector ($\mathbf{A}$) potential, respectively. The third term represents the electronic coupling to a typical Raman scattering process, with an incoming photon of energy $\hbar\omega_I$, momentum $\hbar\mathbf{k}_I$ and polarization along $\mathbf{A}^I$ and a scattered photon with energy $\hbar\omega_S$, momentum $\hbar\mathbf{k}_S$ and polarization along $\mathbf{A}^S$ leaving the sample. This process couples to electronic excitations near the Fermi surface with energy transfer $\hbar\omega = \hbar\omega_I - \hbar\omega_S$ and momentum transfer $\hbar\mathbf{q} = \hbar\mathbf{k}_I - \hbar\mathbf{k}_S$, and is describable by a $\mathbf{k}$–dependent so–called Raman tensor $\boldsymbol{\gamma}_{\mathbf{k}}$, which we have approximated in Eq. (1) by the inverse effective mass tensor $m^{-1}\{\boldsymbol{\gamma}_{\mathbf{k}}\}_{\mu\nu} = \{\mathbf{M}_{\mathbf{k}}^{-1}\}_{\mu\nu} = \partial^2\xi_{\mathbf{k}}/\hbar^2 \partial k_\mu \partial k_\nu$. In Eq. (1) $r_0 = e^2/mc^2$ is the Thompson radius. Assuming the perturbation potentials (1) to vary in space and time $\propto \exp(i\mathbf{q} \cdot \mathbf{r} - i\omega t)$, they give rise to $\mathbf{q}$– and ω–dependent changes in the diagonal

$$\delta n_{\mathbf{k}}(\mathbf{q},\omega) = \delta\langle \hat{c}_{\mathbf{k}+\frac{\mathbf{q}}{2}\sigma}^\dagger \hat{c}_{\mathbf{k}-\frac{\mathbf{q}}{2}\sigma} \rangle(\omega) \;\; ; \;\; \delta\xi_{\mathbf{k}}(\mathbf{q},\omega) = \delta\xi_{\mathbf{k}}^{\rm ext} + \sum_{\mathbf{p}\sigma} V_{\mathbf{q}} \delta n_{\mathbf{k}}(\mathbf{q},\omega) \tag{2}$$

and off–diagonal

$$\delta g_{\mathbf{k}}(\mathbf{q},\omega) = \delta\langle \hat{c}_{-\mathbf{k}+\frac{\mathbf{q}}{2}\downarrow}\hat{c}_{\mathbf{k}-\frac{\mathbf{q}}{2}\uparrow}\rangle(\omega) \;\; ; \;\; \delta\Delta_{\mathbf{k}}(\mathbf{q},\omega) = \sum_{\mathbf{p}} \Gamma_{\mathbf{kp}}\delta g_{\mathbf{p}}(\mathbf{q},\omega) \tag{3}$$

nonequilibrium distribution functions and energies. In (2) $V_{\mathbf{q}} = 4\pi e^2/\mathbf{q}^2$ denotes the Fourier transform of the long–range Coulomb potential coupling to the macroscopic density fluctuation $\delta n(\mathbf{q},\omega) = \sum_{\mathbf{p}\sigma}\delta n_{\mathbf{p}}(\mathbf{q},\omega)$. At finite wavenumbers $\mathbf{q}$ the momenta are shifted according to $\mathbf{k}_{\pm} = \mathbf{k} \pm \mathbf{q}/2$. This introduces two new variables into the description, namely $\eta^-_{\mathbf{k}} \equiv \eta_{\mathbf{k}} = \xi_{\mathbf{k}+} - \xi_{\mathbf{k}-} \equiv \mathbf{q}\cdot\mathbf{v}_{\mathbf{k}}$ and $\eta^+_{\mathbf{k}} = \xi_{\mathbf{k}+} + \xi_{\mathbf{k}-} = 2\xi_{\mathbf{k}} + (\hbar v_{\mathrm{F}}|\mathbf{q}|)^2/8E_{\mathrm{F}}$. The quantity $\eta^+_{\mathbf{k}}$ turns out to allow for a separation of the response kernels into terms *even* and *odd* w.r.t. the operation $\xi_{\mathbf{k}} \to -\xi_{\mathbf{k}}$. A particle–hole–symmetric description of the response implies that one may neglect terms odd in $\xi_{\mathbf{k}}$. This is possible, however, only if one restricts the wavenumbers to the quasi-classical regime $\hbar v_{\mathrm{F}}|\mathbf{q}| \ll E_{\mathrm{F}}$. Keeping this restriction in mind, we turn to the coupled dynamics of the diagonal distribution function $\delta n_{\mathbf{k}}$ and the off–diagonal distribution function $\delta g_{\mathbf{k}}$, which can be described by matrix–kinetic equations in Nambu space [2, 3]. For our purposes it is however convenient to cast these into a form reminiscent of the continuity equation in the normal state [1, 4]:

$$\omega\delta n_{\mathbf{k}} - \mathbf{q}\cdot\mathbf{v}_{\mathbf{k}}\left[\delta n_{\mathbf{k}} + \Phi_{\mathbf{k}}\delta\xi_{\mathbf{k}}\right] = -\lambda_{\mathbf{k}}\left[\omega\delta\xi^+_{\mathbf{k}} + \eta_{\mathbf{k}}\delta\xi^-_{\mathbf{k}}\right] + \lambda_{\mathbf{k}}(\omega^2 - \eta^2_{\mathbf{k}})\frac{\delta\Delta^-_{\mathbf{k}}}{2\Delta_{\mathbf{k}}} \tag{4}$$

the exception being, that there are two terms on r.h.s. of (4) which are absent in the normal state. Here we have defined

$$\Phi_{\mathbf{k}} = \frac{\xi_{\mathbf{k}+}\theta_{\mathbf{k}+} - \xi_{\mathbf{k}-}\theta_{\mathbf{k}-}}{\xi_{\mathbf{k}+} - \xi_{\mathbf{k}+}} \; ; \; \lambda_{\mathbf{k}} = -\frac{4\Delta^2_{\mathbf{k}}\left[\theta^+_{\mathbf{k}}(\omega^2 - \eta^2_{\mathbf{k}})/2 + \Phi_{\mathbf{k}}\eta^2_{\mathbf{k}}\right]}{\omega^2[\omega^2 - 4E^2_{\mathbf{k}}] - \eta^2_{\mathbf{k}}[\omega^2 - \eta^{+2}_{\mathbf{k}}]} \; ; \; \varphi_{\mathbf{k}} = \Phi_{\mathbf{k}} - \lambda_{\mathbf{k}} \tag{5}$$

with $\theta^{\pm}_{\mathbf{k}} = \theta_{\mathbf{k}+} \pm \theta_{\mathbf{k}-}$. The quantity $\delta\xi^{\pm}_{\mathbf{k}} = \frac{1}{2}[\delta\xi_{\mathbf{k}} \pm \delta\xi_{-\mathbf{k}}]$ selects contributions with even (+) and odd (-) parity w.r.t the operation $\mathbf{k} \to -\mathbf{k}$ from the potentials (1). For positive parity one has $\delta\xi^+_{\mathbf{k}} = e\phi + V_{\mathbf{q}}\delta n + \gamma_{\mathbf{k}}\delta\xi_{\gamma}$, with $\gamma_{\mathbf{k}} = \hat{e}_I\cdot\boldsymbol{\gamma}_{\mathbf{k}}\cdot\hat{e}_S$ the *Raman vertex*, $\hat{e}_{I,S}$ the unit vectors in the direction of the photon polarizations $\mathbf{A}_{I,S}$, respectively and $\delta\xi_{\gamma} = r_0|\mathbf{A}_I||\mathbf{A}_S|$. The negative parity contribution reads $\delta\xi^-_{\mathbf{k}} = \mathbf{v}_{\mathbf{k}}\cdot\delta\boldsymbol{\xi}_A$ with $\delta\boldsymbol{\xi}_A = -(e/c)\mathbf{A}$. Finally, the quantity $\delta\Delta^{\pm}_{\mathbf{k}}$ represents the dynamics of the amplitude (+) and the phase (-) of the order parameter. Note that the coupling to $\delta\Delta^+_{\mathbf{k}}$ of the order parameter is odd in the variable $\xi_{\mathbf{k}}$ and has been neglected, assuming particle–hole symmetry. The function $\lambda_{\mathbf{k}}$ is referred to as the Tsuneto function [5], here readily generalized to the case of arbitrary wavenumbers. It describes essentially the condensate response to the perturbations (1). It is difficult to observe from the form of (5), that the Tsuneto function becomes identical to the superfluid density in the limit as $\mathbf{q} \to 0, \omega \to 0$:

$$n^{\mathrm{s}}_{ij} = m\lim_{\omega\to 0}\lim_{\mathbf{q}\to 0}\sum_{\mathbf{p}\sigma}\lambda_{\mathbf{p}}v_{\mathbf{p}i}v_{\mathbf{p}j} = m\sum_{\mathbf{p}\sigma}\left[\left(-\frac{\partial n_{\mathbf{p}}}{\partial\xi_{\mathbf{p}}}\right) - \left(-\frac{\partial\nu_{\mathbf{p}}}{\partial E_{\mathbf{p}}}\right)\right]v_{\mathbf{p}i}v_{\mathbf{p}j}$$

For later purposes we have also defined in (5) a third function $\varphi_{\mathbf{k}}$, which represents the BQP contribution to the response functions and reduces to $\varphi_{\mathbf{k}} = -\partial\nu_{\mathbf{k}}/\partial E_{\mathbf{k}}$ for $\mathbf{q}, \omega \to 0$. The nonequilibrium gap function $\delta\Delta^-_{\mathbf{k}} = i\delta\phi(\mathbf{q},\omega)\Delta_{\mathbf{k}}$, which represents the fluctuations of the phase ϕ of the order parameter, can be obtained from a straightforward variation of the equilibrium gap equation $\delta\Delta_{\mathbf{k}} = \sum_{\mathbf{p}}\Gamma_{\mathbf{kp}}\delta g_{\mathbf{p}}$. After a lengthy calculation the result is obtained as [6]

$$\frac{\delta\Delta^-_{\mathbf{k}}}{2\Delta_{\mathbf{k}}} = \frac{\sum_{\mathbf{p}\sigma}\lambda_{\mathbf{p}}\left(\omega\delta\xi^+_{\mathbf{p}} + \eta_{\mathbf{p}}\delta\xi^-_{\mathbf{p}}\right)}{\sum_{\mathbf{p}\sigma}[\lambda_{\mathbf{p}}(\omega^2 - \eta^2_{\mathbf{p}}) + \delta\theta_{\mathbf{p}}\Delta^2_{\mathbf{p}}]} \tag{6}$$

Note that Eq. (6), simplifies by the use of the fact, that the $\xi_{\mathbf{k}}$–integral of the quantity $\delta\theta_{\mathbf{k}} = \theta^{+}_{\mathbf{k}}/2 - \theta_{\mathbf{k}}$ vanishes identically. Inserting $\delta\Delta^{-}_{\mathbf{k}}$ into (4), one observes that the r.h.s. of (4) vanishes upon summation on $\mathbf{k}$, which reflects the fact, that the gauge–invariant treatment of the order–parameter dynamics is intimately connected with the number conservation law, i. e. the continuity equation for the macroscopic density δn

$$\omega\delta n + \mathbf{q}\cdot\mathbf{j} = 0 \quad ; \quad \mathbf{j} = \sum_{\mathbf{p}\sigma} \mathbf{v}_{\mathbf{p}} \left[\delta n_{\mathbf{p}} + \Phi_{\mathbf{p}}\delta\xi_{\mathbf{p}}\right] \tag{7}$$

From (7) one may identify the current density $\mathbf{j}$ for arbitrary values of $\mathbf{q}$ in the quasiclassical limit. Note that Eqs. (4–7) reduce to those given in ref. [1] in the limit $\hbar v_{\mathrm{F}}|\mathbf{q}| \ll \Delta_0(T)$.

Collisionless electromagnetic response

In what follows, we wish to restrict ourselves to the coupled response of the charge density $\delta n_e = e\delta n$ and the charge current $\mathbf{j}_e = e\mathbf{j}$ to the electromagnetic fields $\mathbf{E} = -i\mathbf{q}\phi + i\omega\mathbf{A}/c$ and $\mathbf{B} = i\mathbf{q}\times\mathbf{A}$ at arbitrary $\mathbf{q}$, i. e. in what follows, we put $\delta\xi_\gamma = 0$. The response of the charge density is obtained from Eq. (4) in the form

$$\delta n_e = ie^2 \frac{\mathbf{q}\cdot\mathbf{L}_{11}(\mathbf{q},\omega)\cdot\mathbf{E}}{1 - V_{\mathbf{q}}\, L^0_{11}(\mathbf{q},\omega)} \quad ; \quad \mathbf{L}_{11}(\mathbf{q};\omega) = \sum_{\mathbf{p}\sigma} \frac{\mathbf{v}_{\mathbf{p}} : \mathbf{v}_{\mathbf{p}}\varphi_{\mathbf{p}}}{\omega^2 - \eta^2_{\mathbf{p}}} + \frac{1}{\omega^2 - \omega^2_{\mathbf{q}}} \frac{\boldsymbol{\lambda}\cdot\mathbf{q} : \mathbf{q}\cdot\boldsymbol{\lambda}}{\mathbf{q}\cdot\boldsymbol{\lambda}\cdot\mathbf{q}} \tag{8}$$

The quantity $\mathbf{L}_{11}$ can be referred to as the *Lindhard tensor* of the superconductor, and

$$L^0_{11} = \mathbf{q}\cdot\mathbf{L}_{11}(\mathbf{q},\omega)\cdot\mathbf{q} = \sum_{\mathbf{p}\sigma}\left(\frac{\eta^2_{\mathbf{p}}\varphi_{\mathbf{p}}}{\omega^2 - \eta^2_{\mathbf{p}}} + \frac{\omega^2_{\mathbf{q}}\lambda_{\mathbf{p}}}{\omega^2 - \omega^2_{\mathbf{q}}}\right) \tag{9}$$

represents the associated *Lindhard function*. Both $\mathbf{L}_{11}$ and L^0_{11} consist of a BQP contribution $\propto \varphi_{\mathbf{k}}$ and a condensate contribution $\propto \boldsymbol{\lambda} = \sum_{\mathbf{p}\sigma}\lambda_{\mathbf{p}}\mathbf{v}_{\mathbf{p}} : \mathbf{v}_{\mathbf{p}}$. In (8) $\omega^2_{\mathbf{q}} = \mathbf{q}\cdot\boldsymbol{\lambda}\cdot\mathbf{q}/\sum_{\mathbf{p}\sigma}\lambda_{\mathbf{p}}$ denotes the frequency of the gauge– or Anderson–Bogoliubov mode of the superconductor. Clearly, the quantity $\varepsilon(\mathbf{q},\omega) = 1 - V_{\mathbf{q}}\, L^0_{11}(\mathbf{q},\omega)$ can be interpreted as the *dielectric function* of the superconductor in the collisionless limit at arbitrary quasi-classical wavenumbers $\mathbf{q}$.
The charge current response is obtained as

$$\mathbf{j}_e = \left[\boldsymbol{\sigma} - \frac{\boldsymbol{\sigma}\cdot\mathbf{q} : \mathbf{q}\cdot\boldsymbol{\sigma}}{\mathbf{q}\cdot\boldsymbol{\sigma}\cdot\mathbf{q}}\left(1 - \frac{1}{\varepsilon(\mathbf{q},\omega)}\right)\right]\cdot\mathbf{E} - \frac{e^2}{c}\boldsymbol{\Delta}\cdot\mathbf{A} \quad ; \quad \boldsymbol{\Delta} = \boldsymbol{\lambda} - \frac{\boldsymbol{\lambda}\cdot\mathbf{q} : \mathbf{q}\cdot\boldsymbol{\lambda}}{\mathbf{q}\cdot\boldsymbol{\lambda}\cdot\mathbf{q}} \tag{10}$$

Here we have expressed the dynamical conductivity tensor $\boldsymbol{\sigma}$ of the superconductor in the usual way through the Lindard tensor $\mathbf{L}_{11}$, namely $\boldsymbol{\sigma}(\mathbf{q},\omega) = i\omega e^2\mathbf{L}_{11}(\mathbf{q},\omega)$.
The interplay between the long–range Coulomb interaction (which gives rise to the plasma mode in the charge density and the longitudinal current response) on the one hand, and the phase fluctuations of the order parameter (giving rise to the gauge– or Anderson–Bogoliubov mode and eventually to the gauge–invariance of the theory) can be seen from our results (8) and (10) in two ways. First we obtain the well–known result that the gauge mode gets shifted to the plasma frequency, as can be observed in the charge density and, equivalently, in the longitudinal current response. Second, the gauge mode contributes to the condensate part of the charge current, which is described by the second ('backflow') term in $\boldsymbol{\Delta}$ such that it is strictly transverse, i. e. $\mathbf{q}\cdot\boldsymbol{\Delta} = 0$. In order to shed some more light on the physical meaning of the term $\boldsymbol{\Delta}$, we rewrite it in the form

$$-\frac{e^2}{c}\boldsymbol{\Delta}\cdot\mathbf{A} \equiv e^2\left[\mathcal{P}\left(\frac{1}{-i\omega}\right) + \pi\delta(\omega)\right]\boldsymbol{\Delta}\cdot\mathbf{E}$$

with the first and second term in square brackets referring to the well–known London– and Drude weight of the transverse conductivity. The longitudinal part of the current, on the other hand, is simply diminished by dielectric screening, described by $\varepsilon(\mathbf{q},\omega)$. It should finally be mentioned that our results (6) and (8) reduce to those discussed in refs. [7] and [8] in the limit $\hbar v_{\mathrm{F}}|\mathbf{q}| \ll \Delta_0$.

Collisionless electronic Raman response

We would now like to turn to the case of the electronic Raman response, i. e. in what follows, we put $\delta\xi_A = 0$. In this case one obtains a set of coupled equations for the Raman fluctuations $\delta n_\gamma = \sum_{\mathbf{p}\sigma} \gamma_{\mathbf{p}} \delta n_{\mathbf{p}}$ and the density fluctuations δn:

$$\delta n_\gamma = \chi^0_{\gamma 1} V_{\mathbf{q}} \delta n + \chi^0_{\gamma\gamma} \delta\xi_\gamma \;\; ; \;\; \delta n = \chi^0_{11} V_{\mathbf{q}} \delta n + \chi^0_{1\gamma} \delta\xi_\gamma \;\; ; \;\; \chi^0_{ab} = L^0_{ab} - \Delta_{ab} \tag{11}$$

Here L^0_{ab} is the Lindhard function weighted with the vertices $a_{\mathbf{p}}, b_{\mathbf{p}} = \gamma_{\mathbf{p}}$ or 1.

$$L^0_{ab} = \sum_{\mathbf{p}\sigma} a_{\mathbf{p}} b_{\mathbf{p}} \frac{\eta^2_{\mathbf{p}} \varphi_{\mathbf{p}}}{\omega^2 - \eta^2_{\mathbf{p}}} + \frac{\omega^2_{\mathbf{q}}}{\omega^2 - \omega^2_{\mathbf{q}}} \frac{\lambda_{a1}\lambda_{1b}}{\lambda_{11}} \tag{12}$$

and

$$\Delta_{ab} = \lambda_{ab} - \frac{\lambda_{a1}\lambda_{1b}}{\lambda_{11}} \;\; ; \;\; \lambda_{ab} = \sum_{\mathbf{p}} a_{\mathbf{p}} b_{\mathbf{p}} \lambda_{\mathbf{p}} \tag{13}$$

The solution of the coupled equations (11) reads

$$\delta n_\gamma = \left[\chi^0_{\gamma\gamma} - \frac{(\chi^0_{\gamma 1})^2}{\chi^0_{11}} \left(1 - \frac{1}{\varepsilon} \right) \right] \delta\xi_\gamma \tag{14}$$

A comparison of our results (10) and (14) for the current and the electronic Raman response reveals strong structural similarities originating from the effects of dielectric screening and the Anderson–Bogoliubov mode, which lead to a decomposition of the electronic Raman response into longitudinal (screened) and transverse (unscreened) contributions. In the special case of a constant Raman vertex $\gamma_{\mathbf{k}}$ =const, we recover the Lindhard response from (14). It should be emphasized, that the condensate contributes to the electronic Raman effect through the term $\propto \Delta_{\gamma\gamma}$, which contains a 'backflow' term (similar to the term $\boldsymbol{\Delta}$ in the transverse current response) which originates from the gauge–invariance of the theory. This term is unaffected by dielectric screening effects ($\Delta_{\gamma 1} \equiv 0$), which have influence only on the longitudinal (Lindhard) part of the electronic Raman effect. We note that our results (11) and (14) reduce to those discussed in refs. [1] and [4] in the limit $\hbar v_{\mathrm{F}}|\mathbf{q}| \ll \Delta_0$.

Conclusion

In summary, we have evaluated both the gauge–invariant electromagnetic and the electronic Raman response in the collisionless limit. For the first time, this analysis applies to the extended regime of arbitrary quasi-classical wavenumbers $\hbar v_{\mathrm{F}}|\mathbf{q}| \ll E_{\mathrm{F}}$, which is limited only by the requirement, that the concept of particle–hole symmetry should still make sense. Our results include necessary generalizations of the Tsuneto function as well as the Lindhard and the dielectric function of the superconductor. The gauge–invariance of the theory is still provided in this general situation and guarantees the transversality of the supercurrent in the static limit. The marginal role of gauge mode persists into the regime of higher wavenumbers, where it gives merely rise to a weakly modified plasmon dispersion.

References

[1] T. P. Devereaux and D. Einzel, Phys. Rev. **B 51**, 16336 (1995) and references therein.
[2] O. Betbeder-Matibet and P. Nozieres, Annals of Physics **51**, 392 (1969).
[3] P. Wölfle, J. Low Temp. Phys. **22**, 157 (1976).
[4] T. P. Devereaux and D. Einzel, Phys. Rev. **B 54**, 15547 (1996).
[5] T. Tsuneto, Phys. Rev. **118**, 1029 (1960); P. J. Hirschfeld, P. Wölfle, J. A. Sauls, D. Einzel, and W. O. Putikka, Phys. Rev. **B 40**, 6695 (1989).
[6] Ludwig Klam, Diploma thesis, TU München (2006).
[7] P. J. Hirschfeld and D. Einzel, Phys. Rev. **B 47**, 8837 (1993).
[8] P. J. Hirschfeld and D. Einzel, Phys. Rev. **B 50**, 6538 (1994).

Interrelation between ordering and superconductivity in cuprates

L. Tassini, W. Prestel, A. Erb, M. Lambacher, and R. Hackl [1]

In copper-oxygen compounds superconductivity is observed in a temperature range up to approximately 160 K with the maximum being obtained in $HgBa_2Ca_2Cu_3O_{9+ffi}$ at elevated pressure. While 100 K is typical, the maximal transition temperature T_c^{max} does not even reach 40 K in one of the most prominent families, i.e. $La_{2-x}Sr_xCuO_4$. This simple observation demonstrates that the mechanism of Cooper pairing is by far not the only important open problem in cuprates.

In spite of the substantial variation of T_c^{max} for different families the doping dependence of T_c is universal following $T_c(p)/T_c^{max} = 1 - 82.6(p - 0.16)^2$ [1]. Hence, all cuprates superconduct for $0.05 < p < 0.27$. Disorder shrinks the superconducting range shifting the onset points p_{sc1} and p_{sc2} together, moves the position of the maximum slightly beyond 0.16 and, of course, reduces T_c^{max} [1]. However, the variation of T_c^{max} is apparently something more subtle but different degrees of order or just the number of adjacent CuO_2 layers.

An early indication of a more complicated mechanism being at work came from the "1/8 anomaly" in $La_{1.875}Ba_{0.125}CuO_4$ [2] and experiments in $La_{2-y-x}Re_ySr_xCuO_4$ with Re = Nd or Eu. Here, static charge and spin superstructures such as sketched in Fig. 1 are observed, and the superconducting transition temperature is reduced or totally suppressed [3, 4]. While the possibility of charge and spin instabilities in the cuprates was recognized early [6, 7] their interrelation with superconductivity was pointed out only later [8–10]. While the suppression of superconductivity by static order is clear by now, the role of other types of ordering instabilities such as fluctuations is an open issue.

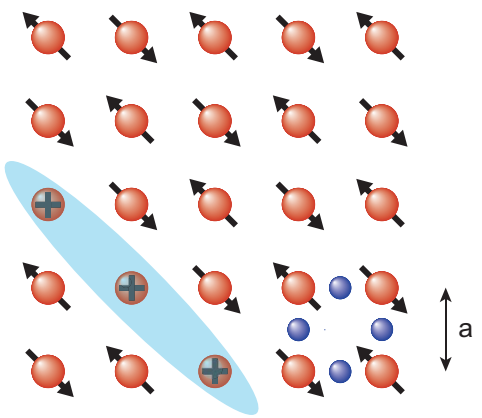

Figure 1: The essential structural elements of the cuprates are the copper (red) oxygen (blue, shown only in the lower right corner) planes with long-ranged antiferromagnetic order at zero doping. At finite but low doping, carriers are not randomly distributed but form stripes which separate antiferromagnetic domains. For $0 < p \leq 0.05$, the stripes are diagonal as shown in the figure and are separated by $(\sqrt{2}p)^{-1}$ lattice units a [5].

In the last year we could gain some insight into this problem by observing how the type of order is related to the maximal T_c. This became possible by the discovery of new structures in the low-energy electronic Raman response of $La_{2-x}Sr_xCuO_4$ (see Annual Report 2005 and Ref. [11]). Here, we describe differences between the "high" and "low" T_c families studied in the last year.

Inelastic (Raman) scattering of light is capable of probing most of the excitations in a solid including lattice vibrations, spins, and electrons, as well as their interactions [12]. Since the polarizations of the incident and the scattered photons can be adjusted independently, many of the excitations can be sorted out via the selection rules. For instance, the transport properties of conduction electrons can be measured independently in different regions of the Brillouin zone [12, 13]. Hence, Raman scattering can provide information beyond conventional optical conductivity. We also study the scattering from spin-flip excitations, charge fluctuations and phonons to clarify the electronic properties of the cuprates around the onset point of superconductivity at p_{sc1}.

[1] This work is supported by the DFG through the Research Unit FOR538 (project No.: HA 2071/3).

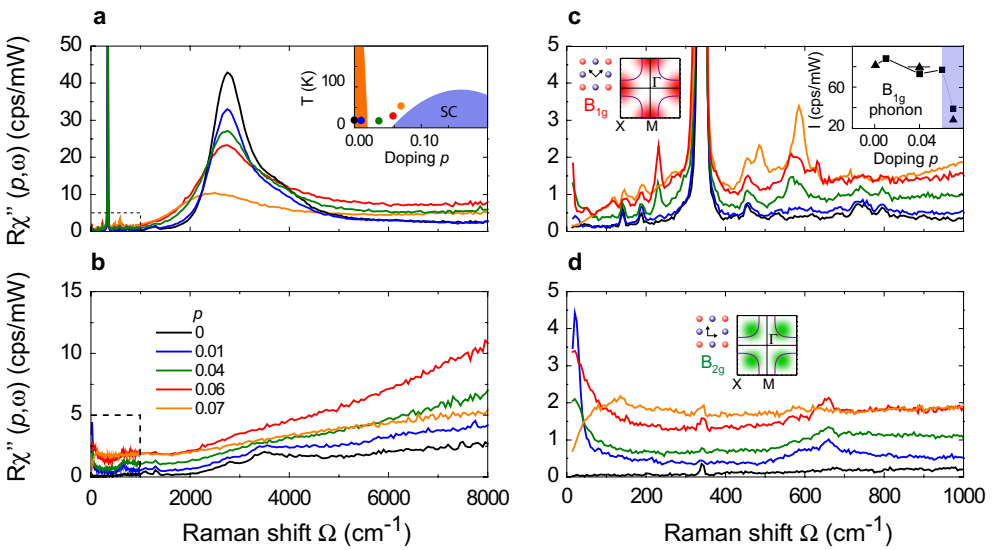

Figure 2: Raman response $R\chi''(p,\omega)$ of $(Y_{1-y}Ca_y)Ba_2Cu_3O_{6+x}$ at low temperature and doping as indicated in the inset of a. The upper (a,c) and lower (b,d) panels correspond to the B_{1g} and B_{2g} symmetries, respectively, with the related polarizations and sensitivities in the Brillouin zone as indicated. The antiferromagnetic (AF) and superconducting (SC) phases are displayed in orange and blue, respectively. Panels a and b show an energy range of 8000 cm^{-1} equivalent to 1 eV. In c and d the low-energy and intensity range is expanded as indicated by dashed boxes in a and b. The inset in c shows the peak intensity of the B_{1g} "buckling" phonon at 340 cm^{-1} (43 meV). Triangles and squares represent Ca-free and Ca-doped Y-123, respectively.

For the studies we selected $(Y_{1-y}Ca_y)Ba_2Cu_3O_{6+x}$ (Y-123) for its superior crystal quality [14]. In particular, doping with Ca allows us to control the number of holes close to the antiferromagnetic phase without introducing strong charge trapping defects [15]. For $x \simeq 0$, doping levels up to $p = 0.06$ are given by the Ca content, $p = y/2$ [1]. Since superconductivity could be induced only by oxygen co-doping ($y = 0.08$, $x = 0.3$) $p \simeq 0.07$ is estimated from the transition temperature $T_c = 28$ K via the universal relationship $T_c(p)$ given above. The material remains tetragonal on the average.

In Figure 2 we show Raman spectra of Y-123 at low temperature in the doping range $0 \leq p \leq 0.07$. In B_{1g} symmetry (Fig. 2 a) an intense phonon at 340 cm^{-1} and scattering from nearest-neighbor spin-flip excitations in the range between 2000 and 4000 cm^{-1} are the most prominent features observed. As long as the doping is below the onset point of superconductivity ($p \leq p_{sc1}$) the peak height changes slowly and continuously while the position is essentially constant. Upon crossing p_{sc1} the two-magnon peak moves discontinuously downwards by approximately 250 cm^{-1}. Independent of doping, positions and intensities of the two-magnon peaks react only mildly when the temperature is raised (see supplementary information). In B_{2g} symmetry (Fig. 2 b) light scattering from spin excitations is weak [12]. A low-energy continuum appears only at finite carrier concentrations. The high-energy response increases continuously until superconductivity sets in. Then, the spectra assume a more convex shape and are depressed at high energy.

Zooming in on low-energies (Fig. 2 c and d) we observe a continuous increase of the electronic response upon doping in B_{1g} symmetry (Fig. 2 c) with no significant changes across $p = p_{sc1}$. On the other hand, the peak height of the B_{1g} phonon at 340 cm^{-1} collapses by factor of two for $p > p_{sc1}$ (inset of Fig. 2 a). In B_{2g} symmetry (Fig. 2 d) we find a complete suppression of the electronic Raman spectra below 400 cm^{-1} for $p = 0$ as expected for an insulator. As soon as carriers are added the response becomes finite and a new peak in the range 15–30 cm^{-1} pops up similar to those in $La_{1.98}Sr_{0.02}CuO_4$ [11] and $(Y_{0.97}Ca_{0.03})Ba_2Cu_3O_{6.05}$ [16]. Up to p_{sc1} the

integrated cross section increases proportional to p, then stays essentially constant.

In Fig. 3 we plot the low-energy B_{2g} spectra at two characteristic doping levels below and above p_{sc1} as a function of temperature in order to further highlight the qualitative changes across the critical doping. At $p = 0.07$ the response develops as expected from the resistivity and the results at $p \geq 0.1$ [13, 17, 18]. As shown in the inset of Fig. 3 a the Raman relaxation rate $\Gamma_0(T)$ at low energies follows the resistivity when properly converted [13]. This is in clear contrast to the non-superconducting sample at $p = 0.04$ where a qualitative difference between the Raman and the transport resistivities is found in the entire temperature range (insetFig. 3 b). As can be seen in the main panel of Fig. 3 b the discrepancy originates in the low-energy peak developing below approximately 250 K. Along with the peak a pronounced pseudogap of approximately 650 cm^{-1} opens up which, if taken alone, could essentially account for the increase of the conventional resistivity towards low temperature.

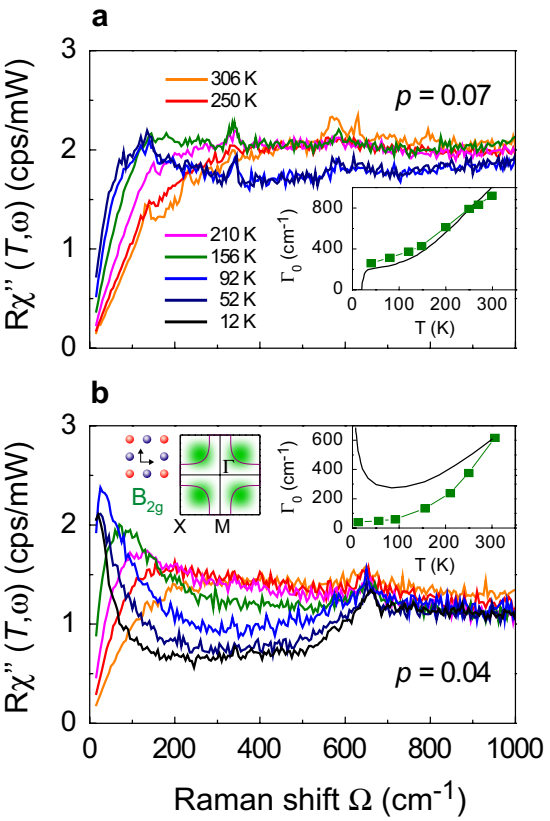

Figure 3: Raman response $R\chi''_{B_{2g}}(T,\omega)$ of $(Y_{1-y}Ca_y)Ba_2Cu_3O_{6+x}$ at $p = 0.07$ (a) and 0.04 (b). In the insets we plot the low-energy "Raman resistivities" $\Gamma_0(T)$ (squares) corresponding to the initial slope of the spectra [13] and compare them with the conventional resistivities (lines) from ref. [17].

The pivotal question is as to what drives the abrupt changes in the magnon, charge, and phonon spectra. We could show that these changes are related to the superstructure in a universal way. So far, the rotation at $p \simeq p_{sc1}$ of the essentially 1D or stripe-like pattern from diagonal to parallel with respect to the Cu–O bond direction is only established in $La_{2-x}Sr_xCuO_4$ [19]. In the compounds with T_c^{max} in the 100 K range evidence of ordering is found only at $p \geq 0.10$. In $YBa_2Cu_3O_{6+x}$ [20, 21] and $Bi_2Sr_2CaCu_2O_{8+ffi}$ [22] the order is more of checkerboard or 2D rather than of 1D or stripe type. For $p_{sc1} < p < 0.1$, the superstructure in Y-123 seems to disappear [24]. There are no experiments below p_{sc1}.

Here, we find collective modes in the Raman spectra at $0 < p < p_{sc1}$ exhibiting shapes as well as symmetry and temperature dependencies similar to those in $La_{2-x}Sr_xCuO_4$ [11]. Apparently, they originate in the same fluctuating spin and charge superstructure with a modulation along the diagonals of the CuO_2 plane [16]. We are aware that our information is not on the structure directly but only via the dynamics. However, the selection rules are a particularly strong argument as to symmetry breaking and orientation. In addition, shape and temperature dependence demonstrate the similarity of the underlying physics. Hence, we find indications of spin and charge ordering in a completely tetragonal cuprate in the doping range between the antiferromagnet and the onset of superconductivity. The type of ordering at $0 < p < p_{sc1}$ is universal and depends neither on the material class nor on structural details of the crystals such as lattice distortions nor on the way of doping. We conclude that the ordering is a collective phenomenon of the charges and that the doping level determines the orientation of the superstructure while defects mainly shift p_{sc1}.

While symmetry arguments and analogies lead to straightforward conclusions for $p < p_{sc1}$ the analysis at $p > p_{sc1}$ is less direct. In contrast to $La_{2-x}Sr_xCuO_4$, where the ordering-induced collective modes change symmetry from B_{2g} to B_{1g} along with the rotation of the superstructure [11], we do not observe any peaks in Y-123 for $p > p_{sc1}$ (see Fig. 2 c), $p = 0.07$ and Ref. [11]). However, all the renormalization effects described above demonstrate indirectly a very strong interaction peaked close to the M points, i.e. with $|d_{x^2-y^2}|$, i.e. B_{1g}, symmetry, (see inset of Fig. 2 c) to become effective at $p > p_{sc1}$. This interaction leads to a shift of the two-magnon peak indicating a reduction of the Heisenberg exchange coupling J by almost 10%. At the same time the related fluctuations also open a new coupling channel of proper symmetry for the B_{1g} phonon as indicated by the discontinuous reduction of the peak intensity and the onset of a (weak) Fano-type line shape. The effect on the $\mathbf{q} \simeq 0$ Raman phonon is relatively weak in contrast to the strong coupling at $\mathbf{q}_{charge} \simeq 0.25(2\pi/a)$ [23].

To summarize, superconductivity and the apparently universal diagonal order at $p < p_{sc1}$ are mutually exclusive. Disorder seems to stabilize diagonal order hence pushing p_{sc1} to higher doping levels. At $p > p_{sc1}$, the phase diagram depends on various details. In the "low"-T_c materials such as $La_{2-x}Sr_xCuO_4$ collinear stripe order prevails. For static stripes superconductivity disappears. In compounds with T_c-s in the 100 K range the order seems to be more 2D, e.g. of checkerboard type, aligned with the CuO_2 plane at least in the range $0.1 < p < 0.18$ [20–22]. For $p_{sc1} < p < 0.1$ we found indirect indications of a strongly momentum dependent interaction which is symmetry compatible with the order at $p > 0.1$ and, hence, with the superconducting gap. Possible candidates are quasi-critical fluctuations of charge stripes [25] or a fluctuating Fermi surface deformation [26] which are expected to be visible only in the charge but not in the spin channel. Clearly, T_c^{max} depends on the type of order being established above p_{sc1}.

References

[1] J. L. Tallon *et al.*, Phys. Rev. B **51**, 12911 (1995).
[2] A.R. Moodenbaugh *et al.*, Phys. Rev. B **38**, 4586 (1988).
[3] J. M. Tranquada *et al.*, Nature **375**, 561 (1995).
[4] H.-H. Klauss *et al.*, Phys. Rev. Lett. **85**, 4590 (2000).
[5] J.M. Tranquada, cond-mat/0512115 (2005).
[6] J. Zaanen and O. Gunnarsson, Phys. Rev. B **40**, 7391 (1989).
[7] K. Machida, Physica C **158**, 192 (1989).
[8] V. J. Emery and S. A. Kivelson, Physica C **85**, 597 (1993).
[9] C. Castellani, C. Di Castro, and M. Grilli, Phys. Rev. Lett. **45**, 4650 (1995).
[10] A. Perali *et al.*, Phys. Rev. B **54**, 16216 (1996).
[11] L. Tassini *et al.*, Phys. Rev. Lett. **95**, 117002 (2005).
[12] T. P. Devereaux and R. Hackl *to appear in* Rev. Mod. Phys. **78**(4) (2006); cond-mat/0607554.
[13] M. Opel *et al.*, Phys. Rev. B **61**, 9752 (2000).
[14] A. Erb, E. Walker, and R. Flükiger, Physica C **258**, 9 (1996).
[15] A. Jánossy, T. Fehér, and A. Erb, Phys. Rev. Lett. **91**, 177001 (2003).
[16] S. Caprara *et al.*, Phys. Rev. Lett. **95**, 117004 (2005).
[17] Y. Ando *et al.*, Phys. Rev. Lett. **93**, 267001 (2004).
[18] F. Venturini *et al.*, Phys. Rev. Lett. **89**, 107003 (2002).
[19] S. Wakimoto *et al.*, Phys. Rev. B **60**, R769 (1999); M. Fujita *et al.*, Phys. Rev. B **65**, 064505 (2002).
[20] V. Hinkov *et al.*, Nature **430**, 650 (2004).
[21] C. Stock *et al.*, Phys. Rev. B **71**, 024522 (2005).
[22] J.E. Hoffman *et al.*, Science **297**, 1148 (2002).
[23] L. Pintschovius *et al.*, Phys. Rev. B **69**, 214506 (2004).
[24] C. Stock *et al.*, Phys. Rev. B **73**, 100504 (2006).
[25] A. Perali *et al.*, Phys. Rev. B **62**, R9295 (2000).
[26] W. Metzner, D. Rohe, and S. Andergassen, Phys. Rev. Lett. **91**, 066402 (2003).

Commensurate splitting effect on field-induced charge-density-wave transitions in α–(BEDT–TTF)$_2$KHg(SCN)$_4$

D. Andres, M. V. Kartsovnik, and W. Biberacher [1]
H. Müller [2]

The layered organic conductor α–(BEDT–TTF)$_2$KHg(SCN)$_4$ undergoes a charge-density-wave (CDW) transition at a temperature of ≈ 8 K that is almost an order of magnitude lower than usually found in CDW materials. This gives rise to a very high sensitivity of the CDW state to external conditions such as pressure and magnetic field. A moderately high hydrostatic pressure of 2.5 kbar leads to a complete suppression of the phase transition in the absence of magnetic field [1]. However, a magnetic field $B \gtrsim 3$ T, applied perpendicular to the layers, restores the CDW state at low temperatures [2]. At changing the strength of the magnetic field, this field-induced CDW (FICDW) state is characterized by a sequence of transitions between substates with quantized values of the CDW wave vector [3]. This phenomenon is similar to the field-induced spin-density wave (FISDW) phenomenon extensively studied on a number of quasi-one-dimensional organic conductors: both are associated with the quantizing effect of a magnetic field on the orbital motion of charge carriers in a low-dimensional conductor. However, by contrast to the FISDW case, the FICDW state is subjected to an additional, Pauli paramagnetic effect which acts in the opposite direction, weakening the CDW coupling [4, 5]. Both, the orbital and Pauli effects enter the condition for the FICDW wave vector which, for $T = 0$, reads [5]

$$Q_x^{\mathrm{CDW}} = 2k_{\mathrm{F}} \pm \frac{2\mu_{\mathrm{B}} B}{\hbar v_{\mathrm{F}}} + NG\,, \quad N = 0, \pm 1, \pm 2, \ldots\,, \tag{1}$$

where

$$G = \frac{2ea_y B_z}{\hbar}\,. \tag{2}$$

Q_x and k_{F} are, respectively, the components of the FICDW wave vector and of the Fermi wave vector in the most conducting direction x, v_{F} is the Fermi velocity, μ_{B} is the Bohr magneton, a_y is the lattice constant in the y direction (lying within the layers and perpendicular to the most conducting direction), and B_z is the field component normal to the layers. The second term on the right-hand side of Eq. (1) reflects the Pauli effect. It is taken with the sign "+" or "-" for the subband with spins parallel or antiparallel to the field direction, respectively. The last term in Eq. (1) represents the quantizing orbital effect which allows, at a given field, only a discrete set of values for the wave vector.

The presence of the Pauli term implies two different CDW wave vectors, corresponding to two spin subbands, to exist at the same time. This makes the FICDW state less stable than the analogous FISDW state characterized by a unique wave vector for the whole system. Indeed, the theory predicts the effective FICDW interaction constant to be a factor of two lower than the corresponding constant in the FISDW case. In particular, this leads to a much narrower range of temperatures and pressures where the FICDW phenomenon can be observed [3]. However, the strength of the FICDW interaction has been predicted [5] to significantly increase if the spin splitting and the distance, G, between the orbitally quantized levels become commensurate.

The commensurability can be achieved by a proper alignment of the magnetic field. While the Pauli effect is almost isotropic, the orbital effect is essentially caused by only the out-of-plane field component B_z. Thus, one should be able to reach the commensurate splitting (CS)

[1] This work was supported by the *Access to Research Infrastructure Action* of the *Improving Human Potential Programme*.

[2] European Synchrotron Radiation Facility, F-38043 Grenoble, France

condition by choosing an appropriate field orientation [5, 6]:

$$\cos\theta_{cs} = \frac{1}{M}\frac{2\mu_B}{ev_F a_y} \,. \tag{3}$$

Here, θ is defined as the angle between the field direction and the z axis, $B_z = B\cos\theta$, and $M \neq 0$ is an integer.

To verify the theoretical prediction, we have performed a study of the influence of the magnetic field orientation on FICDW transitions in α–(BEDT–TTF)$_2$KHg(SCN)$_4$. For that, a single crystal sample of the title compound was mounted into a miniature BeCu pressure cell which was then fixed on a rotation stage capable of precise in-situ rotation at liquid ^{3}He temperatures. A pressure of 2.8 kbar, slightly exceeding the critical value, $p_c = 2.5$ kbar, was applied in order to suppress the zero-field CDW state and enter the FICDW region. Magnetic fields of up to 28 T were generated by the 20 MW resistive magnet at the Grenoble High Magnetic Field Laboratory. To detect the transitions, the interlayer resistance of the sample was measured by a standard a.c. method. The resistance was recorded at $T = 0.4$ K in a series of field sweeps at different fixed angles θ.

Figure 1 shows some representative examples of the magnetoresistance plotted as a function of the out-of-plane field component, for different θ values. Rapid oscillations at high fields originate from the Shubnikov–de Haas effect due to the remaining metallic quasi-two-dimensional band of charge carriers. We will not consider them here and, instead, focus on the slow oscillations associated with the FICDW effect.

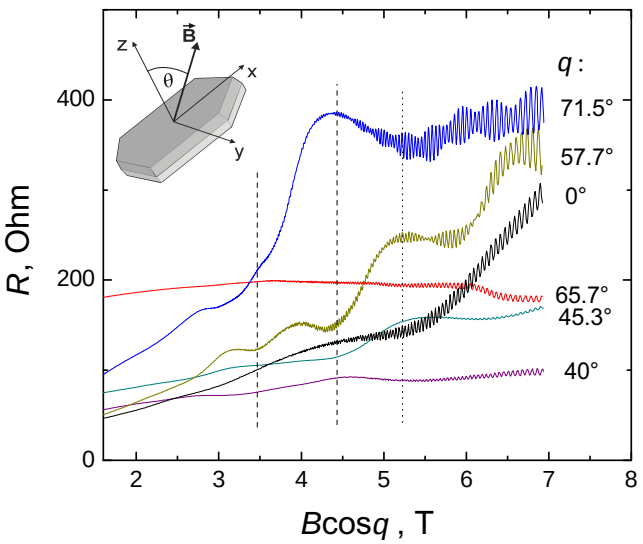

Figure 1: Magnetoresistance of α–(BEDT–TTF)$_2$KHg(SCN)$_4$ at $p = 2.8$ kbar, $T = 0.4$ K as a function of the field component perpendicular to the conducting layers, recorded at different field orientations. Inset illustrates the definition of angle θ. The curves are vertically offset for clarity.

At $\theta = 0°$ ($B \perp$ layers) FICDW transitions are manifested in the magnetoresistance as slow oscillations approximately periodic in the $1/B$ scale, with the period $\Delta(1/B) \simeq 20$ T. At $T \sim 0.1$ K the oscillations exhibit a pronounced non-monotonic hysteresis revealing the first order character of the transitions [3]. In the present setup, allowing rotation under pressure, the temperature is, however, considerably higher. Therefore the quantization effects are damped, the FICDW features, at $\theta = 0°$, are very weak and do not exhibit a significant hysteresis.

At tilting the field away from the normal to the layers, the amplitude of the FICDW features changes in a non-monotonic manner. For example, as can be seen in Fig. 1, the slow oscillations are nearly indiscernible at $\theta = 65.7°$ but reappear at 71.5°. Note that in the latter case and, especially, at $\theta = 57.7°$ the FICDW features are pronounced even stronger than in the field perpendicular to the layers. In Fig. 2 the up- and downward field sweeps at 57.7° are compared. The rather strong hysteresis exhibits a clear structure correlated with the resistance oscillations.

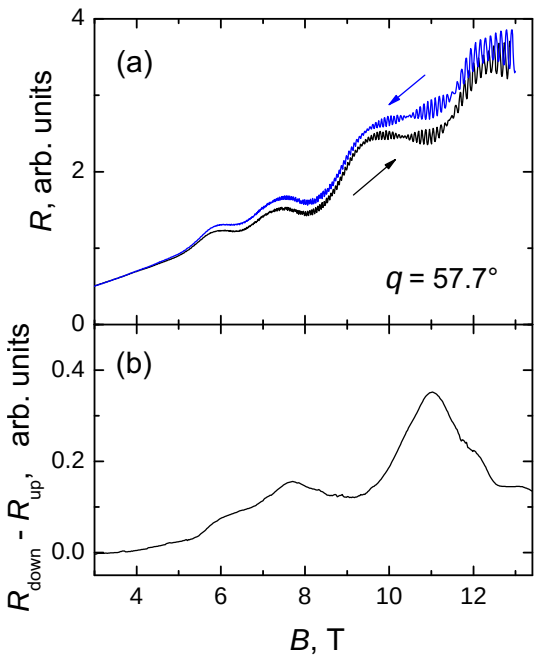

Figure 2: (a) Magnetoresistance at $\theta = 57.7^\circ$ at increasing and decreasing field. Arrows indicate the direction of the field sweep. (b) Difference between the up- and downward sweeps. The hysteresis structure correlates with the slow oscillations.

Furthermore, in contrast to the initially expected $B\cos\theta$ scaling of the transition positions, the oscillations in Fig. 1 are clearly shifted with respect to each other: the dashed vertical lines drawn through oscillation minima (supposed to be the transition points) in the 57.7° curve intersect the curves for $\theta = 0$, 40, and 71.5° in local maxima, and vice versa (dotted line in Fig. 1). A detailed analysis of the field sweeps at different θ has shown that the whole angular range, 0 to 78.5° studied in this work can be divided into 5 intervals. At the borders between the intervals the amplitude of the oscillations vanishes. Within each interval the oscillation positions obey the expected $B\cos\theta$ scaling, whereas in the neighboring intervals their phases differ by π.

The observed behavior can be explained by the mentioned above superposition of the orbital quantization and the Pauli effect. Consider the CDW interaction parameter $g[\vec{Q}(\vec{B}), \vec{B}]$. Due to the orbital quantization, it is a quasi-periodic function of inverse field, $1/B_z$, [5] and can, therefore, be represented in the form of a harmonic expansion. Taking into account the rather smeared character of our FICDW transitions, it is natural to suggest that the periodic dependence $\tilde{g}(1/B_z)$ is dominated by the first harmonic. Such a situation resembles the usual de Haas – van Alphen effect. In the latter case the spin splitting leads to a damping factor [7]

$$R_S = \cos\left(2\pi\frac{\mu_B B}{\hbar\omega_c}\right) , \tag{4}$$

where ω_c is the cyclotron frequency corresponding to a Landau-quantized closed orbit. We assume that in our case the effect of spin splitting can be expressed in the same form; only ω_c should be replaced by a characteristic frequency of the orbital motion on an open Fermi surface: $\omega_0 = ea_y v_F B\cos\theta/\hbar$. Then the spin factor can be written as:

$$R_S = \cos\left(2\pi\frac{\mu_B}{ea_y v_F\cos\theta}\right) , \tag{5}$$

One can see that R_S depends on the orientation but not on the strength of the magnetic field.

The angle dependence of the FICDW transitons can now be explained by the influence of the spin factor (5). Indeed, at changing the angle θ, R_S changes the sign every time when θ passes through a value satisfying the "spin-zero" condition:

$$\cos\theta_{sz} = \frac{1}{M+1/2}\frac{2\mu_B}{ea_y v_F} . \tag{6}$$

This is equivalent to a reversal of the oscillations $\tilde{g}(1/B_Z)$ and, therefore, of the magnetoresistance oscillations. The oscillation amplitude vanishes at spin-zeros (6) and is maximum at the CS angles (3).

In the experiment, the angle dependence of the oscillation amplitude around CS angles is rather smooth which hinders from precise determination of θ_{cs}. More precisely can be determined the spin-zeros (6) at which the oscillations reverse the phase. From our data the spin-zero angles are evaluated as $42.5 \pm 0.5°$, $65.0 \pm 0.2°$, $73.5 \pm 0.2°$, and $77.8 \pm 0.2°$. As shown in Fig. 3, these angles indeed periodically appear in the $1/\cos\theta$ scale, as described by Eq. (6).

According to the data in Fig. 3, the field direction perpendicular to the layers (star in Fig. 3) is far from satisfying the CS condition (3). On the other hand, the first CS angle (cross in the figure) is expected to lie at $\sim 57 - 58°$. This perfectly agrees with the experiment: as noted above, the FICDW features at $\theta = 57.7°$ are much more pronounced than at $\theta = 0°$.

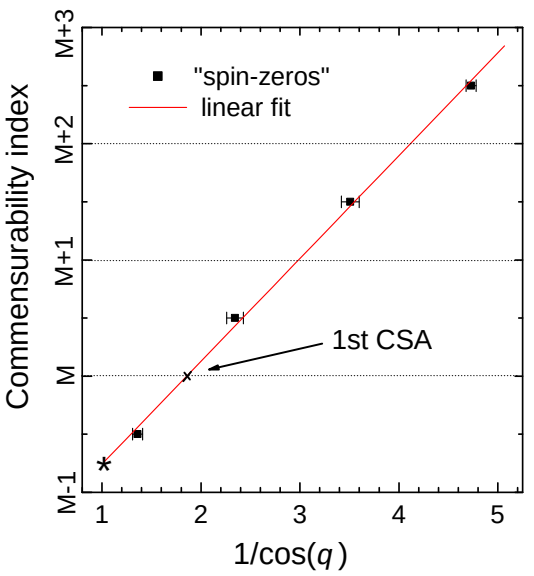

Figure 3: Positions of the "spin-zero" angles (see text) plotted according to the condition (6). Solid line represents a linear fit to the experimental data (squares). The cross indicates the expected position of the first CS angle (3) and the star corresponds to the perpendicular field direction.

Using Eq. (6), we can estimate the Fermi velocity from the slope of the linear dependence $M(1/\cos\theta)$: $v_F \approx 1.2 \times 10^5$ m/s. This value is about two times higher than the velocity obtained from the angle-dependent absorption experiment [8]. The reason for the discrepancy is not quite clear yet. It is possible that the present commensurate splitting model should be further elaborated, taking into account details of the Fermi surface nesting.

References

[1] D. Andres, M.V. Kartsovnik, W. Biberacher, K. Neumaier, E. Schuberth, and H. Müller, Phys. Rev. B **72**, 174513 (2005).
[2] D. Andres, M.V. Kartsovnik, W. Biberacher, H. Weiss, E. Balthes, H. Müller, and N. Kushch, Phys. Rev. B **64**, 161104(R) (2001).
[3] M. Kartsovnik, D. Andres, P. Grigoriev, W. Biberacher, and H. Müller, Physica B **346-347**, 368 (2004); M. Kartsovnik, D. Andres, and W. Biberacher, C. R. Chimie, *in press* (2006).
[4] D. Zanchi, A. Bjeliš, and G. Montambaux, Phys. Rev. B **53**, 1240 (1996).
[5] A. G. Lebed, JETP Lett. **78**, 138 (2003).
[6] A. Bjeliš, D. Zanchi, and G. Montambaux, J. Phys. IV (France) **9**, 203 (1999).
[7] D. Shoenberg, *Magnetic Oscillations in Metals* (Cambridge University Press, Cambridge, 1984).
[8] A. E. Kovalev, S. Hill, and J. S. Qualls, Phys. Rev. B **66** 134513 (2002).

X-ray magnetic circular dichroism in cobalt-doped ZnO

K. Nielsen, S. Bauer, K. Senn, S. T. B. Goennenwein, M. Opel, and R. Gross [1]
J. Simon and W. Mader [2], *J. Cezar* [3], *D. Schmeisser* [4]

Dilute magnetic semiconductors (DMS) are intriguing materials, as they unite long-range magnetic ordering with the versatile electronic properties of semiconductors. Unfortunately, the ferromagnetic transition temperatures $T_C \leq 170$ K of the prototype DMS $Ga_{1-x}Mn_xAs$ or $In_{1-x}Mn_xAs$ are well below room temperature. In contrast, room-temperature ferromagnetism has been predicted in e.g. transition metal (TM)-doped ZnO [1]. Although room-temperature ferromagnetism has been reported in several experimental studies, there is still a controversial discussion on the nature of ferromagnetism in TM doped ZnO. This is caused by the fact that in experimental work both the presence and absence of ferromagnetism has been reported [2–6]. Moreover, it is still unclear whether ferromagnetism originates from a ferromagnetic exchange between TM ions homogeneously distributed in the ZnO matrix, or whether it is related to the presence of ferromagnetic precipitates – such as metallic ferromagnetic TM clusters – in the ZnO host crystal.

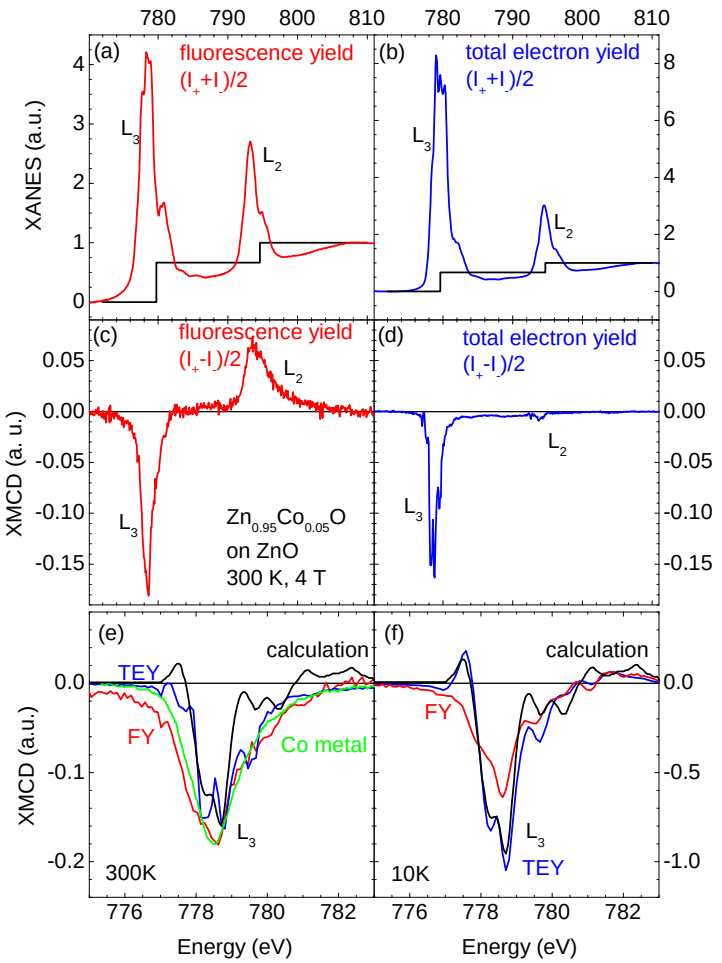

Figure 1: X-ray absorption spectra of a $Zn_{0.95}Co_{0.05}O$ thin film measured at $\mu_0 H = 4$ T in (a) fluorescence yield (FY, red) and (b) total electron yield mode (TEY, blue). In (c) and (d) the x-ray magnetic cirular dichroism (XMCD) is shown for FY and TEY, respectively. In (e) and (f) the XMCD spectra in a narrow energy window around the cobalt L_3 edge are shown for 300 K and 10 K, respectively. For comparison, also an experimental XMCD spectrum for metallic cobalt (green) [7] and a theoretical spectrm for Co^{2+} (black) [10] are shown.

In our study we have grown (0001)-oriented $Zn_{0.95}Co_{0.05}O$ films homoepitaxially on (0001) ZnO substrates using pulsed laser deposition. The films were grown at temperatures T_G between 300 and 600°C in Ar atmosphere. The structural analysis by high-resolution x-ray diffraction (ω-2θ scans in out-of-plane direction and reciprocal space maps of the $(10\bar{1}1)$ reflection) revealed an excellent crystalline quality. The FWHM

[1] This work is supported by the DFG via priority program SPP1187 (GR 1132/13) as well as the ESRF (HE-2089).
[2] Institut für Anorganische Chemie, Universität Bonn
[3] European Synchrotron Radiation Facility ESRF, Grenoble Cedex, France
[4] Brandenburgische TU Cottbus

of the rocking curves of the (0002) reflection was as small as 0.02°. Details are given in [4]. In the following we present data only for films grown at T_G = 400°C to simplify the discussion.

Information on the magnetic ordering of the Co moments was obtained both by XMCD spectroscopy and SQUID magnetometry. XMCD measurements were performed at beamline ID08 at the European Synchrotron Radiation Facility (ESRF) in Grenoble. We measured the x-ray absorption near edge spectra (XANES) on the Co $L_{2,3}$ edges, both in the fluorescence yield (FY) and total electron yield (TEY) mode, in a photon energy range from 765 to 815 eV. The angle between the incident x-ray beam and the film normal was 75° and a magnetic field was applied parallel or anti-parallel to the incident beam. To obtain the XMCD signal, consecutive XANES scans were recorded with different combinations of the helicity of the incoming x-ray beam and the magnetic field orientation. Each XMCD spectrum consists of eight XANES scans taken at constant magnetic field with four spectra taken for left (lcp) and four for right circularly polarized (rcp) light, respectively. The corresponding intensities are denoted by I_+ (lcp) and I_- (rcp).

The data was evaluated in the following way: Firstly, the XANES intensity at energies below the Co L_3 edge (772 eV) was set to zero by subtracting a constant background. Secondly, at 810 eV, i.e. above the L_2 edge, the XANES intensity was normalized to unity. Thereby we assumed that Co does not result in any absorption below the L_3 edge and a constant non-resonant absorption above the L_2 edge. In this way the spectra were corrected for time dependent drifts in the measurement setup. Averaging all corrected spectra results in the quantity $(I_+ + I_-)/2$ shown in Fig. 1(a) and (b) for FY and TEY, respectively. Thirdly, to account for the non-resonant background, step functions as sketched in Fig. 1(a) and (b) were subtracted [7]. Finally, the XMCD signal was determined by subtracting the corrected rcp from the lcp XANES spectra. In Fig 1(c) and (d) the averaged difference $(I_+ - I_-)/2$ is shown for FY and TEY, respectively. The effective spin moment $m_{s,\mathrm{eff}}$ and orbital moment m_l are calculated from the spectra using the magnetooptical sum rules [8, 9]. In Fig 1(e) and (f), the XMCD spectra around the L_3 edge are shown for $T = 300$ K and $T = 10$ K on an enlarged scale. The TEY spectra exhibit a clear multiplet structure, while on the FY spectra this structure is only weakly pronounced.

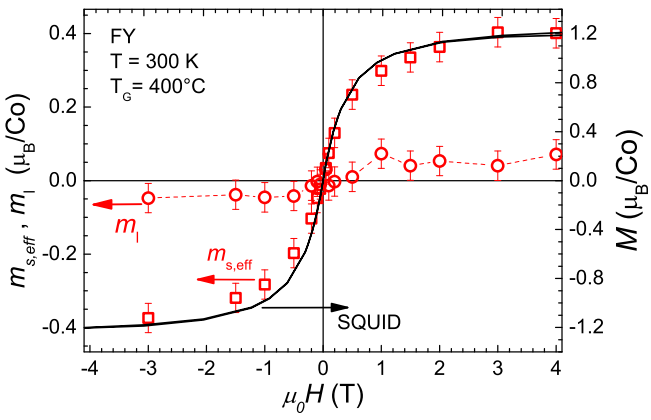

Figure 2: Comparison of magnetization measurements of a $Zn_{0.95}Co_{0.05}O$ thin film by SQUID magnetometry and x-ray magnetic circular dichroism.

To interpret these observations, we note that XMCD in TEY mode is sensitive only to the first few monolayers close to the sample surface because of the small electron escape depth. In contrast, in FY mode more bulk properties are probed due to the much larger escape depth of fluorescence photons. We first discuss the TEY spectra. As evident from Figs. 1(e) and (f), the multiplet structure observed in TEY mode nicely agrees with the XMCD spectrum expected for tetrahedrally coupled Co^{2+} with a crystal-field parameter of $10Dq = -0.7$ eV [10]. Thus, in the surface layer probe in the TEY mode mainly Co^{2+} is present. In contrast, the FY spectra significantly deviate from the XMCD spectra calculated for Co^{2+}, but well agree with those obtained for metallic Co [7]. This suggests that a metallic cobalt impurity phase is present in our sample. As metallic cobalt is a strong ferromagnet, the presence of Co clusters in our $Zn_{0.95}Co_{0.05}O$ thin film makes the interpretation of the magnetic properties tedious.

In Fig. 2, we have plotted the effective spin moment $m_{s,eff}$ of Co derived from the measured FY XMCD spectra as a function of the applied magnetic field. For comparison, we also show the magnetization curve $M(H)$ measured by SQUID magnetometry for the same sample, but with the magnetic field applied parallel to film. The shape of the $m_{s,eff}(H)$ and $M(H)$ curves is almost identical. We note, however, that the magnetic moment per Co atom obtained from the SQUID measurement is by a factor of 3 larger than the moment derived from FY XMCD. In Fig. 2 also the orbital moment m_l is shown. It is aligned parallel to $m_{s,eff}$ with values up to about 0.07 μ_B/Co, i.e. about a factor of 4 smaller than the spin moment 0.4 μ_B/Co in saturation.

In order to further clarify the presence of Co clusters, some samples have been studied by transmission electron microscopy. In Fig. 3(a) a cross-sectional TEM micrograph of a sample grown at 320°C is shown. Evidently, there are regions with different crystalline structure in the ZnO matrix. Element specific imaging (ESI) studies (see Fig. 3(b)) were also performed on the same sample, revealing an enrichment of cobalt in these regions. This supports the conclusion derived from our XMCD FY measurements, giving evidence for the presence of cobalt clusters.

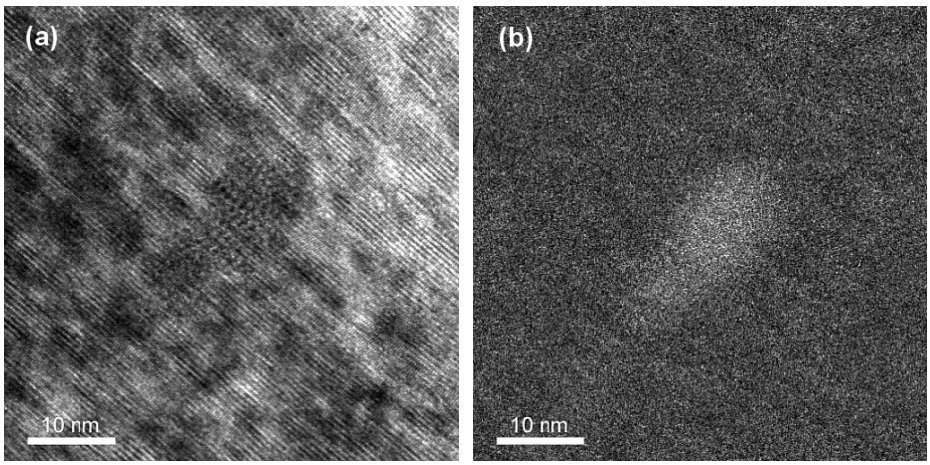

Figure 3: (a) High-resolution transmission electron microscopy image and (b) element specific imaging (element = Cobalt) of the same sample region of a $Zn_{0.95}Co_{0.05}O$ thin film grown on ZnO. In (b) the bright region represents an area with increased Co content.

In summary, we have performed room temperature XMCD and SQUID magnetization measurements in $Zn_{0.95}Co_{0.05}O$ thin films with excellent structural quality. Our results suggest that the presence of metallic cobalt precipitates play an important role for the strong magnetism observed Co doped ZnO.

References

[1] T. Dietl *et al.*, Science **287**, 1019 (2000).
[2] K. Rode *et al.*, J. Appl. Phys. **93**, 7676 (2003).
[3] M. Venkatesan *et al.*, Phys. Rev. Lett. **93**, 177206 (2004).
[4] K. Nielsen *et al.*, phys. stat. sol. (a) **203**, 3581 (2006).
[5] S. Kolesnik *et al.*, J. Appl. Phys. **95**, 2582 (2004).
[6] W. Pacuski *et al.*, Phys. Rev. B **73**, 035214 (2006).
[7] C. T. Chen *et al.*, Phys. Rev. Lett. **75**, 152 (1995).
[8] B. T. Thole *et al.*, Phys. Rev. B **63**, 1943 (1992).
[9] P. Carra *et al.*, Phys. Rev. Lett. **70**, 694 (1993).
[10] M. Kobayashi *et al.*, Phys. Rev. B **72**, 201201(R) (2005).

Magnetotransport in epitaxial Sr_2CrWO_6 thin films

P. Majewski, A. Boger, S. Geprägs, S. T. B. Goennenwein, M. Opel, R. Gross [1]
J. Simon, W. Yu, W. Mader [2]

Over the last years, the physics of ferromagnetic double perovskites of composition $Sr_2BB'O_6$ (with B a magnetic transition metal ion and B' a non-magnetic ion) as well as the growth of epitaxial thin films and heterostructures of these materials has been in the focus of the research activities at WMI (see [1] and references therein). The interest was triggered both by the unusually strong exchange mechanisms resulting in high Curie temperatures well above room temperature and the fact that band structure calculations were predicting half metallic behavior [2–4], making the double perovskites very promising for spintronics applications. Among the various ferromagnetic double perovskites, Sr_2CrWO_6 with a Curie temperature well above 400 K is an interesting candidate. This material can be grown as high quality epitaxial film on $SrTiO_3$(001) substrates by pulsed laser deposition (PLD) [5, 6]. Since single crystals are very difficult to grow due to the volatility of Cr and transport measurements on polycrystalline materials suffer from grain boundary problems, epitaxial thin films are the optimum choice for obtaining reliable transport data on Sr_2CrWO_6 and other double perovskites. Although we succeeded in growing Sr_2CrWO_6 films of excellent quality on $SrTiO_3$ (100) substrates, it turned out that the substrates become oxygen deficient at the deposition conditions (high temperature and low oxygen partial pressure) resulting in a conducting surface layer shunting the films [7]. Therefore, no reliable transport data can be achieved for Sr_2CrWO_6 films directly grown on $SrTiO_3$ [5]. To overcome this problem, we have used an epitaxial $NdGaO_3$ buffer layer. This layer is insulating and avoids oxygen loss of the $SrTiO_3$(001) substrate during the growth of the epitaxial Sr_2CrWO_6 film [8]. In the following we present magnetotransport data of the Sr_2CrWO_6 films grown on $SrTiO_3$ (100) substrates with epitaxial $NdGaO_3$ buffer layer.

The buffer $NdGaO_3$ layer and the Sr_2CrWO_6 film were grown by UHV pulsed laser deposition from polycrystalline stoichiometric targets. First, a thin $NdGaO_3$ buffer layer was deposited at $T_S = 900°C$ in a pure O_2 atmosphere of 0.12 Torr. The laser repetition rate was chosen to $f_L = 5$ Hz and the energy density on the target to $\rho_L = 2.0\,J/cm^2$. The unit cell of bulk $NdGaO_3$ is orthorhombic with $a = 5.433$ Å, $b = 5.504$ Å and $c = 7.716$ Å [9]. On the $SrTiO_3$(001) substrate (cubic, $a = 3.905$ Å), $NdGaO_3$ grows c-axis oriented with the ab-plane rotated by 45° with respect to the substrate. Nevertheless, the lattice mismatch is significant (1.9%), restricting the thickness of the $NdGaO_3$ buffer layer to $\approx$ 7 nm to avoid relaxation and thus to obtain a homogeneously strained film. For the deposition of Sr_2CrWO_6, the sample temperature was set to $T_S = 800°C$ and the deposition atmosphere was switched to Ar ($p = 3 \times 10^{-4}$ Torr) or Ar(99%)/O_2(1%) ($p = 6 \times 10^{-4}$ Torr). For the deposition of Sr_2CrWO_6 both directly on $SrTiO_3$ and on $SrTiO_3$ with a $NdGaO_3$ buffer layer we have chosen ($f_L = 2$ Hz and $\rho_L = 1.3\,J/cm^2$. For these parameter a layer-by-layer growth mode could be obtained. Details have been published elsewhere [5, 6]. The thickness of the samples discussed here were ≈ 7 nm for the $NdGaO_3$ buffer layers and 33 nm to 45 nm for the Sr_2CrWO_6 films. A key parameter for the properties of double perovskites is the amount of anti-site defects ASD (Cr ions on W sites and vice versa). From x-ray analysis we obtained $ASD > 40\%$ ($ASD = 0\%$ for a totally ordered and $ASD = 50\%$ for a completely disordered sample), i.e. the films show a high sublattice disorder.

Fig. 1 shows a cross-sectional transmission electron microscopy image from one sample. The rough interface between the Sr_2CrWO_6 film and the $NdGaO_3$ buffer shows that the thin

[1] This work is supported by the DFG (project No.: GR 1132/13).
[2] Institut für Anorganische Chemie, Universität Bonn, 53117 Bonn, Germany

$NdGaO_3$ buffer layer tends to grow in a three-dimensional island growth mode. However, the $NdGaO_3$ buffer layer does not show any pin holes, which would cause oxygen loss from the $SrTiO_3$ substrate. The TEM image also reveals an epitaxial growth of the double perovskite film on the buffer and confirms the high crystalline quality of the Sr_2CrWO_6 film.

The magnetotransport measurements were carried out in a liquid ^{4}He cryostat at temperatures between 5 K and 300 K and in magnetic fields up to 14 T, using a standard four-point technique. Fig. 2 shows the temperature dependence of the in-plane resistivity for two representative Sr_2CrWO_6 films grown on $NdGaO_3/SrTiO_3(001)$ at zero magnetic field. It is obvious that there are two distinct types of transport behavior. For samples of type A (full circles), the resistivity increases with decreasing temperature over the whole temperature range. At temperatures above 100 K, the resistance follows a variable range hopping-like behavior, $\rho \propto \exp(T_0/T)^{-\nu}$ (see inset). The parameter ν was found to range between 0.2 and 0.4. This behavior is comparable to that found for disordered Sr_2CrWO_6 films grown on $LaAlO_3$ substrates [10]. For samples of type B (open circles), the transport behavior is more complex. With decreasing temperature, the resistivity slightly increases between 300 K and 200 K and then decreases below about 200 K according to a power law $\rho \propto T^{\alpha}$, with $\alpha \sim 0.6$ [11]. Finally, at low temperatures ($T < 25$ K) a weak upturn of the $\rho(T)$ curve is observed. The resulting minimum in the $\rho(T)$ curve at about 25 K has also been seen in Sr_2CrWO_6 films with low ASD density grown on $LaAlO_3$ [10].

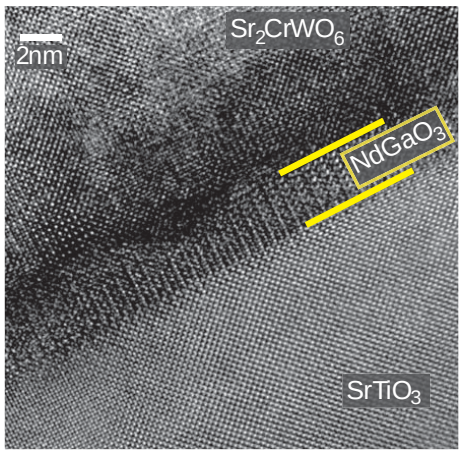

Figure 1: High-resolution transmission electron microscopy image from a $NdGaO_3/Sr_2CrWO_6$ double layer stack on $SrTiO_3(001)$.

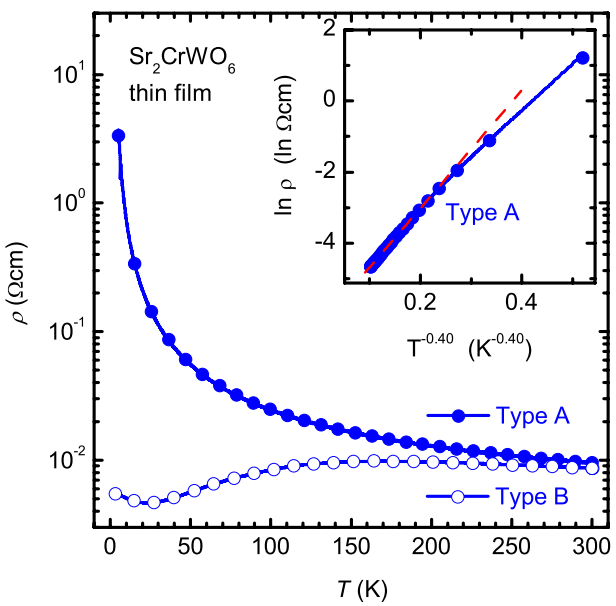

Figure 2: Temperature dependence of the in-plane resistivity for type A and type B Sr_2CrWO_6 films. In the inset ln ρ is plotted versus $1/T^{0.4}$ for a type A sample demonstrating the variable range hopping behavior above about 100K.

In order to explain the observed transport behavior we propose a percolation model. This model is based on spatially inhomogeneous samples, in which regions of a locally ordered double perovskite with metallic conductivity are surrounded by an insulating matrix of disordered material. On the one hand, if there is no continuous conducting connection between the ordered islands, the measured resistivity is dominated by hopping transport in the insulating matrix. This situation is valid for samples of type A showing a variable range hopping behavior over a wide temperature range. On the other hand, if the conducting islands are percolating, a continuous conducting path is formed dominating the measured resistivity. This situation is valid for samples of type B showing a power law behavior of the resistivity over a wide temperature range.

We note that compared to fully ordered films reported in literature [10, 12] the high degree of antisite disorder in our films is expected to lead to additional scattering processes within the conducting path having significant influence on the transport properties. Hence, even for a percolating sample of type B, the transport behavior is expected to deviate from that reported for well ordered samples. Fig. 2 shows that at room temperature the resistivity of the type A and B samples is almost identical. This suggests that the size of the conducting islands is growing with decreasing temperature resulting in a percolation path in the more ordered type B below about 150 K. In contrast, the percolation threshold is not reached for the more disordered type A samples. The physics behind this percolation model is simple. A large density of ASD results in a large density of neighboring Cr^{3+} ions showing antiferromagnetic superexchange. The resulting locally antiferromagnetically ordered regions are insulating. In contrast, in ordered regions we have neighboring Cr^{3+} and W^{5+} ions resulting in ferromagnetic double exchange type interaction and metallic conductivity.

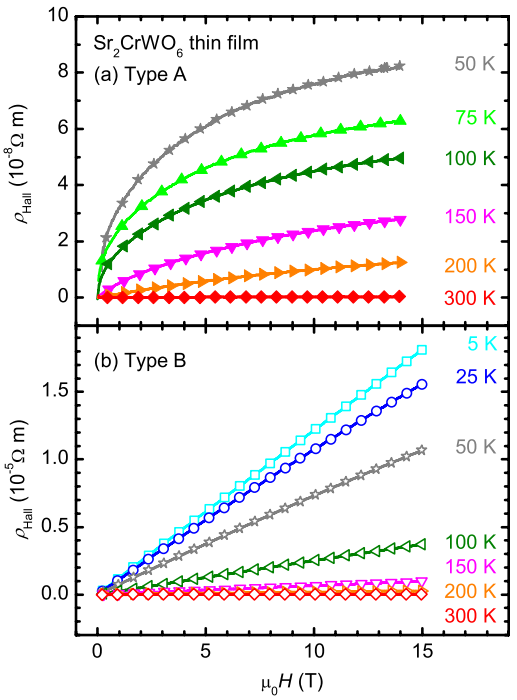

Figure 3: Hall resistivity versus the applied magnetic field measured at different temperatures for a (a) type A sample and (b) type B sample.

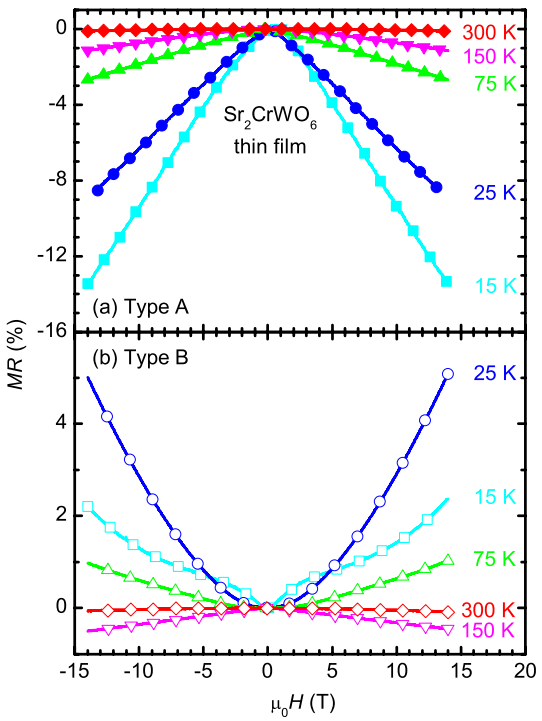

Figure 4: $MR(H) = [R(H) - R(0)]/R(0)$ of a (a) type A and (b) type B sample plotted versus **H** applied perpendicular to the film plane for different temperatures (geometry G1).

For the two types of samples, also the measured Hall effect is different. For samples of type A (Fig. 3(a)) the Hall resistivity varies nonlinearly with applied magnetic fields up to 14 T. In contrast, for samples of type B (Fig. 3(b)), the Hall resistivity is almost linear. Moreover, the difference in the magnitude of the Hall resistivity is remarkable. The Hall effect of the type A samples is not understood so far. Certainly, a simple one band model cannot be applied. If one would do so, an unphysically high carrier density is obtained.

The magnetotransport properties of the Sr_2CrWO_6 films have been measured for three orientations of the applied magnetic field with respect to the film plane and the current direction: field out-of-plane (G1), field in-plane and perpendicular to the current (G2), and field in-plane and parallel to the current (G3). The magnetoresistive (MR) effect, $MR(H) = [R(H) - R(0)]/R(0)$, is shown in Fig. 4 for the G1 geometry. For samples of type A (Fig. 4(a)), the MR is negative for all temperatures. In contrast, for samples of type B a positive MR is measured at low T, whereas a

negative MR is obtained at high T.

The temperature dependence of the MR is shown in Fig. 5, where the MR effect is plotted versus temperature for $\mu_0 H = 14\,\mathrm{T}$. For samples of type A (Fig. 5(a)), a negative MR effect was found for all geometries, which increases with decreasing temperature. Only a the lowest temperatures, a small difference between the different field orientations is visible. The observed isotropy of the MR effect is attributed to the hopping transport mechanism in the type A samples discussed above. Investigating a series of type A samples, we found that those with a lower resistivity at low temperatures (and with a smaller hopping parameter ν) also show a reduced isotropy of the negative MR effect. In contrast, type B samples reveal a strongly anisotropic MR effect (Fig. 5(b)). The MR is negative for both in-plane orientations (geometries G2 and G3), but its magnitude is significantly reduced compared to the MR measured for type A samples. For the out-of-plane geometry (G1), a clear *positive* MR effect was detected for temperatures below about 110 K. It increases with decreasing temperature and shows a maximum at around 25 K. Note that this is exactly the same temperature where the $\rho(T)$ curves have a minimum (c.f. Fig. 2). Towards lower temperatures the MR decreases again. Above about 110 K, a negative MR is found and the anisotropy of the MR effect vanishes at $T \sim 150$ K. Discussing the observed MR effect within the percolation model introduced above, the disappearance of the anisotropy with increasing temperature for type B samples is not surprising. At temperatures above about 150 K one is below the percolation threshold in the type B samples and a similar behavior as for type A samples is expected. In the temperature interval between 175 and 300 K, $MR(14\mathrm{T})$ follows a similar power-law behavior for both types of samples: $|MR(14\mathrm{T})_\mathrm{A}| \propto T^{-3.5}$ and $|MR(14\mathrm{T})_\mathrm{B}| \propto T^{-3.1}$. This suggests that the magnetotransport behavior is dominated by the same transport mechanism as expected, since the type B sample is above the percolation threshold. The pronounced anisotropy of the MR effect found for samples of type B at low temperatures is not understood and is subject of further investigations.

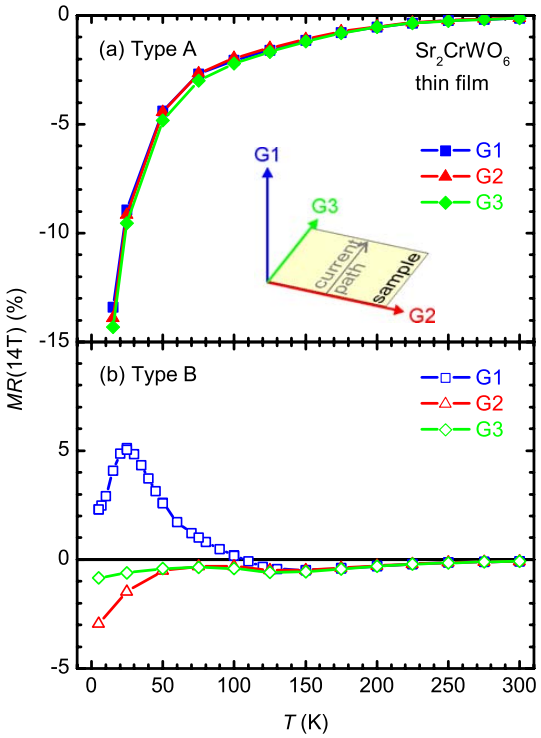

Figure 5: Temperature dependence of $MR(14\mathrm{T})$. The magnetic field **H** was applied in three different geometries G1, G2, and G3 (see inset). (a) Type A sample. (b) Type B sample.

In summary, we have successfully fabricated high quality epitaxial Sr_2CrWO_6 thin films on deposited on $SrTiO_3$ (001) substrates with thin $NdGaO_3$ buffer layer. The magnetotransport properties of Sr_2CrWO_6 show a complex behavior. Measurements of both the temperature dependence of the resistivity and the Hall effect give clear evidence for spatially inhomogeneous Sr_2CrWO_6 thin film samples. The observed behavior can be consistently explained by assuming conducting regions with a high local sublattice ordering, which are surrounded by an insulating matrix formed by disordered material. Below the percolation threshold, the electrical transport properties are dominated by a hopping transport mechanism in the insulating matrix. This hopping transport is expected to be isotropic what is confirmed by our magnetotransport measurements for different orientations of the magnetic field relative to the current direction. Above the percolation threshold, the magnetotransport is dominated by the conduct-

ing percolation path leading to a metallic behavior of both the resistivity and the Hall effect and a large anisotropy of the low-temperature magnetoresistance.

References

[1] P. Majewski, PhD Thesis, TU München (2006).
[2] K.-I. Kobayashi *et al.*, Nature **395**, 677 (1998).
[3] G. Vaitheeswaran, V. Kanchana, and A. Delin, Appl. Phys. Lett. **86**, 032513 (2005).
[4] P. Majewski *et al.*, Phys. Rev. B **72**, 132402 (2005).
[5] J. B. Philipp *et al.*, J. Appl. Phys. **93**, 6853 (2003).
[6] P. Majewski *et al.*, J. Magn. Magn. Mater. **290-291**, 1154 (2005).
[7] K. Szot *et al.*, Phys. Rev. Lett. **88**, 075508 (2002).
[8] P. Majewski *et al.*, *submitted to* Eur. Phys. J. B (2006).
[9] W. Marti *et al.*, J. Phys.: Condens. Matter **6**, 127 (1994).
[10] A. Venimadhav *et al.*, Solid State Commun. **138**, 314 (2006).
[11] Note that the power law exponent α does not correspond to one of the "classical" exponents like $\alpha = 2$ (electron-magnon scattering) or $\alpha = 5$ (electron-phonon scattering).
[12] D. Sánchez *et al.*, J. Appl. Phys. **96**, 2736 (2004).

Fast spin relaxation in solid ^{3}He determined by pulsed NMR

M. Kath, S. Bago, and E. Schuberth

Nuclear magnetism in the quantum solid ^{3}He is unique among the magnetic systems since it is mediated solely by the exchange interaction of weak, localized nuclear spins in a cubic lattice. The system was initially regarded as the simplest version of a Heisenberg nearest neighbor antiferromagnet before it was realized that this picture is not enough to describe the magnetic phase diagram which was established after more than two decades of intensive work [1] [2].

Solid ^{3}He magnetism is rather dominated by frustration between competing ferromagnetic and antiferromagnetic interactions which originate from three and four spin permutations respectively. This leads to two nuclear magnetically ordered phases below a few milliKelvin, commonly denoted as low field phase (lfp) and high field phase (hfp) above 0.4 T. While the low field phase in bulk material most probably has the U2D2 structure proposed by Osheroff et al. [3], with two planes in the bcc lattice pointing "up" and two pointing "down" (orthogonal to the applied magnetic field), the spin structure of the "weak ferromagnetic" high field phase is indirectly inferred from its magnetization as a canted antiferromagnetic alignment.

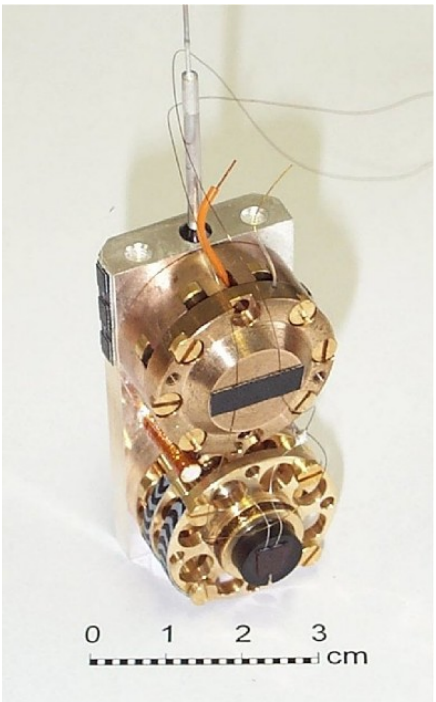

Figure 1: Pressure cell used to grow ^{3}He crystals with capacitive pressure transducer (upper part) and NMR plus gradient coils (below)

The theoretical description of the magnetic interaction is based on the fact that the quantum mechanical exchange interaction can be mapped on permutation operators in real space i.e. by physical exchange of atoms between lattice sites. Three and four spin exchange is favored in the dense lattice (bcc structure below 10 MPa and hcp structure above) since the two particle exchange requires too much deformation of the lattice. Exchange processes of odd or even parity lead to competing ferromagnetic and antiferromagnetic interactions respectively and thus to frustration. The multiple spin exchange model has been worked out in a very elaborate way by Roger et al. [4] but quantitative details and even some qualitative features of the experimental phase diagram [2] are still not reproduced. To clarify experimentally the spin structures of the two phases in the sinters needed for cooling and adsorbing the heat released from the neutron absorption in ^{3}He, neutron scattering experiments are the method of choice. Ultimately one could even try to reach the high pressure hcp ordered phase below 20 μK [5]. For more information see the feasibility study by Siemensmeyer et al. [6].

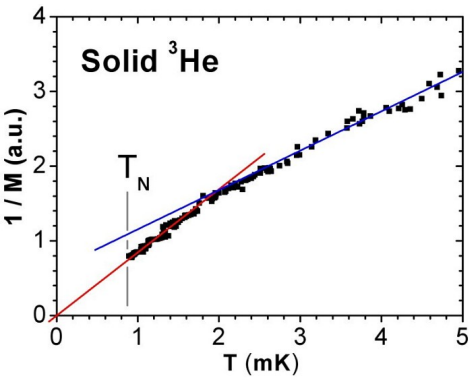

Figure 2: Inverse magnetization of solid ^{3}He vs temperature above T_{Nel}. The kink around 2 mK is also described by the multiple ring exchange model.

In our work we investigated the ordered phases of solid ^{3}He by pulsed NMR including spin echo techniques. Fig. 1 shows the pressure cell used to grow crystals of ^{3}He. The upper part consists of a capacitive pressure transducer to accurately determine the pressure in the cell, the lower part is a Sintimid coil former for the NMR coil together with a Helmholtz gradient coil. The latter can be used for a 1-dimensional "Zeugmatography", the spacial resolution of the solid contributions of ^{3}He from inside the coil. The result for the T_1 measurement ist astonishing: there is a very efficient initial relaxation process on a time scale of less than 100 μs which prevents a tipping angle larger than 10Âř. This process is much faster than either T_1 or T_2 which are about 300 ms and 4.6 ms respectively. The first follows from Fig.4 the latter we measured by the spin echo method.

Most probably, the fast recovery of M_z originates from a precession of the nuclear spins about the demagnetizing field of the sample since this is strong in the ^{3}He case. The second feature which favors this effect is the fact, that due to the strong multiple ring exchange interaction T_2 is very long compared to the usual cases of classical solids because of motional narrowing. For a quantitative analysis the situation in our pressure cell filled with Ag sinter is unfavorable. Only without sinter and with an superimposed field gradient one can hope to be able to calculate precisely how the motion of spins during and after the NMR pulse takes place. Corresponding experiments are planned for the future.

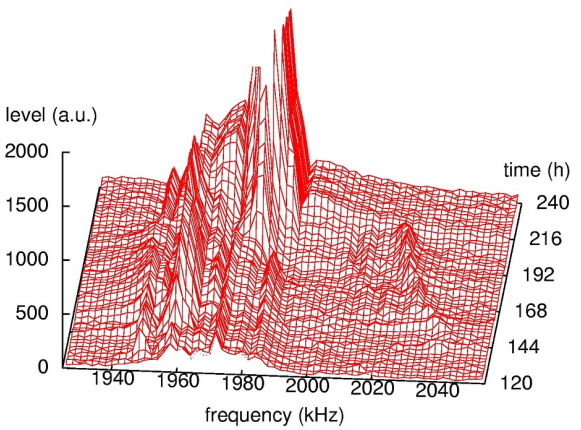

Figure 3: Series of NMR spectra around 2 MHz while the crystal is slowly warming out of the low field ordered state. On the high frequency side a series of split lines can be seen which disappear above T_{Neel} while the line groups on the low frequency side are due to a different part of the solid which has a higher temperature than the main part at 1980 kHz. Above T_{Neel} the latter remain as a shoulder on the Larmor line.

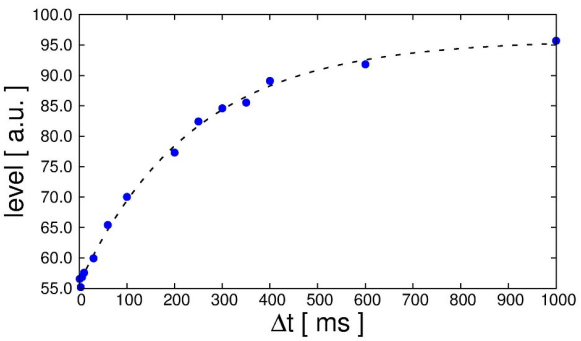

Figure 4: Recovery of the longitudinal magnetization after a nominally 90Âř pulse. Due to an effective spin relaxation even during the puls no reduction of M_z below 70 % can be obtained. The resulting T_1 after this initial process is 240 ms at a temperature of 10 mK.

References

[1] D. D. Osheroff, J. Low Temp. Phys. **87**, 297 (1992).
[2] J. S. Xia, W. Ni, and E. D. Adams, Phys. Rev. Lett. **70**, 1481 (1993).
[3] D. D. Osheroff, M. C. Cross, and D. S. Fisher, Phys. Rev. Lett. **44**, 792 (1980).
[4] M. Roger, J. H. Hetherington, and J. M. Delrieu, Rev. Mod. Phys. **55**, 1 (1983).
[5] T. Lang, P. L. Moyland, D. A. Sergatskov, E. D. Adams, and Y. Takano, Phys. Rev. Lett. **77**, 322 (1996).
[6] K. Siemensmeyer, E. A. Schuberth, E. D. Adams, Y. Takano, and K. Guckelsberger, Physica B **284-286**, 363 (2000).

Iron uptake in vermiculites from Spain

A. Lerf
F.E. Wagner, [1] *J. Poyato, J.L. Perez-Rodriguez, and V. Ramirez del Valle* [2]

Natural clay minerals of the 2:1 type very often contain Fe ions in the octahedral and/or tetrahedral layers. It has been known for fifty years that at least the octahedral iron ions are easily accessible to redox reactions; a striking example for this are the color reactions of some amines intercalated into smectites. Oxidation of the octahedral structural iron ions has also been considered as an important step in the weathering of micas to vermiculite.

An interesting electron mediator in the interlayer space could be the Fe-ion itself. It is known to bind organic species in the interlayer space [1] and, especially, the Fe^{3+}-ions induce oxidation reactions, including the formation of the conducting polypyrrole system [2, 3]. In addition, this ion is magnetic and could induce some magnetic ordering between the iron sites in the host layers [4]. Apart from the intercalation of isolated Fe^{3+} ions it is known that complex iron-oxypolycations obtained by hydrolysis can be inserted in the interlayer space [5]. It is known that these large cations lead to high layer distances in case of low charged montmorillonites and to the formation of mesopores which make the products interesting for catalysis.

We report here on a Mössbauer study at room temperature and at 4.2 K of the iron loaded vermiculites of Ojén and Santa Olalla, Spain, obtained by means of various reactions conditions since preliminary experiments show that most of the Fe^{3+} is deposited on the external surface of the clay particles, even at low pH.

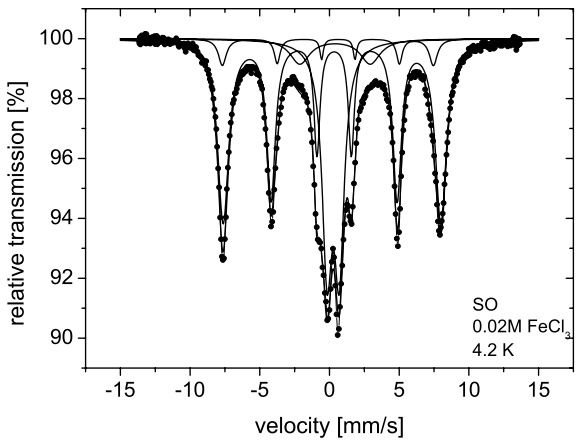

Figure 1: Mössbauer spectrum taken at 4.2 K for a Santa Olalla vermiculite treated with an aqueous iron chloride solution. Black dots are data points; the black line through the data points is the simulated spectrum; the other lines show individual components of the spectrum

In the vermiculites treated with as prepared $FeCl_3$ solutions akaganeite is always deposited on the external surfaces (see figure 1) in the concentration range 0.2 to 1 M; its amount increases with iron concentration in solution. Even at room temperature the two iron sites of the akaganeite dominate the Mössbauer spectra and hide the Fe^{3+} contribution of the clay mineral. At lower concentrations ferrihydrite has been deposited, but to a minor extent. In these cases there is a second Fe^{3+} site (QS:0.6-0.71mm/s) which cannot be easily assigned to a peculiar Fe^{3+} species; it could originate at least in part from Fe^{3+} inserted in the interlayer space. The question arises which species is really present in the interlayer space. In almost all cases we found layer distances of 14.3 Å which is very similar to fully hydrated sodium or magnesium vermiculites. However, the intercalated species cannot be just a hydrated $[Fe(H_2O)_6]^{3+}$ monomer since it is a minority speciesat the pH of the supernatant solution [6]. The most probable species for insertion should be the dimer $[Fe_2(OH)_2(H_2O)_y]^{4+}$. However, different Mössbauer parameters has been described in literature upon this ion [7], though a definite assignment is not possible. In addition, if the pH is increased a little (for example in more dilute

[1]Physik-Department, TU München
[2]CSIC, Instituto de Ciencia de Materiales de Sevilla, Spain

solutions) further polymerization of the dimer occurs which leads to a high molecular polymer with very similar quadrupole splitting.

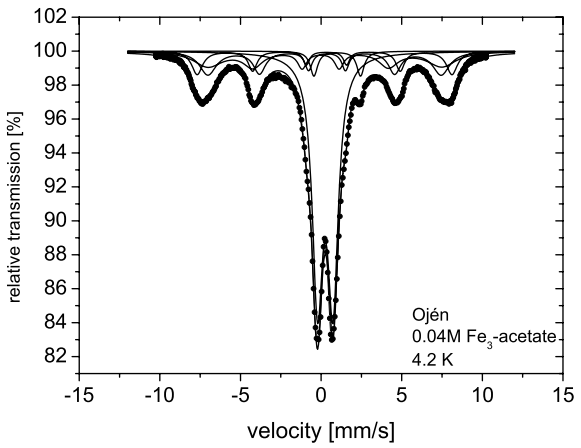

Figure 2: Mössbauer spectrum taken at 4.2 K for a Ojen vermiculite treated with the iron acetate cluster.Black dots are data points; the black line through the data points is the simulated spectrum; the other lines show individual components of the spectrum

This hydrolysis can be triggered by adding a well adjusted amount of OH^-. Such hydrolyzed solutions are applied for inserting the polyoxycations in the interlayer space to obtain a so-called "pillared clay" which is characterized by its high mesoporosity. Again one observes deposited iron oxides, but which one depends on the age of the hydrolyzed solution. If the solution has been brought in contact with the clay immediately after hydrolysis one gets a sample showing a small amount of ferrihydrite. After ten days of aging one observes again the formation of akaganeite. A peculiar feature characteristic for the iron polymer cannot be detected in the Mössbauer spectra, because they show similar parameters as the deposited oxides.

The deposition of oxides or other iron oxo species is not surprising because all of these species are positively charged in an aqueous medium and thus interact strongly with the negatively charged clay surfaces prior to intercalation or trigger clay flocculation [8]. If one tries to circumvent this problem by insertion of more stable positively charged polynuclear iron clusters like the trinuclear acetate clusters [9], the same result is obtained since the clusters become destroyed before intercalation. Only the amount of iron-oxides deposited seems to be lower and the species deposited is very probably ferrihydrite (figure 2).

The only chance to suppress the iron oxide deposition is the treatment of the vermiculites with a methanol solution of hydrous $FeCl_3$ according to Letaïef [3]. And indeed we obtained samples showing no magnetic ordering at 4.2 K in case of the Santa Olalla vermiculite, but a tiny amount of a magnetic compound in case of the Ojén vermiculite and the Wyoming smectite.

These results have interesting implications for the evaluation of catalysts based on pillaring reactions.

References

[1] M.M. Mortland and L.J. Halloran, Soil Science Soc. Amer. J. **40**, 367 (1976).
[2] A. Moreale, P. Cloos, and C. Badot, Clay Miner. **20**, 29 (1985).
[3] S. Letaïef, P. Aranda, and E. Ruiz-Hitzky, Appl. Clay Science **28**, 183 (2005).
[4] N.H.J. Gangas, J. von Wonterghem, S. Mørup, and C.J.W. Koch, J. Phys. C: Sol. State Phys. **18**, L1011 (1985).
[5] E.G. Rightor, M-S. Tzou, and T.J. Pinnavaia, J. Catal. **130**, 29 (1991).
[6] C.M. Flynn, Chem. Rev. 84, 31 (1984).
[7] A. Vertes, L. Korecz, and K. Burger, *Mössbauer Spectroscopy* (Elsevier, Amsterdam, 1979).
[8] E. Tombácz, in *Role of Interfaces in Environmental Protection*, edited by S. Barany (Kluver, Dordrecht, 2003), pp. 397-424.
[9] S. Yamanaka, T. Doi, S. Sako, and M. Hattori, Mat. Res. Bull. **19**, 161 (1984).

Magnetic properties of the ferrous tainiolite $Cs[Fe_2Li]\langle Si_4\rangle O_{10}F_2$ and its oxidation product

A. Lerf and M. Opel
R. Mariychuk and J. Breu [1]; *F.E. Wagner* [2]

Various natural clay minerals of the 1:1 and 1:2 types in which Fe^{2+} ions occupy at least one third of the possible sites in the octahedral layers show magnetic ordering phenomena. The Mössbauer spectra of such samples taken at 4.2 K are rather complex [1–3]. This complexitity could originate from the partial oxidation of the Fe^{2+} occurring normally in the natural samples. In addition, the crystallinity of the natural samples is often not very high and there is some contamination with other metal ions in the octahedral layers. To understand the magnetic phenomena in the clay minerals it might be helpful to investigate synthetic samples which can be obtained without contamination with foreign elements and with controlled and well-defined Fe^{2+} content. First studies on synthetic clay minerals were devoted to annite $K[Fe_3]\langle AlSi_3\rangle O_{10}(OH)_2$, but this system contains also some Fe^{3+} [4].

Some of us were successful in the preparation of a tainiolite $Cs[Fe_2Li]\langle Si_4\rangle O_{10}F_2$ which contains less Fe^{2+}, but definitely no Fe^{3+} [5]. This sample can be easily oxidized to a different extent [5]. Here we report about the magnetic properties of this new clay mineral and their change by partial oxidation.

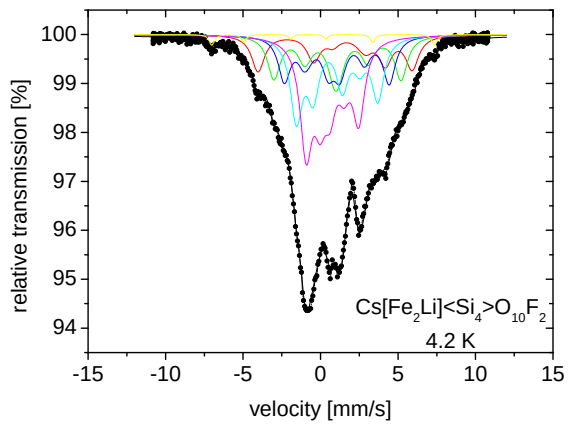

Figure 1: Mössbauer spectrum taken at 4.2 K for the original tainiloite. Black dots are data points; the black line through the data points is the simulated spectrum; the colored lines show individual components of the spectrum

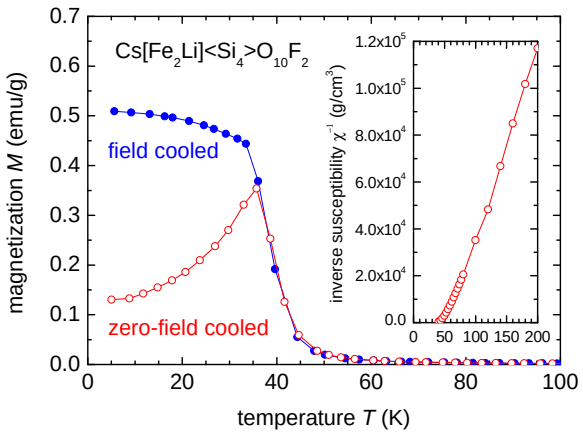

Figure 2: Magnetization vs temperature for the original tainiolite. The sample has been cooled down to 5 K at zero field. Then the field was switched to 6 Oe and the data were taken while sweeping T to 300 K (red) and cooling back to 5 K (blue). The inset shows the inverse magnetic susceptibility (Curie-Weiss plot) measured at 6 Oe with an additional alternating field of 0.5 Oe and 20 Hz after zero-field cooling.

The room temperature Mössbauer spectrum of the unoxidized tainiolite show two Fe^{2+} quadrupole doublets and almost no Fe^{3+}. The Mössbauer spectrum at 4.2 K is shown in fig. 1. The spectrum is as complex as those of the natural iron rich phyllosilicates, thus is dominated by the Fe^{2+} interactions. The magnetic hyperfine splitting start to appear at about 40 K and the complexity of the spectra increases with decreasing temperature. This phase transition to

[1]Institut für Anorganische Chemie II, Universität Bayreuth
[2]Physik-Department, Technische Universität München

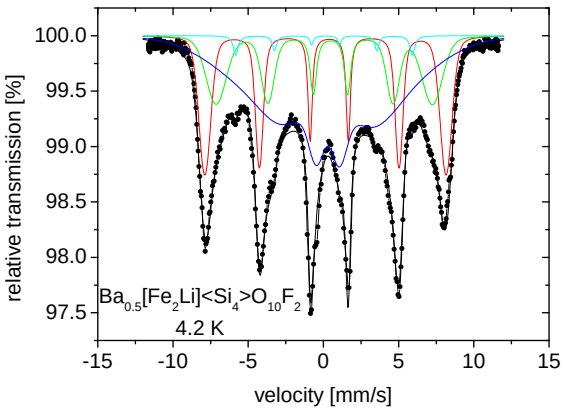

Figure 3: Mössbauer spectrum taken at 4.2 K for the fully oxidized and Ba exchanged tainolite. Black dots are data points; the black line through the data points is the simulated spectrum; the colored lines show individual components of the spectrum.

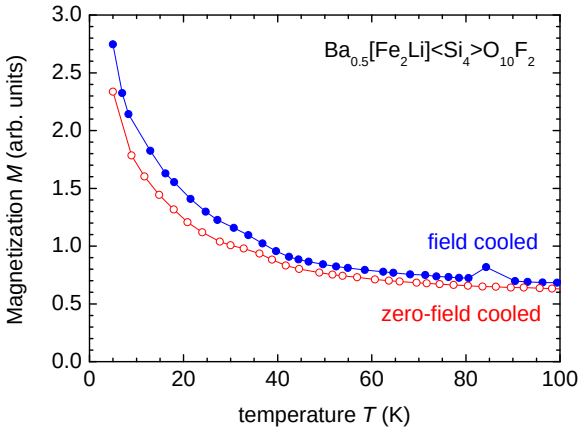

Figure 4: Magnetization vs temperature for the oxidized sample $Ba_{0.5}[Fe_2Li]\langle Si_4\rangle O_{10}F_2$. The sample has been cooled down to 5 K at zero field. Then the field was switched to 6 Oe and the data were taken while sweeping T to 300 K (red) and cooling back to 5 K (blue).

the magnetically ordered phase is clearly visible in the temperature-dependent magnetization $M(T)$ (fig. 2). When the sample was cooled at 6 (field cooled, blue) or at 0 Oe (zero-field cooled, red) $M(T)$ behaves differently below $\approx$ 35 K. In a Curie-Weiss plot (inset in fig. 2), the inverse magnetic susceptibility $\chi^{-1}(T)$ shows linear behavior over a wide temperature range. The regression line through the data points cuts the temperature axes at a positive temperature of 35 K, indicating that the sample enters a ferromagnetic state. The behavior is quite similar to the synthetic annite [5], but the temperature of the transition is shifted to lower temperatures.

If the sample has been oxidized to the maximum possible level (composition: $Ba_{0.5}[Fe_{2.0}Li_{1.0}]\langle Si_4\rangle O_{10}F_2$) the behavior at low temperature changes completely. The Mössbauer spectrum at 4.2 K (fig. 3) is now dominated by the interaction of the Fe^{3+} ions and can be fitted with two sextets showing a hyperfine splitting of 44.5 T and 49 T, respectively. In addition there is a broad distribution of hyperfine fields. However, in the magnetic susceptibility vs. temperature curve (fig. 4) there is no indication for an ordering transition down to 4.2 K.

References

[1] J.M.D. Coey, O. Ballet, A. Moukarika, and J.L. Soubeyroux, Phys. Chem. Miner. **7**, 141 (1981).
[2] J.M.D. Coey, A. Moukarika, and O. Ballet, J. Appl. Phys. **53**, 8320 (1982).
[3] O. Ballet and J.M.D. Coey, Phys. Chem. Miner. **8**, 218 (1982).
[4] D.G. Rancourt, I.A.D. Christie, G. Lamarche, I. Swainson, and S. Flandrois, J. Magn. Magn. Mater. **138**, 31 (1994).
[5] R. Mariychuk, A. Baumgartner, F.E. Wagner, A. Lerf, A. Dubbe, R. Moos, and J. Breu, *submitted*.

Fréchet dendrons: a general motif for molecular self-organization

B. A. Hermann [1]
L. Merz, L. Scherer, E. Constable, and C. Housecroft [2]

Introduction

Self-organised molecular [1] layers provide a promising route to constructing new (switchable) nanodevices and optimising nanosensors. The design of such molecules involves control of structure and stabilisation on the surface as well as control of functionality. The development of synthetic routes of molecules bearing functionality and at the same time exhibiting excellent self-organization properties is tedious and time consuming. Hence, the search for a potentially universal "adapter", which can control the self-organisation and stabilisation on a particular type of surface is a worthwhile challenge. High-quality nanoscale imaging using scanning tunnelling microscopy (STM) [2] provides the means to significantly advance such studies. Due to the limited space, the conclusion drawn from extensive current and former STM-studies on dendrons can only be sketched in this report - details can be found in [3], [4].

Fréchet-type dendrons: self-organising of molecular components on graphite surfaces

How powerfully Fréchet dendrons can affect various central components (catalytic, switchable, redox-active) on a *graphite surface* is addressed by analysing self-organised monolayers of nine different molecules, each containing at least one first or second-generation [5] Fréchet-type dendron.

n-octyl-substituted catalytic Fréchet dendrons

The strategy behind using Fréchet dendrons as a motif for molecular self-organization was to increase the conformational flexibility (conformation = constellation of the molecule) of our systems and thereby provide more reliable self-organisation by achieving better commensurability of the SAM with the substrate. Using such systems, we were able to obtain sub-molecularly resolved STM images of catalytic Fréchet dendrons under ambient conditions. In the case of the Fréchet-type systems, the contrast in the STM images is mainly caused by the π-orbitals of the aryl rings (see Figure 1(a)) oriented in a direction perpendicular to the basal plane of the substrate. The flexibility of the central unit allows both arms of the dendron to optimise their interactions, thus prohibiting sub-molecular resolved images. In addition, in order to maximise the 2-dimensional crystallisation energy, the alkyl chains of neighbouring molecules form interdigitated patterns.

Four different 2,2′:6′,2″-terpyridine-substituted (L-substituted) Fréchet dendrons,

first generation molecules with octyl chains, with benzyl decoration, with benzyl decoration and sulphur substituted for the inner oxygen and second-generation molecules with *n*-octyl chains: The most commonly observed molecular domains of the

[1]This work is supported through the Swiss National Science Program (NRP 47 project of B.A.H.).
[2]Institute of Inorganic Chemistry, University of Basel, Switzerland

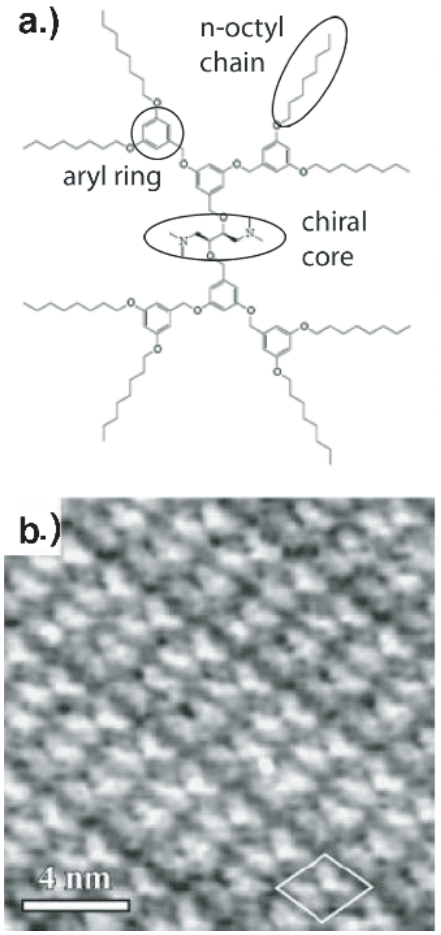

Figure 1: (a) Structural formula of the chiral dendron. (b) STM image of a self-organised monolayer of *n*-octyl-substituted dendritic compounds with chiral core moiety on a dry HOPG surface. The aryl rings lie down flat on the graphite surface, while the perpendicular π-orbitals account for the contrast in the STM-image. A unit cell of the molecular lattice is drawn in white (U_{bias} = 700 mV, $|I_{\mathrm{t}}|$ = 0.01 nA).

second-generation molecules with *n*-octyl chains consist of rows of dimers formed by intermeshing 2,2′:6′,2″-terpyridine head-groups each of which locked with adjacent dimers by the interdigitation of the octyl chains. Every second to fourth row, the orientation of the molecular dimers changes as a result of a rotational dislocation in the 2-dimensional array. This failure in sequential growth of the second-generation *L*-Fréchet dendrons with *n*-octyl substitution may be caused by domains of slightly different orientation growing together, or a lack of commensurability of the molecule with the graphite surface. As the benzene decorated dendrons lack the octyl chains, the intermolecular interactions are no longer dominated by interdigitation of the octyl groups, but rather by van der Waals interlocking of the aromatic rings. The structure and symmetry of the observed self-organised monolayers is sensitive to the substitution of one atom within the dendron (inner oxygen substituted with sulphur).

Second- and first-generation dendrons with a switchable bipyridine-central core

Basic pattern formation and symmetries were discussed in the last report and in [6]. In particular, the conformational change (switching) of the first-generation dendron from the *trans* (stretched) arrangement of nitrogen atoms (as in a free ligand) to the *cis* (u-shaped) conformation (as in a coordinated ligand) is expected to have a high activation barrier for molecules on a surface. Associated with the mechanical motion (from *trans* to *cis*) of the dendritic substituents is a non-planar bipyridine which cannot lie flat on the surface during the conformational change. Despite this fact, we could induce a conformational chance of the 2,2′-bipyridine-domain of the first-generation 2,2′-bipyridine dendron through protonation, resulting in the formation of *new* species under solution and normal solid-state conditions (see Figure 2 bottom). Qualitative modelling to the known protonation chemistry of 2,2′-bipyridine is consistent with the molecule adopting a *cis* (u-shaped) conformation.

Hexafluorophosphate salt of a complex cation, $[Ru(4'\text{-}X\text{-}L)_2][PF_6]_2$, and a charge neutral bis(alkynyl)platinum(II) dendron

Pre-formed complexes were delivered to the surface by solution casting. As with the dendrons discussed above and below, there are no covalent bonds between the complexes and the surface or between monolayer subunits. The complexes form self-organised monolayers predominantly in a lamellar phase. Within the domains, row dislocations could be observed. The

rows of the Ru-complex appear very condensed (and hence the distance between the ruthenium centres of adjacent cations is small). These observations do indicate that the anions are not incorporated in the assembly. Despite being charge neutral the bis(alkynyl)platinum(II) dendrons organize also in a lamellar phase, but show a distinctly different electronic structure of the molecular core in the STM image.

Alcohol and aldehyde terminated Fréchet dendritic wedges

A molecular model of the proposed arrangement of molecules of the aldehyde and alcohol Fréchet- type dendrons was discussed in the last report and in [7].

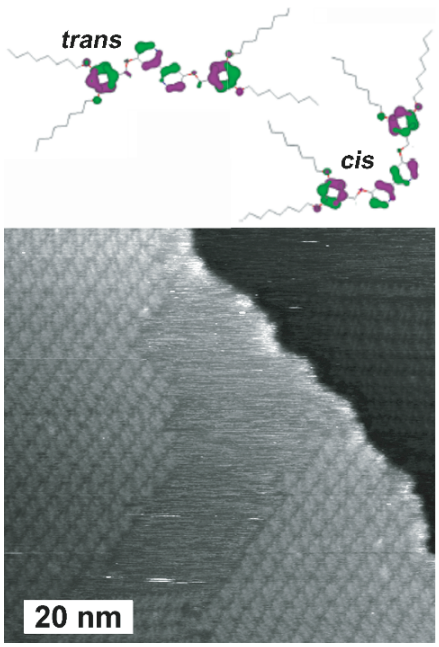

Figure 2: STM image of a monolayer of a first-generation bipyridine dendron on HOPG after treatment with gaseous HCl (50 nm × 50 nm, U_{bias} = 800 meV, $|I_t|$ = 9 pA).

Conclusions

From the material of our recent STM studies presented here, we conclude that we have succeeded in finding a modular approach for the design of large molecules suitable for self-organisation. Each molecule possesses a core bearing the functionality of interest and a Fréchet dendron responsible for self-organisation and intermolecular as well as molecule-substrate stabilisation. Hence, we have been able to adapt a wide range of molecular cores with varying functionalities (catalytic, redox- and photoactive), varying degrees of freedom and flexibility (chiral, switchable, bulky), and either being charge-carrying or charge-neutral to optimise binding on graphite surfaces by self-organisation. In conclusion, it is possible to use Fréchet dendritic wedges as a general visualisation marker and "self-organiser" for functionalised fragments (molecular centres), with respect to both visualisation with STM and triggering of self-organisation processes on graphite surfaces. The work in progress involves the structural transition observed on the Fréchet wedges with change in temperature and small changes of the molecular structure.

H.J. Güntherodt is gratefully acknowledged for hosting part of this research.

References

[1] B.A. Hermann, in *Encyclopedia on Supramolecular Chemistry*, edited by J.A. Atwood and J.W. Steed (Marcel Dekker, New York, 2006), p. 1.
[2] B.A. Hermann, in *Analytical Methods of Supramolecular Chemistry*, edited by C.A. Schalley (Wiley-VCH, Weinheim, 2006) p. 337.
[3] B.A. Hermann *et al.*, Adv. Funct. Mat. **16**, 221 (2006).
[4] E.C. Constable *et al.*, *submitted to* Cryst. Eng. Com. (2006).
[5] Second generation means that the outer aromatic unit is repeated once resulting in a branched structure.
[6] L. Scherer *et al.*, J. Am. Chem. Soc. **127**, 4033 (2005).
[7] L. Merz *et al.*, Chemistry **11**, 2307 (2005).

Observation of macroscopic quantum behavior in π Josephson junctions with ferromagnetic interlayer

K. Madek, S. Beutner, G. Wild, Ch. Probst, A. Marx, and R. Gross [1]
M. Weides and H. Kohlstedt [2]

Superconducting circuits based on Josephson junctions (JJs) have been successfully used for the realization of quantum bits (qubits) in quantum information processing. With regard to materials choice and fabrication technology, JJ based quantum circuits so far mainly have been implemented with metallic superconductors. However, more recently the interest has been extended to junctions based on high temperature superconductors (HTS) [1] or to so-called π-Josephson junctions (π-JJs), which involve thin ferromagnetic interlayers and have a π phase difference between the superconducting junction electrodes in their ground state [2–4]. The origin of the π phase shift is the finite momentum $Q \propto h_{ex}/v_F$ of Cooper pairs penetrating into the ferromagnetic layer. Here, h_{ex} is the exchange splitting between the spin up and down bands and v_F the Fermi velocity. The finite momentum results in a spatial oscillation of the superconducting order parameter $\Psi \propto \cos(2Qx)$ along the direction x perpendicular to the SF interface. At an appropriate thickness of the ferromagnetic layer the order parameter can change sign resulting in a π phase shift across the insulating barrier in the ground state [5], which has been confirmed by experiment [2, 3]. At present, there is strong interest in the quantum behavior of both HTS based JJs and superconductor/insulator/ferromagnet/superconductor (SIFS) π-JJs. On the one hand, this interest is stimulated by the possibility of exploiting the d-wave order parameter of HTS or the intrinsic π phase shift in the ground state of SIFS-JJs for the realization of "quiet" qubits, which allows an optimum protection from external fluctuations and hence to avoid decoherence [6, 7]. On the other hand, the study of such systems allows to address fundamental issues related to the nature of superconductivity, dissipation mechanisms or quantum coherence.

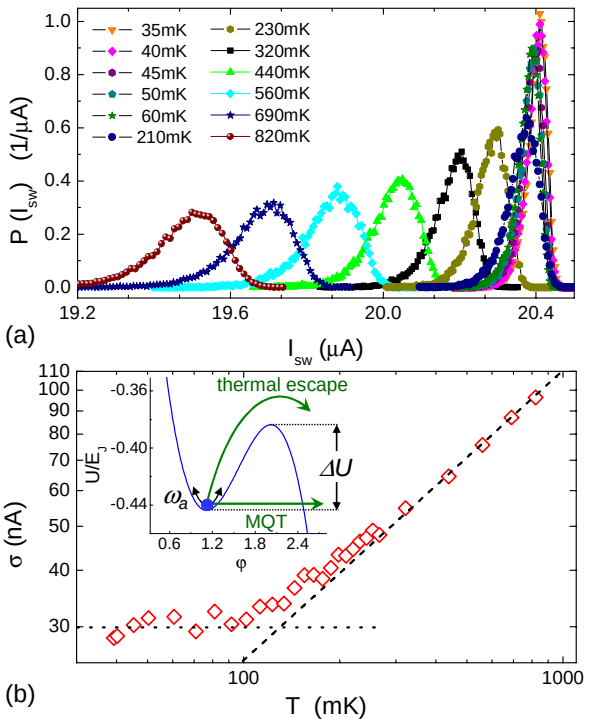

Figure 1: (a) Switching current probability distribution $P(I_{sw})$ of a $Nb/AlO_x/Ni_{60}Cu_{40}/Nb$ SIFS π-JJ recorded at different temperatures. (b) Standard deviation σ of $P(I_{sw})$ plotted versus temperature on a double logarithmic scale. The dashed line shows the theoretically expected $T^{2/3}$ dependence in the thermal regime. The inset shows the tilted washboard potential for $\gamma = I/I_c = 0.9$.

Although HTS and ferromagnetic JJs are very promising for superconducting quantum circuits, a key issue in these systems is the presence of low-energy excitations causing dissipation. This is perturbing for the occurrence of macroscopic quantum phenomena and may even prevent the use of such junctions in quantum circuits such as superconducting qubits. Fortunately,

[1] This work is supported by the DFG through the Cooperative Research Center 631.
[2] Institut für Festkörperforschung and CNI, Forschungszentrum Jülich

very recently macroscopic quantum behavior has been demonstrated for HTS grain boundary [8] and intrinsic JJs [9], whereas no experimental study is available for SIFS π-JJs so far. We therefore systematically studied the quantum behavior of SIFS π-JJs in collaboration with M. Weides from the Research Center in Jülich. For the first time, macroscopic quantum behavior of the phase difference φ could be observed in SIFS π-JJs. In our experiments both MQT of the phase difference and energy level quantization have been studied in detail. Our results provide clear evidence for macroscopic quantum behavior in SIFS π-JJs. Furthermore, they suggest that the dissipation in these junctions is sufficiently small to result in sharp energy levels as required for qubits.

Fig. 1a shows a set of switching current probability distributions $P(I_{\rm sw})$ at different temperatures. The data were obtained on an SIFS junction fabricated by M. Weides at FZ Jülich. Switching current measurements were performed by ramping up the junction current at constant rate and measuring the current value $I_{\rm sw}$ at which a voltage across the junction appears via a sample-and-hold technique. At high temperatures the switching into the voltage state due to the escape of the phase difference from a local potential minimum is dominated by thermal escape, whereas quantum tunneling is expected to prevail below a characteristic cross-over temperature $T^\star$. Accordingly, the distribution width σ of $P(I_{\rm sw})$ is expected to decrease with T and finally to saturate below $T^\star$. The temperature dependence of σ is plotted in Fig. 1b) on a double logarithmic scale. For T well above $T^\star \simeq 120\,$mK we observe $\sigma \propto T^{2/3}$ as expected for thermal escape. For T below $T^\star$ a saturation is obtained as expected for MQT. The data shown in Fig. 1 provide clear evidence for a transition from the thermal to the MQT regime in the investigated π-JJ.

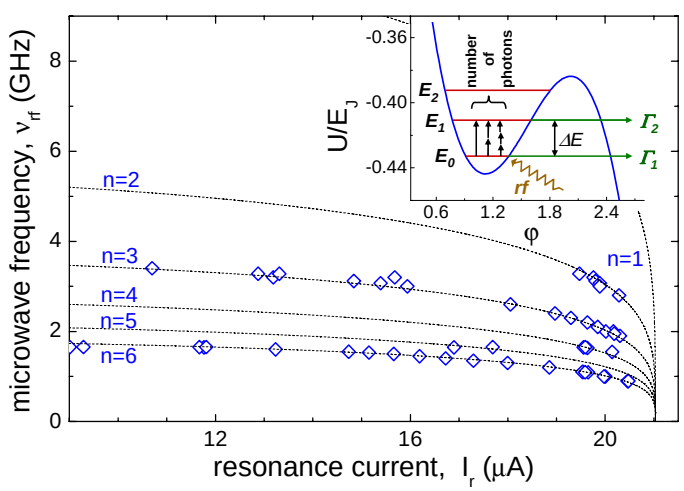

Figure 2: Microwave frequency plotted versus the resonance current I_r, for which the escape rate is maximally enhanced at $T = 110\,$mK. The dashed lines represent fits of the data to the expression $\nu_{\rm rf} = (\nu_p/n)[1-(I_r/I_c)^2]^{1/4}$. The inset shows the tilted washboard potential for $\gamma = I/I_c = 0.9$ with the lowest energy levels. Microwave induced transitions from the ground state to the first excited state are indicated for single-, two- and three-photon processes. Note that $\Gamma_1 \gg \Gamma_0$ due to the lower and thinner potential barrier both for thermal and quantum escape.

We also have performed microwave spectroscopy of the energy levels in the local potential wells of the tilt washboard potential (see Fig. 2) [10]. Measuring the switching current distribution in the presence of microwaves with frequency $\nu_{\rm rf}$ one expects an enhancement of the escape rate Γ from the quantum well at the resonance condition $h\nu_{\rm rf} = \Delta E$, where $\Delta E = E_1 - E_0$ is the separation of the ground and first excited level. The enhancement of the escape rate results from the fact that the escape from the excited level is exponentially faster due to the lower and narrower barrier. We determined the resonance current I_r, which is given by the bias current value at which the escape rate is maximally enhanced. Such a measurement does not only allow the analysis of the bias current dependence of the energy level spacing but also gives information on the width of the first excited level and thus on the dissipation processes in the junction. Due to the anharmonic potential for the phase difference not only single photon but also multi-photon transitions at $n \cdot h\nu_{\rm rf} = \Delta E$, with n the number of absorbed photons, are allowed between neighboring energy levels. In Fig. 2 we have plotted the microwave frequency $\nu_{\rm rf}$ versus I_r. The measured data

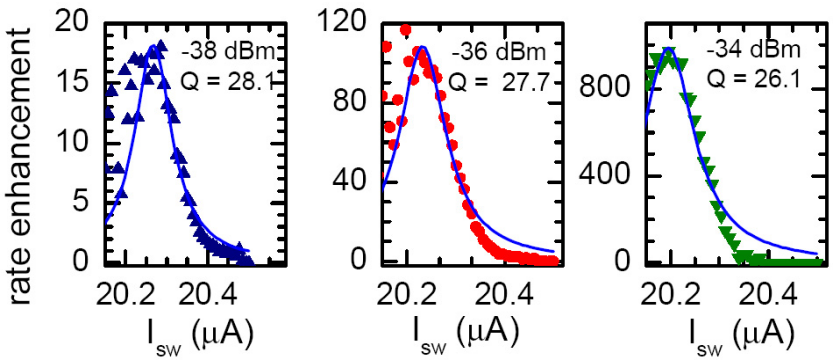

Figure 3: The rate enhancement for the two photon process at $T = 110\,\mathrm{mK}$ is plotted for three values of the microwave power around the resonance current I_r given by the maximum of the curves. The lines are fits of the data to Lorentzians. From the FWHM of the Lorentzians the quality factor Q is derived.

can be nicely fitted by the theoretically expected dependence $\nu_{\mathrm{rf}} = (\nu_p/n)[1-(I_r/I_c)^2]^{1/4}$ with the fitting parameters $\nu_p = \omega_p/2\pi = 10.95\,\mathrm{GHz}$ and the junction critical current $I_c = 21.03\,\mu\mathrm{A}$. From this value of the plasma frequency ν_p and the critical current I_c we could determine the junction capacitance to $C = 2eI_c/\hbar\omega_p^2 \simeq 14\,\mathrm{pF}$ and, in turn, with the junction resistance $R \sim 30\,\Omega$ the quality factor to $Q = \omega_p RC \sim 30$.

We further measured the enhancement $[\Gamma(P_{\mathrm{rf}}) - \Gamma(0)]/\Gamma(0)$ of the escape rates $\Gamma(I_{\mathrm{sw}})$ for different values of the microwave power P_{rf} as shown in Fig. 3 [10]. The rate enhancement as function of I_{sw} could be fitted by Lorentzians, which indicates a resonant activation mechanism induced by level quantization. The width of the curves provides a measure for the quality factor $Q = \nu_{\mathrm{rf}}/\delta\nu$. Fitting the data yields $Q = 28 \pm 2$. This value is in good agreement with the value $Q = \omega_p RC \sim 30$.

In conclusion, our results show that dissipative effects due to the potential presence of low-energy quasiparticles in the ferromagnetic metallic layer are small enough not to prevent true quantum behavior of SIFS junctions. These findings are highly promising for the application of such junctions in superconducting quantum circuits such as qubits. They are a major step towards experiments aiming at the demonstration of macroscopic quantum coherence in superconducting systems involving SIFS π-JJs such as qubits in a particularly quiet configuration. More experimental details on the fabrication and characterization of SIFS junctions can be found in [10, 11].

References

[1] T. Bauch, T. Lindström, F. Tafuri, G. Rotoli, P. Delsing, T. Claeson, F. Lombardi, Science **311**, 57 (2006).
[2] V. V. Ryazanov, V. A. Oboznov, A. Y. Rusanov, A. V. Veretennikov, A. A. Golubov, and J. Aarts, Phys. Rev. Lett. **86**, 2427 (2001).
[3] T. Kontos, M. Aprili, J. Lesueur, F. Genêt, B. Stephanidis, and R. Boursier, Phys. Rev. Lett. **89**, 137007 (2002).
[4] M. Weides, M. Kemmler, E. Goldobin, D. Koelle, R. Kleiner, H. Kohlstedt, and A.Buzdin, Appl. Phys. Lett. **89**, 122511 (2006).
[5] A. I. Buzdin, Rev. Mod. Phys. **77**, 935 (2005).
[6] G. Blatter, V. B. Geshkenbein, and L. B. Ioffe, Phys. Rev. B **63**, 174511 (2001).
[7] T. Yamashita, K. Tanikawa, S. Takahashi, and S. Maekawa, Phys. Rev. Lett. **95**, 097001 (2005).
[8] T. Bauch, F. Lombardi, F. Tafuri, A. Barone, G. Rotoli, P. Delsing, and T. Claeson, Phys. Rev. Lett. **94**, 087003 (2005).
[9] K. Inomata, S. Sato, Koji Nakajima, A. Tanaka, Y. Takano, H. B. Wang, M. Nagao, H. Hatano, and S. Kawabata, Phys. Rev. Lett. **95**, 107005 (2005).
[10] Sven Beutner, Diploma thesis, TU München (2006).
[11] Karl Madek, Diploma thesis, TU München (2005).

Orthogonally-driven superconducting qubit in circuit QED

M. Mariantoni, A. Emmert, A. Marx, R. Gross [1]
H. Christ [2]; *E. Solano* [3]; *M. J. Storcz and F. K. Wilhelm* [4]; *W. D. Oliver* [5]

In recent years, superconducting quantum circuits have demonstrated key elements required for quantum information processing [1], including the possibility to prepare a desired qubit state, coherently manipulate it, read it out, and perform preliminary conditional gate operations [2–4]. In analogy to quantum-optical cavity QED, superconducting charge and flux qubits have been coupled to on-chip microwave resonators [5, 6], and universal two-qubit gates mediated by a single cavity mode have been proposed [7]. In such an architecture, the scaling of the system would require a homogeneous coupling of many qubits with the same cavity mode and a means to address each logical qubit individually. Prototypical advanced manipulation schemes have already been implemented in quantum-optical systems. In trapped ion experiments, tuned lasers can be switched between single-ion carrier excitations and ion-motion JC dynamics [8]. Also, in 3D microwave cavities, a flying atom can perform local rotations in Ramsey zones before and after entering the cavity, in which a Jaynes-Cummings (JC) interaction takes place [9]. In the emerging field of circuit QED [5, 6], a higher level of addressability and control is also desirable. For instance, it is important to enable controlled *intracavity* qubit rotations, while keeping a switchable coupling to the cavity modes, aiming at *intercavity* qubit-qubit transfer of information. This implies the necessity to generate nonclassical field states, a task that could be implemented coupling the qubit to two (or more) independent modes with orthogonal field polarizations.

We have investigated an architecture consisting of a superconducting charge qubit coupled to the quantized, discrete-mode spectrum of a quasi-1D coplanar wave guide (CWG) resonator, which we will call the cavity [5], and to a multi-layer microstrip transmission line (MTL), which will be utilized to tune the qubit-cavity resonance. This archetypical construction ideally subjects the qubit to two orthogonal electromagnetic fields and constitutes the system for our theoretical investigations. We will show that strongly driving the MTL with coherent field pulses modulates the strength of the qubit-cavity interaction and, in the strong-driving limit [10], mediates the emergence of a simultaneous JC and anti-JC dynamics in the system, allowing the generation of nonclassical qubit-cavity states [11]. Our scheme could be also utilized with superconducting flux qubits.

The Hamiltonian describing the interaction between a single Cooper-pair box (SCPB) charge qubit, the second harmonic of the undriven CWG resonator, and the MTL, driven with a propagating coherent state acting as an AC gate charge, can be written as

$$\begin{aligned}\hat{H} &= -2E_{\mathrm{C}}\left(1-2n_{\mathrm{C}}^{\mathrm{DC}}\right)\hat{\sigma}_z - \frac{E_{\mathrm{J}}\left(\Phi_{\mathrm{x}}\right)}{2}\hat{\sigma}_x + \hbar\omega_{\mathrm{C}}\hat{a}_2^{\dagger}\hat{a}_2 \\ &\quad + \hbar g_{\mathrm{QC}}\hat{\sigma}_z\left(\hat{a}_2^{\dagger}+\hat{a}_2\right) + 4E_{\mathrm{C}}n_{\mathrm{M}}^{\mathrm{AC}}(t)\hat{\sigma}_z, \qquad (1)\end{aligned}$$

where $E_{\mathrm{C}} = e^2/2C_{\Sigma}$ represents the charging energy of the SCPB (C_{Σ} is the total box capacitance), $n_{\mathrm{C}}^{\mathrm{DC}}$ is the number of pairs induced by the DC gate voltage applied through the

[1] This work is supported by the DFG through the Cooperative Research Center 631.
[2] Max-Planck Institute for Quantum Optics (MPQ), Garching
[3] MPQ, Garching and Departamento de Ciencias, Pontificia Universidad Católica del Perú, Lima, Peru
[4] Physics Department, CeNS and ASC, Ludwig-Maximilians-Universität, München
[5] MIT Lincoln Laboratory, Lexington, Massachussets, USA

CWG resonator, $E_{\rm J}$ is the qubit Josephson energy, which can be tuned by an external quasi-static flux bias $\Phi_{\rm x}$, applied through an adequately engineered loop [2, 7], $\{\hat{a}_2^\dagger, \hat{a}_2\}$ are the bosonic creation and destruction operators relative to the second harmonic of the CWG resonator, $\omega_{\rm C}$ and $g_{\rm QC}$ are the corresponding angular frequency and qubit-cavity vacuum Rabi coupling, respectively [7], $n_{\rm M}^{\rm AC}(t)$ is the pair number induced by the AC gate voltage applied via the MTL, and $\{\hat{\tilde{\sigma}}_x, \hat{\tilde{\sigma}}_z\}$ are Pauli spin-1/2 operators. Hamiltonian (1) shows that the qubit can be driven via the MTL without populating the CWG resonator (which thus remains in the vacuum state $|0_{\rm C}\rangle$) by applying a coherent state, which results in an AC gate charge $n_{\rm M}^{\rm AC}(t) = \left(C_{\rm QM}/2e\right)|\beta| \exp i\,(\omega_{\rm M} t + \vartheta_\beta)$. Here, $C_{\rm QM}$ is the qubit-MTL cross-capacitance, $|\beta|$ the driving voltage amplitude, $\omega_{\rm M}$ its angular frequency, and ϑ_β a phase (hereafter, $\beta \doteq |\beta| \exp i\vartheta_\beta$). The effective qubit-MTL coupling is thus $g_{\rm QM}(\beta) = e\,(C_{\rm QM}/C_\Sigma)\,\beta/\hbar$. The direct coupling between the CWG resonator and the MTL is suppressed by the high isolation between their respective modes [see Fig. 1(g) and (h)]. Also, the MTL magnetic field distribution [12] threads the split-SCPB loop almost tangentially, thus avoiding unwanted jitters of the $\hat{\tilde{\sigma}}_{\rm x}$ term in Eq. (1).

Working in the eigenbasis $\{|{\rm g}\rangle, |{\rm e}\rangle\}$ of the first two terms of Eq. (1), the system Hamiltonian takes the form

$$\begin{aligned} \hat{H} &= \frac{\Omega}{2}\hat{\sigma}_z + \left[\hbar g_{\rm QC}\left(\hat{a}_2^\dagger + \hat{a}_2\right) + 4E_{\rm C} n_{\rm M}^{\rm AC}(t)\right] \times \\ &\quad \times \left(\cos\theta\hat{\sigma}_z - \sin\theta\hat{\sigma}_x\right) + \hbar\omega_{\rm C}\hat{a}_2^\dagger\hat{a}_2\,, \end{aligned} \tag{2}$$

where $\{\hat{\sigma}_x, \hat{\sigma}_z\}$ are Pauli matrices in the $\{|{\rm g}\rangle, |{\rm e}\rangle\}$ eigenbasis, $\Omega = \sqrt{E_{\rm J}^2 + \left[4E_{\rm C}\left(1 - 2n_{\rm C}^{\rm DC}\right)\right]^2}$ is the qubit level separation, and $\theta = \arctan\left[E_{\rm J}/4E_{\rm C}\left(1 - 2n_{\rm C}^{\rm DC}\right)\right]$ is the mixing angle. Operating the SCPB at the degeneracy point, i.e., for $n_{\rm C}^{\rm DC} = 1/2$, under complete resonance conditions [$E_{\rm J}/(2\hbar) = \omega_{\rm C} = \omega_{\rm M}$], and within a standard rotating-wave approximation (RWA) in the interaction picture, Eq. (2) can be rewritten as

$$\hat{H}_{\rm I} = \hbar g_{\rm QC}\left(\hat{\sigma}_+\hat{a}_2 + \hat{\sigma}_-\hat{a}_2^\dagger\right) + \hbar g_{\rm QM}(\beta)\hat{\sigma}_x\,. \tag{3}$$

An advanced application of Eq. (3) is obtained in the strong-driving limit, $g_{\rm QM}(\beta) \gg g_{\rm QC}$. In this case, following Ref. [10], we utilize an additional interaction representation with respect to the second term on the r.h.s. of Eq. (3). Decomposing $\hat{\sigma}_\pm = (\hat{\sigma}_x \pm i\hat{\sigma}_y)/2$ allows one to omit the quickly-precessing $\hat{\sigma}_y$ term through a second RWA, yielding the effective Hamiltonian

$$\hat{H}_{\rm eff} = \hbar\frac{g_{\rm QC}}{2}\left(\hat{\sigma}_+ + \hat{\sigma}_-\right)\left(\hat{a}_2^\dagger + \hat{a}_2\right)\,. \tag{4}$$

This strong-driving limit results in a circuit-QED realization of a simultaneously resonant JC and anti-JC dynamics. It is characterized here by a large coupling $g_{\rm QC}/2$, and it enables the generation of mesoscopic superposition states between the qubit and the cavity field. For example, taking the initial qubit-cavity state to be $|{\rm g}, 0_{\rm C}\rangle = (|+\rangle + |-\rangle)|0_{\rm C}\rangle/\sqrt{2}$, where $|\pm\rangle$ are the $\hat{\tilde{\sigma}}_x$ eigenstates of the qubit, the evolution associated with Eq. (4) after an interaction time $t_{\rm int}$ yields the following Schrödinger cat state

$$|\Psi_{\rm cat}\rangle = \frac{(|+\rangle|\alpha\rangle + |-\rangle|-\alpha\rangle)}{\sqrt{2}} \tag{5}$$

with $\alpha = ig_{\rm QC}t_{\rm int}/2$, typically referred to as Schrödinger cat state. Using realistic experimental parameters, e.g., $g_{\rm QC} \approx 100\,{\rm MHz}$ [13] and $\kappa_{\rm C} \approx 0.1\,{\rm MHz}$, would allow the generation of a

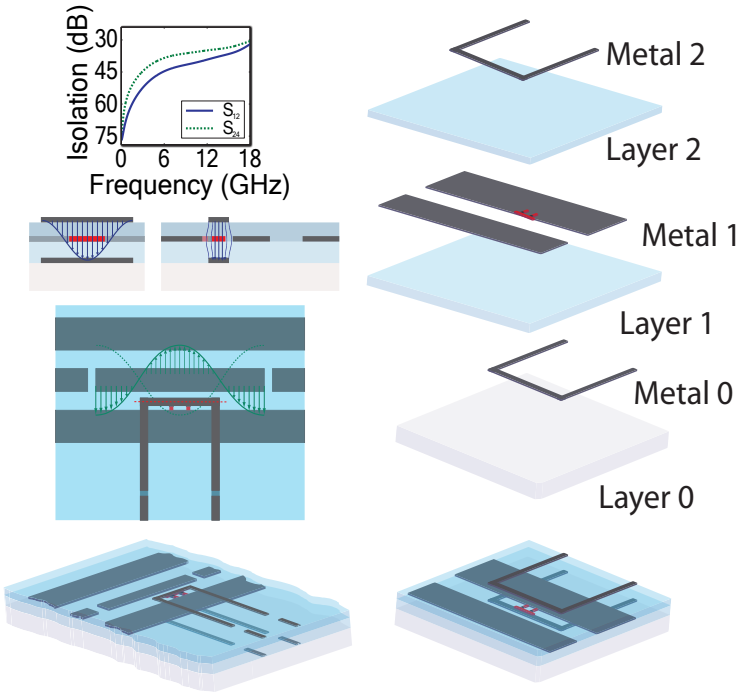

Figure 1: The SCPB coupled to a CWG resonator and a MTL. On the r.h.s. of the figure, a blow-up of the system which clearly shows the method to construct the architecture studied here. The role played by the different *layers* and *metals* is explained in the text. The plot shows some of our simulations indicating that a high isolation (expressed with S-parameters) between the CWG resonator and the MTL is possible.

Schrödinger cat state with amplitude $|\alpha| = \sqrt{\langle \hat{n}_{\rm cat} \rangle} = (g_{\rm QC}/2\kappa_{\rm C})^{1/3} \approx 8$, obtained for a maximum interaction time $t_{\rm int} = 1/\kappa_{\rm C}^{\rm eff}$, where $\kappa_{\rm C}^{\rm eff} = |\alpha|^2 \kappa_{\rm C}$. This amplitude is comparable to the best values obtained in 3D microwave cavity QED with circular Rydberg atoms [14].

In order to generate successfully the specific state $|\Psi_{\rm cat}\rangle$ inside the cavity, it is necessary to decouple the qubit-cavity system after the desired interaction time $t_{\rm int}$. This may be implemented by applying a second strong coherent state to the MTL, with decoupling frequency $\omega_{\rm dec}$ and amplitude $|\gamma_{\rm dec}|$, that AC-Stark shifts the SCPB by an amount δ. At this point, a single-shot measurement of the qubit state $|{\rm g}\rangle$ ($|{\rm e}\rangle$) would leave the field state in an even (odd) coherent state $|\Psi_\alpha^{\rm e}\rangle = (|\alpha\rangle + |-\alpha\rangle)/\sqrt{1+\exp(-|\alpha|^2)}$ [$|\Psi_\alpha^{\rm e}\rangle = (|\alpha\rangle - |-\alpha\rangle)/\sqrt{1-\exp(-|\alpha|^2)}$] [10]. This qubit measurement may be made, for instance, by driving a probing field via the third harmonic of the CWG resonator, which is strongly detuned from the qubit transition frequency by an amount $\omega_{\rm C} \gg g_{\rm QC}$, for a time $t_{\rm meas}$, and thereby allowing an independent QND read-out of the qubit population via the resultant phase shift of the probing field [15].

One means of coupling a SCPB to two quasi-orthogonal electric fields is to make use of a multilayer technology (1). Following the figure, dielectric *Layer 0* is the substrate for the entire structure, and the MTL ground plane is *Metal 0*. Dielectric *Layer 1* serves as a substrate for the CWG resonator-SCPB structures, which are made from *Metal 1*. Dielectric *Layer 2* supports the MTL made from *Metal 2*. The proper engineering of this structure results in quasi perpendicular electric fields at the SCPB. These fields are described by dyadic Green's functions and can be evaluated numerically with the method of moments [16]. The results of our simulations indicate about -40 dB isolation at 5 GHz (Fig. 1). Hence, driving the MTL with a coherent state of $\langle \hat{n} \rangle \approx 10^3$ photons would populate the CWG resonator with ~ 0.1 photons.

In conclusion, we have considered a SCPB coupled to the orthogonal modes of a CWG resonator and a MTL. This architecture allows the engineering of simultaneous JC and anti-JC dy-

namics, which we utilized to generate mesoscopic entangled states of the SCPB and the CWG. The multimode concepts described here should bring greater flexibility to the field of circuit QED, in particular those aiming at the systematic scaling-up of quantum gates and quantum information devices.

This work was supported by DFG through SFB 631. The work at Lincoln Laboratory was sponsored by the US DoD under Air Force Contract No. FA8721-05-C-0002. ES acknowledges support of EU RESQ and EuroSQIP projects.

References

[1] M.A. Nielsen and I.L. Chuang, *Quantum Computation and Quantum Information* (Cambridge University Press, Cambridge, 2000).
[2] Y. Makhlin, G. Schön, and A. Shnirman, Rev. Mod. Phys. **73**, 357 (2001).
[3] M.H. Devoret, A. Wallraff, and J.M. Martinis, cond-mat/0411174 (2004).
[4] T. Yamamoto *et al.*, Nature **425**, 941 (2003).
[5] A. Wallraff *et al.*, Nature **431**, 162 (2004).
[6] J. Johansson *et al.*, Phys. Rev. Lett. **96**, 127006 (2006).
[7] A. Blais *et al.*, Phys. Rev. A **69**, 062320 (2004).
[8] D. Leibfried, R. Blatt, C. Monroe, and D. Wineland, Rev. Mod. Phys. **75**, 281 (2003).
[9] J. M. Raimond, M. Brune, and S. Haroche, Rev. Mod. Phys. **73**, 565 (2001).
[10] E. Solano, G. S. Agarwal, and H. Walther, Phys. Rev. Lett. **90**, 027903 (2003).
[11] M. Brune *et al.*, Phys. Rev. Lett. **77**, 4887 (1996).
[12] T. Itoh, *Numerical Techniques for Microwave and Millimeter-Wave Passive Structures* (John Wiley & Sons, New York, 1989).
[13] D.I. Schuster, *private communications*.
[14] A. Auffeves *et al.*, Phys. Rev. Lett. **91**, 230405 (2003).
[15] A. Wallraff *et al.*, Phys. Rev. Lett. **95**, 060501 (2005).
[16] R.E. Collin, *Field Theory and Guided Waves*, 2nd Edition (Wiley-IEEE Press, New York, 1990).

Superconducting resonant circuits for cQED experiments

T. Niemczyk, S. Hofmann, A. Marx, and R. Gross [1]

Superconducting resonant circuits have gained increasing interest since 2004, when Wallraff *et al.* [1] demonstrated strong coupling of a single microwave photon to a superconducting qubit for the first time and thereby established the new field entitled *circuit Quantum Electrodynamics (cQED)*, the circuit analogue of optical cavity QED. In analogy to optical cavity QED, a microwave resonator – e.g. a quasi-1D transmission line in coplanar waveguide (CPW) geometry as shown in Fig. 1a – acts as a cavity with high quality factor, which is coupled to an artificial atom – e.g. a superconducting quantum bit (qubit). The coplanar resonator consisting of a narrow center conductor separated by a small gap ($\sim 5\,\mu$m) from the lateral ground planes, can be fabricated by standard thin film technology. A superconducting charge qubit is placed in this gap at the anti-node of the microwave field (Fig. 1c). The resonator is coupled to the incoming and outgoing transmission lines via two coupling capacitors as shown in Fig. 1b. Due to the small spatial dimensions, the electric field in the resonator, $E_{\mathrm{rms}} \approx 0.2\,\mathrm{Vm}^{-1}$, is some hundred times larger than in the 3D-cavities used in optical cavity QED. The quantum nature of the microwave field gives rise to coherent oscillations of a single excitation between the charge qubit and the cavity at the vacuum Rabi frequency ω_{rabi}. These oscillations can be observed, if ω_{rabi} exceeds the relaxation rates of both the qubit and the microwave cavity. To keep the cavity decay rate $\kappa = \omega_{\mathrm{r}}/Q$ small, resonators with a high quality factor Q have to be developed. Here, ω_{res} is the resonant frequency of the cavity. We note that the loaded quality factor of any resonator is very sensitive to the value of the in- and output coupling capacitors.

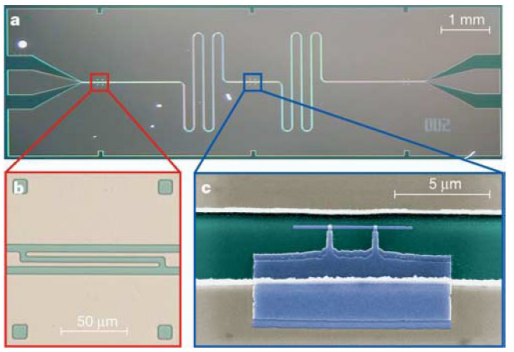

Figure 1: (a) Optical micrograph of a superconducting coplanar waveguide resonator. (b) Enlarged view of the coupling capacitor ($\sim 6\,$fF). (c) SEM micrograph of the charge qubit positioned in the gap between the center conductor and the ground planes (from A. Wallraff *et al.* [1]).

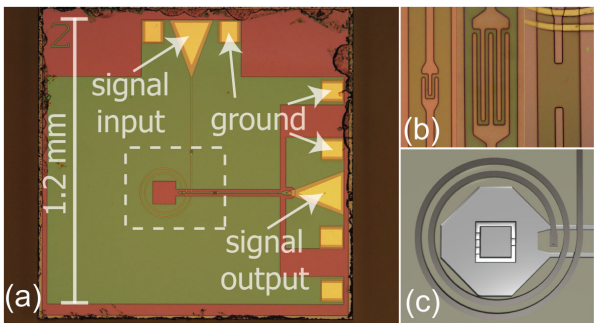

Figure 2: (a) Optical micrograph of the microstrip resonator. The hole in the ground plane is 100 μm x 100 μm. The resonant circuit in the dashed box is defined by a transmission line section coupled capacitively to the input and output as shown on an enlarged scale in (b). (c) Sketch of a three junction flux qubit positioned in the center of the resonator.

The research activities at the WMI are focussing on the development of superconducting flux qubits. Coupling such qubits to microwave resonators, an essential prerequisite to reach the strong coupling regime of a flux qubit embedded in the resonator is a sufficiently large quality factor of the superconducting resonator. With $\omega_{\mathrm{rabi}}/2\pi \simeq 100\,\mathrm{MHz}$ and $\omega_{\mathrm{res}} \simeq 10\,\mathrm{GHz}$, the quality factor should be of the order of 10^4 to achieve $1/\kappa \ll \omega_{\mathrm{rabi}}$. In contrast to superconducting charge qubits, flux qubits have to be coupled to the *magnetic field mode* of the cavity, i.e. they have to placed in the anti-node of the magnetic field. Based on the concept of the DC SQUID microstrip amplifier introduced by Clarke and Mück [2] we have developed

[1] This work is supported by the DFG through the Cooperative Research Center 631.

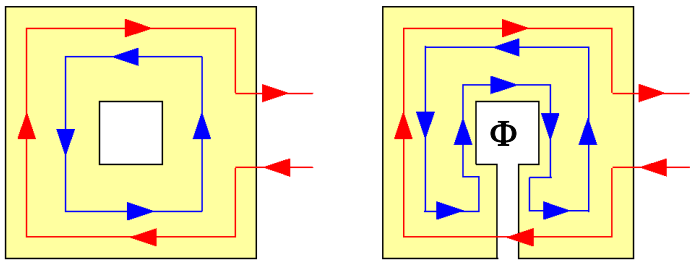

Figure 3: (a) In the absence of a slit in the GP, the current in the input coil (red) is fully screened by a counter-flowing image current in the GP (blue). (b) The presence of the slit forces the screening current in the washer GP to flow around the hole in the center of the GP. This generates a net flux Φ in the center of the washer and thus increases the inductance reflected back into the input coil.

a *Microstrip Resonator (MR)* (Fig. 2), which is promising for achieving strong coupling for flux qubits. Preliminary calculations show that $\omega_{\text{rabi}}/2\pi \simeq 100\,\text{MHz}$ should be achievable. In contrast to the coplanar waveguide resonator of Fig. 1, the MR is a three-layer device. The signal line (dark yellow) and washer ground plane (GP) (green) are made from niobium and are separated by an insulating SiO_2 layer (500 nm). The actual resonant circuit is defined between the two coupling capacitors and consists mainly of the spiral input coil. The qubit has to be placed in the center of the resonator as schematically shown in Fig. 2c. It couples inductively to the washer. In the Ketchen-Jaycox model [3], the spiral input coil and the washer type GP are coupled in essentially the same manner as a $n:1$ turn thin-film transformer. Due to the Meißner-Ochsenfeld effect, a current in the spiral signal line induces screening currents in the GP.

Fig. 3 shows a schematic comparison between the paths of the screening currents (blue) with and without a slit in the washer GP. In the absence of any slit, the current in the input coil is fully screened by a counter-flowing image current in the GP. In contrast, in the presence of the slit in the GP the screening currents are forced to flow around the center hole of the washer, thus establishing a net flux in the hole. This flux, in turn, increases the inductance reflected back into the input coil. The fundamental resonant frequency of the MR is dominated by the inductance L_{GP} of the GP and therefore is very sensitive to changes in of L_{GP}. It is given by

$$f_{0,\lambda/2} = \frac{1}{2\sqrt{(\ell L + n^2 L_{\text{GP}}) \cdot \ell C}} \quad ,$$

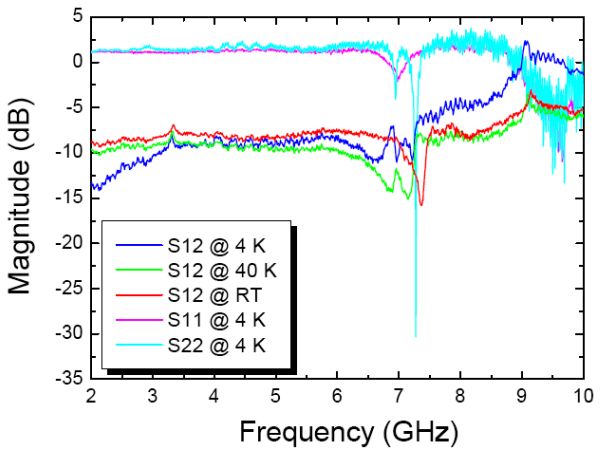

Figure 4: Transmission and reflection spectra of a superconducting MR. The resonance around 6.9 GHz has a quality factor of 50 (transmission) and 128 (reflection) at 4.2 K.

where ℓ is the length of the resonant circuit and n the number of turns of the spiral input coil. L and C are the inductance and capacitance per unit length of the resonant circuit. More detailed information about the design and the mode of operation of the MR are given in [4]. We designed several MRs with different coupling capacitors (cf. Fig. 2b), as well as length and width of the signal line. In a first run a large number of MRs has been fabricated at Hypres, Inc. with a broad range of coupling capacitances and resonance frequencies. We have performed S-parameter measurements at 4.2 K. The samples were wire bonded to a printed circuit board

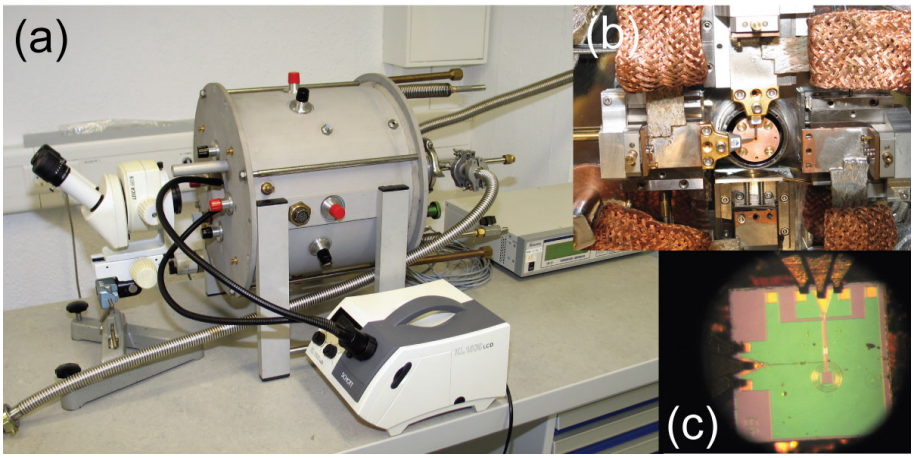

Figure 5: (a) Cryogenic wafer probing system (CWPS). (b) Two GSG probing tips are mounted on xyz positioning tables with Cu-ribbons attached to the lN_2 precooling reservoir for thermal anchoring. (c) The close-up shows two GSG probing tips establishing contact to a MR with coplanar terminals.

(PCB) inside a brass box and the connection to the outer circuitry was provided by SMA connectors. The whole setup was response calibrated with a calibration PCB. Fig. 4 shows the transmission and reflection spectra of one of our MRs. The resonance peak around 6.9 GHz has a quality factor of $Q_{12} \approx 50$ in transmission (S_{12}) and $Q_{22} \approx 128$ in reflection (S_{22}). Until now, the best quality factor we measured was 250. As discussed above, the quality factor Q of resonators suitable for cQED experiments at 4.2 K should be of the order of 10^4 [5].

Our MRs are extremely small devices and the influence of the bonding wires on the measured spectra cannot be removed by means of a calibration procedure. Therefore, we set up a cryogenic wafer probing system (CWPS), which is shown in Fig. 5 and discussed in detail in reference [6]. Up to 25 MRs can be glued onto the copper sample holder and can be characterized in the same cool-down cycle. The minimum achievable temperature of the system is well below 4.2 K.

In parallel to the measurements of our MRs we presently develop several resonant circuits in CPW geometry similar to the resonators described in [1, 5]. The niobium resonators are fabricated on both sapphire and silicon substrates by means of dc-magnetron sputtering, optical lithography, and reactive ion etching. Up to now 36 different resonator geometries have been designed for measurements in a specially designed box as well as for the CWPS. The advantage of the resonators with CPW geometry is their – compared to MRs – simple structure. The first measurements on these resonators are presently performed.

References

[1] A. Wallraff, D. I. Schuster, A. Blais, L. Frunzio, R.-S. Huang, J. Majer, S. Kumar, S. M. Girvin, and R. J. Schoelkopf, Nature **431**, 162 (2004).
[2] M. Mück and J. Clarke, J. Appl. Phys. **88**, 6910 (2000).
[3] M.B. Ketchen and J.M. Jaycox, IEEE Trans. on. Magn. **17**, 400 (1982).
[4] T. Niemczyk, Diploma Thesis, TU München (2006).
[5] L. Frunzio, A. Wallraff, D. Schuster, J. Majer, R. Schoelkopf, IEEE Trans. Appl. Supercond. **15**, 860 (2005).
[6] G.J. Höfer, F. Jäger, H.A. Kratz, Rev. Sci. Instrum. **64**, 788 (1993).

Phase-coherent dynamics of a superconducting flux qubit measured with the capacitive bias readout

F. Deppe, M. Mariantoni, and R. Gross [1]
S. Saito, K. Kakuyanagi, and K. Semba, [2] *T. Meno,* [3] *H. Takayanagi* [4]

A key research activity of WMI within SFB 631 is focussed on the fabrication of superconducting three Josephson junction flux quantum bits (SF qubits) [1] and the study of their phase coherent dynamics. These systems are especially attractive as basic building blocks in solid-state quantum information processing, because they are fabricated as circuits on silicon chips using standard lithographic and thin film techniques. As a consequence, scaling to large qubit arrays is expected to be easily possible. However, although the superconducting gap provides some protection from uncontrolled interaction of the qubit with other solid-state degrees of freedom, the loss of phase coherence (decoherence) caused by the influence of the qubit environment is still a severe problem. Thus, it is an important task to identify the main sources of decoherence.

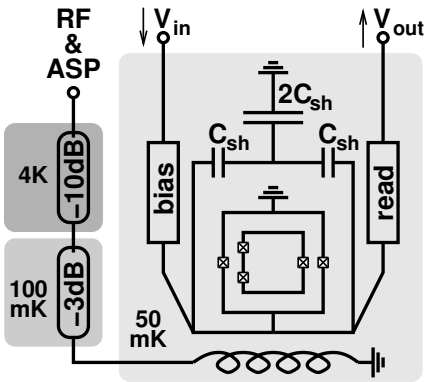

Figure 1: Sketch of the sample layout. The checked squares denote Josephson junctions. The rounded boxes are the cold attenuators used to improve the signal-to-noise ratio of the RF control pulses. The adiabatic shift pulse (ASP) is also applied via the RF line. The readout and bias circuit elements are different for capacitive and resistive bias method.

In collaboration with the NTT Basic Research Laboratories at Atsugi, Japan we studied the dependence of the phase coherent dynamics of a SF qubit on the externally applied magnetic flux. In our experiments we used the capacitive bias readout method, which is a novel variant of the pulsed switching dc SQUID detection scheme and allows for a controlled engineering of the electromagnetic environment of the qubit. We measured the qubit in the frequency domain (RF spectroscopy) as well as in the time domain (Rabi oscillations, energy relaxation, Ramsey fringes, spin echo) In particular, we focused on the region around the so-called degeneracy point, where the externally applied flux bias is about 1.5 magnetic flux quanta ($1.5\Phi_0$). We found that the qubit is limited by energy relaxation directly at the degeneracy point. In the close vicinity of this point, the Ramsey and spin echo data are consistent with $1/f$-noise as the dominant dephasing source. Far away from the degeneracy point white noise contributions appear in the spin echo data. Measuring the same qubit with the conventional resistive bias method essentially gives similar results, i.e. we could experimentally prove that neither for the energy relaxation nor for the dephasing the noise due to the bias circuit is the limiting factor in our setup. On the contrary, our results rather support the idea that the $1/f$-noise arises from internal sources in close vicinity to the qubit (e.g. fluctuators due to impurities in the qubit junctions).

Using aluminum thin film technology on a SiO_2-covered silicon chip we fabricated a $5.1 \times 5.2\ \mu m^2$ SF qubit (cf. Fig. 1). The qubit state is read out by a surrounding dc SQUID, which

[1]This work is supported by the DFG through the Cooperative Research Center 631.
[2]NTT Basic Research Laboratories, NTT Corporation, Kanagawa, 243-0198, Japan
[3]NTT Advanced Technology, NTT Corporation, Kanagawa, 243-0198, Japan
[4]Tokyo University of Science, 1-3 Kagurazaka, Shinjuku, Tokyo 162-8601, Japan

is coupled inductively to the qubit via a mutual inductance $M = 6.7$ pH. The SQUID actually detects the flux associated with the state-dependent persistent current in the qubit loop. The $Al/AlO_x/Al$ Josephson junctions were made with the angled shadow evaporation technique. The area of the two larger qubit junctions was $0.03\ \mu m^2$. The third one was designed to be smaller by a factor of $\alpha_{design} = 0.7$. Both SQUID junctions had the same design as the larger qubit junctions. The SQUID was shunted with an on-chip capacitance $C_{sh} = 6.3$ pF. The sample chip was placed within the opening of an alumina printed circuit board (PCB) inside a gold-plated copper box, which was mounted at the mixing chamber stage of a He_3/He_4 dilution refrigerator. In the following we will call components "on-chip" when they are located on the sample chip and "off-chip" when they are located on the PCB. The lines used to apply the SQUID bias current and to readout the SQUID response voltage (dc lines) are low-pass filtered for high-frequency noise > 2 GHz using a combination of copper powder filters and ultrathin stainless steel coaxial cables at the mixing chamber level (cf. Fig. 2).

For the detection of qubit state we used a switch&hold technique, which is based on the hysteretic current-voltage characteristic of the dc SQUID: the amplitude of the switching pulse was chosen in a way that switching events occur only for one of the two qubit states. The longer hold pulse cannot induce switching events by itself but it stops the SQUID from retrapping to the zero voltage state and thus holds the output voltage long enough to allow a sufficient signal integration time for the room temperature amplifier. The current bias pulse to the SQUID is applied in two ways: first, as in other experiments [2, 3], we use a combination of resistors (on-chip: $R^{on}_{Rbias} = 250\ \Omega$, $R^{on}_{Rread} = 2.25\ k\Omega$; off-chip: $R^{off}_{Rbias} = 1\ k\Omega$, $R^{off}_{Rread} = 3\ k\Omega$). In order to remove low-frequency noise components an additional commercial low-pass filter with a cutoff frequency of 10.7 MHz was installed into the bias line at room temperature. In the novel capacitive bias configuration we apply the bias current pulse via a resistor-capacitor combination: $R^{off}_{Cbias} = 510\ \Omega$, $C^{off}_{bias} = 0.5$ pF, $R^{off}_{Cread} = 1.5\ k\Omega$, and $C^{off}_{read} = 480$ pF. Due to technical reasons, we could not use on-chip components in this case. The room temperature filter could be relaxed to a 100 MHz cutoff. In this way we actually achieved a band-pass filter in the dc lines, which only provided a narrow frequency band necessary for the readout pulse. Since the SQUID current bias is produced by the biasing element from a voltage signal, the voltage pulse in the capacitive bias setup has to be the integral of the desired current pulse. For this reason this bias scheme is referred to as the integrated pulse method. Sketches of the dc line configuration and the pulse shapes for both biasing methods are shown in Fig. 2.

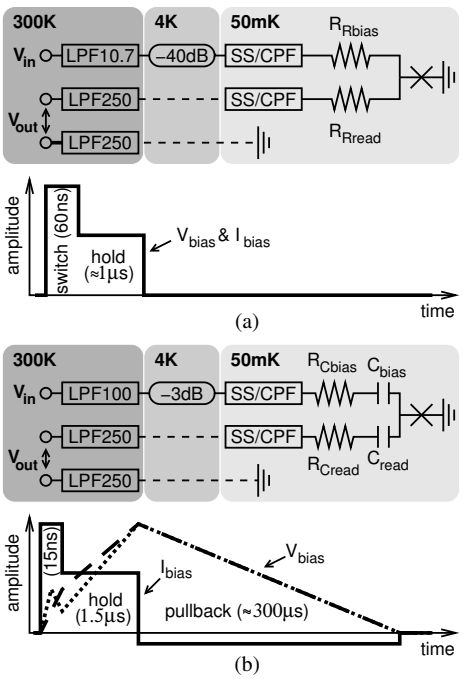

Figure 2: Resistive (a) vs. capacitive (b) bias setup and corresponding bias pulses for the readout SQUID. The cross denotes the qubit/SQUID/shunt system. The SQUID response voltage is differentially amplified at room temperature against a cold ground. LPF: commercial low-pass filters with the cutoff-frequency in MHz. SS: stainless steel ultrathin coaxial cables. CPF: copper powder filters.

The readout described above is restricted to bias points sufficiently away from the degeneracy point, where the qubit state is represented by a well defined persistent current. To measure near the degeneracy point, where the superposition of the clockwise and counterclockwise persistent current states result in a vanishing net magnetic flux, we used the adiabatic shift

pulse (ASP) technique. In this context adiabatic means that the pulse rise time of 800 ps is not fast enough to induce transitions between the qubit states. At an external flux bias away from the degeneracy point (readout point) we waited for about 300 μs to make sure that the qubit relaxes to the ground state. Then we applied the ASP via the RF line, which brings the qubit to its actual operation point.

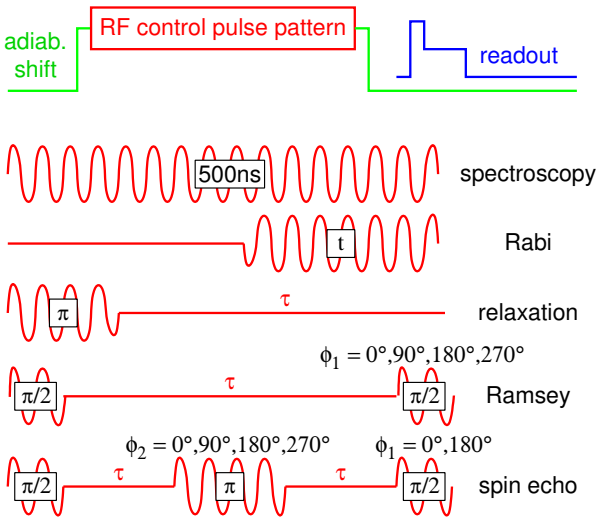

Figure 3: Adiabatic shift pulse readout method and RF control pulse patterns for different experiments.

To perform qubit operations we have to add the RF control pulse pattern on top of the ASP. The fall-off of the ASP brings the qubit back to the readout point, where the state detection can be performed. This scheme and the various pulse patterns are visualized in Fig. 3. In multi-pulse RF sequences we used the so-called phase cycling method to cancel the effect of imperfect control pulses [4]. This is achieved by varying the relative phase between the initial pulse and the subsequent pulses.

The basic qubit properties are determined from a microwave spectroscopy experiment. Looking at the results displayed in Fig. 4 we see that they can be described by a two-level approximation, where the qubit Hamiltonian reads $H = \frac{1}{2}\left[\epsilon(\delta\Phi_x)\sigma_z + \Delta\sigma_x\right]$. Here $\Delta/h = 4.22\,\mathrm{GHz}$ is the tunnel coupling between the uncoupled energy levels and $\epsilon(\delta\Phi_x) = 2I_p\delta\Phi_x$. $\delta\Phi_x \equiv \Phi_x - 1.5\Phi_0$ is proportional to the external flux Φ_x applied to the qubit loop. The persistent current $I_p = I_0\sqrt{1-\frac{1}{(2\alpha)^2}} = 360 \pm 1\,\mathrm{nA}$ depends on the critical current I_0 of the larger qubit junctions slightly modified by the junction asymmetry α. Comparison to the SQUID junction properties gives $\alpha = 0.62 \pm 0.04$ reasonably close to the designed value $\alpha_{\mathrm{design}} = 0.7$. The red line in Fig. 4 represents the transition frequency $\nu_{01} = \omega_{01}/2\pi = \left(\sqrt{\epsilon(\delta\Phi_x)^2 + \Delta^2}\right)/h$ between the coupled levels. We found signals up to the four-photon process. Estimating the junction capacitance C from [5] we obtained $E_J/E_C = 47 \pm 13$, where $E_J \equiv I_0\Phi_0/2\pi$ is the Josephson energy and $E_C \equiv e^2/2C$ the charging energy. Note that the visibility obtained by the integrated pulse method ($28 - 36\%$) is significantly larger than that measured for the resistive bias method ($20 - 25\%$). This is most likely due the fact that shorter switching pulses could be used (15 ns instead of 60 ns).

Quantitative information about the noise spectral density affecting the coherent dynamics of the qubits thereby limiting the phase coherent time of the qubit can be achieved from time domain measurements (Rabi, Ramsey, spin echo). Here, the magnetic flux dependence of the corresponding decay times (see Fig. 5) is of particular interest. There are two main types of decay: the energy or longitudinal relaxation, which is induced by noise along the z axis on the Bloch sphere, and the phase or transverse relaxation, which is induced by noise in the xy-plane of the Bloch sphere. For simplicity, in the following will use the expressions relaxation and dephasing for the energy and the phase relaxation, respectively. All time domain measurements have been performed for an external flux in the range $\delta\Phi_x = \pm 0.6\,\mathrm{m}\Phi_0$ using an ASP readout point of $\delta\Phi_x^r = 6.007\,\mathrm{m}\Phi_0$ (corresponding to $E_{01}^r = 14.125\,\mathrm{GHz}$). However, it is often more convenient to express the external flux via the Bloch angle θ, which is defined as $\tan\theta \equiv \Delta/\epsilon(\delta\Phi_x)$.

The relaxation rate T_1^{-1} can be described by Bloch-Redfield theory and is determined by the symmetrized spectral density $S_\Phi^{\mathrm{BR}}(\omega_{01})$ of the flux noise at the qubit transition frequency: $T_1^{-1} = \pi \left(\frac{1}{\hbar}\frac{\partial \epsilon}{\partial \Phi_x}\right)^2 \sin^2\theta \, S_\Phi^{\mathrm{BR}}(\omega_{01})$ [6]. We find a minimum relaxation rate $T_1(\delta\Phi_x = 0) \simeq 82\,\mathrm{ns}$ and a white noise spectral density $S_\Phi(\Delta/\hbar) = \left[(1.4 \pm 0.1) \times 10^{-10}\Phi_0\right]^2\ \mathrm{Hz}^{-1}$ near the qubit gap frequency.

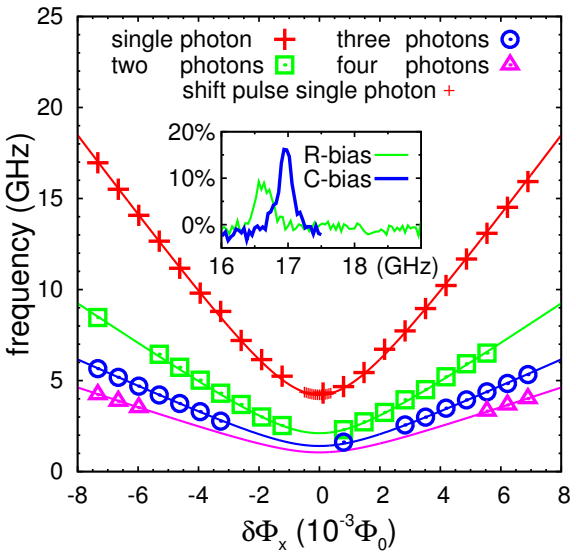

Figure 4: Magnetic flux dependence of the RF spectroscopy signals measured with the integrated pulse method. The insert shows the increased visibility of the capacitive bias readout compared to the resistive bias readout.

The analysis of the dephasing rates is complicated by two reasons: First, the experimental rates T_{2R} for the Ramsey and T_{2E} for the spin echo decay always contain a T_1 component. Second, we can see in Fig. 5 that the flux dependence of T_{2R} and T_{2E} are peaked at $\delta\Phi_x = 0$, indicating a significant influence of $1/f$-noise [6] which cannot be treated in the simple Bloch-Redfield approach. Taking into account this fact we can write $T_{2E,R}^{-1} = T_1^{-1}/2 + (T_\varphi^0)^{-1} + (T_\varphi^{BR})^{-1} + (T_\varphi^{1/f})^{-1}$, where the three dephasing terms describe the influence of flux-independent fluctuations, Bloch-Redfield, and $1/f$-noise, respectively. The Bloch-Redfield term is related to a white spectral density via $\left(T_\varphi^{\mathrm{BR}}\right)^{-1} = \pi \left(\frac{1}{\hbar}\frac{\partial \epsilon}{\partial \Phi_x}\right)^2 \cos^2\theta \, S_\Phi^{\mathrm{BR}}(\omega \to 0)$. The $1/f$ component originates from a spectral density $S_\Phi^{1/f}(\omega) = A/|\omega|$ and reads as $(T_\varphi^{1/f})^{-1} = \frac{1}{\hbar}\frac{\partial \epsilon}{\partial \Phi_x}\cos\theta\sqrt{A \ln 2}$ [6].

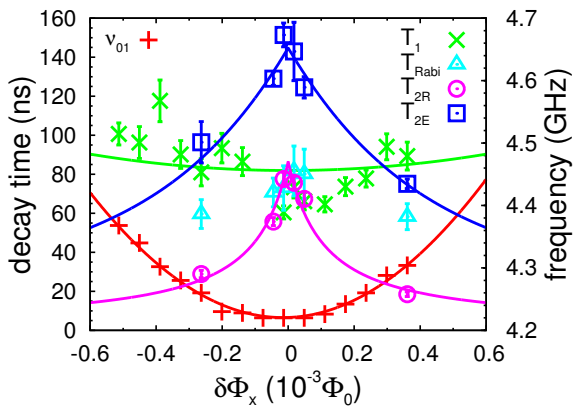

Figure 5: Magnetic flux dependence of the characteristic energy relaxation time, as well as Rabi, Ramsey, and spin echo decay times, measured by the integrated pulse method. Also shown is the qubit transition frequency $\nu_{01} \equiv E_{01}/h$ obtained from spectroscopy.

The peaked shape of $T_{2E,R}$ vs. $\delta\Phi_x$ in Fig. 5 already indicated the influence of $1/f$-noise in our data. Analyzing the data we see that the spin echo decay shows a white noise contribution $S_\Phi^{\mathrm{BR}}(\omega \to 0) = \left[(2.0 \pm 0.1) \times 10^{-10}\Phi_0\right]^2\ \mathrm{Hz}^{-1}$ and a $1/f$-amplitude $A_{\mathrm{E}} = \left[(2.3 \pm 0.4) \times 10^{-6}\Phi_0\right]^2$. This corresponds to a transition from a $1/f$-noise dominated regime in the close vicinity of the degeneracy point to a regime with considerable white noise influence around the readout point. The flux-independent contribution is determined to $T_\varphi^0 = 1.2 \pm 0.3\ \mu\mathrm{s}$ right at the degeneracy point. We note that very similar results have been obtained for the same qubit using the resistive bias method.

In summary, we have studied the phase coherent dynamics of one and the same flux qubit with two different SQUID biasing circuits: the conventional resistive and the novel capacitive bias scheme. We find that the qubit coherence at the degeneracy point is energy relaxation limited in both cases. The integrated-pulse

method allows faster switching pulses (15 ns instead of 60 ns) and gives an increased visibility ($28-36$ % compared to $20-25$ %). On the other hand, the maximum T_1 and T_2 times were slightly reduced by about a factor of two for the capacitive bias scheme. This was caused by an uncontrolled change in the setup when switching between the two configurations. Detailed impedance calculations clearly showed that bias noise is not the limiting factor for the studied qubit. Interestingly, the dephasing is clearly limited by the large amount of $1/f$-noise. Such noise is typically generated by an ensemble of microscopic fluctuators on the sample chip close to or within the qubit structure. The amplitude of the $1/f$-noise obtained from the spin echo experiment is of the same order for the capacitive and resistive bias and also consistent with recent experiments on a flux qubit with a galvanically coupled readout SQUID [3].

References

[1] J. E. Mooij, T. P. Orlando, L. Levitov, L. Tian, C. H. van der Wal, and S. Lloyd, Science **285**, 1036 (1999).
[2] I. Chiorescu, Y. Nakamura, C. J. P. M. Harmans, and J. E. Mooij, Science **299**, 1869 (2003).
[3] F. Yoshihara, K. Harrabi, A. O. Niskanen, Y. Nakamura, and J. S. Tsai, Phys. Rev. Lett. **97**, 167001 (2006).
[4] K. Kakuyanagi, T. Meno, S. Saito, H. Nakano, K. Semba, H. Takayanagi, F. Deppe, and A. Shnirman, *submitted to* Phys. Rev. Lett. (2006).
[5] F. Deppe, S. Saito, H. Tanaka, and H. Takayanagi, J. Appl. Phys. **95**, 2607 (2004).
[6] G. Ithier, E. Collin, P. Joyez, P. J. Meeson, D. Vion, D. Esteve, F. Chiarello, A. Shnirman, Y. Makhlin, J. Schriefl, and G. Schön, Phys. Rev. B **72**, 134519 (2005).

Growth and properties of epitaxial Sr_2CrReO_6 thin films

F. Czeschka, S. Geprägs, S. T. B. Goennenwein, M. Opel, and R. Gross [1]

In the last couple of years, a tremendous interest in new materials with high spin polarization has emerged. One group of such materials are the ferromagnetic double perovskites $Sr_2BB'O_6$ (with B a magnetic transition metal ion, and B' a non-magnetic ion). For applications, e.g. in spintronic devices, materials with both a high spin polarization and a high Curie temperature T_C well above room temperature are important. Among the ferromagnetic double perovskites, Sr_2CrReO_6 has the highest T_C observed so far [1] and band structure calculations predict a very high spin polarization [2] for this compound. In spite of these interesting properties, only few attempts of thin film growth have been made so far [3].

We have prepared Sr_2CrReO_6 thin films by laser molecular beam epitaxy on (001)-oriented $SrTiO_3$ (STO) substrates. The pulsed laser deposition was performed using a KrF excimer laser (248 nm) and a stoichiometric target, obtained by an oxygen getter-controlled technique [4]. Sr_2CrReO_6 thin films were grown in various atmospheres (Ar, O_2) at different pressures (6×10^{-4} mbar $\leq p_{O2} \leq 5 \times 10^{-2}$ mbar) and a wide range of substrate temperatures (450°C$\leq T_S \leq$ 900°C). The energy density of the laser at the target was $\rho_E = 2\,J/cm^2$ and the laser repetition rate was $f_L = 2$ Hz. In-situ reflection high-energy electron diffraction (RHEED) was used to control the growth process. We found, that thin films grown at $T_S = 700$°C in an oxygen atmosphere with $p_{O2} = 6.6 \times 10^{-4}$ mbar show optimal crystallographic and magnetic properties. Despite of the small lattice mismatch of 0.8%, a layer-by-layer growth mode could be obtained for the first 8 monolayers. Then, the thin film started to grow in an island growth mode.

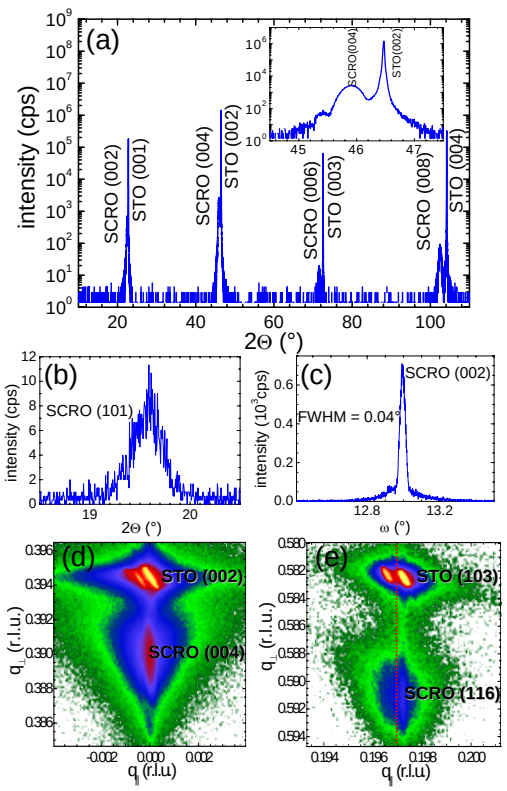

Figure 1: X-ray diffraction analysis of a 31 nm thick Sr_2CrReO_6 film grown at $T_S = 700$°C in O_2 on a $SrTiO_3$(001) substrate: (a) ω-2θ scan, the inset shows an enlargement around the (004) peak; (b) ω-2θ scan around the (101) peak; (c) rocking curve of the (002) peak. In (d) and (e) reciprocal space maps around the (004) and (116) peak are shown.

To investigate the crystalline quality of our thin films, high resolution x-ray diffraction analysis was performed with a four-circle x-ray diffractometer. Fig. 1(a) shows the result of an ω-2θ scan. Only (00ℓ) reflections and no parasitic phases could be detected. We derive an out-of-plane lattice parameter of $c = 7.903$ Å. The narrow full width at half maximum for the (004) reflection of only 0.04° (see Fig. 1(c)) demonstrates the high crystalline quality of our films. To analyze the mosaic spread and the relaxation state of the thin films, reciprocal space maps around the (004) and (116) reflections have been made. The result is shown in Fig. 1(d) and Fig. 1(e). The (004) reflection of the film is well defined in both length and orientation. This indicates that the mosaic spread is very small and no tilt of the film relative to the substrate takes

[1] This work is supported by the DFG via the priority program SPP 1157 (project No.: GR 1132/13).

place. The reciprocal space map around the (116) reflection shows no evidence for relaxation. Therefore, our Sr_2CrReO_6 thin films are coherently strained and exhibit a compressive biaxial in-plane strain, which causes an elongation of the c-axes of about 1%. Another important point in ferromagnetic double perovskites is the amount of antisite defects which result in a mixture of the B and B'-sites (here: Cr ions on Re sites and vice versa). These defects are detrimental for the magnitude of the saturation magnetization. An indicator for the degree of order in tetragonal double perovskite thin films is the intensity of (101) reflection (Fig. 1(b)), which yields an ordering of 12%.

Magnetization curves of the Sr_2CrReO_6 films are shown in Fig. 2(a), which reveals a very high saturation magnetization at 25 K of 0.7 μ_B per formula unit (f.u.) close to the theoretical value of 1 μ_B/f.u. In a simple ionic model, the Cr and Re ions are ferromagnetically coupled, resulting in a net spin of 1 μ_B/f.u. as recently confirmed by x-ray magnetic circular dichroism measurements [6]. Note also that the coercive field $\mu_0 H_c = 1.2$T is very high. The temperature dependence of the magnetization (not shown here) displays no significant change up to 390 K, demonstrating that the Curie temperature is well above 390 K.

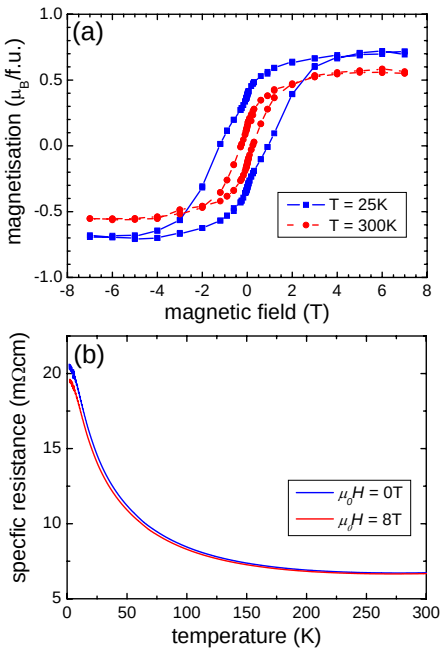

Figure 2: (a) Magnetization versus applied magnetic field at 25 K and 300 K; (b) resistivity versus temperature at 0 T and 8 T for an epitaxial Sr_2CrReO_6 thin film.

We have also performed electronic transport measurements in a liquid ^{4}He cryostat with a variable temperature insert. Fig. 2(b) shows $\rho(T)$ measured in four-point geometry. The data displayed in the figure are very similar to the ones reported in literature for polycrystalline samples [1]. The resistivity slightly increases from 8.5 mΩcm at room temperature to 30.5 mΩcm at 5 K. This increase could be due to a reduction of carrier scattering by thermally excited spins [1]. Moreover, a significant anomalous Hall signal has been observed in Sr_2CrReO_6 thin films (not shown here) and is currently investigated in more detail.

In summary, we have grown Sr_2CrReO_6 thin films with high crystalline and magnetic quality using laser molecular beam epitaxy. The structural properties reveal that the films are c-axis oriented, coherently strained and show a high degree of B site order. The films are clearly magnetic with a saturation magnetization of 0.7 μ_B/f.u. close to the theoretical value. Furthermore, the thin films are metallic with a slight increase of resistivity at lower temperature. These properties make the Sr_2CrReO_6 films attractive for applications in spintronics.

References

[1] H. Kato, T. Okuda, Y. Tomioka, Y. Takenoya, A. Ohkubo, M. Kawasaki, and Y. Tokura, Appl. Phys. Lett. **81**, 328 (2002).
[2] G. Vaitheeswaran, V. Kanchana, and A. Delin, Appl. Phys. Lett. **86**, 032513 (2005).
[3] H. Asano, N. Kozuka, A. Tsuzuki, and M. Matsui, Appl. Phys. Lett. **85**, 263 (2004).
[4] T. Yamamoto, J. Liimatainen, J. Linden, M. Karppinen, and H. Yamauchi, J. Mater. Chem. **10**, 2342 (2000).
[5] J. B. Philipp, D. Reisinger, M. Schonecke, M. Opel, A. Marx, A. Erb, L. Alff, and R. Gross, J. Appl. Phys. **93**, 6853 (2003).
[6] P. Majewski, S. Geprägs, O. Sanganas, M. Opel, F. Wilhelm, A. Rogalev, L. Alff, and R. Gross, Appl. Phys. Lett. **87**, 202503 (2005).

Epitaxial growth of (111)-oriented Fe_3O_4 thin films on ZnO

A. Boger, A. Brandlmaier, S. T. B. Goennenwein, M. Opel, and R. Gross [1]
J. Simon and W. Mader [2]

Substantial research efforts have been made over the last decade aiming at a combination of magnetic degrees of freedom with semiconducting properties for novel spintronic devices. One possibility is to inject spin-polarized charge carriers directly from a ferromagnetic electrode into a semiconductor. However, for direct diffusive spin injection from a conventional ferromagnetic metal like Fe or Co the "conductivity mismatch" between the two materials is a major problem [1]. To circumvent this issue, materials with a high spin polarization P are mandatory, half metals with $P = 100\,\%$ being ideal. The ferrimagnet magnetite (Fe_3O_4) with a Curie temperature of 860 K is supposed to be such a half metal [2]. Moreover, this material offers the advantage of a comparably low electrical conductivity ($\approx 225\,\Omega^{-1}\mathrm{cm}^{-1}$ at room temperature [3]). Spin-resolved photoelectron spectroscopy (PES) of (100)-oriented Fe_3O_4 thin films shows a spin polarization of $-(55 \pm 10)\%$ [4]. A clearly higher value of $-(80 \pm 5)\%$ is found for (111) orientation [5]. Although half-metallic behavior ($P = 100\%$) has not yet been demonstrated in experiment, the use of (111)-oriented magnetite thin films for spin injection into semiconductors appears promising.

Here, we report on (111)-oriented magnetite thin films grown directly on the semiconductor ZnO. The Fe_3O_4 films have been deposited epitaxially by pulsed laser deposition on ZnO (0001) substrates, without using any buffer layer. The substrate temperature was 320 °C and the growth took place in Ar atmosphere at a pressure of 3.7×10^{-3} mbar. The energy density of the KrF excimer laser ($\lambda = 248$ nm) on the stoichiometric target was $2\,\mathrm{J/cm^2}$ with a repetition rate of 2 Hz.

The structural quality of the films was determined by high-resolution x-ray diffractometry (HRXRD). Fig. 1(a) shows a ω-2θ scan in out-of-plane direction. The (0002) and (0004) reflections of the ZnO substrate are visible. The other peaks correspond to the magnetite (111), (222), (333), (444), and (555) reflections. In order to determine the in-plane lattice constants, ω-2θ scans of the Fe_3O_4 (004) and (008)

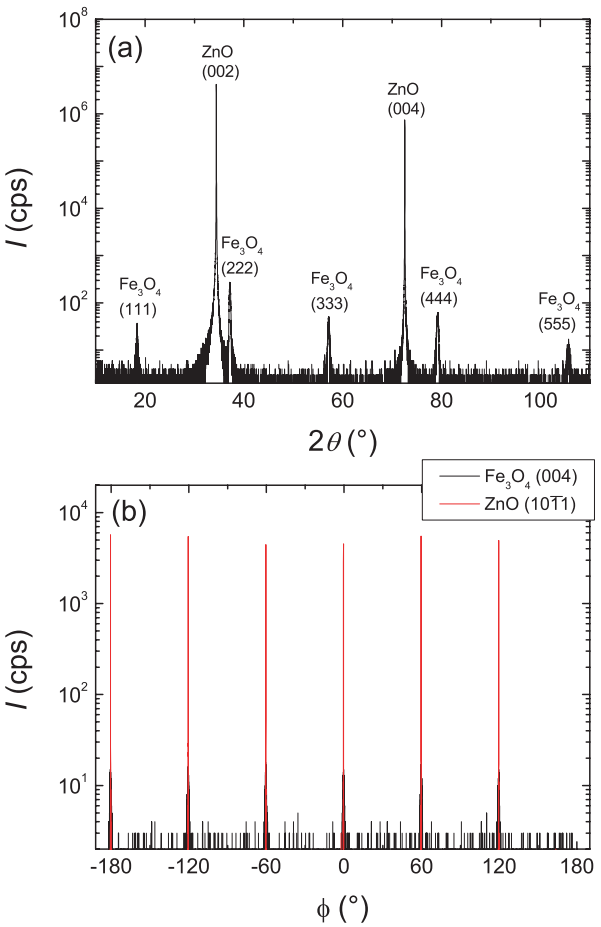

Figure 1: X-ray diffraction patterns of a (111)-oriented 31.4 nm thick Fe_3O_4 film grown on a ZnO (0001) substrate. (a) ω-2θ scan: The (111), (222), (333), (444), and (555) reflections of Fe_3O_4 as well as (0002) and (0004) of ZnO are clearly resolved. (b) From the ϕ scans of the Fe_3O_4 (004) and the ZnO (10$\bar{1}$1) reflections, the relative orientation of the magnetite film with respect to the substrate can be determined.

[1] This work is supported by the DFG via the priority program SPP1157 (project No.: Gr 1132/13).
[2] Institut für Anorganische Chemie, Universität Bonn

reflections were performed. The evaluation of both types of scans was made for four samples with thickness values between 26.1 nm and 31.4 nm. As compared to bulk magnetite with the cubic lattice constant of $a_{Fe_3O_4} = 8.3963$ Å at 298 K [6], the films are almost completely relaxed apart from a small tensile in-plane strain between -0.06% and -0.18% in combination with an out-of-plane compressive strain between 0.22 % and 0.25 %. This phenomenon can possibly be explained by the difference in the thermal expansion of ZnO and Fe_3O_4 while cooling the samples from the growth temperature (320 °C) to room temperature. In addition, the orientation of the two materials with respect to each other has been determined. The (004) reflections of magnetite appear at the same in-plane rotation angles ϕ as the ZnO $(10\bar{1}1)$ reflections (see Fig. 1(b)). Due to the hexagonal symmetry of a cubic system rotated around its (111)-axis, the (004) reflection of magnetite is observed with a periodicity of 60° like the ZnO $(10\bar{1}1)$ reflection. This means that the substrate $(2\bar{1}\bar{1}0)$ in-plane direction is parallel to Fe_3O_4 $(1\bar{1}0)$. Finally, the films exhibit high crystalline quality in the out-of-plane direction. The rocking curve of the Fe_3O_4 (222) reflection shows a small full width at half maximum (FWHM) $\Delta\omega$ between 0.02° and 0.06°.

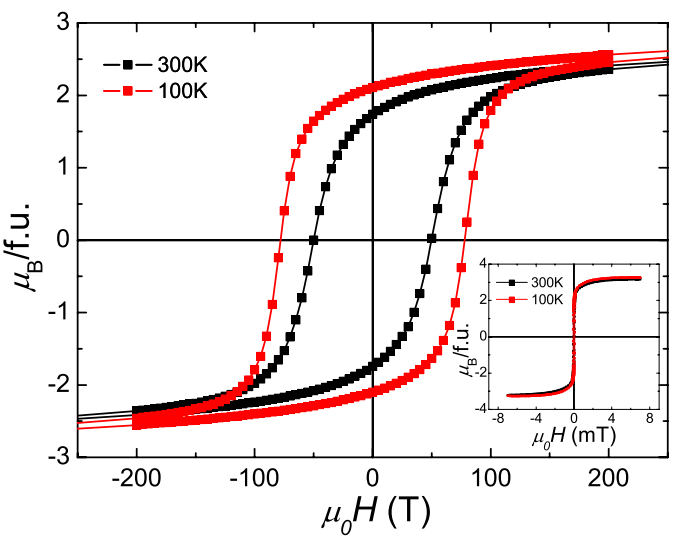

Figure 2: Magnetization as a function of the applied magnetic field **H** at 100 K and 300 K for a 31.4 nm thin Fe_3O_4 film on ZnO. **H** is oriented along the $(1\bar{1}0)$ axis of the Fe_3O_4 film.

We also have investigated the magnetic behavior of the thin films by magnetization measurements in a commercial SQUID magnetometer (MPMS XL-7, Quantum Design). In Fig. 2, the magnetization of a 31.4 nm (111)-oriented magnetite film is plotted versus an in-plane oriented magnetic field at 300 K and 100 K. The diamagnetic contribution of the substrate has been subtracted. The observation of a hysteresis loop verifies ferromagnetic behavior with a coercive field $H_c = 50$ mT and a remanence $M_{rem} = 1.7\,\mu_B$ per formula unit (f.u.) for 300 K ($H_c = 78$ mT and $M_{rem} = 2.1\,\mu_B$/f.u. for 100 K). This coercivity is in good agreement with that reported for (111)-oriented Fe_3O_4 films grown on sapphire with thickness values between 15 nm and 68 nm: 31 mT $\leq H_c \leq$ 60 mT [7–10]. At 7 T and 300 K, the magnetization reaches 3.2 μ_B/f.u. which is 20 % lower than the theoretical value of 4 μ_B/f.u. Moussy *et al.* found comparable values in (111)-oriented single crystalline films on sapphire, with 2.6 μ_B/f.u. for a 25 nm thick and 3.2 μ_B/f.u. for 50 nm thick film at 2 T and 300 K [8]. In summary, the magnetic properties of (111)-oriented magnetite films on ZnO substrates are similar to those of magnetite grown on sapphire.

The successful growth of Fe_3O_4 on ZnO opens the possibility to grow Fe_3O_4/ZnO heterostructures. To study the Fe_3O_4t′/ZnO interface we performed high-resolution transmission electron microscopy (HRTEM) studies. The cross-sectional HRTEM image (Fig. 3) shows a single crystalline ZnO layer on top of a Fe_3O_4 film grown epitaxially on a ZnO(0001) substrate. The growth parameters of the ZnO and the magnetite layers were identical. Electron diffractometry shows that this ZnO film is oriented $(000\bar{1})$ in contrast to the (0001)-oriented substrate. Smooth interfaces between the layers are visible. AFM measurements of a 31.4 nm thick Fe_3O_4 film show a rms roughness of only 0.3 nm on an area of 0.9 μm × 0.9 μm. Consequently, our films exhibit small surface roughness and good interface quality. With respect to multilayer devices

for spin injection this is an important prerequisite to reduce spin scattering at the interfaces.

In summary, we have grown (111)-oriented Fe_3O_4 thin films on ZnO (0001) substrates using pulsed laser deposition. The samples are free of impurity phases. High crystalline quality with a FWHM of the rocking curve down to 0.02° for the Fe_3O_4(222) reflection was obtained. Magnetic field and temperature dependent magnetization measurements show clear ferromagnetic behavior, similar to (111)-oriented magnetite films grown on sapphire. Moreover, ZnO films can be grown on top of Fe_3O_4. HRTEM and AFM measurements prove the single crystalline growth of these layers with high interface and surface quality. With the growth of Fe_3O_4/ZnO thin film heterostructures at hand, spin injection experiments from the supposed half-metallic ferromagnet magnetite into the semiconductor ZnO can now be envisaged.

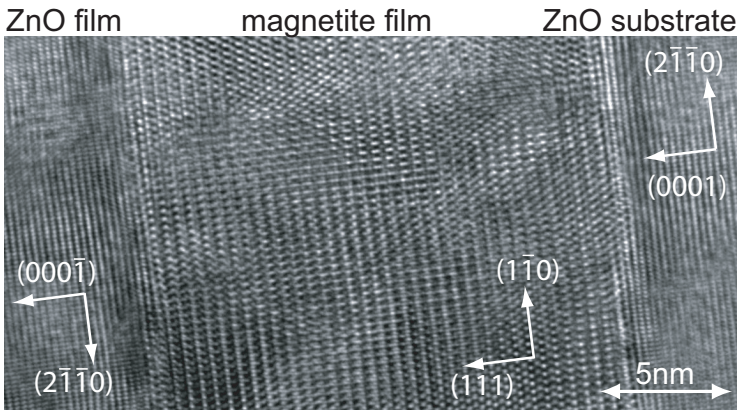

Figure 3: HRTEM image of a Fe_3O_4/ZnO bilayer grown on a ZnO (0001) substrate. The 18 nm thick (111) oriented Fe_3O_4 film was grown on the ZnO (0001) substrate followed by a 29 nm thick (000$\bar{1}$) oriented ZnO film on top.

References

[1] G. Schmidt, D. Ferrand, L. W. Molenkamp, A. T. Filip, and B. J. van Wees, Phys. Rev. B **62**, R4790 (2000).
[2] Z. Zhang and S. Satpathy, Phys. Rev. B **44**, 13319 (1991).
[3] D. Reisinger, P. Majewski, M. Opel, L. Alff, and R. Gross, J. Appl. Phys. **58**, 4980 (2004).
[4] M. Fonin, R. Pentcheva, Yu. S. Dedkov, M. Sperlich, D. V. Vyalikh, M. Scheffler, U. Rüdiger, and G. Güntherodt, Phys. Rev. B **72**, 104436 (2005).
[5] Yu. S. Dedkov, U. Rüdiger, and G. Güntherodt, Phys. Rev. B **65**, 064417 (2002).
[6] A. J. Gorton, G. Bitsianes, and T. L. Joseph, Trans. AIME **233**, 1519 (1965).
[7] F. Dellile, B. Diny, J.-B. Moussy, M.-J. Guittet, S. Gota, M.Gautier-Soyer, and C. Marin, J. Magn. Magn. Mater. **294**, 27 (2005).
[8] J.-B. Moussy, S. Gota, A.Bataille, M.-J. Guittet, M. Gautier-Soyer, F. Dellile, B. Dieny, F. Ott, T. D. Doan, P. Warin, P. Bayle-Guillemoud, C. Gatel, and E. Snoeck, Phys. Rev. B **70**, 174448 (2004).
[9] I. Yamaguchi, T. Terayama, T. Manabe, T. Tsuchiya, M. Sohma, T. Kumagai, and S. Mizuta, J. Solid State Chem. **163**, 239 (2002).
[10] R. F. C. Farrow, P. M. Rice, M. F. Toney, R. F. Marks, J. A. Hedstrom, R. Stephenson, M. J. Carey, and A. J. Kellock, J. Appl. Phys. **93**, 5626 (2003).

In-situ manipulation of magnetic anisotropy in magnetite thin films

A. Brandlmaier, S. Geprägs, M. Opel, S. T. B. Goennenwein, and R. Gross [1]
C. Bihler, H. Huebl, and M. S. Brandt [2]

The functionality of most magneto-electronic or spintronic devices is intimately linked to the orientation of the magnetization in (different) ferromagnetic layers [1]. Usually, magnetic fields are exploited to control the magnetization orientation, but this approach becomes ever more problematic in modern micro- or nanostructures, as it is very difficult to generate sufficiently large magnetic fields in sufficiently small volumes. Thus, novel schemes allowing to control the magnetization orientation by means of a non-magnetic parameter – in particular an electric field – are investigated vigorously at present. The application of strain to a ferromagnetic layer also is appealing, as strain alters the magnetic anisotropy, which in turn governs the magnetization orientation. Along this line of thought, we have investigated how the strain exerted in-situ by a piezoelectric actuator on a ferromagnetic Fe_3O_4 thin film alters its magnetic anisotropy.

We use magnetite (Fe_3O_4) as a prototype modern magnetic material, which unites a high ferromagnetic transition temperature $T_C \gg 300$K and a high electronic spin polarization $P \geq 60\%$, and thus is a promising material for spintronic applications. The Fe_3O_4 thin films were deposited on $\langle 100 \rangle$-oriented MgO substrates by laser molecular beam epitaxy in Ar atmosphere at a pressure of 48 mtorr [2]. We heated the MgO substrate to 320°C, and used KrF laser pulses with a fluence of 2.5 J/cm^2 and a repetition rate of 2 Hz to ablate material from a stoichiometric Fe_3O_4 target. The structural and magnetic properties of the samples were characterized with high-resolution x-ray diffraction (Bruker D8 Discover) and SQUID magnetometry (Quantum Design MPMS XL-7). To quantify the magnetic anisotropy, we relied on ferromagnetic resonance (FMR) experiments in the *X*-band. The FMR spectra were recorded at room temperature in a Bruker ESP 300 spectrometer, using magnetic field modulation at 100 kHz with an amplitude $\mu_0 H_{\mathrm{mod}} = 3.2$ mT to allow for phase sensitive detection.

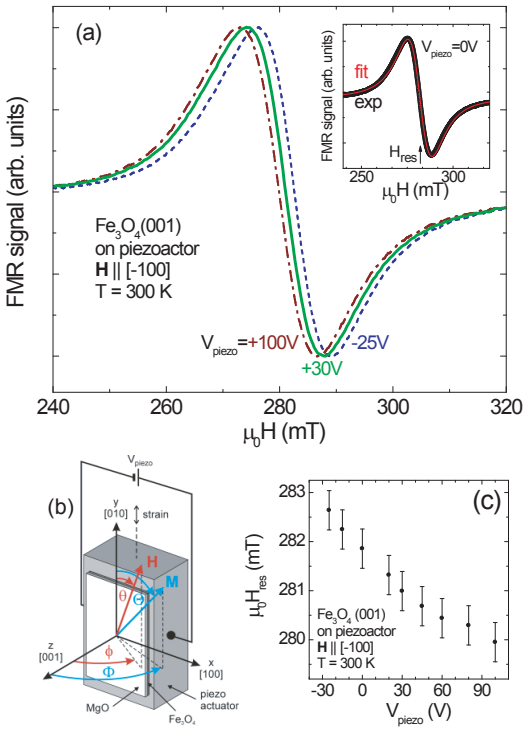

Figure 1: (a) The room-temperature FMR spectra of a Fe_3O_4 film mounted on a piezo-actuator shift with the bias voltage V_{piezo} applied to the actuator. The inset shows the Lorentzian line shape. The arrow indicates the FMR resonance field $\mu_0 H_{\mathrm{res}}$. (b) Sketch of the sample. (c) $\mu_0 H_{\mathrm{res}}$ varies linearly with V_{piezo} in good approximation. The error bars represent the maximal change in linewidth over the whole bias range.

As we obtained qualitatively and quantitatively very similar results from several different magnetite thin films, we will focus on a 44 nm thick Fe_3O_4 layer grown directly on the MgO substrate in the following. X-ray diffraction experiments show that this magnetite film is highly crystalline and coherently strained, with an in-plane lattice constant of 0.8427 nm (corresponding to twice the lattice constant of the MgO substrate within experimental error), and an out-of-plane lattice constant

[1] This work is supported by the DFG via the priority program SPP1157 (project No.: GR 1132/13).
[2] Walter Schottky Institut, Technische Universität München, 85748 Garching, Germany

of 0.8305 nm, obtained from reciprocal space maps around the (044) and (022) reflections. The mosaic spread is very small, as evident e.g. from the full width at half maximum $\Delta\omega = 0.04^\circ$ of the rocking curve of the magnetite (004) reflection. To allow for an in-situ variation of the strain, we cut the sample into pieces with lateral dimensions of 2×2 mm^2, and polished the MgO substrate down to a thickness of about 50 ¯m. Using a two-component epoxy [3], these samples are then glued onto the face of a piezoelectric actuator [4] (see Fig.1(b)) such that the dominant uniaxial deformation of the piezo-stack is parallel to the magnetite [010] direction, and the epoxy is annealed for one hour at 100°C.

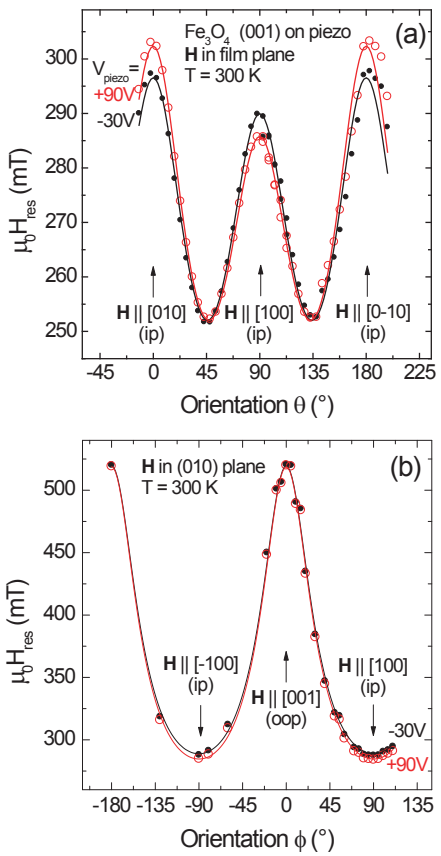

Figure 2: (a),(b) The FMR resonance field $H_{\rm res}$ sensitively depends on the orientation of the external magnetic field **H**, and the voltage applied to the piezoelectric actuator (symbols). The full lines represent the simulated FMR fields. For **H**||[100] and **H**||[010], the magnetic field is aligned in the plane of the film (ip) while it points out of plane (oop) for **H**||[001].

Fig. 1 shows that the room temperature FMR spectrum of a magnetite film-piezoelectric actuator sandwich characteristically shifts as a function of the voltage $V_{\rm piezo}$ applied to the actuator. When no bias voltage is applied to the piezoelectric actuator ($V_{\rm piezo} = 0$ V), the FMR spectrum consists of a single resonance at $\mu_0 H_{\rm res} \approx 282$ mT, with a peak-to-peak line width of $\mu_0 \delta H_{\rm pp} \approx 13$ mT, which is well described by a Lorentzian lineshape (inset Fig. 1(a)). Upon the application of $V_{\rm piezo} > 0$ V (which corresponds to a dilation of the actuator), the FMR shifts to lower magnetic fields, while the opposite is true for $V_{\rm piezo} < 0$ V. Within the voltage range -30 V $< V_{\rm piezo} <$ 100 V in which the stroke of the actuator linearly depends on the applied voltage, the FMR resonance field $\mu_0 H_{\rm res}$ also is proportional to $V_{\rm piezo}$ in good approximation (Fig. 1(c)).

The shift of the FMR spectrum with $V_{\rm piezo}$ is unambiguously due to a stress-induced change of the magnetic properties of the magnetite film. Firstly, because of the linear dependence $H_{\rm res} \propto V_{\rm piezo}$, temperature fluctuations or changes in the microwave coupling can be ruled out as an explanation for the effect. In this regard, we note that the resonance frequency of the microwave cavity is constant to about 10^{-4} over the whole voltage range. Secondly, the line width $\mu_0 \delta H_{\rm pp}$ changes by less than 0.8 mT for -30 V $< V_{\rm piezo} < 100$ V, so that a variation of the FMR line *shape* can be ruled out as an explanation for the maximum shift of the FMR resonance field $\mu_0 \Delta H_{\rm res} = \mu_0 H_{\rm res}(-30\ {\rm V}) - \mu_0 H_{\rm res}(+100\ {\rm V}) = 2.7$ mT achievable. Thirdly, the dependence of $H_{\rm res}\left(V_{\rm piezo}\right)$ characteristically changes as a function of the orientation of the external magnetic field, as discussed later.

The FMR resonance field $H_{\rm res}$ sensitively depends on the orientation of the external magnetic field with respect the Fe_3O_4 crystalline directions. This dependence allows to quantify the magnetic anisotropy contributions in the film. Figure 2 shows how $H_{\rm res}$ changes when the externally applied magnetic field is applied along different directions in the (010)- and the (001)-plane. In this figure, only the data for the two extreme bias voltages $V_{\rm piezo} = -30$ V and $V_{\rm piezo} = +90$ V are displayed for the sake of clarity. In the experiments, we also measured FMR spectra at intermediate bias voltages, and invariably obtained a quasi-linear dependence $H_{\rm res} \propto V_{\rm piezo}$ as already discussed in Fig. 1(c). However, the maximal FMR line shift $\Delta H_{\rm res} = H_{\rm res}(-30\ {\rm V}) - H_{\rm res}(+90\ {\rm V})$ is very different depending

on the orientation of the external field. ΔH_{res} is large and negative for $\mathbf{H}||[010]$, vanishes for $\mathbf{H}||[110]$, and becomes large and positive for $\mathbf{H}||[100]$ (Fig. 2(a)). Moreover, ΔH_{res} also vanishes if the field is applied along [001], perpendicular to the film plane. The effect of V_{piezo} on the FMR spectrum thus is qualitatively different along the three cubic axes of the magnetite crystal. Note also that for $\mathbf{H}$ in the film plane, the FMR shows a fourfold symmetry as expected for a cubic material, although the resonance fields do not coincide every 90 ° (even for $V_{\mathrm{piezo}} = 0$ V, not shown).

To model the angular dependence of the FMR resonance fields we use the free energy density

$$F = F_{\mathrm{Zeeman}} + K_{\mathrm{u,eff}}^{[001]} \sin^2\Theta\cos^2\Phi + K_{\mathrm{u}}^{[010]}\cos^2\Theta + \frac{1}{4}K_{\mathrm{c1}}\left(\sin^2(2\Theta) + \sin^4\Theta\sin^2(2\Phi)\right). \quad (1)$$

F_{Zeeman} is the Zeeman energy, and the angles Θ and Φ parameterize the orientation of the magnetization $M = M(\Theta, \Phi)$. In the following, we assume that the applied external field suffices to saturate the magnetization to $M = 305$ kA/m measured with SQUID magnetometry. The effective uniaxial anisotropy contribution along [001] $K_{\mathrm{u,eff}}^{[001]} = \frac{1}{2}\mu_0 M^2 + K_{\mathrm{u}}^{[001]}$ comprises the demagnetization contribution $\frac{1}{2}\mu_0 M^2$ and the uniaxial contribution $K_{\mathrm{u}}^{[001]} < 0$ resulting from strained growth of the magnetite film, which can not be separated with FMR as they have the same symmetry. $K_{\mathrm{u}}^{[010]}$ represents a uniaxial anisotropy within the film plane along [010], and K_{c1} is the first-order cubic anisotropy constant. The FMR resonance fields are obtained numerically from Eq. (1) by evaluating the equation of motion $(\omega/\gamma)^2 = \left(M^2\sin^2\Theta\right)^{-1}\left[\left(\partial_\Phi^2 F\right)\left(\partial_\Theta^2 F\right) - \left(\partial_\Phi\partial_\Theta F\right)^2\right]$ at the equilibrium orientation $(\Theta_0,\ \Phi_0)$ of the saturation magnetization given by $\partial_\Theta F\big|_{\Theta=\Theta_0} = \partial_\Phi F\big|_{\Phi=\Phi_0} = 0$ [5]. The corresponding resonance fields are shown as full lines in Fig. 2. The anisotropy constants for the different V_{piezo} are summarized in Table 1. The good agreement between the simulated and the measured resonance fields demonstrates that the magnetic anisotropy contributions included in Eq. (1) are sufficient to describe the magnetic properties of the magnetite film within the accuracy of the FMR experiment.

The magnetic anisotropy constants for $V_{\mathrm{piezo}} = 0$ V (Table 1) agree well with the values quoted in the literature [6], with the exception of the uniaxial anisotropy contribution $K_{\mathrm{u}}^{[010]}$ within the film plane which is not observed in as-grown magnetite films. This anisotropy contribution can be understood by considering the non-isotropic thermal expansion of the PZT piezo-stack onto which the magnetite sample is glued. The magnetite sample is "grafted" onto the actuator lattice during the curing of the two-component epoxy at $T = 100$ °C. Upon cooling to room temperature, the anisotropic contraction of the actuator builds up tensile stress along the [010]-direction in the plane of the magnetite layer. Due to magneto-elastic coupling, stress in a ferromagnetic crystal induces magnetic anisotropy [7]. This effect can be expressed as a contribution to the free energy $F_\sigma = K_\sigma\alpha^2$ with the direction cosine α, where the stress-induced uniaxial anisotropy constant

$$K_\sigma = -(3/2)\sigma\lambda \quad (2)$$

depends on the stress σ and the magnetostriction coefficient λ. Considering that the magnetostriction coefficient along the cubic axes $\lambda = -19.5\times10^{-6}$ is negative in bulk magnetite [8], a tensile strain ($\sigma > 0$) in the magnetite film will yield a magnetically hard axis, in qualitative agreement with $K_{\mathrm{u}}^{[010]} > 0$ observed.

To quantify the stress in our magnetite film, we start from the elastic energy density of a cubic system $F_{\mathrm{elastic}} = (1/2)c_{11}\left(\epsilon_1^2 + \epsilon_2^2 + \epsilon_3^2\right) + c_{12}\left(\epsilon_1\epsilon_2 + \epsilon_2\epsilon_3 + \epsilon_1\epsilon_3\right)$, with the elastic constants c_{ij}, and the strain variables ϵ_i in Voigt notation (and neglecting shear strains) [7]. In an epitaxial film, the strain components ϵ_1 and ϵ_2 within the film plane can not be adjusted at will.

Instead, they are determined by the interplay of epitaxial strain, the strain resulting from different thermal expansion coefficients of e.g. the actuator, the substrate and the film, and in our case also the strain due to the expansion of the piezoelectric actuator for finite V_{piezo}. According to continuum elasticity theory, the out-of-plane strain ϵ_3 is a consequence of the in-plane strains, with $\sigma_3 = \partial F_{\mathrm{elastic}}/\partial\epsilon_3 = c_{11}\epsilon_3 + c_{12}\left(\epsilon_1 + \epsilon_2\right)$. Using $\sigma_3 = 0$ (no stress is applied perpendicular to the film plane) and thus $\epsilon_3 = -\left(\epsilon_1 + \epsilon_2\right) c_{12}/c_{11}$, one obtains the stresses along the three cubic directions [7]

$$\sigma_x = \sigma_1 = \left(c_{11} - \frac{c_{12}^2}{c_{11}}\right)\epsilon_1 + \left(c_{12} - \frac{c_{12}^2}{c_{11}}\right)\epsilon_2 \quad (3)$$

$$\sigma_y = \sigma_2 = \left(c_{12} - \frac{c_{12}^2}{c_{11}}\right)\epsilon_1 + \left(c_{11} - \frac{c_{12}^2}{c_{11}}\right)\epsilon_2 \quad (4)$$

$$\sigma_z = \sigma_3 = 0. \quad (5)$$

We model the strain exerted by the actuator along its principal expansion direction as $\epsilon_2 = \alpha\Delta L/L$, and use $\epsilon_1 = -\epsilon_2/2$ to take into account that due to the elastic properties of the actuator, the expansion along one direction is always accompanied by a compression with half the magnitude in the two orthogonal directions. $\Delta L/L = 1.4 \times 10^{-3}$ is the full nominal stroke of the actuator, and the constant $\alpha \leq 1$ represents imperfect strain transmission by the epoxy glue. With the bulk magnetite values [8] for the elastic constants $c_{11} = 2.73 \times 10^{11}\,\mathrm{N/m^2}$, and $c_{12} = 1.06 \times 10^{11}\,\mathrm{N/m^2}$ in Eqs. (3) and (4), and assuming $\alpha = 0.1$, we calculate a change in the magnetic anisotropy constants $\frac{\Delta K_{\mathrm{u}}^{[010]}}{M_{\mathrm{s}}} = 3.4$ mT and $\frac{\Delta K_{\mathrm{u}}^{[001]}}{M_{\mathrm{s}}} = 0.7$ mT, in good quantitative agreement with experiment (see Table 1). We note that the ratio $\Delta K_{\mathrm{u}}^{[010]} : \Delta K_{\mathrm{u}}^{[001]} \approx 5 : 1$ of the calculated anisotropy changes, as well as $\Delta K_{\mathrm{u}}^{[010]} : \Delta K_{\mathrm{u}}^{[001]} \approx 3 : 1$ observed experimentally, is very different from the ratio $\epsilon_2 : \epsilon_1 = 2 : -1$ of the strains.

Table 1: Magnetic anisotropy constants of the Fe_3O_4 film obtained from the numerical simulations for different bias V_{piezo} applied to the piezoelectric actuator. The last three columns show the change of the anisotropy constants with respect to $V_{\mathrm{piezo}} = 0$ V.

V	g	$\frac{K_{\mathrm{u,eff}}^{[001]}}{M_{\mathrm{s}}}$	$\frac{K_{\mathrm{u}}^{[010]}}{M_{\mathrm{s}}}$	$\frac{K_{\mathrm{c1}}}{M_{\mathrm{s}}}$	$\frac{\Delta K_{\mathrm{u}}^{[001]}}{M_{\mathrm{s}}}$	$\frac{\Delta K_{\mathrm{u}}^{[010]}}{M_{\mathrm{s}}}$	$\frac{\Delta K_{\mathrm{c1}}}{M_{\mathrm{s}}}$
-30	2.02	79.9	2.0	-14.7	-0.3	-0.8	0
0	2.02	80.2	2.8	-14.7	–	–	–
+90	2.02	80.9	5.1	-14.9	0.7	2.3	-0.2

In summary, we have investigated the interplay between crystalline strain and the magnetic anisotropy properties of a thin magnetite film. We modified the strain in the film in situ by means of a piezoelectric actuator, and determined the resulting modification of the magnetic anisotropy via ferromagnetic resonance experiments. We find that the strain induced by the piezoelectric actuator significantly alters the magnetic anisotropy at room temperature, as the in-plane and out-of-plane uniaxial magnetic anisotropy constants $K_{\mathrm{u}}^{[010]}$ and $K_{\mathrm{u}}^{[001]}$ can be tuned by several 10 percent and about one percent, respectively.

References

[1] M. Ziese and M. Thornton (Eds.), *Spinelectronics* (Springer, Berlin, 2001).
[2] D. Reisinger *et al.*, Appl. Phys. A **77**, 619 (2003).
[3] UHU plus Endfest 300.
[4] No: PSt 150/2x3/5, Piezomechanik München (Germany).
[5] C. Bihler *et al.*, Appl. Phys. Lett. **89**, 012507 (2006).
[6] P. A. A. van der Heijden *et al.*, J. Magn. Magn. Mater. **182**, 71 (1998).
[7] D. Sander, Rep. Prog. Phys. **62**, 809 (1999).
[8] R. A. Lefever, *Landolt-Börnstein*, Part B, Group III Condensed Matter (Springer, 1970).

Electrically detected ferromagnetic resonance

S. T. B. Goennenwein, S. W. Schink, A. Brandlmaier, and R. Gross [1]
H. Huebl, C. Bihler, and M. S. Brandt, [2] *R. S. Keizer and T. M. Klapwijk,* [3] *A. Gupta* [4]

The occurrence of ferromagnetic resonance (FMR) affects the quasi-static properties of a magnetic material, such as its magneto-resistance [1–4], magneto-impedance [5], or caloric properties [6]. These effects can be used to detect FMR in magnetic microstructures [4, 6]. This is attractive, as FMR is one of the most sensitive methods for the investigation of magnetic anisotropy. However, to exploit the potential of such novel FMR detection methods, their full equivalence with the well established conventional cavity-based FMR must first be demonstrated.

Here, we report on resonant and non-resonant changes of the magneto-resistance of thin ferromagnetic CrO_2 and Fe_3O_4 films upon microwave irradiation. We show that these electrically-detected ferromagnetic resonance (EDFMR) signals are spectroscopically equivalent to conventional FMR measured simultaneously, and that the sign and the magnitude of the EDFMR signals can be quantitatively understood in terms of a Joule heating effect. These findings open the way for selective investigations of particular transport processes in ferromagnets via magnetic resonance techniques, in analogy to the well established influence of paramagnetic resonance on electronic transport in semiconductors. [7–9]

Two different types of ferromagnetic thin film samples have been investigated. On one hand, the single-crystalline, 100 nm thick CrO_2 films were deposited on (100)-oriented TiO_2 substrates by chemical vapor deposition [10]. After patterning them into 80 ¯m wide and 600 ¯m long Hall-bar structures using optical lithography and wet chemical etching, we fabricated Ohmic contacts by depositing Au in-situ immediately after sputter-cleaning the film surface in an Ar plasma [11]. On the other hand, magnetite (Fe_3O_4) layers were grown on (100)-oriented MgO substrates by pulsed laser deposition [12]. In the following, we

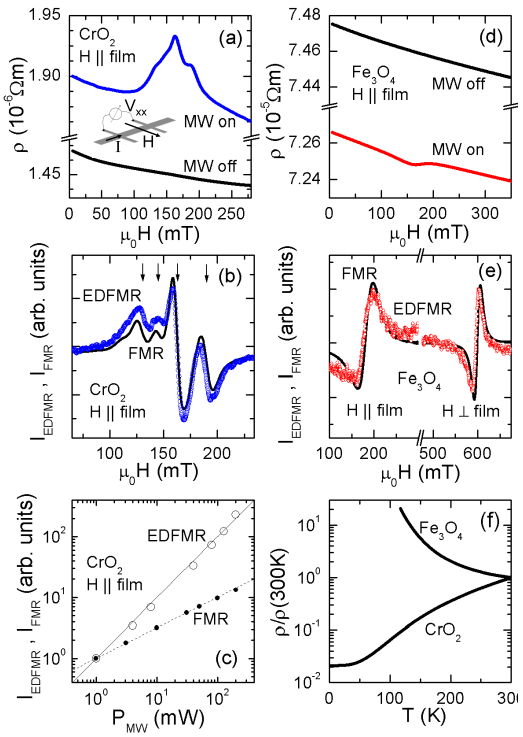

Figure 1: (a) The magneto-resistance ρ of a CrO_2 Hall bar at room temperature characteristically increases upon microwave irradiation, with additional peaks at the FMR resonance fields $\mu_0 H_{\rm res} \approx 163$ mT. ((b) The microwave-induced changes in ρ (electrically detected ferromagnetic resonance) $I_{\rm EDFMR} = \Delta\rho/\Delta H$ (open circles) reproduce the conventional FMR signal (full line). (c) The EDFMR signal amplitude $I_{\rm EDFMR}$ in CrO_2 is proportional to the incident microwave power $P_{\rm MW}$, while the FMR signal amplitude scales with $\sqrt{P_{\rm MW}}$. (d),(e) In Fe_3O_4, ρ decreases upon microwave irradiation, with a dip at the FMR resonance field $\mu_0 H_{\rm res} = 170$ mT. The EDFMR signal (open circles) again reproduce the conventional FMR signal (full lines), for **H** both parallel and perpendicular to the Fe_3O_4 film plane. (f) The resistivities of CrO_2 and Fe_3O_4 show opposite temperature dependencies around 300 K, with ρ of CrO_2 increasing and ρ of Fe_3O_4 decreasing with increasing temperature.

[1] This work is supported by the DFG via the priority program SPP 1157 (project No.: GR 1132/13).
[2] Walter Schottky Institut, Technische Universität München, 85748 Garching
[3] Kavli Institute of NanoScience, Delft University of Technology, 2628 CJ Delft, The Netherlands
[4] MINT Center, University of Alabama, Tuscaloosa, AL 35487, U.S.A.

focus on a 32 nm thick, coherently strained Fe_3O_4 film with Ohmic contacts in Van-der-Pauw-geometry, realized by wedge bonding Al wires. The FMR spectra of these samples were measured in a *X*-band (9 GHz) electron spin resonance setup at room temperature, using magnetic field modulation at 100 kHz with an amplitude $\mu_0 \Delta H = 3.2$ mT. Simultaneously to the FMR, we recorded the longitudinal magneto-resistance or the Hall effect in the samples in four-point geometry, with an ac current bias I at a frequency $\nu_I \leq 1.1$ kHz. The magnetization measurements were performed in a Quantum Design MPMS XL-7 SQUID magnetometer, and the resistivity as a function of temperature and the magneto-transport properties were recorded in a superconducting magnet cryostat.

Figure 1(a) shows how the longitudinal magneto-resistivity $\rho \propto V_{xx}$ of the CrO_2 Hall bar changes upon microwave irradiation, for **H** in the film plane. When the microwave source is "off", one observes the typical negative low-field magneto-resistance of CrO_2 [13, 14]. When the microwave source is turned "on" to an output power level of 200 mW, ρ increases by about 30% (see Fig. 1(a)), and a broad resonant structure appears around $\mu_0 H_{\rm res} = 163$ mT. This structure is the signature of FMR in the electrical resistance. Figure 1(b) shows the conventional FMR signal, recorded simultaneously with the magneto-resistance. Because we use magnetic field modulation, the FMR signal amplitude $I_{\rm FMR} \propto (\partial \chi''/\partial H) \sqrt{P_{\rm MW}}$ scales with the first derivative of the imaginary part of the magnetic susceptibility, and with the incident microwave power $P_{\rm MW}$. As indicated in Fig. 1(b), at least four different FMR modes can be resolved around $\mu_0 H_{\rm res} \approx 160$ mT. Rameev *et al.* reported similar observations in their FMR study of CrO_2 films, and attributed the resonances to spin wave modes [15, 16]. To allow for a direct comparison between the conventional FMR signal and the microwave-induced resistivity changes, we have plotted the resistivity data under microwave irradiation from Fig. 1(a) as the difference quotient $I_{\rm EDFMR} = \Delta\rho/\Delta H$ in Fig. 1(b). In this representation, the peaked structure around $\mu_0 H_{\rm res} = 163$ mT in the magneto-resistance can be unambiguously identified as an electrically-detected ferromagnetic resonance (EDFMR) [2–4]. Note that all FMR modes in the conventional FMR signal are reproduced in the EDFMR trace with good fidelity. The slight discrepancies in signal shape and intensity between EDFMR and FMR are due to the bolometric nature of the EDFMR signal, as discussed below.

Upon microwave irradiation, the sample temperature T increases by ΔT, resulting in a corresponding change $\Delta\rho$ in resistivity. This bolometric effect can be written as [17]

$$\Delta\rho = \left(\frac{\partial\rho}{\partial T}\right) \Delta T = \left(\frac{\partial\rho}{\partial T}\right) \frac{P_{\rm abs}\, \tau}{C}, \qquad (1)$$

with the microwave power $P_{\rm abs} \propto P_{\rm abs}$ absorbed by the sample, the thermal relaxation time constant τ between sample and environment, and the heat capacity C of the sample. A purely bolometric EDFMR signal should thus obey $I_{\rm EDFMR} \propto \Delta\rho \propto (\partial_T \rho)\, P_{\rm MW}$, with $\partial_T \rho = \partial\rho/\partial T$. Indeed, we show in Fig. 1(c) that the EDFMR signal amplitude increases linearly with $P_{\rm MW}$ over more than two decades, as also observed by others [3, 4]. Simultaneously, the amplitude of the FMR signal increases as $\sqrt{P_{\rm MW}}$ (Fig. 1(c)), as expected for conventional FMR below saturation. The line widths of both the FMR and the EDFMR signals of the CrO_2 Hall bar sample are constant within experimental error for 1 mW $\leq P_{\rm MW} \leq$ 200 mW.

To further test the validity of Eq. (1), we now consider the influence of $\partial_T \rho$ on the EDFMR signal. CrO_2 is a good metal [13, 14], with $\partial_T \rho > 0$ around room temperature (Fig. 1(f)). A temperature increase $\Delta T > 0$ due to the absorption of microwave (in either a resonant or a non-resonant process) should thus lead to $\Delta\rho > 0$. Both the non-resonant and the resonant *increase* of ρ upon microwave irradiation of the CrO_2 sample shown in Fig. 1(a) are thus straightforwardly explained. In contrast to CrO_2, Fe_3O_4 has $\partial_T \rho < 0$ (Fig. 1(f)) [18], so that

both non-resonant and resonant microwave absorption should result in a resistance *decrease*. This is indeed the case (Fig. 1(d)): ρ decreases non-resonantly when the microwave source is switched on, with an additional, dip-like decrease around a resonance field $\mu_0 H_{\rm res} \approx 170$ mT for **H** in the film plane. The EDFMR and the conventional FMR signals closely match, as evident from Fig. 1(e) for the external magnetic field both parallel and perpendicular to the Fe_3O_4 film. The sign of the microwave-induced resistivity changes thus corresponds to $\partial_T \rho$, as expected for a bolometric effect. While we can only speculate about the microscopic origin of the non-resonant Joule heating effect, eddy currents or cyclotron resonance probably contribute.

The microwave-induced resistivity changes respond slowly to temperature changes. The agreement between FMR and EDFMR spectra shown in Figs.1(b) and (d) is only obtained if the magnetic field is swept at a rate of 1 mT/s or slower. In faster sweeps, the shape of the EDFMR signal is strongly distorted, showing that long time constants of the order of seconds must be relevant for the EDFMR. The non-resonant, microwave-induced changes in ρ also exhibit such a slow response. When the microwave power level is abruptly changed, ρ exponentially decays to the new resistance value, with time constants of several seconds. These observations suggest that in Eq. (1), C is the heat capacity of the sample, and $\tau = C/G$ is determined by the thermal conductance G between sample and heat sink.

In addition to EDFMR in the longitudinal resistivity ρ, we also have observed EDFMR in the Hall signal or transverse voltage $V_{\rm trans}$ in CrO_2 (Fig. 2). In these experiments, the external magnetic field was applied perpendicular to the film plane. To exclude spurious longitudinal resistance contributions in the Hall signal, we measured $V_{\rm trans}$ for both magnetic field polarities, and antisymmetrized the corresponding traces to obtain $V_{\rm Hall}(H) = \{V_{\rm trans}(H) - V_{\rm trans}(-H)\}/2$. We again observe a clear non-resonant increase in $V_{\rm Hall}$ upon microwave irradiation (Fig. 2). Additionally, a peak appears around $\mu_0 H_{\rm res} = 998$ mT, the field at which conventional FMR is observed in this sample for this magnetic field orientation.

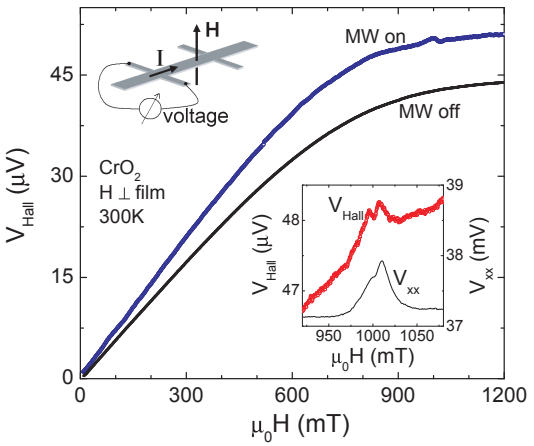

Figure 2: The Hall voltage $V_{\rm Hall}(H)$ of the CrO_2 Hall bar at room temperature increases upon microwave irradiation, with an additional resonant increase around the FMR at $\mu_0 H_{\rm res} = 998$ mT. In the inset, the EDFMR signals in the longitudinal and the transverse (Hall) signals are compared.

To address the mechanism leading to this Hall-EDFMR signal, we recall that the Hall voltage $V_{\rm Hall} = (R_0 \mu_0 H + R_{\rm A} M_z) I/d$ in a ferromagnetic film of thickness d comprises both the ordinary and the anomalous Hall effect [19]. The ordinary Hall coefficient R_0 is inversely proportional to the carrier density. The anomalous Hall voltage $V_{\rm AHE} = R_{\rm A} M_z I/d$ depends on the magnetization component M_z perpendicular to the sample, and the anomalous Hall coefficient $R_{\rm A} = c\rho^{\alpha}$ usually scales with the resistivity [19], with material-dependent constants c and α. In CrO_2, $R_{\rm A} M_z \gg R_0 \mu_0 H$ and $\alpha \lesssim 2$ for temperatures $T > 100$ K [13, 20]. This is confirmed by conventional magneto-transport experiments in our samples, which yield $1.4 \leq \alpha \leq 1.6$. Using $V_{\rm Hall} \approx c\rho^{\alpha} M_z I/d$, Eq. (1) gives

$$\frac{\Delta V_{\rm Hall}}{V_{\rm Hall}} = \frac{(\partial V_{\rm Hall}/\partial T)\,\Delta T}{V_{\rm Hall}} = \alpha \frac{\Delta \rho}{\rho} + \frac{\Delta M_z}{M_z}, \tag{2}$$

with $\Delta M_z = (\partial M_z/\partial T)\,\Delta T$. If the relative resonant change in magnetization $\Delta M_z/M_z$ is small, one has $\Delta V_{\rm Hall}/V_{\rm Hall} \approx \alpha \Delta\rho/\rho$, so that the value of α can be directly extracted from EDFMR measurements.

In CrO_2 at room temperature, however, $\Delta M_z/M_z$ can not be neglected. SQUID magnetometry experiments on a larger piece of the same CrO_2 sample give $\partial_T M_z/M_z = (-4 \pm 2) \times 10^{-3} \mathrm{K}^{-1}$ in the relevant temperature and magnetic field range, while conventional resistance measurements yield $\partial_T \rho/\rho = (8 \pm 1) \times 10^{-3}$ K^{-1}. With these values and $\alpha = 1.5$, one expects $\partial_T V_{\mathrm{Hall}}/V_{\mathrm{Hall}} = (8 \pm 3) \times 10^{-3}$ K^{-1} according to Eq. (2), closely matching $\partial_T V_{\mathrm{Hall}}/V_{\mathrm{Hall}} = (6 \pm 1) \times 10^{-3}$ K^{-1} experimentally determined from the conventional magneto-transport data. The EDFMR measurements quantitatively corroborate this picture. The Hall-EDFMR trace shown in Fig. 2 corresponds to $\frac{\Delta V_{\mathrm{Hall}}}{V_{\mathrm{Hall}}} \approx 1.1\%$, while $\frac{\Delta V_{\mathrm{Hall}}}{V_{\mathrm{Hall}}} = \frac{\Delta \rho}{\rho} \approx 1.6\%$ for similar conditions (see the inset of Fig. 2). The ratio $\frac{\Delta \rho}{\rho} / \frac{\Delta V_{\mathrm{Hall}}}{V_{\mathrm{Hall}}} \approx 1.5$ thus determined from EDFMR agrees well with $\frac{\partial_T \rho}{\rho} / \frac{\partial_T V_{\mathrm{Hall}}}{V_{\mathrm{Hall}}} \approx 1.3$ obtained from conventional magneto-transport. These numbers also show that the temperature increase in resonance is a few Kelvin at most, warranting the use of Eqs. (1) and (2) a posteriori.

In conclusion, we have investigated the magneto-resistance properties of thin ferromagnetic CrO_2 and Fe_3O_4 films under microwave irradiation. Both the resistivity ρ and the Hall voltage V_{Hall} characteristically change when ferromagnetic resonance (FMR) occurs in the film. The electrically-detected ferromagnetic resonance (EDFMR) spectra closely match the conventional FMR, measured simultaneously, in both resonance fields and line shapes. This demonstrates that EDFMR is spectroscopically equivalent to FMR. The sign and the magnitude of the EDFMR signals $\Delta\rho/\rho$ and $\Delta V_{\mathrm{Hall}}/V_{\mathrm{Hall}}$ can be consistently described as a Joule heating effect. Taken together, EDFMR thus is a powerful tool for the investigation of magnetic anisotropy and magneto-resistive phenomena in ferromagnetic thin films and could allow the detailed study of micro- and nanostructures too small to be investigated by conventional FMR.

The work at the University of Alabama was supported by National Science Foundation MR-SEC Grant No. DMR0213985, the work at the Walter Schottky Institut by the Deutsche Forschungsgemeinschaft (SFB 631).

References

[1] W. G. Egan and H. J. Juretschke, J. Appl. Phys. **34**, 1477 (1963).
[2] M. Toda, Appl. Phys. Lett. **17**, 1 (1970).
[3] K. Kaski, P. Kuivalainen, and T. Stubb, J. Appl. Phys. **49**, 1595 (1978).
[4] Y. S. Gui, S. Holland, N. Mecking, and C. M. Hu, Phys. Rev. Lett. **95**, 056807 (2005).
[5] M. R. Britel, D. Ménard, L. G. Melo, P. Ciureanu, A. Y. R. W. Cochrane, M. Rouabhi, and B. Cornut, Appl. Phys. Lett. **77**, 2737 (2000).
[6] J. Moreland, M. Löhndorf, P. Kabos, and R. D. McMichael, Rev. Sci. Instrum. **71**, 3099 (2000).
[7] J. Schmidt and I. Solomon, Compt. Rend. **263**, 169 (1966).
[8] J. N. Chazalviel and I. Solomon, Phys. Rev. Lett. **29**, 1676 (1972).
[9] M. S. Brandt, S. T. B. Goennenwein, T. Graf, H. Huebl, S. Lauterbach, and M. Stutzmann, phys. stat. sol. (c) **1**, 2056 (2004).
[10] G. Miao, G. Xiao, and A. Gupta, Phys. Rev. B **71**, 094418 (2005).
[11] R. S. Keizer, S. T. B. Goennenwein, T. M. Klapwijk, G. Miao, G. Xiao, and A. Gupta, Nature **439**, 825 (2006).
[12] D. Reisinger, B. Blass, J. Klein, J. B. Philipp, M. Schonecke, A. Erb, L. Alff, and R. Gross, Appl. Phys. A **77**, 619 (2003).
[13] S. M. Watts, S. Wirth, S. Molnar, A. Barry, and J. M. D. Coey, Phys. Rev. B **61**, 9621 (2000).
[14] K. Suzuki and P. M. Tedrow, Phys. Rev. B **58**, 11597 (1998).
[15] B. Z. Rameev, A. Gupta, A. Anguelouch, G. Xiao, F. Yildiz, L. R. Tagirov, and B. Aktas, J. Magn. Magn. Mater. **272-276**, 1167 (2004).
[16] B. Z. Rameev, R. Yilgin, B. Aktas, A. Gupta, and L. R. Tagirov, Microel. Eng. **69**, 336 (2003).
[17] F. Neppl, J. P. Kotthaus, and J. F. Koch, Phys. Rev. B **19**, 5240 (1979).
[18] D. Reisinger, P. Majewski, M. Opel, L. Alff, and R. Gross, Appl. Phys. Lett. **85**, 4980 (2004).
[19] R. C. O'Handley, *Modern Magnetic Materials: Principles and Applications* (John Wiley, New York, 2000).
[20] H. Yanagihara and M. B. Salamon, Phys. Rev. Lett. **89**, 187201 (2002).

Multiferroic materials based on artificial thin film heterostructures

S. Geprägs, M. Opel, S. T. B. Goennenwein, and R. Gross [1]

Recent advances in understanding the coexistence of different ferroic ordering phenomena (such as ferroelectricity and ferromagnetism) together with the progress in the preparation techniques for bulk and thin film materials triggered a tremendous research activity on so-called multiferroic materials [1]. The combination of ferroelectricity and ferromagnetism in novel multi-functional materials is particularly interesting, since this would allow to realize new functionalities in electronic and magnetic devices, such as the electric field control of magnetisation. Unfortunately, it turned out that there are very few ferroelectric/ferromagnetic multiferroics because the standard microscopic mechanisms driving ferroelectricity and ferromagnetism are incompatible. They usually require empty and partially filled transition metal orbitals, respectively [2]. This has initiated the search for other mechanisms favouring the coexistence of ferroelectricity and magnetic order as, for example, in $HoMnO_3$. An alternative approach for the realization of multiferroics is the use of two component multiferroic thin film heterostructures [3, 4]. The double perovskite Bi_2CrFeO_6 (BCFO) for example could be build up from $BiFeO_3$ (BFO) and $BiCrO_3$ (BCO) perovskites. To realise such superlattices with new material properties, one must be able to grow e.g. BCO and BFO layers only one monolayer thick in an alternating sequence.

The compound $BiFeO_3$ itself is considered as a good candidate for multiferroicity at room temperature. It is both ferroelectric ($T_C = 1103\,\mathrm{K}$) and antiferromagnetic ($T_N = 643\,\mathrm{K}$) [5]. Unfortunately it seems to be difficult to achieve a large spontaneous polarisation comparable to that of ferroelectric compounds with similar T_C. The crystal structure of thin films and its relation to the ferroelectric properties also is ambiguous. Bulk bismuth ferrite crystallises in a rhombohedrally distorted perovskite structure ($a^r = 5.6343\,\text{Å}$, $\alpha^r = 59.348°$) [6]. Therefore, it has a lattice mismatch of 1.4% with respect to the $SrTiO_3$ substrate ($a^c = 3.905\,\text{Å}$). Thus, epitaxial BFO films grown on STO (001) substrates may be considerably strained depending on the thickness and the growth mode. The detailed knowledge of the strain state of BFO is important, since recent experimental [7] and theoretical [8] reports suggested that BFO thin films show enhanced ferroelectric and ferromagnetic properties at room temperature due to epitaxial coherency strain causing a tetragonal or monoclinic crystal symmetry. However, also this observation is discussed controversially [9]. $BiCrO_3$ is another promising candidate for multiferroic and magnetoelectric thin film systems. Bulk BCO was synthesised already in the 1960s and found to have a triclinic structure with $a = b = 3.90\,\text{Å}$, $c = 3.87\,\text{Å}$, $\alpha = \beta = 90.55°$, and $\gamma = 89.15°$ [10]. The in-plane lattice constant is perfectly matched to that of STO with a lattice mismatch as small as about 0.1%. For bulk material, theoretical considerations predicted a *G*-type antiferromagnetic ground state with an anti-ferrodistortive structural distortion [11]. Polycrystalline samples were also found to show a structural phase transition from a non-centrosymmetric to a centrosymmetric structure at 410 K and a parasitic ferromagnetic ordering below 114 K [12]. However, until now there are only very few studies of the ferroelectric properties, and almost no attempts have been made to grow high quality epitaxial films [13].

Thin film growth and characterization

We have grown *c*-axis oriented epitaxial $BiFeO_3$ (BFO) and $BiCrO_3$ (BCO) films by laser molecular beam epitaxy on (001) $SrTiO_3$ (STO) substrates [3]. The pulsed laser

[1] This work is supported by the DFG via priority program SPP1157 (project No.: GR 1132/13).

deposition was performed using a KrF excimer laser (248 nm) and $Bi_{1.15}MO_3$ (with M=Fe, Cr) targets to prevent Bi deficiency inside the films. During deposition the growth process has been monitored by in-situ reflection high-energy electron diffraction (RHEED). For both materials the growth process (optimal parameters) was performed in pure O_2-atmosphere at a pressure of 8×10^{-3} Torr and a substrate temperature $T_S = 540°C$. The energy density of the laser at the target was $\rho_E = 2\,J/cm^2$ and the laser repetition rate varied between $f_L = 0.5$ and 10 Hz, depending on the growth mode.

Fig. 1 shows the RHEED patterns and intensity oscillations of the $(0,0)$ peak for different growth modes of $BiFeO_3$. Prior to deposition, the RHEED pattern shows the characteristic sharp diffraction spots on the corresponding Laue circle as expected for a very flat $SrTiO_3$ surface. For continuous growth with $f_L = 2$ Hz at too low substrate temperature $T_S = 460°C$, the RHEED intensity oscillations rapidly damp out and the RHEED pattern turns into a transmission like pattern expected for Stranski-Krastanov growth (see Fig. 1a). This growth mode results in a large surface roughness unsuitable for heterostructures. The situation can be improved by using the optimum deposition temperature $T_S = 540°C$ and applying the so-called imposed layer-by-layer interval deposition technique, where the material for a complete unit cell is supplied by a rapid sequence of laser pulses (6-7 pulses at $f_L = 10$ Hz) followed by a break of $\delta = 20$ s allowing the film to relax. As

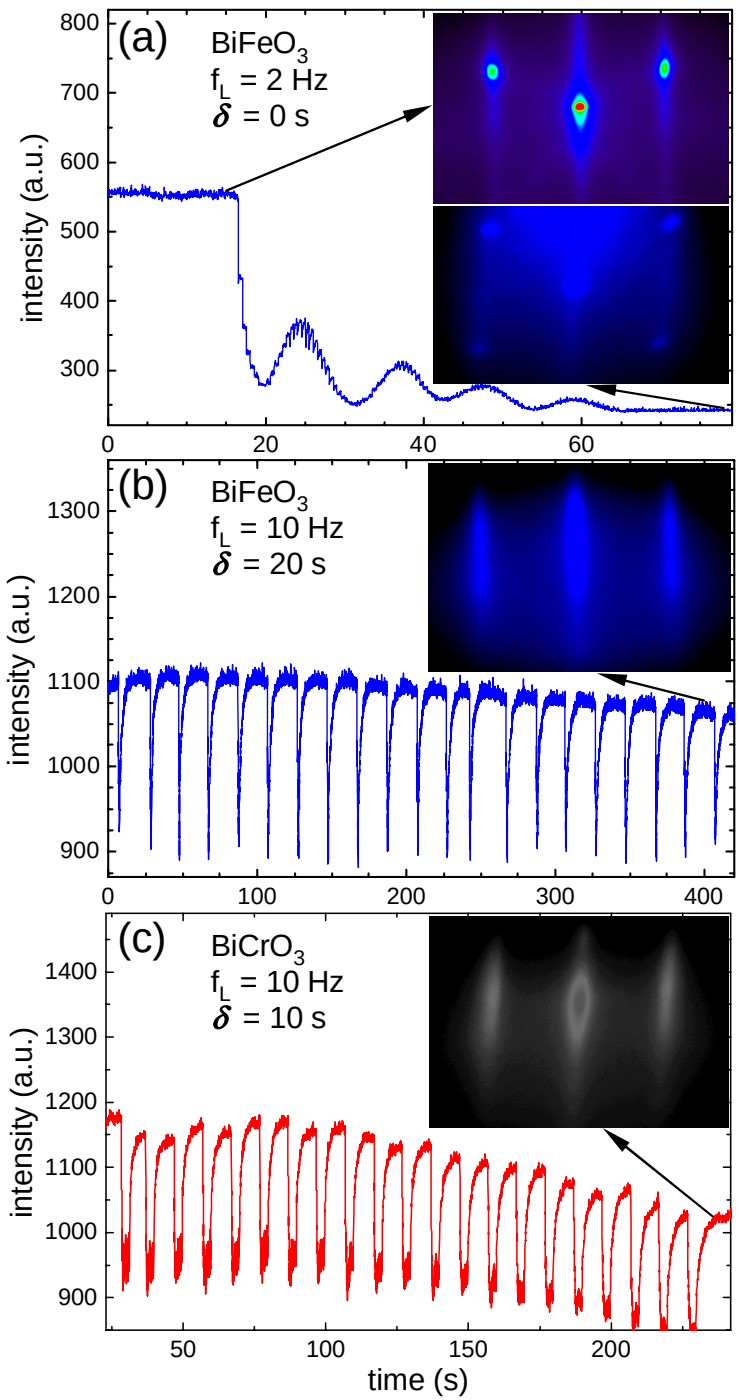

Figure 1: RHEED patterns and RHEED intensity oscillations during the deposition of $BiFeO_3$ ((a) and (b)) and $BiCrO_3$ (c) on $SrTiO_3$ (001) substrates. (a) Continuous deposition of BFO ($\delta = 0$ s) at $f_L = 2$ Hz and $T_S = 460°C$. The inset shows the RHEED patterns of the $SrTiO_3$ substrate (top) and the $BiFeO_3$ film after the deposition of about 4 unit cells. (b) Imposed layer-by-layer interval deposition of BFO at $T_S = 540°C$ with $f_L = 10$ Hz and $\delta = 20$ s. The inset shows the RHEED pattern of the BFO film after the deposition of about 20 unit cells. (c) Imposed layer-by-layer interval deposition of BCO at $T_S = 540°C$ with $f_L = 10$ Hz and $\delta = 10$ s. The inset shows the RHEED pattern of the BCO film after the deposition of about 30 unit cells.

shown by Fig. 1b, in this case the RHEED intensity stays about constant and the slightly streaky RHEED pattern indicates tow-dimensional growth. A layer-by-layer growth mode resulting in a flat surface also could be achieved by a slow growth process with $f_{\mathrm{L}} = 0.5\,\mathrm{Hz}$ at $T_S = 540°\mathrm{C}$. The optimum deposition conditions for the BCO films are about identical to those of BFO. Fig. 1c shows the RHEED intensity oscillations and the RHEED pattern measured during the interval deposition of BCO ($f_L = 10\,\mathrm{Hz}$, $\delta = 10\,\mathrm{s}$, $T_S = 540°\mathrm{C}$). In the same way as for BFO a two-dimensional layer-by-layer growth mode is achieved resulting in a flat surface.

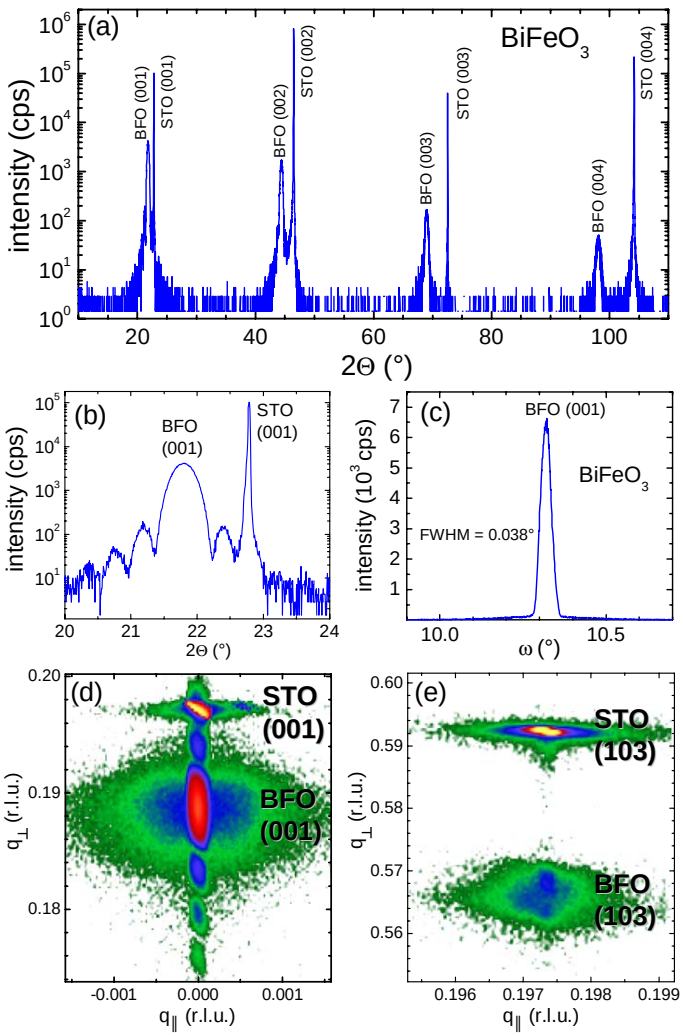

Figure 2: (a) ω-2θ scan, (b) ω-2θ scan around the (001) peak, and (c) rocking curve of the (001) peak for a 22 nm thick BFO film grown on a STO (001) substrate. In (d) and (e) reciprocal space maps around the (001) and (103) peak are shown.

Fig. 2 shows the result of the x-ray analysis of a 22 nm thick BFO film grown on a STO (001) substrate. In addition to a ω-2θ scan, a rocking curve of the (001) peak, and reciprocal space maps around the (001) and (103) peak are shown. From the positions of the (00ℓ) reflections, we derive an out-of-plane lattice parameter $c = 4.082\,\text{Å}$, which is about independent of film thickness up to the maximum film thickness of 40 nm in our study and considerably larger than the pseudocubic lattice parameter of BFO. This is caused by the compressive in-plane coherency strain causing an increase of the out-of-plane lattice parameter. The in-plane lattice constant of BFO was found to perfectly agree with that of the STO substrate demonstrating that the BFO films are coherently strained up to a film thickness of 40 nm. The small surface roughness and coherent growth of the BFO films is evident from the observation of Laue oscillations (see Fig. 2b). The FWHM of the rocking curves of the (001) peak was found to be below 0.04°. This small value demonstrates the high epitaxial quality of our films. We also measured the in-plane epitaxial relations between film and substrate by recording ϕ-scans. We found $\langle 001\rangle_{\mathrm{STO}} \| \langle 001\rangle_{\mathrm{BFO}}$ using a pseudocubic lattice.

In Fig. 2(d) and (e) we show reciprocal space maps around the (001) and (103) Bragg peaks. The (001) reflection of the film is a single peak (with satellites due to Laue oscillations) showing that the c-axis of the film is well defined in both length and orientation. The large peak width in ℓ direction results from the small film thickness. The map around the (103) reflection shows no indication of any splitting suggesting a tetragonal rather than a monoclinic or rhombohedral symmetry of the BFO film. This is in agreement with the data of Béa *et al.* [14] but in contrast to several other studies [15, 16].

Fig. 3 shows the result of the x-ray analysis of a BCO film grown on a STO (001) substrate. The ω-2θ scan shows only (00ℓ) reflections. The c-axis lattice parameter is determined to $c = 3.880$ Å, the a-axis lattice constant corresponds to that of the STO substrate ($a = 3.905$ Å). The slightly reduced out-of-plane lattice parameter indicates that the epitaxial film is under small tensile biaxial strain. The rocking curves of the (001) reflections show a FWHM of around 0.04°, again demonstrating the high epitaxial quality of our BCO films. Fig. 3(b) and (c) show reciprocal space maps around the (002) and (103) Bragg peaks. As for BFO, the (002) reflection of the BCO film is a single peak showing that the c-axis of the film is well defined in both length and orientation. The map around the (103) reflection shows no splitting suggesting a tetragonal rather than a triclinic symmetry as reported recently [13]. This may be caused by different strain states of the studied films.

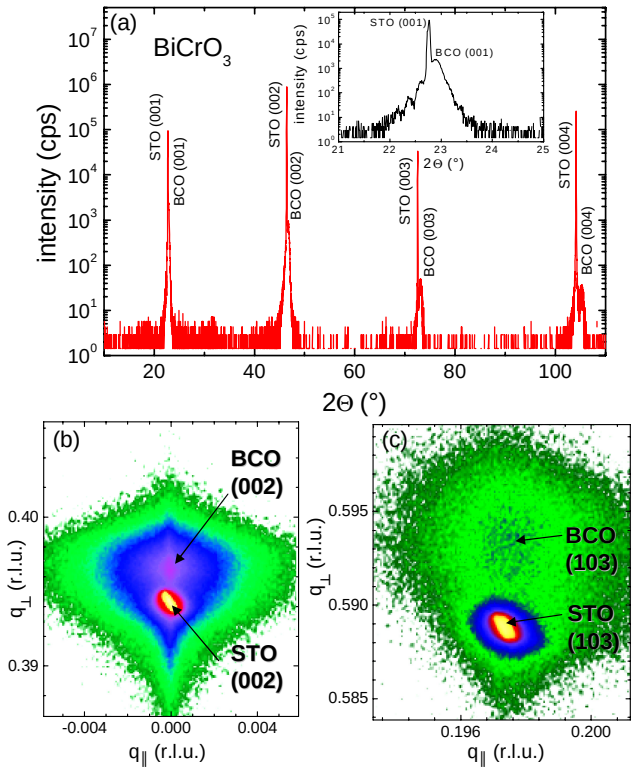

Figure 3: (a) ω-2θ scan of an epitaxial BCO film grown on a STO (001) substrate. The inset shows the region around the (001) peak on an enlarged scale. In (b) and (c) reciprocal space maps around the (002) and (103) peak are shown.

Magnetic properties

Fig. 4(a) shows the magnetisation curves from epitaxial BFO and BCO films grown on STO (001) substrates. The saturation magnetisation measured for these films is very small and typically ranges between about 0.02 and 0.04 μ_B per formula unit (f.u.). For BCO films we observe a larger coercive field than for BFO films. The significant scatter in the data is caused by the very small sample volume bringing the absolute value of the magnetisation close to the resolution

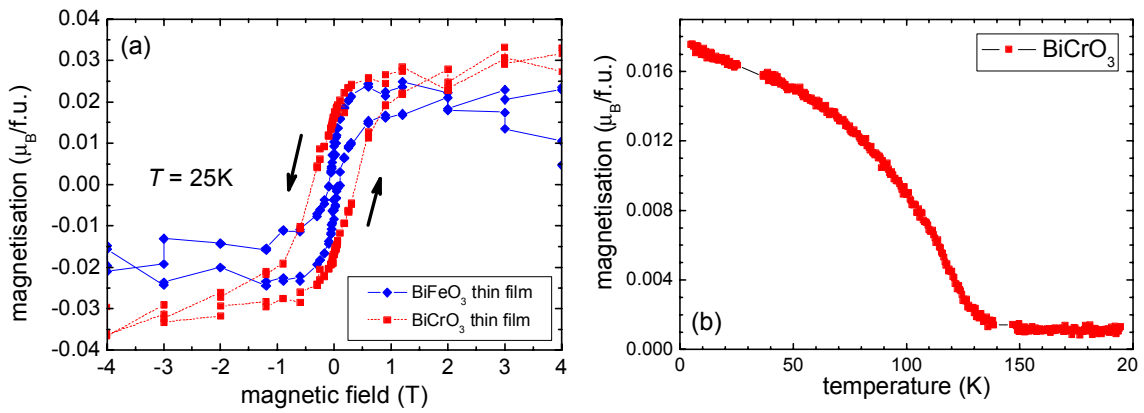

Figure 4: (a) Magnetisation versus applied magnetic field for an epitaxial BFO and BCO thin film at 25 K. (b) Magnetisation versus temperature for a BFO film. The data are taken in zero applied field with increasing temperature after field cooling in 7 T.

limit of the SQUID magnetometer. For both materials the observed magnetic properties are consistent with the picture that the Fe or Cr spins are coupled antiferromagnetically and that a slight canting of the spins gives rise to a weak ferromagnetism [8, 18]. The only difference between BFO and BCO is the fact that for BFO ferromagnetism sets in already well above room temperature, whereas for our BCO films a critical temperature of only about 135 K is observed (see Fig. 4(b)). We note that this value of the ordering temperature is slightly larger than the ones reported recently for BCO [12, 13]. So far it is not clear whether this is related to the small tensile strain in our BCO films. If this would be the case, epitaxial coherency strain would provide a promising way to increase the ordering temperature of BCO.

For BFO there is still a controversial discussion of the measured saturation magnetisation [9]. In particular, a strong interest in BFO was triggered by the observation of room-temperature multiferroic behavior with large magnetisation (1 μ_B/f.u.) and polarisation ($\sim 50 - 60\,\mu$C/cm^2) [7]. The small magnetisation obtained in our study on strained BFO films cannot confirm the large values of up to 1 μ_B/ formula unit reported by Wang *et al.* [7] for relaxed BFO films. However, our data are in full agreement with other recent reports on strained BFO films [9, 17] and also with density functional calculations [8]. This suggests that epitaxial strain does not enhance the magnetisation in BFO films as initially believed. This conclusion is further supported by our observation that the saturation magnetisation is very similar for highly strained BFO and almost unstrained BCO films. We finally note that the small magnetisation values observed for our BCO films confirm the small value reported recently by Murakami *et al.* [13].

Summary

We have successfully grown epitaxial BFO and BCO thin films with very high structural quality and small surface roughness in a two-dimensional layer-by-layer growth mode using laser molecular beam epitaxy. These films are promising for the realization of artificial multiferroic and magnetoelectric thin film heterostructures. Due to epitaxial coherency strain both BFO and BCO films have tetragonal crystal structure in contrast their bulk counterparts. For both BFO and BCO films only a small saturation magnetisation below about 0.05 μ_B/f.u. were found in contrast to previous reports. Furthermore, no indication for a strain induced enhancement of magnetisation could be observed.

References

[1] M. Fiebig, J. Phys. D **38**, R123 (2005).
[2] N.A. Hill, J. Phys. Chem. B **104**, 6694 (2000).
[3] S. Gepraegs, M. Opel, S.T.B. Goennenwein, and R. Gross, Phil. Mag. Lett., *accepted for publication* (2006).
[4] N.A. Spaldin and M. Fiebig, Science **309**, 391 (2005).
[5] G. A. Smolenskii and I. E. Chupis, Sov. Phys. Usp. **25**, 475 (1982).
[6] F. Kubel and H. Schmid, Acta Crystallogr. B **46**, 698 (1990).
[7] J. Wang *et al.*, Science **299**, 1719 (2003).
[8] C. Ederer and N.A. Spalding, Phys. Rev. B **71**, 060401(R) (2005).
[9] W. Eerenstein *et al.*, Science **307**, 1203a (2005).
[10] F. Sugawara *et al.*, J. Phys. Soc. Jpn. **25**, 1553 (1968).
[11] N.A. Hill, J. Phys. Chem. B **106**, 3383 (2002).
[12] S. Niitaka *et al.*, Solid State Ionics **172**, 557 (2004).
[13] M. Murakami *et al.*, Appl. Phys. Lett. **88**, 152902 (2006).
[14] H. Béa *et al.*, Appl. Phys. Lett. **88**, 062502 (2006).
[15] J. Li *et al.*, Appl. Phys. Lett. **84**, 5261 (2004).
[16] X. Qi *et al.*, Appl. Phys. Lett. **86**, 071913 (2005).
[17] H. Béa *et al.*, Appl. Phys. Lett. **87**, 072508 (2005).
[18] C. Ederer and N.A. Spalding, Phys. Rev. B **71**, 224103 (2005).

Fabrication of aluminum based superconducting quantum circuits

T. Heimbeck, S. Dandl, M. Goeppl, A. Marx, and R. Gross [1]

Extrapolating the ever shrinking size of logic gates in classical semiconductor logic circuits, the few atom dimension will be approached within the near future. Obviously, in this size regime quantum effects become dominant and a classical description of the involved logic circuits in no longer possible. Whereas we already make use of quantum effects such as level quantization or quantum tunneling in our today's information and communication systems, information processing is still based on purely classical grounds. However, over the last two decades it has been shown that quantum information systems based on quantum mechanical principles would have a large variety of advantages such as an exponential speed-up of some numerically expensive tasks because of the inherent quantum-parallelism or secure communication. In contrast to classical computers, where the elementary piece of information is a classical bit which can take either of two discrete values ("0" or "1"), the basic element of a quantum computer, the quantum bit (qubit, corresponding to a quantum two-level system) can take any superposition of the two basis states. For solid-state physicists an important task is to develop a hardware platform for implementing quantum information systems. A promising choice are superconducting quantum circuits. Therefore, we have developed fabrication techniques for such circuits. Here, we report on the fabrication of Al based superconducting quantum circuits fabricated by electron beam lithography and shadow evaporation techniques.

Up to now qubits already have been realized by several groups in a variety of different microscopic systems, for example ion traps [1], nuclear spins [2] or neutral atoms [3]. This systems have disadvantages regarding scaling to complex systems. In contrast, solid-state qubits (e.g. based on quantum dots [4] or superconducting circuits [5]) are implemented using well-established techniques for micro- and nanofabrication, thus inherently providing the potential of scaling to systems with a large number of qubits. However, their disadvantage is significant decoherence due to the coupling to environmental degrees of freedom. In this respect, superconducting systems are promising since here the energy gap separates the ground state from the electronic excitations. Among the different versions of superconducting qubits that have been proposed and realized so far, the flux qubit consisting of a superconducting ring interrupted by an odd number of Josephson junctions is a promising candidate. Here, the quantum two-level system is defined by the clockwise and counterclockwise circulating current states in the ring. One way

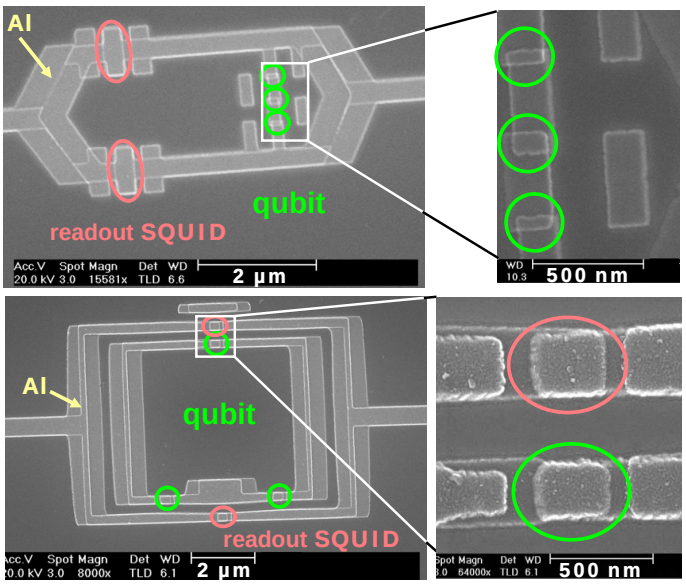

Figure 1: SEM micrograph of two different superconducting flux qubits. The upper part shows a flux qubit with directly coupled readout dc-SQUID, whereas in the lower part the readout SQUID is inductively coupled to the qubit. The red circles mark the Josephson junctions in the readout dc-SQUID, whereas the green circles mark the qubit junctions.

[1]This work is supported by the DFG through the Cooperative Research Center 631.

to readout the state of a flux qubit is to use a dc-SQUID to detect the magnetic flux associated with the different current states.

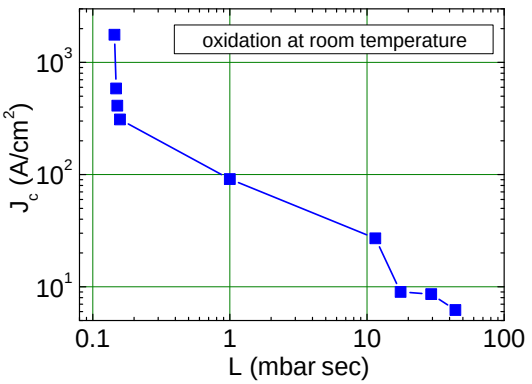

Figure 2: Critical Josephson current density J_c of several Josephson junctions plotted versus the product $L = p_{O_2} t_{ox}$ of the oxygen pressure and the oxidation time.

Figure 1 shows SEM micrographs of two different versions of superconducting three junction flux qubits fabricated at the WMI. The qubit is either directly or inductively coupled to the hysteretic readout dc-SQUID. The dc-SQUID is connected to the readout electronics via two bias lines extending to the left and the right in Fig. 1. The qubit is biased by an external magnetic flux close to the degeneracy point, corresponding to half a flux quantum threading the qubit loop. In Fig. 1 the circles mark the Josephson junctions, which are the basic components of these superconducting quantum devices.

A simple analysis for the optimum junction parameters for flux qubit shows that the dimensions of the Josephson junctions have to be in sub-μm range. Thus electron beam lithography is required to well define the junction area. The thin aluminum films are deposited using the well established shadow evaporation technique. This technique has the advantage that the whole junction can be fabricated without breaking vacuum using evaporation under different angles through the openings of a free-standing resist mask. This results in the typical double structures shown in Fig. 1. The oxide layer, which separates the two Al junction electrodes and defines the tunneling barrier, is produced by an in-situ thermal oxidation step after the deposition of the Al base electrodes.

For flux qubits the value of the Josephson coupling energy, which is proportional to the critical Josephson current density J_c, is a key design parameter. Since J_c depends exponentially on the oxide barrier thickness, the precise control of the barrier thickness is a key issue. Therefore, we have measured the dependence of J_c on the oxidation parameters by fabricating a large number of Josephson junctions with different values of the product $L = p_{O_2} t_{ox}$ of the oxygen pressure p_{O_2} and the oxidation time t_{ox}. The result is shown in Fig. 2, where we have plotted J_c versus L. Evidently, over a large range of L we have a well defined $J_c(L)$ dependence, allowing the reproducible fabrication of junctions with J_c-values up to about 500 A/cm^2.

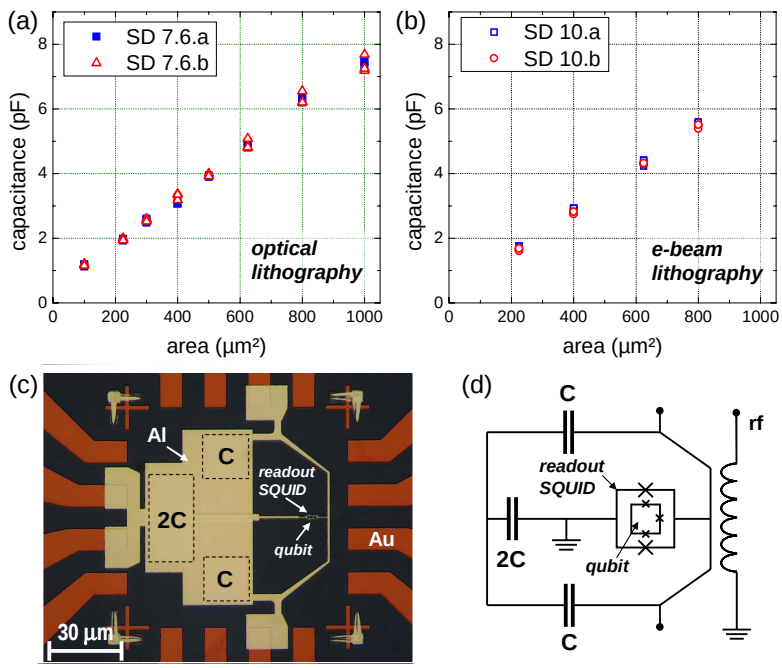

Figure 3: Capacitance vs. area for Al/AlO$_x$/Al capacitors fabricated by (a) optical and (b) electron beam lithography. (c) shows and optical micrograph of a complete circuit including a flux qubit, and a C-shunted readout dc-SQUID. (d) shows the corresponding equivalent circuit.

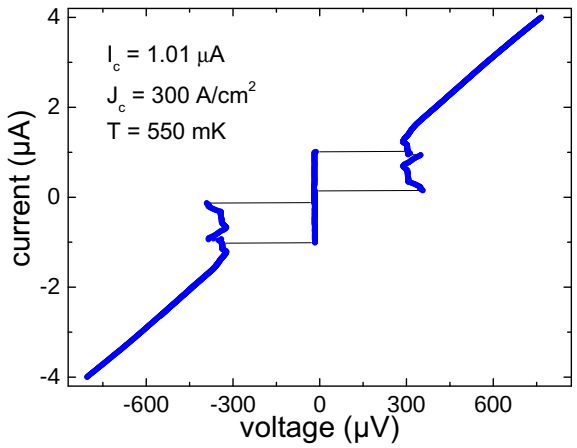

Figure 4: Current-voltage characteristics of a readout dc-SQUID enclosing a three-junction flux qubit. The SQUID is shunted by on-chip capacitors.

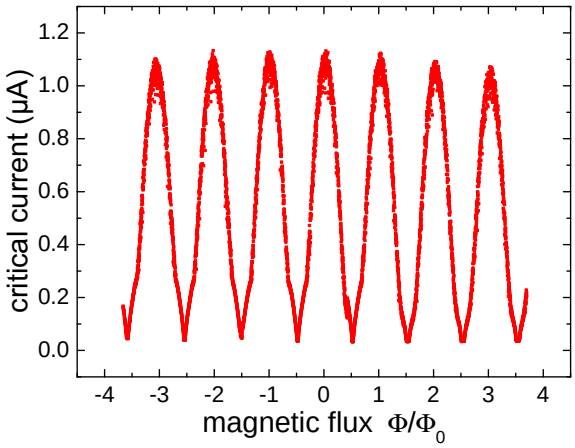

Figure 5: Critical current of the dc-SQUID of Fig. 4 plotted versus the normalized applied magnetic flux at $T = 550\,\mathrm{mK}$.

To protect flux qubits from external noise introduced via the leads connected to the readout dc-SQUID, the readout dc-SQUID can be shunted by on-chip capacitors. We have successfully realized on-chip $Al/AlO_x/Al$ trilayer capacitors. A thick AlO_x layer resulting in a low enough leakage current of the capacitors could be realized by an ex-situ thermal oxidation process, which includes an oxidation at ambient atmosphere for 3 hours at $T = 100°C$. In Figs. 3a and b we have plotted the capacitance of these planar capacitors versus the capacitor area. A nice linear scaling is obtained demonstrating the good control of our fabrication process. The specific capacitance was determined to $8\,\mathrm{fF}/\mu\mathrm{m}^2$ and the leakage resistance was larger than $100\,\mathrm{M}\Omega$ up to an area of $1000\,\mu\mathrm{m}^2$.

For the shunting capacitors of the readout dc-SQUIDs typical capacitance values in the 5 pF range are required. First flux qubit structures surrounded by a *C*-shunted readout dc-SQUIDs have already been fabricated (see micrograph in Fig. 3c). Here, the shunting capacitors have been defined by electron beam lithography. Fig. 4 shows the hysteretic IVC of a *C*-shunted readout dc-SQUID measured at 550 mK in a ^{3}He insert. Fig. 5 shows the dependence of the SQUID critical current on the applied external magnetic flux. An almost ideal pattern with a large modulation depth is found.

In summary, we have developed a process for the reproducibly fabrication of sub-μm sized Josephson junctions with quite well-defined critical current densities. These junctions are well-suited for the realization of superconducting flux qubits. Furthermore, we succeeded to fabricate on-chip shunting capacitors with well defined capacitance values and low leakage currents to shield superconducting flux qubits from the influence of the electromagnetic environment.

References

[1] D. Leibfried, R. Blatt, C. Monroe, and D. Wineland, Rev. Mod. Phys. **75**, 281 (2003).
[2] D. Cory, A. Fahmy, and T. Havel, Proc. Natl. Acad. Sci. USA **94**, 1634 (1997).
[3] P.W.H. Pinske, P. Maunz, T. Fischer, and G. Rempe, Nature **404**, 365 (2000).
[4] E. Beham, M. Betz, S. Trumm, M. Kroutvar, Y. Ducommun, H.J. Krenner, M. Bichler, A. Leitenstorfer, J.J. Finley, A. Zrenner, and G. Abstreiter, phys. stat. sol. (c) **1**, 2131 (2004).
[5] J. E. Mooij, T. P. Orlando, L. Levitov, L. Tian, C. H. van der Wal, and S. Lloyd, Science **285**, 1036 (1999).

Fabrication of superconductor/insulaor/ferromagnet/superconductor (SIFS) Josephson junctions

G. Wild, A. Marx, R. Gross [1]

For the implementation of solid-state quantum information processing superconducting quantum circuits are very promising. In superconducting qubits the energy gap separates the ground state of the condensate from the excited quasiparticle states thus reducing decoherence. Up to now different types of superconducting quantum bits (flux, charge and phase qubits) have been realized and coherence times up to the μs range have been achieved. Our activities are focusing on superconducting flux qubits, which are formed by a superconducting ring interrupted by an odd number of Josephson junctions. In these flux qubits, the states with clockwise and counterclockwise circulating screening currents define the quantum two-level system forming the qubit. For the operation of the standard three-junction flux qubit [1] an external flux bias of half a flux quantum (flux degeneracy point) is required making these qubits susceptible for flux noise. To circumvent this problem it has been proposed to use π-phase shift elements which would allow to implement "quiet" qubits with an optimum protection from external fluctuations [2–6]. Here, a π-phase shift element is inserted into the qubit loop, which formally replaces the phase shift due to half a flux quantum threading the loop.

Suitable π-phase shift elements can be realized by π–Josephson junctions (π-JJs), which involve thin ferromagnetic interlayers and have a π phase difference between the superconducting junction electrodes in their ground state [7–12]. The origin of the π phase shift is the finite momentum $Q \propto h_{ex}/v_F$ of Cooper pairs penetrating into the ferromagnetic layer. Here, h_{ex} is the exchange splitting between the spin up and down bands and v_F the Fermi velocity. The finite momentum results in a spatial oscillation of the superconducting order parameter $\Psi \propto \cos(2Qx)$ along the direction x perpendicular to the SF interface. At an appropriate thickness of the ferromagnetic layer the order parameter can change sign resulting in a π phase shift across the insulating barrier in the ground state [8], which has been confirmed recently by experiment [9–11]. Here, we report on the fabrication of superconductor/(insulator)/ferromagnet/superconductor (SIFS) π-JJs. In SIFS junctions the electrical transport through the ferromagnetic layer is established by correlated electron-hole pairs (formally generated by Andreev reflections at the SF boundaries). The additional tunneling barrier (I) reduces the critical current I_c, however, at the same time increases the junction normal resistance R_n and thus leaves the I_cR_n product of the junction unchanged. The main effect of insulating layer is to increase the quality factor $Q \propto \sqrt{I_cR_n^2C}$ of the junction. Here, C is the junction capacitance. Hence, in contrast to SFS type junctions without insulating barrier, SIFS type junctions show less dissipation what is required for quantum circuits. Indeed, we recently could

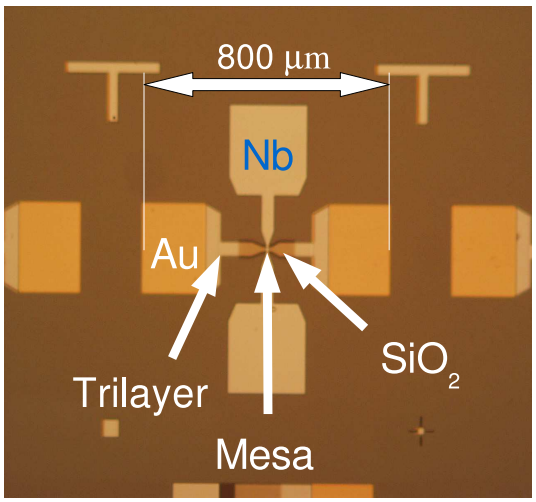

Figure 1: Optical micrograph of a $5\,\mu m \times 5\,\mu m$ SIFS Josephson junction fabricated with a so-called self-aligned process including gold wiring. The marked niobium layer indicates the top electrode of the trilayer structure.

[1] This work is supported by the DFG through the Cooperative Research Center 631.

observed for the first time macroscopic quantum behavior of the phase difference φ in SIFS π-JJs (see report by Madek *et al.*).

For the fabrication of SIFS type Josephson junctions we have developed a self-aligned multilayer process. In a first optional step a gold wiring layer is defined. This layer provides bonding pads for the subsequent multilayer structure consisting of a 85 nm niobium base electrode, 4 nm aluminum, a few nm thick ferromagnetic $Ni_{18}Pd_{82}$ layer, and a 50 nm thick niobium top electrode. The complete layer structure is deposited in-situ by dc-magnetron sputtering. The 4 nm thick Al layer is partly oxidized for 60 min (junction in Fig. 4) and 90 min (junctions in Fig. 3) in a pure oxygen atmosphere of 0.107 mbar. The Nb and NiPd layers are sputtered in pure Ar atmosphere. The sputtering rates are 0.7 nm/s for Nb (at 2.7×10^{-3} mbar and 200 W), 0.2 nm/s for Al (at 2.7×10^{-3} mbar and 200 W), and 0.4 nm/s for $Ni_{18}Pd_{82}$ (at 2.0×10^{-2} mbar and 40 W). For defining the junction area, a mesa structure is etched into the Nb top electrode using optical lithography and reactive ion etching (RIE). The removed material is replaced by SiO_2 deposited by rf-sputtering. Here, the resist stencil of the RIE process is used for the lift-off process of the SiO_2 layer. To improve the coverage of the mesa edges by SiO_2 and thereby to prevent shorts between the bottom electrode and the wiring layer of the top electrode, an intermediate resist ashing step is introduced just after the RIE process to etch back the resist stencil behind the mesa edges prior to the SiO_2 sputtering process. In this way the insulating SiO_2 layer nicely covers the mesa edges as shown in Fig. 2. Finally, the wiring of the top electrode consisting of a 250 nm thick Nb layer is deposited.

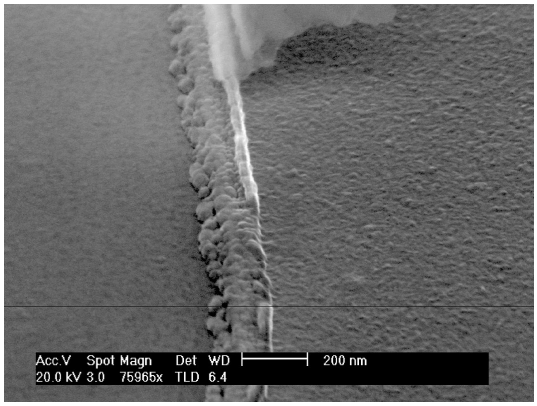

Figure 2: SEM micrograph showing the edge of the SiO_2 layer surrounding the mesa structure in the SIFS stack after SiO_2-liftoff. The SiO_2 layer is required for the insulation of the wiring of the top electrode. By introducing an additional resist ashing step after the RIE etching process, a tunable overlap of the SiO_2 layer (left hand side) over the mesa (right hand side) is achieved preventing shorts.

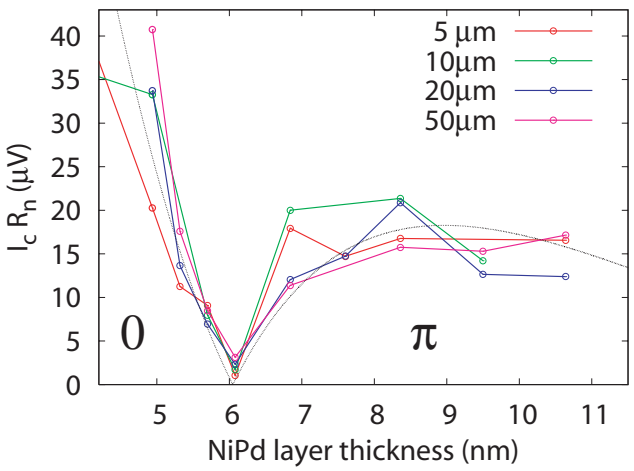

Figure 3: Critical current vs. thickness of the ferromagnetic interlayer for square shaped SIFS junctions with different lateral dimensions (5, 10, 20, 50 μm). The dotted line shows the theoretical dependence according to [8] for the parameters $\xi_f = 3.85$ Å and $\pi\Delta^2/eT_c = 270\,\mu$V.

The quality of the interfaces between the individual layers strongly influences the junction quality and the reproducibility of the fabrication process. Therefore, it is essential to minimize time interval between the niobium and aluminum sputtering step to avoid any oxidation of the highly reactive Nb surface. In our process the period between the deposition of both materials is less then 10 s at a background oxygen partial pressure of less than 10^{-9} mbar). Another crucial point is the surface roughness of the Nb base electrode and the NiPd layer. By optimization of the sputtering parameters the surface roughness has been improved as confirmed by in-situ noncontact atomic force microscopy after completion of the individual layers. We obtained rms roughness

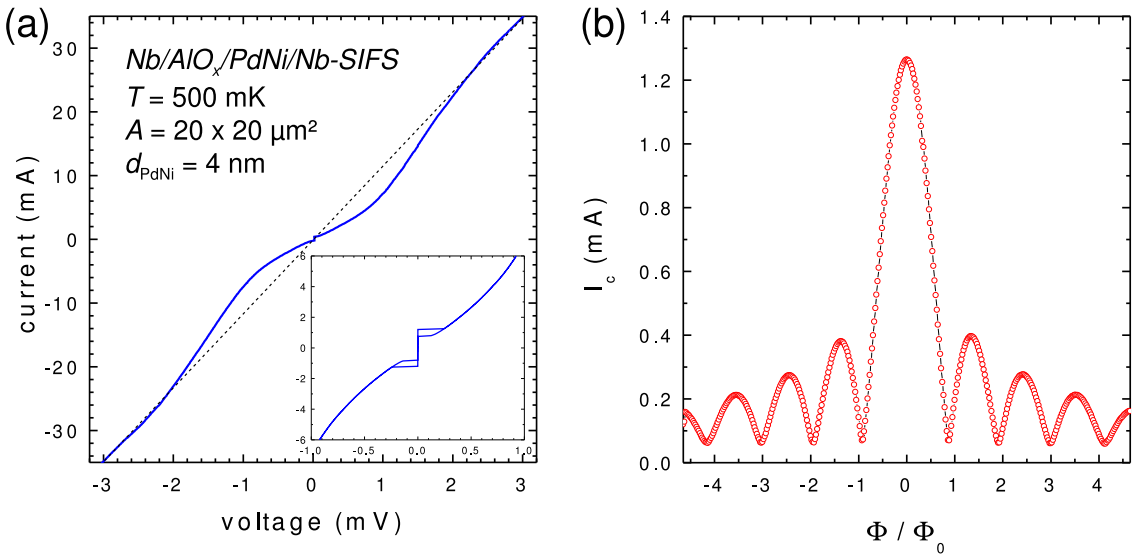

Figure 4: (a) Current-voltage-characteristics (IVC) and (b) magnetic field dependence of the critical current I_c measured for a $20 \times 20\,\mu\text{m}^2$ $Nb/AlO_x/Pd_{0.82}Ni_{0.18}/Nb$ (SIFS) Josephson junction at $T = 500\,\text{mK}$. The inset shows the inner part of the IVC on an enlarged scale. The dashed line marks the ohmic line determined by the normal resistance R of the junction.

values of 2.5 Å for the substrate, 5 Å for the niobium base electrode, 6 Å for the oxidized aluminum layer, and finally 8.5 Å for an additional 6 nm thick $Ni_{18}Pd_{82}$ layer.

The characteristic thickness of the ferromagnetic layer determining the crossover from a 0- to a π-junction was obtained by measuring the critical currents and the I_cR_n products of a large number of junctions with different thickness of the $Ni_{18}Pd_{82}$ layer. Fig. 3 shows the dependence of I_cR_n product of square shaped junctions with lateral dimensions of 5, 10, 20, and 50 μm on the thickness of the ferromagnetic $Ni_{18}Pd_{82}$ layer. Evidently, the I_cR_n product decreases up to about 6 nm and increases again for large thickness values. Since in the experiment only the modulus of the critical current can be determined, the observed behavior can be associated with a decreasing positive valued critical current in the 0-state crossing over to a negative critical current value in the π-state. The dotted line in Fig. 3 shows the theoretical dependence according to [8] calculated for the parameters $\xi_f = 3.85$ Å and $\pi\Delta^2/eT_c = 270\,\mu$V.

References

[1] J. E. Mooij, T. P. Orlando, L. Levitov, L. Tian, C. H. van der Wal, and S. Lloyd, Science **285**, 1036 (1999).
[2] L. B. Ioffe *et al.*, Nature (London) **398**, 679 (1999).
[3] G. Blatter, V. B. Geshkenbein, and L. B. Ioffe, Phys. Rev. B **63**, 174511 (2001).
[4] M. H. S. Amin *et al.*, Phys. Rev. B **71**, 064516 (2005).
[5] T. Yamashita, K. Tanikawa, S. Takahashi, and S. Maekawa, Phys. Rev. Lett. **95**, 097001 (2005).
[6] T. Yamashita, S. Takahashi, and S. Maekawa, Appl. Phys. Lett. **88**, 132501 (2006).
[7] A. I. Buzdin, L. N. Bulaevskii, and S. V. Panyukov, JETP Lett. **35**, 179 (1982).
[8] A. I. Buzdin, Rev. Mod. Phys. **77**, 935 (2005).
[9] V. V. Ryazanov *et al.*, Phys. Rev. Lett. **86**, 2427 (2001); see also J. Low Temp. Phys. **136**, 385 (2004).
[10] T. Kontos *et al.*, Phys. Rev. Lett. **89**, 137007 (2002).
[11] A. Bauer *et al.*, Phys. Rev. Lett. **92**, 217001 (2004).
[12] M. Weides, M. Kemmler, H. Kohlstedt, R. Waser, D. Koelle, R. Kleiner, and E. Goldobin, Phys. Rev. Lett. 97, 247001 (2006).

Sampling the phase diagram of the cuprate superconductors

Andreas Erb and Michael Lambacher [1]

In 2004 the DFG (Deutsche Forschungsgemeinschaft) founded the research unit FOR 538: "Doping Dependence of Phase Transitions and Ordering Phenomena in Cuprate Superconductors", which initially consisted of 7 different projects, one of which is "Crystal Growth of p and n-doped cuprate superconductors". The goal of this project is the growth and characterization of high purity single crystals of the high temperature superconductors to provide samples for different spectroscopic experiments within FOR 538. By the end of 2006 the renewed proposal for the Research Unit was not only reviewed positively, but was even enlarged and now consists of 9 projects. The project crystal growth within the research unit is of particular importance in the sense, that it provides the common sample basis to the different experimental projects. Only such a common sample basis of high quality single crystals of the cuprates makes the comparison of the results obtained by the various experimental techniques reliable.

Accessible sample space

In order to cover the whole phase diagram of the high temperature superconductors, which is one of the central ideas of this research unit, crystals with well defined and homogeneous doping of both, the p and n-doped compounds need to be grown. On the hole doped side of the phase diagram we focused on the systems of $YBa_2Cu_3O_{7-\delta}$ and $Bi_2Sr_2CaCu_2O_8$. There are restrictions in the accessible doping regime for the $YBa_2Cu_3O_{7-\delta}$ even when co-doping with Ca is applied (see Fig. 1).

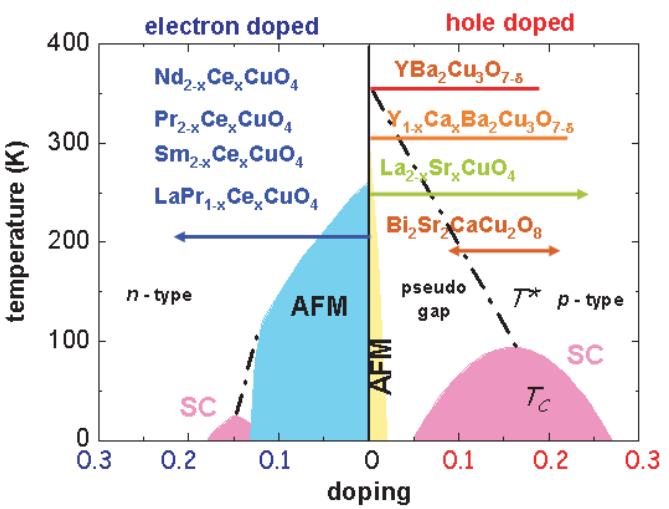

Figure 1: Accessible doping regime in the phase diagram for the different compounds of the high temperature superconductors.

For the $Bi_2Sr_2CaCu_2O_8$ system one is actually limited to a relatively small region around optimal doping. For this reason we have started to grow single crystals of the $La_{2-x}Sr_xCuO_4$ system, since they can be used to access the reminder part of the phase diagram as well as it is possible to access the whole doping range of the hole doped side by using one compound only. Moreover, they allow a more direct comparison of the n- and p-doped side of the phase diagram, due to the similarity of both the critical temperature and the structure with the electron doped 214-compounds.

For the electron doped side of the phase diagram only 214-compounds are available to probe the phase diagram. We concentrated our efforts on the crystal growth of $Pr_{2-x}Ce_xCuO_4$, $Nd_{2-x}Ce_xCuO_4$ $Sm_{2-x}Ce_xCuO_4$ or mixtures such as $LaPr_{1-x}Ce_xCuO_4$.

[1] This work is supported by the DFG through the Research Unit FOR538.

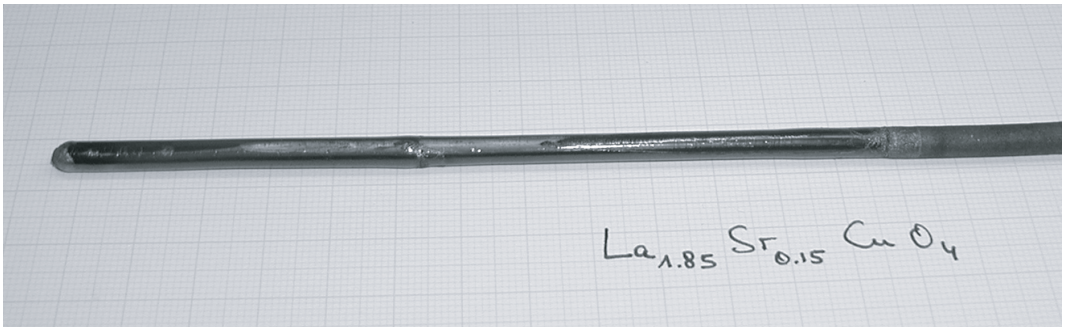

Figure 2: Single crystal of $La_{2-x}Sr_xCuO_4$ grown in the mirror furnace at WMI. The last about 6 cm on the left end of the sample are formed by a single crystallite.

Research status

There are several families of cuprate superconductors. However, by materials or technical reasons there are only a few families that are suitable for achieving the goals of our research unit. There are the following compounds of the high temperature superconductors, from which a set of high quality single crystals with different doping level can be produced:

- $YBa_2Cu_3O_{7-\delta}$:

  Due to the peculiarities of the phase diagram (the small solubility in the solvent) of the 123-compounds, high quality crystals of the 123-compounds without solvent inclusions have to be grown in a crucible. Due to the highly reactive melts of the CuO-BaO flux system all usual refractory crucible materials are heavily corroded by the flux and the crystals grown in such experiments were contaminated by the crucible material. The problem has been solved with the development of the adapted crucible material $BaZrO_3$ [1, 2], in which crystals with a purity of up to 99.995 % can be grown. In general it should be remarked that due to the perfection of the available crystals the stoichiometric compound $YBa_2Cu_3O_{7-\delta}$ would be the ideal sample system for a systematic study of high temperature superconductors. However, unfortunately some regions in the overdoped range can not be accessed by this compound. Furthermore, $YBa_2Cu_3O_{7-\delta}$ does not cleave easily, which makes the use of this compound more complicated for techniques requiring cleaved surfaces such as angle resolved photo emission.

- Bi-2212 ($Bi_2Sr_2CaCu_2O_8$):

  Besides the 123-compounds, the Bi-based family of high temperature superconductors with 3 different compounds are interesting candidates for sample systems for the coordinated work within our research unit. The family consists of the following three members: the single layer compound $Bi_2Sr_2CuO_6$ with a transition temperature of T_c up to 40 K, the double layer compound $Bi_2Sr_2CaCu_2O_8$ with T_c around 96-98 K and the 3-layer compound $Bi_2Sr_2Ca_2Cu_3O_{10+\delta}$ with a T_c of around 110 K. While the first crystals of these compounds have been grown from the flux with the same problem of crucible corrosion like in $YBa_2Cu_3O_{7-\delta}$, meanwhile the development of crystal growth in mirror furnaces has made the use of crucibles obsolete and has led to a considerable improvement of the crystal quality in these systems. Nevertheless, the crystal quality is limited by the intergrowth of the three superconducting phases and by a partial solubility of Bi on Sr sites. The optimization of the growth parameters [3–6] has led to a pronounced improvement of the crystal quality in the last years. In particular, for the double layer compound Bi-2212 high quality crystals of several grams and with low defect concentration can be grown

using the zone melting technique in a mirror furnace. Due to the fact that this compound cleaves very easily perpendicular to the *c*-direction, samples of this system are ideal for angle resolved photo emission spectroscopy and other surface sensitive spectroscopies used within the research unit. However, as already stated above crystals of large size and good crystalline quality are only obtained in a narrow region around optimal doping.

- 214-Systems ($La_{2-x}Sr_xCuO_4$, $Nd_{2-x}Ce_xCuO_4$ and $Pr_{2-x}Ce_xCuO_4$):

  The so-called 214-systems with the compounds $La_{2-x}Ba_xCuO_4$ and $La_{2-x}Sr_xCuO_4$ have been the first cuprate superconductors discovered. [7] Starting from the antiferromagnetic compounds Re_2CuO_4 doping with Sr^{2+} on the hole doped side or with Ce^{4+} on the electron doped side leads to the formation of solid solutions, which become superconducting at certain doping levels. The formation of simple solid solutions in these compounds makes them in principle very attractive as a basis of a sample set. However, on the other hand, the formation of solid solutions makes it quite difficult or even impossible to grow big homogeneous samples in crucibles. This is caused by the fact that the distribution coefficient of the dopant is unequal to unity, which obviously leads to concentration gradients of the dopant during the growth process. Fortunately, this problem has been greatly overcome by the development of the TSFZ-method (travelling solvent floating zone). With this method large and homogeneous crystals of the 214-compounds can be grown (see Fig. 2), especially in long lasting growth experiments, when the equilibrium state for the dopant concentration has been reached within the solvent.

  - *$La_{2-x}Sr_xCuO_4$:*

    This hole doped compound has some particular advantages compared to the other hole doped systems such as $YBa_2Cu_3O_{7-\delta}$ and $Bi_2Sr_2CaCu_2O_8$, which are the most promising systems for the sample set on the hole doped side of the phase diagram. Firstly, the doping range that is in principle accessible with this compound extends from the undoped antiferromagnet to the overdoped metal. In this way, basically the whole doping regime of the hole doped side of the phase diagram of the cuprates can be accessed by using only a single compound. Secondly, the critical temperature as well as the structure is similar to the electron doped compounds $Nd_{2-x}Ce_xCuO_4$ and $Pr_{2-x}Ce_xCuO_4$, which are considered in this project to serve as the sample basis for the study the electron doped side of the phase diagram of the high T_c superconductors. Certainly, there are also some shortcomings for this compound. In particular, compared to the $Bi_2Sr_2CaCu_2O_8$ system it is much more difficult to cleave them, thereby hampering their use for ARPES experiments. Nevertheless, first experiments have shown that it is possible to cleave them. For the Raman and infrared spectroscopies first experiments have shown that measurements are possible using single crystals with extremely fine polished surfaces. Finally, since large $La_{2-x}Sr_xCuO_4$ crystals with a weight of several grams (see Fig. 2) can be produced in very good quality, they are ideal samples for the inelastic neutron scattering experiments.

  - *$Nd_{2-x}Ce_xCuO_4$ and $Pr_{2-x}Ce_xCuO_4$:*

    Similar arguments as for $La_{2-x}Sr_xCuO_4$ also apply for the electron doped compounds. Upon doping with Ce^{4+} solid solution crystals are formed up to the solubility limit of the different compounds. However, superconductivity exists only in a narrow range of cerium concentrations, e.g. between $x = 0.14$ and $x = 0.17$ in the $Nd_{2-x}Ce_xCuO_4$ compound [8]. The width of this doping regime is known to depend on the rare earth ion. In these materials one of the most striking properties

is that Ce-doping alone is insufficient. In addition, removal of oxygen is a necessary step to achieve superconducting samples. Usually this is done by annealing the samples at elevated temperatures in a low pressure oxygen environment. The way this reduction procedure is performed can lead to different transition temperatures [9] and ultimately can lead to unstable samples that decompose with time. The recipes for both the growth of the crystals as well as for oxygen reduction [9–12] differ between the different groups working in this field. The preparation of big, well-defined and stable crystals of these compounds was and partially remains one of the most challenging parts of our work.

– *$LaPr_{1-x}Ce_xCuO_4$:*
Since the magnetic moment of Nd^{3+} hampers the use of the Nd-214 compound in various experiments and a solubility limit of $x = 0.15$ for Ce^{4+} has been found in the Pr-214 compound, the system of $LaPr_{1-x}Ce_xCuO_4$ might be a solution to access the further overdoped region of the electron doped side of the phase diagram. The superconducting region within this system seems to have a broader doping range and neither the La nor Pr ions have a magnetic moment. Therefore, we will also try to grow single crystals of $LaPr_{1-x}Ce_xCuO_4$.

Own previous work

Within the last years the crystal growth laboratory at the Walther-Meißner-Institut has been further extended and the applied crystal growth techniques have been considerably refined to improve the quality of the fabricated single crystals. Moreover, the methods for the characterization of the single crystals have been improved and broadened. For example, the possibility to orient the crystals of the 214-compounds has been brought to high perfection. It is possible to orient to a precision of better then 0.5° and to ultra fine polish the surfaces to a perfection that Raman and infrared spectroscopies can be performed on such samples. This important work has been performed using also the facilities of the crystal laboratory of the Department of Physics (TUM), which is headed by A. Erb.

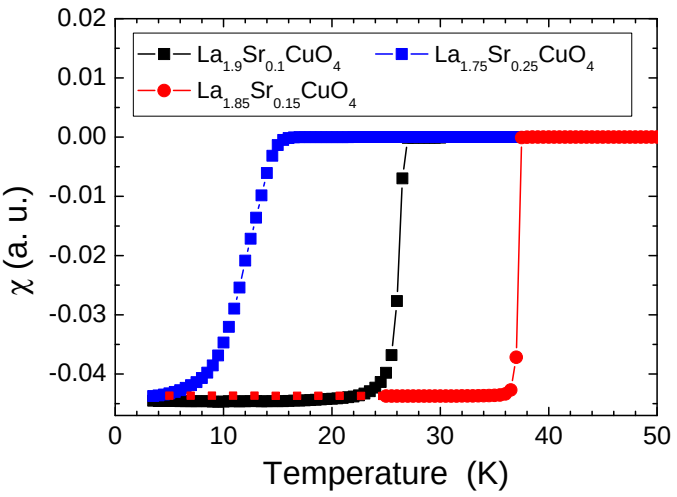

Figure 3: Transition curves of various $La_{2-x}Sr_xCuO_4$ single crystals. The optimally doped one consists of a 588 mg (about 6 mm long disc) piece of the single crystal of $La_{2-x}Sr_xCuO_4$, shown in Fig.2

The production of the particularly important $BaZrO_3$ crucibles has been improved, leading to a higher success rate of the growth of the 123-compounds and thus to a higher output of samples. For the growth process both flux growth in crucibles and crucible free growth using the TSFZ-technique have been applied. The flux growth method of $YBa_2Cu_3O_{7-\delta}$ out of $BaZrO_3$-crucibles [1, 2], which so far has been accomplished only by a few other groups worldwide, meanwhile has been developed to the standard method for the growth of $YBa_2Cu_3O_{7-\delta}$ crystals with highest purity. Moreover, several special methods to homogenize the oxygen distribution and thus the doping homogeneity in the samples have been developed. These developments

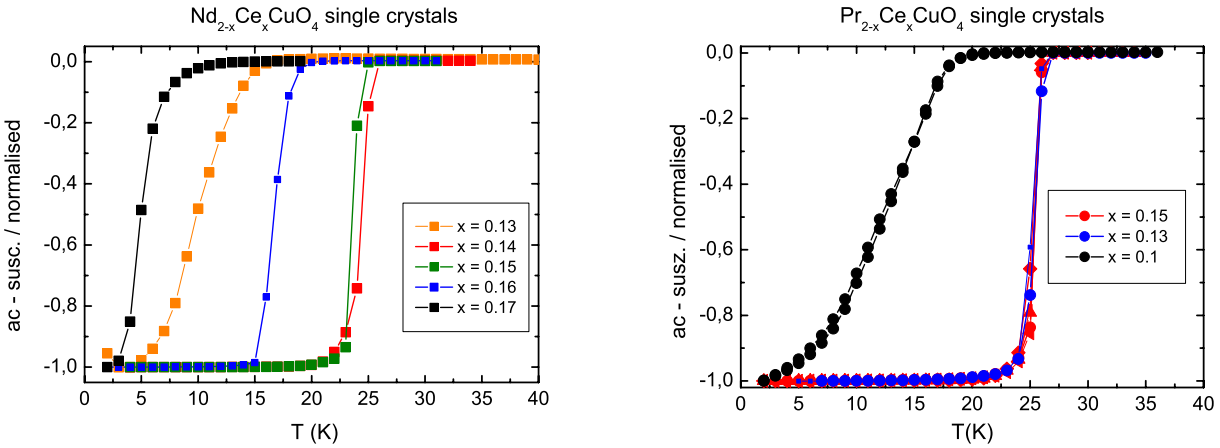

Figure 4: Normalized ac susceptibility plotted versus temperature for several $Nd_{2-x}Ce_xCuO_{4-\delta}$ (left) and $Pr_{2-x}Ce_xCuO_{4-\delta}$ (right) single crystals with different doping level.

and the resulting improved sample quality had considerable effects on the physical properties of the samples, like for instance on the flux pinning [13] or the general behavior of the vortex state [14–16] of the high temperature superconductors. The basis of these developments was an intensive study of oxygen diffusion [17, 18] and oxygen ordering.

For the other compounds the TSFZ technique has been used for the growth of single crystals and brought to high perfection. In particular, the use of different values of the oxygen partial pressure for the growth atmosphere during the growth of crystals with different doping concentrations has led to much more stable growth conditions and thus to a higher perfection (typical values of the mosaic spread are below 0.07° for the electron doped 214-compounds and 0.03° for $La_{2-x}Sr_xCuO_4$) and bigger size (up to 6 grams in the case of $La_{2-x}Sr_xCuO_4$) of the crystals.

Results

In the following we summarize the status achieved recently for the growth of the various high-T_c compounds.

- $YBa_2Cu_3O_{7-\delta}$

  We have grown Ca-doped $Y_{1-x}Ca_xBa_2Cu_3O_{7-\delta}$ crystals with various doping concentration from the undoped ($x = 0$) compound up to a Ca-concentration of $x = 0.14$ in intervals of 0.02. These crystals have been used in various experiments within and outside [19] of the research unit. These studies (Raman and infrared spectroscopy) were mainly focussed on the underdoped region $\delta = 1$ and have brought new insight in the phenomena of the formation of stripes in this compound.

- $Bi_2Sr_2CaCu_2O_8$

  For the $Bi_2Sr_2CaCu_2O_8$ system the main activity was dedicated to the growth of Ni- and Zn-doped samples, which have been used again in various activities within the research group [20]. These crystals reach several cm in length and about 8 mm in diameter and can therefor also be used in neutron experiments. Upon doping with Yttrium on the Ca-site the crystals tend to become smaller in size and the superconducting transitions, which are sharp for the undoped system as well as for Ni-doped samples, tend to become

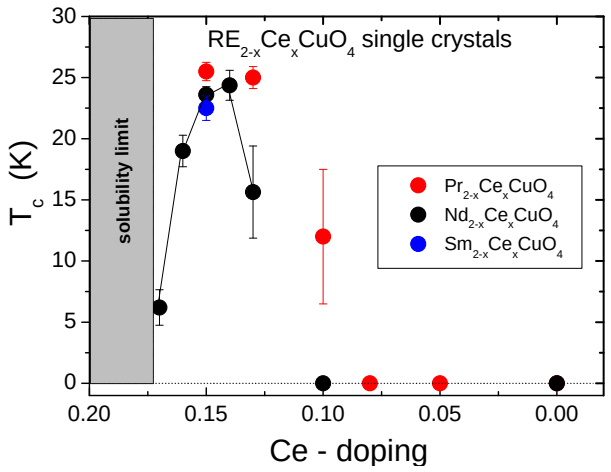

Figure 5: Transition temperatures for various $RE_{2-x}Ce_xCuO_4$ single crystals.

broader with increasing Y-doping. This indicates a spatially inhomogeneous distribution of the Y dopant atoms. To improve the situation, probably the use of different oxygen partial pressure during growth might lead to more homogeneous samples with narrower superconducting transition. To achieve this improvement is especially important for the ARPES experiments on the underdoped side of the phase diagram.

- 214-systems: $La_{2-x}Sr_xCuO_4$, $Nd_{2-x}Ce_xCuO_4$ and $Pr_{2-x}Ce_xCuO_4$

  Within the first period of the project extensive work on the crystal growth of the 214-compounds has been performed. Especially the growth of high quality 214-single crystals on the electron doped side of the phase diagram is very challenging as has already been outlined above. In our systematic study of the growth process we learned that depending on the desired doping level an adapted oxygen partial pressure has to be used for the growth atmosphere. This led to a much better stability of the growth conditions and, in turn, to a higher perfection and larger size of the crystals.

- $La_{2-x}Sr_xCuO_4$

  Our work on the $La_{2-x}Sr_xCuO_4$ compound was started only in the 3rd year of the first project period. Nevertheless, a rapid progress in the crystal growth of this compound was possible due to the broad experience with the electron doped 214-systems. Already the first experiments have led to very big (several grams) and homogeneous single crystals of this compound (see Fig. 2). The crystals with optimal doping have a transition temperature of $T_c = 37.5\,K$ with a transition width of less than 1 K [21](see Fig. 3). Up to now we have produced crystals in the doping range of x = 0, 0.15, 0.2, 0.25. Crystals of the optimally doping have been distributed to various members of the research unit and abroad. They are currently under investigation.

- $Nd_{2-x}Ce_xCuO_4$, $Pr_{2-x}Ce_xCuO_4$

  Single crystals of the compounds $Nd_{2-x}Ce_xCuO_4$ and $Pr_{2-x}Ce_xCuO_4$ have been successfully grown within the first period of the project. The stability of the growth conditions have been found to strongly depend on oxygen partial pressure and doping for these compounds. After optimization of the growth conditions we reproducibly obtain large single crystals of these compounds. For optimally doped samples of $Nd_{2-x}Ce_xCuO_4$ and $Pr_{2-x}Ce_xCuO_4$ the maximum transition temperatures are $T_c = 23.5\,K$ and $T_c = 25.5\,K$, respectively, which are the highest T_c values reported so far [22]. In both cases the transition

width was only about 1 K (see Fig. 4). Crystals of the whole series of $Nd_{2-x}Ce_xCuO_4$ and $Pr_{2-x}Ce_xCuO_4$ compounds from the antiferromagnet up to the solubility limit of Cerium, which has been found to be $x = 0.18$ and $x = 0.15$, respectively, have been grown. The crystals have also been proven to be absolutely stable over more than one year without any sign of decomposition. Both the chemical stability and the good superconducting properties were achieved by an optimization of the conditions for the critical annealing process, which is necessary to remove the interstitial oxygen from the crystals after the growth process. On well oriented samples with extremely fine polished surfaces successful Raman- and infrared spectroscopy experiments have been performed. For the ARPES experiments it was possible to cleave the samples. Fig. 5 shows the dependance of T_c versus doping for different rare earth atoms in the electron doped 214-compounds. It is interesting that the maximum of T_c increases for the lighter rare earth atoms. This is one of the reasons why we want to grow crystals of the $LaPr_{1-x}Ce_xCuO_4$.

Summary

In summary, we are able to probe the whole sample space of both the hole and electron doped superconductors with high quality single crystals.

References

[1] A. Erb *et al.*, Physica C **245**, 245 (1995).
[2] A. Erb, E. Walker, and R. Flükiger, Physica C **258**, 9 (1996).
[3] B. Liang *et al.*, J. Cryst. Growth **237-239**, 756 (2002).
[4] H. Eisaki *et al.*, Phys. Rev. B **69**, 064512 (2004).
[5] A. Maljuk *et al.*, Physica C **355**, 140 (2001).
[6] Y. Ando and T. Murayama, Phys. Rev. B **60**, R6991 (1999).
[7] J. G. Bednorz and K. A. Müller, Z. Phys. B **64**, 189 (1986).
[8] H.Takagi, S. Uchida, and Y. Tokura, Phys. Rev. Lett. **62**, 1197 (1989).
[9] J. S. Higgins *et al.*, Phys. Rev. B **75**, 104501 (2006).
[10] N. P. Armitage *et al.*, Phys. Rev. B **68**, 064517 (2003).
[11] R. W. Hill *et al.*, Nature **414**, 711 (2001).
[12] Y. Onose *et al.*, Phys. Rev. Lett. **82**, 5120 (1999).
[13] A. Erb *et al.*, Solid State Commun. **112**, 245 (1999).
[14] B. Revaz, A. Junod, and A. Erb, Phys. Rev. B **58**, 11153 (1998).
[15] M. Roulin *et al.*, Phys. Rev. Lett. **80**, 1722 (1998).
[16] S. P. Brown *et al.*, Phys. Rev. Lett. **92**, 067004 (2004).
[17] A. Erb, B. Greb, and G.Müller-Vogt, Physica C **259**, 83 (1996).
[18] M. Kläser *et al.*, Physica C **306**, 188 (1998).
[19] A. Janossy, T. Fehér, and A.Erb, Phys. Rev. Lett. **91**, 177001 (2003).
[20] V. B. Zabolotnyy *et al.*, Phys. Rev. Lett. **96**, 037003 (2006).
[21] A. Erb and M. Lambacher, *in preparation*.
[22] M. Lambacher and A. Erb, *in preparation*.

Raman studies at high pressure

L. Tassini and R. Hackl [1]

In systems with (quantum) phase transitions pressure is an important control parameter [1, 2], since the sample can be tuned quasi-continuously and reversibly between different states. Generally, highly correlated systems are characterized by the proximity of various typically competing phases making pressure an indispensable tool for studying them. In high-T_c cuprates for instance, the doping level can be changed in certain limits [3] or the static stripe order in, e.g., $La_{2-y-x}Eu_ySr_xCuO_4$ can be suppressed [4]. Hence, various new insights are to be expected when electronic Raman spectra are measured under pressure [5].

For this reason, we started setting up a diamond anvil cell (DAC) which facilitates Raman experiments in a pressure range up to approximately 20 GPa (200,000 kbar) (see Fig. 1). The cell has a containment (not shown) with an outer diameter of 38 mm into which the static anvil support is inserted followed by the piston (see figure). The required force on the piston comes from a membrane which is connected to a gas handling system capable of He-pressures up to approximately 150 bar. The two anvils attached to support and piston are pressed against a gasket with a small hole (approximately 0.3 mm) in the center providing space for the sample and, usually, for a small piece of ruby as an optical pressure sensor. The volume has to be filled with a pressure transmission medium. Liquids such as kerosine or mixtures of ethanol and methanol lead to substantial uniaxial components particularly at higher pressures. The best medium for establishing hydrostatic pressure is He followed by Ar. Therefore, the cell can be inserted into a He-cryostat with a base temperature of 1.7 K, i.e. below the $\lambda-$point. Alternatively, we also have an Ar-cryostat. The maximal pressure in the cell is determined by the area of the cutlet and the type of stones. With a sapphire anvil having an outer diameter of 4 mm and a cutlet of 0.7 mm diameter we can reach approximately 3.5 GPa as determined from the shift of the ruby fluorescence.

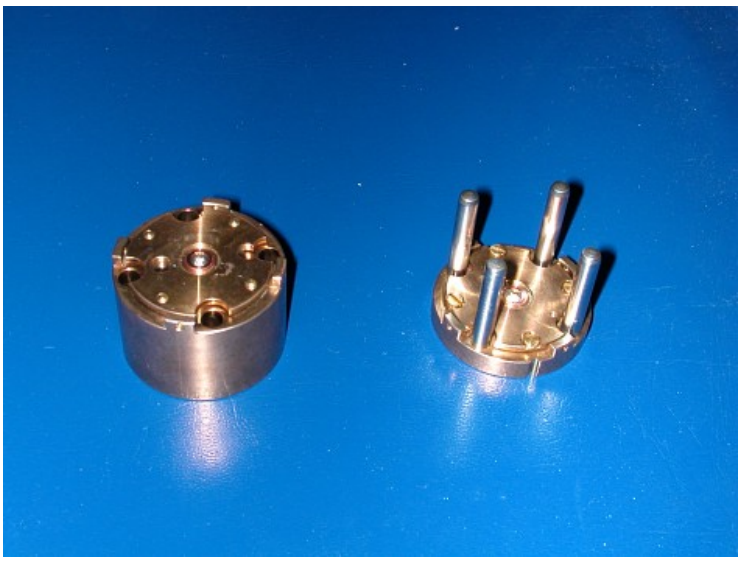

Figure 1: Photograph of the new pressure cell for Raman spectroscopy. The static part with the optically transmitting anvil is on the r.h.s. The piston driven by a membrane is on the l.h.s. The anvils (here moissanites) can be recognized by the facets. The containment, the gasket and the membrane are not shown.

The optical part is relatively complicated since the laser light has to be coupled in as a spatially filtered Gaussian beam and the scattered light has to be transmitted to the spectrometer with only small losses. At the same time the beams reflected from the sample's and the anvil's surfaces should be blocked effectively. Since we are interested in the relatively weak and broad continuum the fluorescense in the anvils has be negligible and the polarizations must be preserved. In addition, a microscope with high optical quality is required for getting a good image

[1] This work is supported by the DFG through the Research Unit FOR538 (project No.: HA 2071/3).

of the sample volume and for alignment. These requirements are best met with artificial diamonds [5] but good approximations can be achieved by selected natural stones. Moissanite (6H-SiC) is very cheap and mechanically as stable as diamond but the optical quality is insufficient. Sapphire is only useful in the pressure range up to 5 GPa.

In our first experiments we used sapphire for the anvils and Ar as pressure transmission medium. The results on a single crystal of $(Y_{0.97}Ca_{0.03})Ba_2Cu_3O_{6+x}$ (Y-123) are shown in Fig. 2. The dominant line in the figure is from the anvil. The intensity of the B_{1g} line of Y-123 at 340 cm^{-1} has the expected intensity if the attenuation by the various surfaces and the solid angle of the objective lens are properly taken into account. The continuum is more intense than expected due to fluorescence in the anvils.

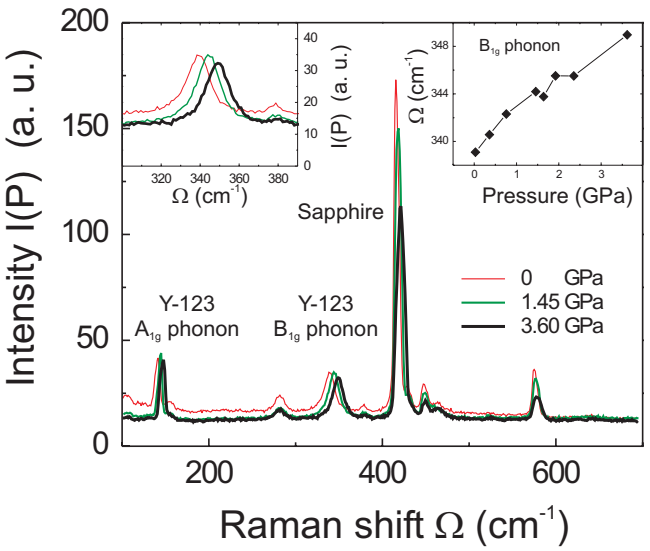

Figure 2: First Raman results on phonons on $Y_{1-y}Ca_yBa_2Cu_3O_{6+x}$ in the pressure range up to 3.6 GPa. The main panel shows the raw data. In the upper left inset we show a zoom on the B_{1g} phonon. In the right inset the variation with pressure of the B_{1g} phonon is plotted.

At present we have reliable results only on phonons. A zoom on the B_{1g} phonon is shown in the left inset of Fig. 2. The variation with pressure can be found in the right inset. In the range up to 3.6 GPa it is smaller by at least 30% than that at optimal doping [5].

In order to study the continuum the sapphire anvils have to be replaced by low-fluorescence and low-birefringence diamonds. This is presently under way as is the use of He as pressure transmission medium. Application on the continuum in Y-123 will be part of the work in the new funding period of the Research Unit (see also "Highlights and perspectives in high-T_c research").

References

[1] S. Sachdev, Science **288**, 475 (2000).
[2] M. Vojta, Physik Journal **1**(3), 55 (2002).
[3] J.S. Schilling, cond-mat/0604090 (2006).
[4] B. Simovič *et al.*, Europhys. Lett. **66**, 722 (2004).
[5] A.F. Goncharov and V.V. Struzhkin, J. Raman Spectrosc. **34**, 532 (2003).

Two-axes rotation of a magnetic field at mK temperatures

S. Jakob, K. Neumaier, M. V. Kartsovnik, and W. Biberacher

Our previous studies of the "magnetic field - pressure - temperature" phase diagram of the layered organic conductor α-(BEDT-TTF)$_2$KHg(SCN)$_4$ have revealed an interesting interplay between a charge density wave (CDW) and a superconducting state [1]. At a critical pressure of 2.5 kbar the CDW state is completely suppressed and a sharp transition into a superconducting state is observed below 100 mK. For pressures below 2.5 kbar there is a coexistence of the superconducting and CDW state, but this is most likely a spatially inhomogeneous state. Recent theories [2, 3] propose that a spin- triplet f-wave-like SC pairing can occur in the vicinity to the CDW instability due to charge- and spin-fluctuations. Our compound, in which the SC state directly neighbors with the CDW ordering, is a perfect candidate to test these predictions. The low SC critical temperature needs special methods of refrigeration (for instance dilution refrigerator), but only small magnetic fields to check whether the paramagnetic limit can be considerably exceeded in this compound. Of course, the necessary requirement for such an experiment is a sufficient suppression of the orbital pair-breaking mechanism. Due to the extremely high electronic anisotropy of our material, this can be achieved by the exact alignment of the field parallel to the layers. Of special interest is the study of the in-plane anisotropy of the critical field. But studying the complete anisotropy of the critical fields in a single run requires a dilution refrigerator unit with pressure cell and two-axes rotation of a magnetic field.

Since such an equipment was not available at the WMI, we built up a new dilution refrigerator system in combination with a home made small superconducting vector magnet [4]. The dilution unit is very similar to the standard dip stick dilution refrigerator inserts of the WMI (see Fig. 17 in the chapter "Experimental Facilities"). The pressure cell is fixed to the mixing chamber by three copper rods to position the pressure cell and sample in the center of the magnetic field coils. Fig. 1 shows a picture of the magnet system. The bore of the main magnet is 38.5 mm, the maximal axial field amounts to 1.5 T and is reached at a current of 63 A. In the perpendicular direction a maximal field of 0.33 T is applicable. The two field components are produced by two computer controlled power supplies. By this way we can do field sweeps at any field direction in the plane spanned by the two field components (polar plane, polar angle θ), but we are also able to

Figure 1: Home made vector magnet used in the experiment.

continuously rotate the field at constant value of the magnetic field within this plane.

To get a real two-axes rotation facility we use the fact that the small field component of our vector magnet is almost by a factor 2 larger than the calculated paramagnetic limit of the samples under investigation. We therefore position the sample with the axial field perpendicular to the conducting layers and fix all the tubings and wirings of the dilution insert in a central unit, whereas the magnets with wiring are connected to the 4-He Dewar. This outer unit can be rotated manually by 360° with respect to the fixed inner part allowing to position the polar plane of the magnet system at any azimuthal direction.

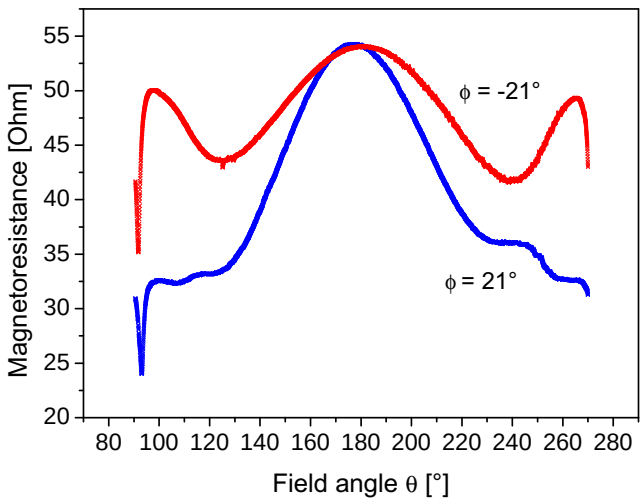

Figure 2: Angular dependent magnetoresistance at $B = 0.3\,\mathrm{T}$ and $T = 30\,\mathrm{mK}$ for two different azimuthal angles ϕ.

In a first run of the complete system (dilution unit with pressure cell, vector magnet) we found very promising results: The refrigerator reaches a base temperature of 24 mK. Due to the quite large pressure cell (diameter 20 mm, length 40 mm, material CuBe) changes of the magnetic field can be done only at a moderate rate. Field sweeps at 5 mT/min and continuous rotation of the polar angle (B = 0,3 T) at 3°/min can be performed at 30 mK. In the first experiment we measured the magnetoresistance of a high-quality sample of α-(BEDT-TTF)$_2$KHg(SCN)$_4$ at ambient pressure. Fig. 2 shows the angular dependent magnetoresistance at a magnetic field of 0.3 T at 30 mK. The two curves belong to different azimuthal angles of the rotation plane. The azimuthal angle ϕ is calculated from the crystal c-axis, which was determined prior to the experiment by X-ray analysis. The dips at 90° and 270° are due to superconductivity. As mentioned above α-(BEDT-TTF)$_2$KHg(SCN)$_4$ shows an incomplete transition to superconductivity at ambient pressure with an onset temperature of 300 mK.

References

[1] D. Andres, M. V. Kartsovnik, W. Biberacher, K. Neumaier, E. Schuberth, and H. Müller, Phys. Rev. **B 72**, 174513 (2005).
[2] S. Onari, R. Arita, K. Kuroki, and H. Aoki, Phys. Rev. **B 70**, 094523 (2004).
[3] K. Kuroki, R. Arita, and H. Aoki, Phys. Rev. **B 63**, 094509 (2001).
[4] The vector magnet was built by G. Eska (Bayreuth) during his employment at the WMI.

Dry fridges ... cooool!

K. Uhlig

Recent developments

Dry dilution refrigerators (DR) do not require cryoliquids for precooling. Instead, precooling is accomplished by two-stage pulse tube refrigerators (PTR). Dry fridges offer substantial economical and practical advantages compared to their predecessors with liquid helium precooling. This has been explained in detail before [1]. In Fig. 1 a cross-sectional view of our cryostat is shown. The main components of the fridge are a commercial PTR [2], a Joule-Thomson refrigerator (JT) and a dilution refrigeration unit (DU). Our PTR (model PT-4-05) is a two-stage closed cycle refrigerator with a power consumption of its compressor of 5 kW. It is the smallest among its PTR brethren. The cooling capacity of the 1st stage is 42 W@77 K, and its base temperature (temperature with vanishing heat load) is 31 K. This stage cools a big radiation shield and a charcoal trap to purify the ^{3}He gas stream of the fridge to $T \approx 60$ K.

The cooling power of the 2nd stage is 0.5 W@4 K, and its base temperature is 2.48 K. It cools the vacuum can and the ^{3}He of the DR to a temperature $T < 4$ K. Then the ^{3}He is further precooled in the JT stage and, after further precooling in heat exchangers, is diluted in the mixing chamber into liquid ^{4}He, where the dilution process produces the lowest temperatures of the fridge [3]. In order to condense the ^{3,4}He mash before an experiment the DR can be operated like a helium liquefier with a pressure at the gas inlet of $\approx$ 4 bar. The enthalpy of the cold non-liquefied fraction of the flow is used to precool the inflowing ^{3,4}He. No additional low temperature gadgets are needed for condensation.

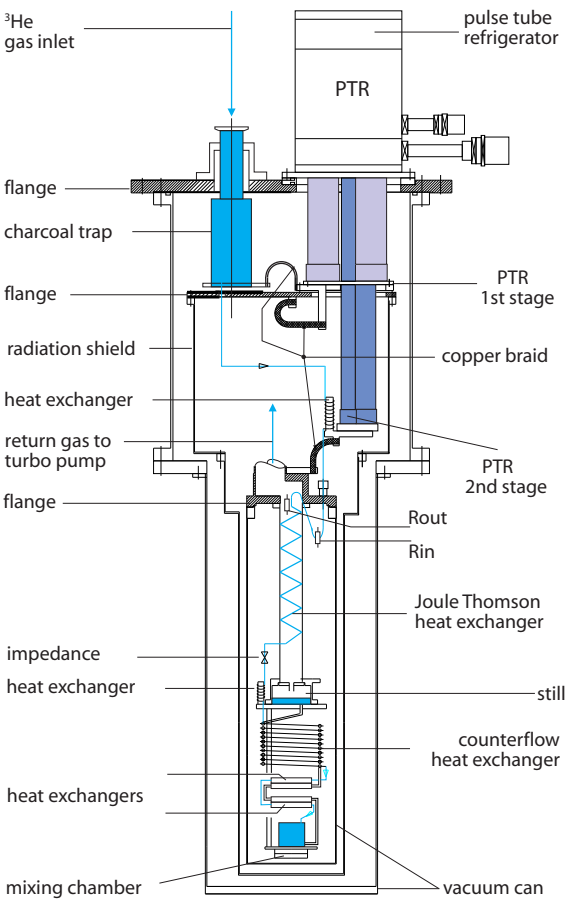

Figure 1: Cross-section view of our DR with PTR precooling.

DRs are often characterized by their cooling capacity at a temperature of the mixing chamber of 100 mK. In our fridge we reached a typical value of $\dot{Q} = 250\,\mu$W@100 mK. There is a long list of applications, however, where an even higher $\dot{Q}$ is necessary (e.g. for nuclear research, astronomy or X-ray spectroscopy). For higher $\dot{Q}$ the ^{3}He flow $\dot{n}_3$ has to be increased since $\dot{Q} \propto \dot{n}_3$. For the time being, the task is to reach 500 μW@100 mK. In this case the corresponding ^{3}He flow is mainly limited by the flow resistance of the present cryostat and its pumping lines.

On increasing the helium flow, heat transfer problems in the JT counterflow heat exchanger (hex) are expected, as well as instabilities of the helium flow in the hexs of the DU and vortex creation in the mixing chamber (MC). Regarding the flow resistance of the JT stage, a critical

element is its counterflow hex. It was redesigned, and in particular its diameter was increased to lower the flow impedance.

Fig. 2 shows the insert of the JT hex. It is made from a pair of twisted capillaries which are bent to form a row of little cones. The insert fits into a SS tube (25 mm diameter, Fig. 1). The adequacy of the new hex was controlled with two resistance thermometers at the hot end of the hex, which measured the temperatures of the ^{3}He flow at the inlet (R_{in}, T_{in}) and the outlet (R_{out}, T_{out}, Fig. 1).

Figure 2: Insert of the JT hex.

In Fig. 3 the calibration curve of R_{out} is depicted (black). To plot the experimental points taken at different flow rates, R_{out} is plotted versus T_{in} (red). The temperature gradient between in- and outflowing streams is small, indicating almost perfect enthalpy transfer.

The new hex was installed in our cryostat and tested in combination with a simple DU. The cooling power diagram of the experiment is shown in Fig. 4. Three temperatures of the DU are shown, the temperature $_{Tin,mc}$ of the ^{3}He just before it entered the MC, the temperature of the liquid (T_{mc}) in the MC, and the temperature of the bottom plate of the MC T_{pl} which is connected with a silver sponge to provide thermal contact between the liquid and the MC plate (Fig. 1). The heater used to take the cooling power data was attached to the MC plate. The main information from this experiment was that the cooling power was 350 μW@100 mK. Moreover, the ratio $T_{in,mc}/T_{mc} \approx 2.8$ at the base temperature was determined as expected [3]. The ^{3}He flow rate was 700 μmol/s in the experiment above. This was the highest flow possible with the turbo pump available. ^{3}He flow and cooling capacity will be increased soon by adding a second turbo pump to the gas circuit.

Transfer

Last year we agreed to transfer sufficient know-how to a local engineering company (VeriCold Technologies GmbH) so that they are able to manufacture their own version of a dry dilution

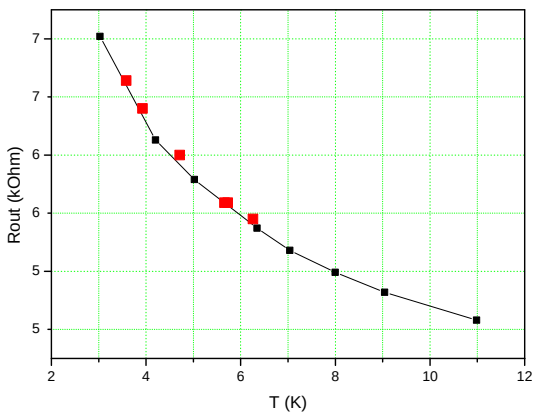

Figure 3: Temperature difference between incoming and outflowing ^{3}He at the hot end of the JT hex. See text.

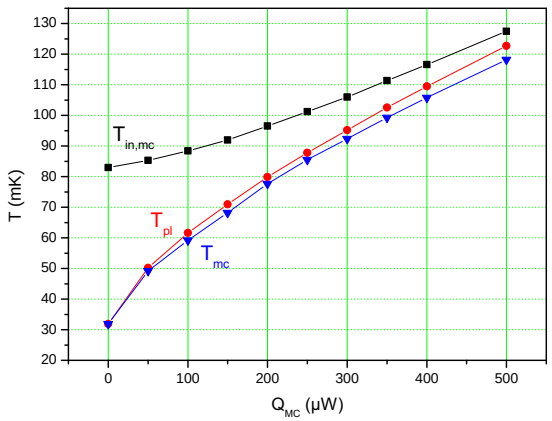

Figure 4: Mixing chamber temperatures versus cooling capacity.

refrigerator. To get them started we also agreed to make three cold units operational (design, assembly, testing). Two of them have been finished, so far, with the third one being well on its way. The DRs will be used for microwave spectroscopy experiments. Fig. 5 shows a picture of the finished fridge units. They each consist of a JT condenser, and a DU. Below the concentric tube hex the DU has two step hexs to reach a base temperature well below 15 mK.

In Fig. 6 we show the cooling capacity of one of the fridges near 100 mK as a function of the ^{3}He flow, where a constant heat load of 250 μW was applied at the bottom plate of the MC. At 95 mK in the liquid ^{3,4}He we find $T = 102$ mK at the sinter plate. The thermal boundary resistance which gives rise to a temperature gradient of ≈ 7 mK between the liquid ^{3,4}He and the MC plate is relatively high compared to earlier MC versions.

Figure 5: Dilution units with a cooling power of 250 μW@100 mK.

Fridge for the microwave spectroscopy lab

For microwave spectroscopy experiments at the WMI a cryostat insert was made available, which originally was intended for experiments on solid ^{3}He. The insert had not been used before. The insert was of the "traditional" type and fitted into a dewar with liquid helium. Furthermore, a DU which originally had been used for ^{3}He work and had been sitting in the author's treasure chest idle for some years was reactivated so that it could be installed at the aforementioned cryostat insert. The DU consisted of a still, a concentric tube hex and two step exchangers. The MC was made new [4]. A plot of the refrigeration power of the fridge at 100 mK is given in Fig. 7. The performance of the fridge is quite similar to that of the nuclear demag cryostat of the WMI (BMM2) [5], or to the performance of a commercial KELVINOX 100 fridge of Oxford Instruments [6].

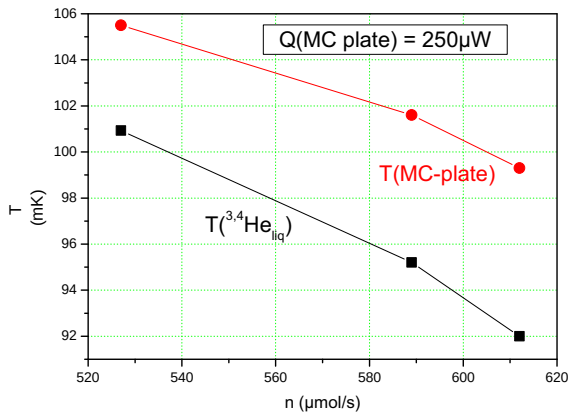

Figure 6: MC temperatures near 100 mK as a function of ^{3}He flow rate. The heat load to the MC plate was kept constant ($\dot{Q} = 250\,\mu$W). Black data points are for temperatures of the liquid ^{3,4}He, red points for the mixing chamber plate.

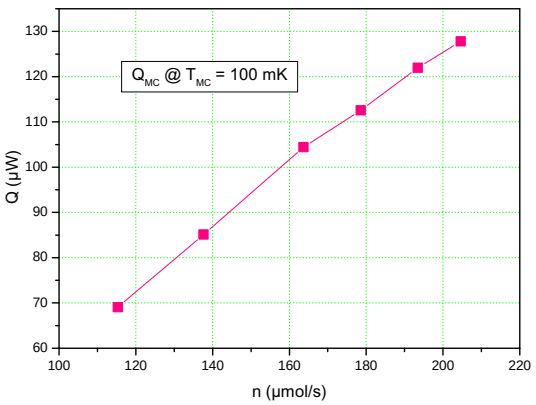

Figure 7: Cooling capacity of the MC as a function of the ^{3}He flow at a fixed MC temperature of 100 mK.

References

[1] K. Uhlig, Cryogenics **44**, 53 (2004); and references cited therein.
[2] Cryomech Inc., Syracuse, New York.
[3] F. Pobell, *Matter and methods at low temperatures* (Springer, Berlin, 1992).
[4] A. Marx was subcontracted for the sintering chore.
[5] E. Schuberth, *private communication*.
[6] Oxford Instuments GmbH, Wiesbaden.

Experimental Facilities and Infrastructure

In the following basic information on the key experimental facilities and components of the technical infrastructure installed at the Walther-Meißner-Institute (WMI) is given.

UHV-Laser-MBE

The WMI operates a UHV-Laser-Molecular Beam Epitaxy (L-MBE) system for the growth of complex oxide heterostructures. The system has been designed to meet the special requirements of oxide epitaxy. The UHV cluster tool consists of the following main components:

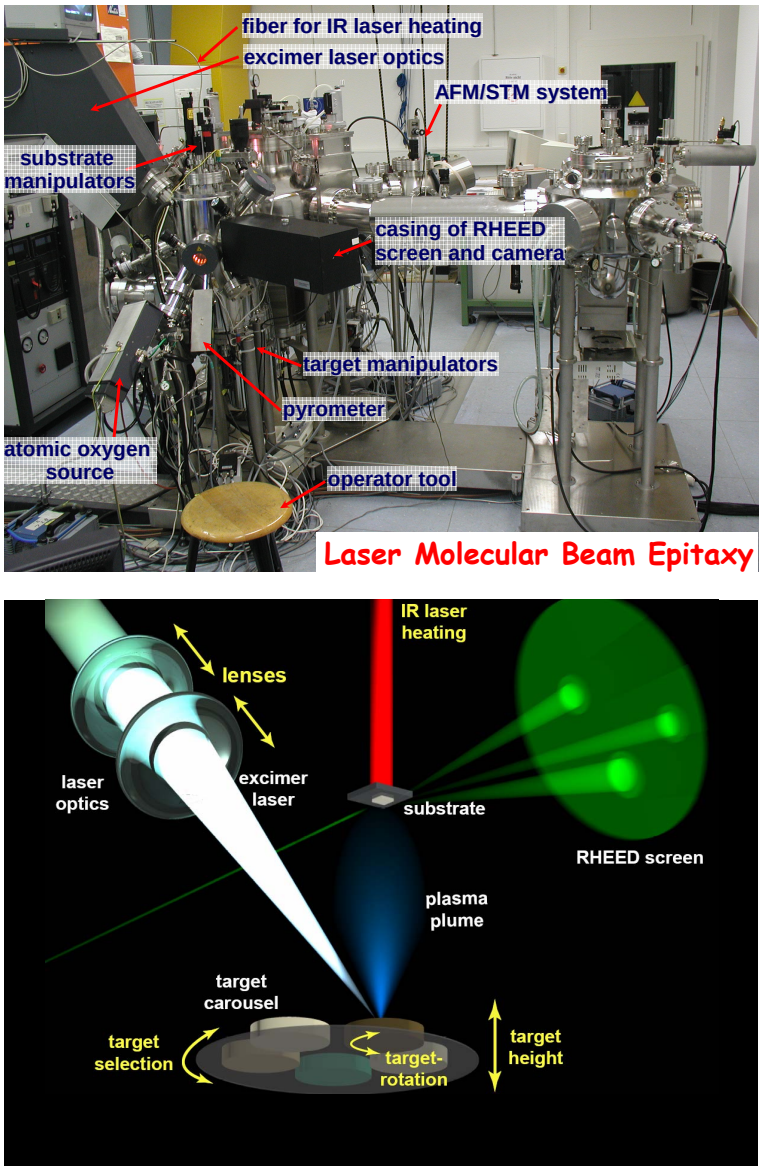

Figure 1: Top: UHV-Laser-Molecular Beam Epitaxy System. Bottom: Principle of the deposition process.

- central transfer chamber;
- load-lock chamber with heater system for substrate annealing;
- laser deposition chamber with in-situ reflection high energy electron diffraction (RHEED) system, laser substrate heating system, and atomic oxygen source, the RHEED system has been modified to allow for the operation at high oxygen partial pressure up to 0.5 mbar;
- surface characterization chamber with UHV scanning force microscope (Omicron);
- metallization chamber with a four heart electron gun system and a liquid nitrogen cooled sample stage. The sample holder can be tilt for shadow evaporation;
- KrF excimer laser.

The system is used for the growth of complex oxide heterostructures consisting of superconducting, magnetic and dielectric materials such as the high-temperature superconductors, the doped manganites, the double perovskites, magnetite etc..

The original laser molecular beam epitaxy system (laser-MBE) designed already in 1995/96 until now has been permanently extended and modified. In particular, the substrate heating system and the temperature control unit was changed from a resistive radiation heater to a new infrared laser heating system (see Fig. 3, left) including a pyrometer for determining the sample temperature. In addition, a source for atomic oxygen has been added. The main advantage of the new heating system is that only the substrate is heated while the surrounding parts are hardly affected (Fig. 3, right). In this way one can achieve an essentially better vacuum at temperatures well above 1000°C. The achievable substrate temperature is limited by the melting point and the size of the substrate material (approx. 1410°C for a 5×5 mm^2 silicon substrate). The laser heating system has already been successfully used for removing the amorphous silicon oxide layer form the surface of silicon substrates at 1150°C. This is required for the epitaxial growth of oxide thin films on this substrate.

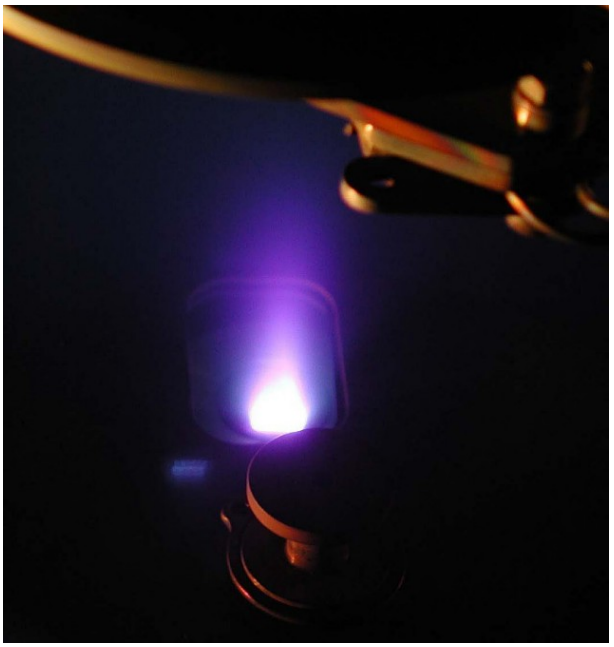

Figure 2: Pulsed Laser Deposition (PLD): When the pulse of the UV laser (KrF excimer laser, 248 nm) hits the target, the target material is ablated and the so-called laser "plume" containing highly excited atoms and molecules is formed.

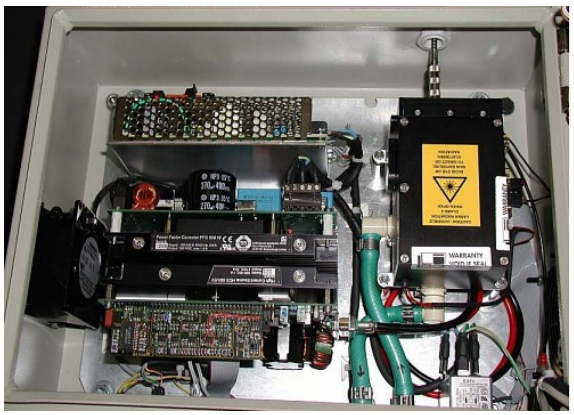

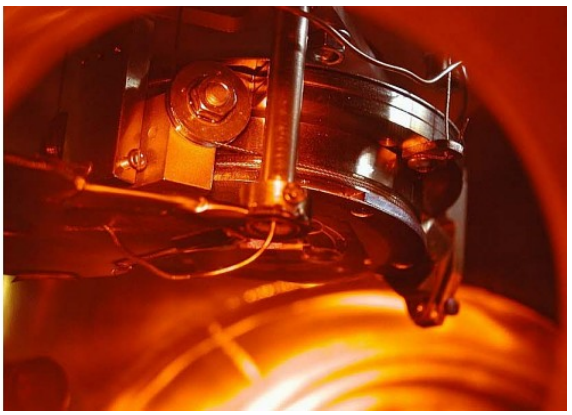

Figure 3: Components of the laser heating system: The substrate is heated using an IR diode laser head that is located in a separate box far away from the deposition chamber (left). The laser light is brought to the substrate (right) via an optical fiber.

Single Crystal Growth and Synthesis of Bulk Materials

Transition metal oxides are of great interest due to their various interesting physical properties (e.g. high temperature superconductivity, colossal magnetoresistance, ferroelectricity, nonlinear optical properties etc.) and their high potential for applications. Therefore, the WMI operates a laboratory for the synthesis of bulk materials and single crystals of transition metal oxides. Besides various chamber- and tube furnaces a four-mirror image furnace is used in the crystal growth of various oxide systems. With this furnace crystals of many different compounds of the high temperature superconductors and various other transition metal oxides have been grown as single crystals using the traveling solvent floating zone technique. The furnace consists basically of 4 elliptical mirrors with a common focus on the sample rod and with halogen lamps in their other focus. By irradiation of the focused light the sample rod is locally heated and eventually molten. The molten zone can be moved up and down along the entire sample rod under simultaneous rotation. Due to the anisotropic growth velocity a preferential growth of the those grains with the fastest growth velocity along the pulling direction is obtained and the formerly polycrystalline rod is transformed into a single crystal. Single crystal growth can be performed with this furnace at maximum temperatures up to 2200°C in the pressure range from 10^{-5}mbar up to 10 bar and in oxidizing, reducing as well as inert atmosphere.

Figure 4: The four-mirror image furnace installed at the crystal laboratory of the WMI. Crystals can be grown by the floating zone and traveling solvent floating zone technique at temperatures up to 2200°C and pressures up to 10 bar.

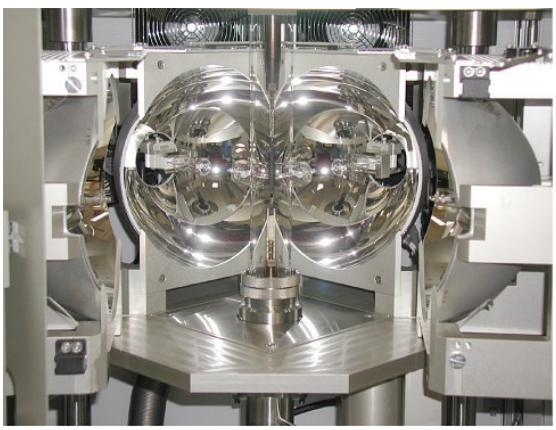

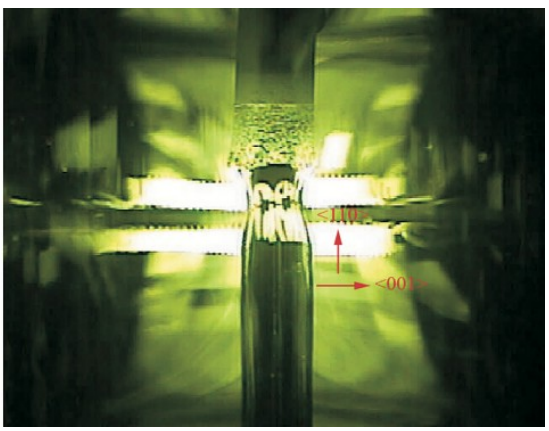

Figure 5: Left: Central part of the image furnace with the four elliptical mirrors. In the center one can see the quartz tube with the poly-crystalline rod. Right: View on the molten zone of $Pr_{2-x}Ce_xCuO_4$ (melting point: 1280°C) obtained by a CCD camera.

The X-ray diffraction systems

For x-ray analysis the Walther-Meissner-Institute operates two X-ray diffractometers (Bruker D8 Advance and D8 Discover). The two-circle system is used for powder diffraction. In this system the samples can be heated in oxygen atmosphere up to 1600°C. It is equipped with a Göbel mirror and an area detector to save measuring time. The second system is a high resolution four-circle diffractometer that can be used for reciprocal space mappings. It is equipped with a Göbel mirror and an asymmetric two-fold monochromator and allows for the texture analysis of thin film superlattices and single crystalline materials. In both systems measurements can be carried out fully computer controlled.

Figure 6: The two-circle X-ray diffractometer Bruker D8 Advance.

Beyond these two Bruker x-ray systems a Laue camera for single crystal analysis and a Debye-Scherrer camera are available.

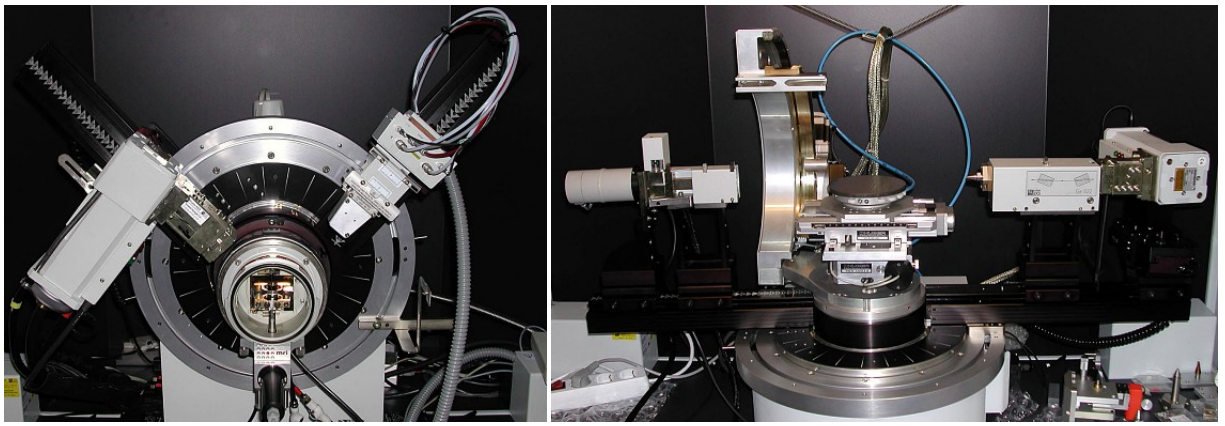

Figure 7: Left: High temperature sample holder of the D8 Advance system. Right: Four-circle high resolution X-ray diffractometer Bruker D8 Discover.

Figure 8: Quantum Design SQUID magnetometer.

The SQUID-magnetometer

For the analysis of the magnetic properties of materials, a Quantum Design SQUID magnetometer system as shown in Fig. 8 is used at the WMI. The SQUID magnetometer allows for measurements in the temperature regime from 1.5 to 400 K and provides excellent sensitivity particularly in the low field regime. Due to the excellent sensitivity of the system, thin film samples with a very small sample volume can be analyzed. In a special inset, samples can be measured up to temperatures well above room temperature (up to 700°C). For this option the sample volume has to be reduced. The SQUID magnetometer is equipped with a superconducting solenoid allowing for a maximum field of 7 T. At present, the magnetometer is used for the characterization of magnetic materials (both in bulk and thin film form). Examples are the doped manganites, magnetite, the double perovskites or magnetic semiconductors.

The High Field Laboratory

Transport and thermodynamic properties of samples are often studied as a function of applied magnetic field. For such measurements several superconducting magnets are available at the WMI. Two of them (8/10 and 15/17 Tesla magnet system) are located in the high magnetic field laboratory in the basement of the WMI. The magnet systems are lowered below the ground level to facilitate the access to the top flange and the change of the sample sticks. The magnet systems are decoupled from the building to avoid noise due to mechanical vibrations. A variety of sample holders can be mounted allowing for e.g. sample rotation during the measurement. For standard sample holders the accessible temperature regime is 1.5 K$< T <$ 300 K. However, also ^{3}He/^{4}He dilution refrigerator inserts ($T >$ 20 mK) or high temperature units ($T <$ 700 K) can be mounted. All measurements are fully computer controlled (by the use of the LabView software tool) allowing for remote control and almost continuous measurements.

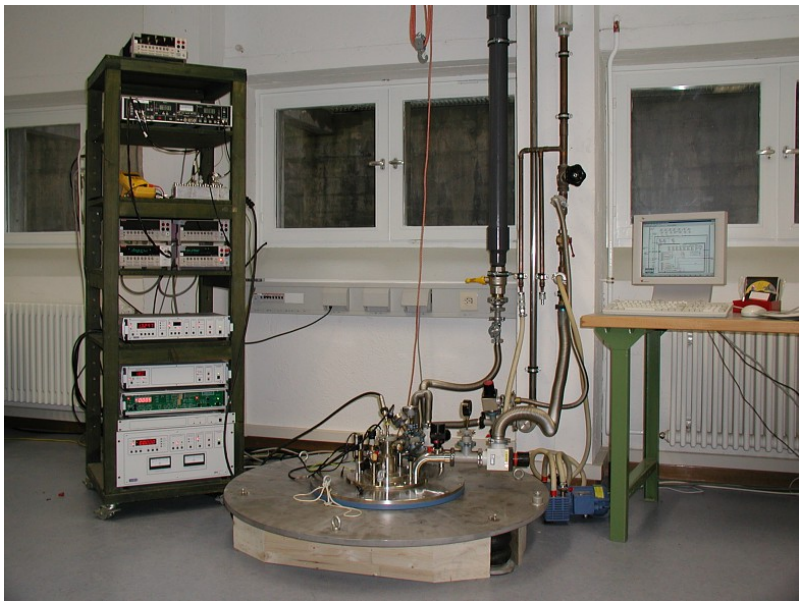

Figure 9: High field laboratory with Oxford 17 T magnet system.

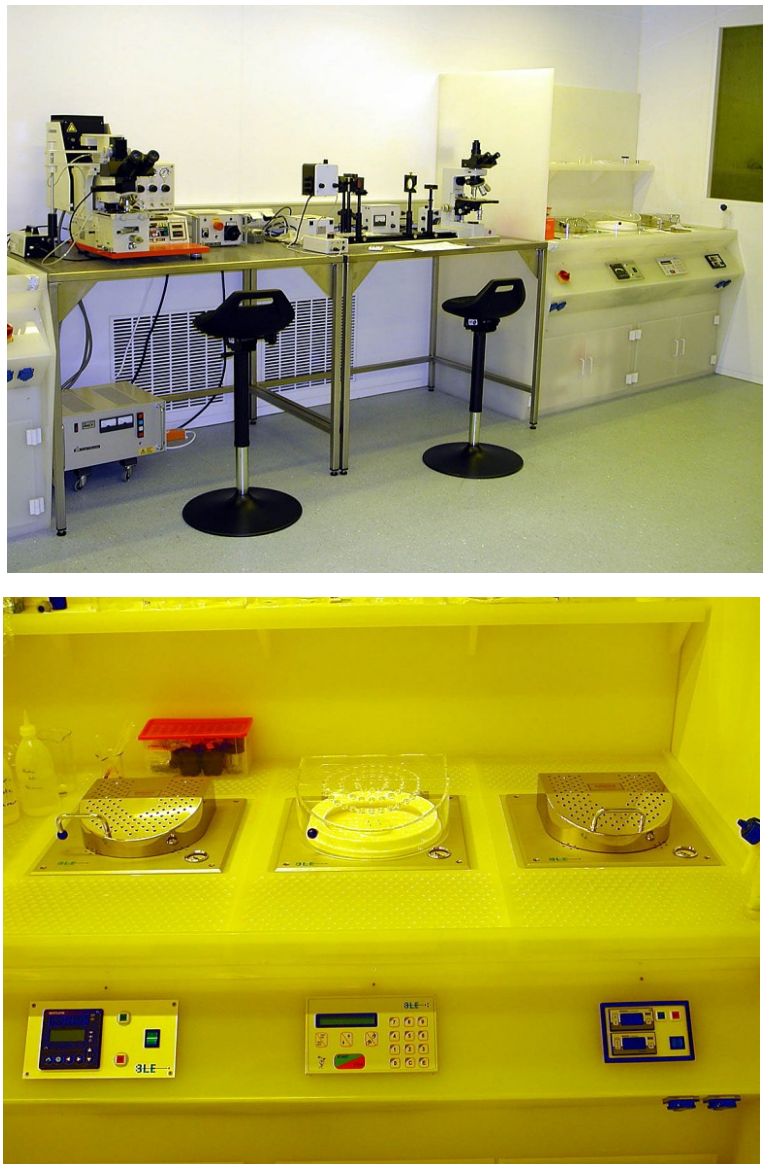

Figure 10: Top: Part of the clean room facility with optical lithography equipment and clean room benches. Bottom: Resist coater and hot plates.

The Clean Room Facility

For the fabrication of nanostructures and superconducting as well as spintronic devices the WMI operates a class 1000 clean room facility with an area of about $50\,m^2$. This clean room facility has been put into operation at the WMI within the year 2001. The clean room is subdivided into two parts for optical lithography and electron beam lithography, respectively. The clean room facility is equipped with the standard tools for optical lithography such as resist coaters, hot plates, wet benches, a Karl Süss MJB3 mask aligner and an optical projection lithography system. The technical infrastructure for the clean room is located in the basement of the WMI directly below the clean room area.

Since 2005 the clean room also is equipped with a reactive ion etching system, Plasmalab 80 Plus with ICP plasma source (Oxford Instruments Plasma Technology).

Electron Beam Lithography

The Electron Beam Lithography System is installed in one part of the clean room facility. It consists of a Philips XL 30 SFEG scanning electron microscope (SEM) with a Raith Elphy Plus electron beam lithography system and a laser interferometer table for precise stitching of writing fields.

The SEM is equipped with a hot field emitter and typically provides a beam diameter of less than 1.5 nm at $\geq$ 10 keV or about 2.5 nm at 1 keV. The lithography unit allows the fabrication of nanostructures down to about 10 nm. We have realized the controlled fabrication of metallic strip patterns with a strip width of about 20 nm. The electron beam lithography is used for the fabrication of nanostructures in metallic and oxide systems required for the study of quantum effects in mesoscopic samples.

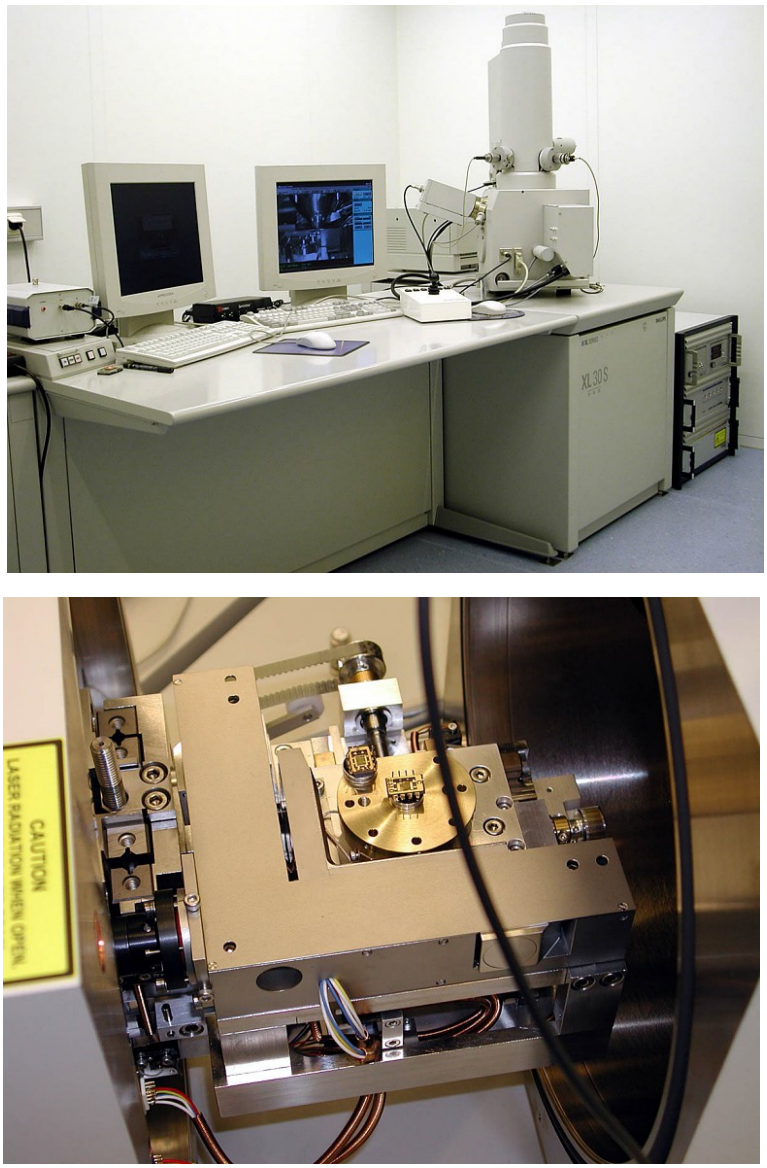

Figure 11: Top: Philips XL 30 SFEG Scanning Electron Microscope with Raith Elphy Plus Lithography System. Bottom: Raith Laser Stage.

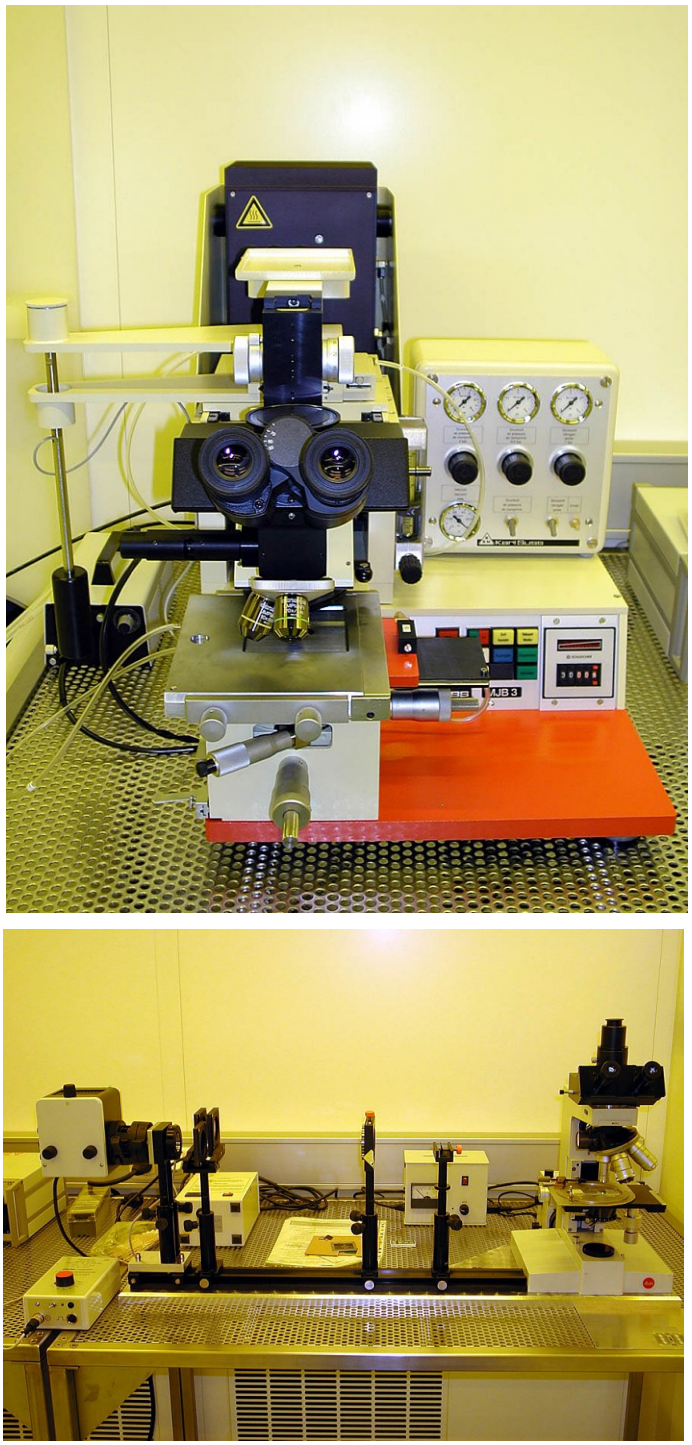

Figure 12: Top: Süss MJB 3 maskaligner for optical lithography. Bottom: Optical projection lithography based on an optical microscope.

Optical Lithography

For optical lithography a Karl Süss MJB 3 maskaligner or an optical microscope based projection system are used. The maskaligner is operating in the 1 : 1 soft or hard contact mode and is using chromium metal masks. In the projection system the mask pattern is demagnified by a factor of 5 to 100. Therefore, cheap foil masks can be used. With both systems microstructures with a lateral dimension down to 1 μm can be fabricated.

Low and Ultra-low Temperature Facilities

The WMI operates several low and ultra-low temperature facilities that have been developed and fabricated in-house.

The lowest temperature is achieved by the nuclear demagnetization cryostat "Bayerische Millimühle 2". This ultra-low temperature facility consists of an in-house built dilution refrigerator and originally of two nuclear demagnetization stages. The first of those is based on a hyperfine enhanced van Vleck paramagnet $PrNi_5$ (0.9 mole), the second, which has been removed a few years ago, was based on purified copper (0.2 mole). The lowest temperature reached with this system was slightly below 30 μK in the copper nuclear spin system. At the moment, the first stage can be cooled to below 400 μK and, due to the large heat capacity of $PrNi_5$, it stays below the mixing chamber temperature (5 mK) for nearly 3 weeks. In this cryostat three measuring sites are provided, two in a magnetic field compensated region and one in the center of an 8 T magnet. They are suitable for specific heat measurements, for capacitive torque- and SQUID magnetometry, as well as for transport measurements (electrical und thermal conductivity). The cryostat is also equipped with a pressure cell for liquid and solid ^{3}He, which at the moment is used for nuclear spin resonance measurements below 1 mK.

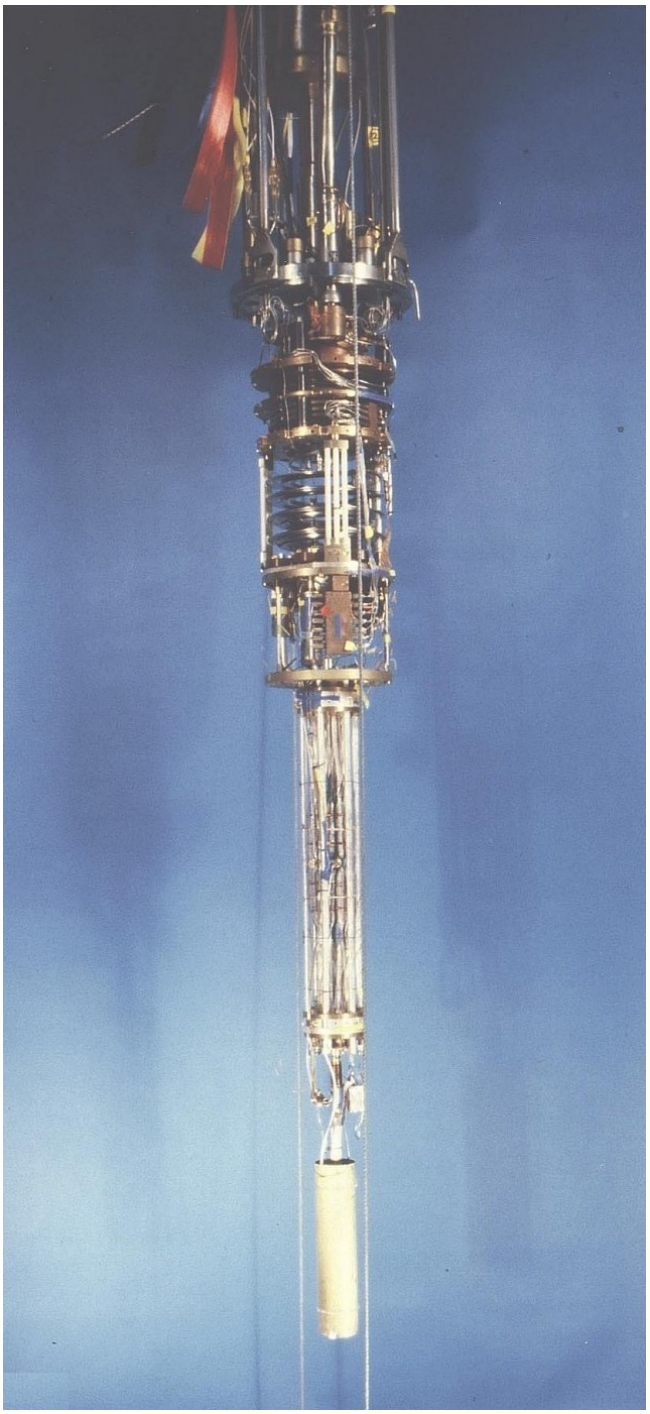

Figure 13: The dilution refrigerator and the nuclear demagnetization stage of the nuclear demagnetization cryostat "Bayerische Millimühle 2".

Within the past years a dilution refrigerator has been developed at the WMI, which does no longer need any cryogens for precooling. Instead, a closed-cycle refrigerator, a so-called pulse tube refrigerator, takes over the precooling. This new type of fridge is generally a more practical and economical compared to fridges using liquid helium precooling.

Figure 14: The "dry" dilution refrigerator of the WMI.

Figure 15: Low-temperature unit of a WMI dilution refrigerator ready to go into a cryostat.

In many low-temperature applications high refrigeration capacities are required. Therefore, our design allows for a high circulation rate of ^{3}He, which in the end determines the cooling power of a dilution refrigerator. Presently our "dry" fridge reaches a refrigeration capacity of 350 μW at a temperature of the mixing chamber of 100 mK, more than three times as much as the fridge of our nuclear demagnetization cryostat. The base temperature of the mixing chamber is usually below 10 mK.

Figure 16: Two mixing chamber mounting plates with silver sponges. Those are needed to overcome the thermal resistance (Kapitza resistance) between the liquid ^{3,4}He and the mounting plate of the mixing chamber. To fabricate the mounting of the sponge (square pins embedded in the sponge) a spark erosion technique has been employed.

A somewhat smaller version of our "dry" fridge has become commercially available at VeriCold Technologies, Ismaning. Their order backlog is high. At this time it stands at about a dozen dilution units.

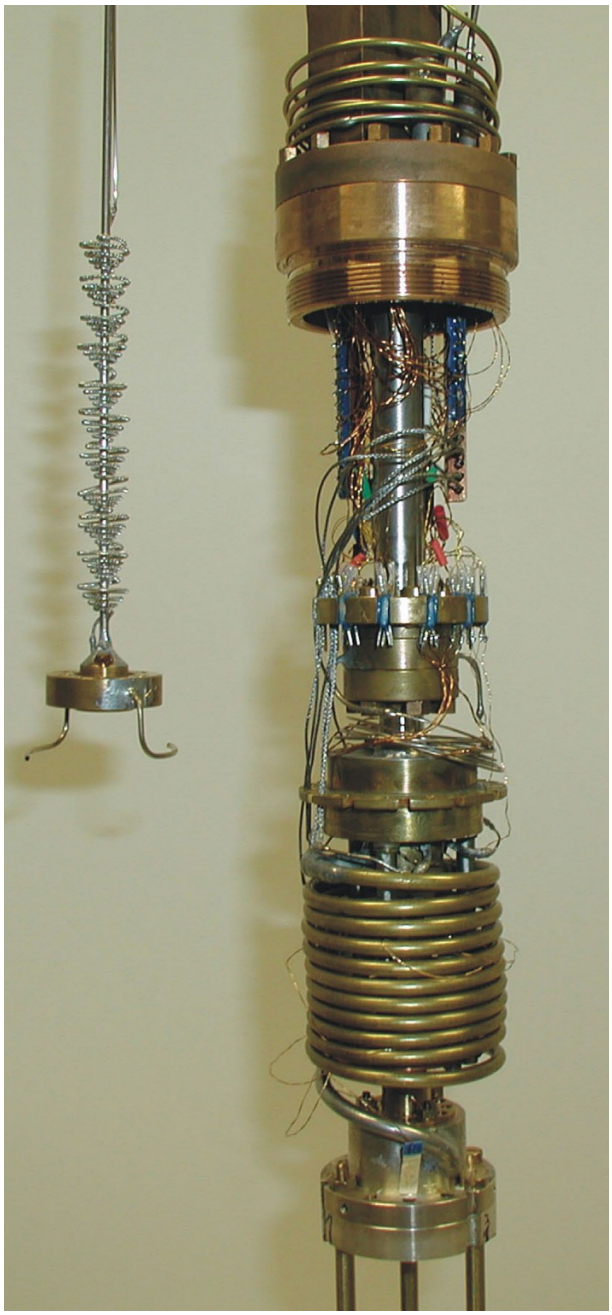

Figure 17: Dilution refrigerator insert with the Joule-Thompson stage, the heat exchanger and the mixing chamber.

The WMI also develops and fabricates dilution refrigerator inserts for temperatures down to about 20 mK. The inserts fit into all cryogenic systems (e.g. superconducting magnets) having a two inch bore. They allow fast sample change and rapid cool down cycles of less than five hours.

The dilution refrigerator inserts are engineered and fabricated in-house and are also provided to other low temperature laboratories for ultra low temperature experiments.

Low Temperature Scanning Tunneling Microscope (LT-STM) with Ultra-High-Vacuum (UHV) Characterization and Preparation Possibilities

The low-temperature scanning tunneling microscope installed at WMI allows the investigation of low dimensional systems such as self-organized molecules, superconductors, magnetic and heterostructure surfaces. The LT-STM is integrated into a UHV chamber together with a variety of analytical as well as preparation tools. The LT-STM and the preparation facilities listed below are operated by the Hermann group. Prof. Hermann is heading an experimental physics group at the LMU-Munich and is member of the Center for Nano Science (CeNS).

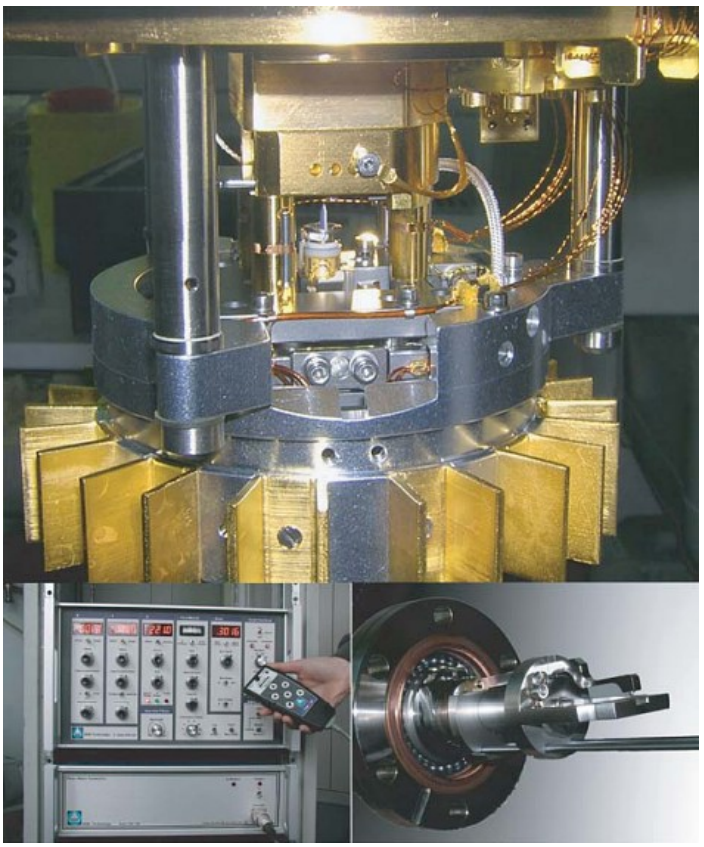

Figure 18: Top: low temperature STM, bottom left: scan electronics, bottom right: manipulator

The Microscope

The LT-STM (top picture) is designed for easy handling under UHV as well as low temperature conditions. We control the Omicron STM by an electronics of the company RHK (bottom picture, left side).

The STM offers the following features:

- in-situ sample and tip exchange (manipulator see bottom picture, right side)
- vibration isolation ensured by a spring suspension system with eddy current damping and pneumatic damping legs
- variable temperatures from 5 K (pumped 2 K) up to room temperature ($\sim$ 300 K)
- fast system cool-down (5 K within $\approx$ 6 hours)
- sample pre-cooling to 50 K on the manipulator stage
- fast sample cool-down (5 K within $\approx$ 2 hours)
- on-line optical access
- on-line four terminal transport measurements
- up to 6 samples can be stored at low temperature (77 K)

Preparation and Characterization Possibilities

Additional to the LT-STM analysis chamber another UHV-preparation chamber (see top picture, right side) allows for sample preparation and characterization under UHV-conditions. Substrates can be prepared by an argon sputter gun and thermal annealing. Molecules can be deposited onto the surface employing a three crucible evaporator. For sample characterization low-energy-electron-diffraction (LEED) and quadrupole mass spectrometry can be utilized.

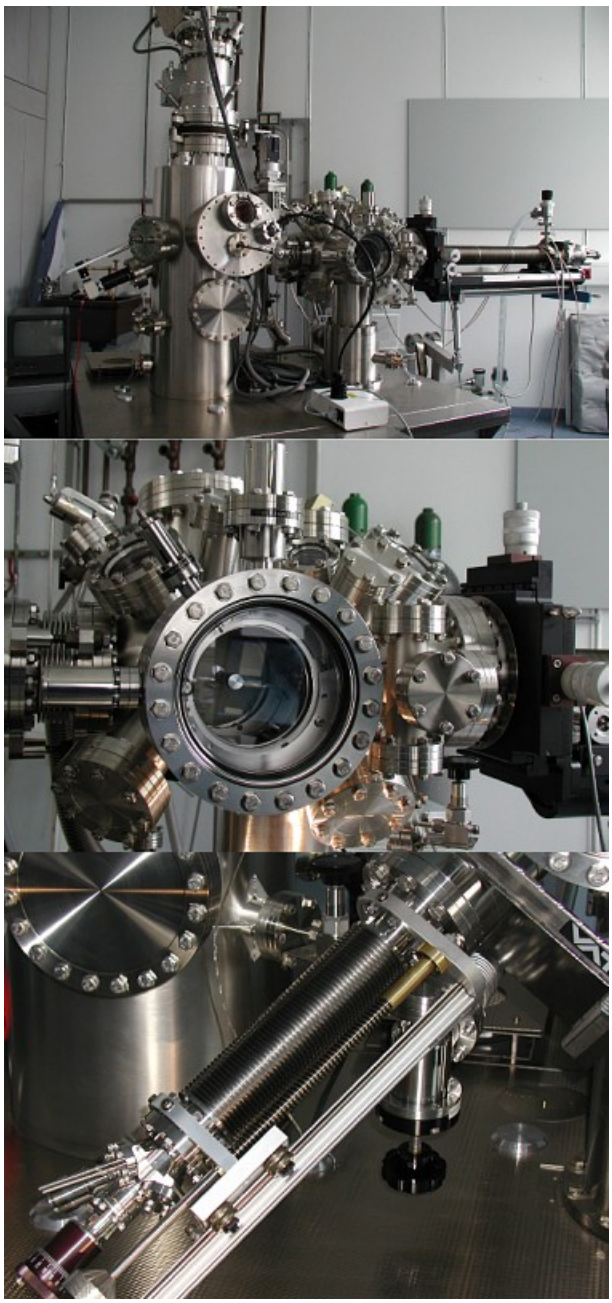

Figure 19: top: entire setup viewed from the main operation side, bottom: LEED system enlarged.

The preparation and characterization include:

Argon Sputter Gun:

Inside the right chamber clean single crystalline substrates are prepared by ion-sputtering and subsequent thermal annealing, which can be controlled by a three grid LEED (middle picture) in a vacuum of 10^{-11} mbar.

Evaporator for Organic Material:

A microprocessor controlled evaporator allows deposition of up to three different organic materials at the same time. Crucibles are refilled without breaking the vacuum of the main chamber.

Sample Heating/Cooling Stage:

The preparation facilities allow a direct current and indirect heating of the sample up to 800 °C and sample cooling to 50 K on the manipulator (top picture, far right).

Low Energy Electron Diffraction (LEED):

The surface ordering of (reconstructed) substrate/single crystal surfaces or molecular ad-layers can be analyzed by low energy electron diffraction.

Quadrupole Mass Spectrometer:

Samples are additionally characterized by desorption spectroscopy with a quadrupole mass spectrometer. The desorbing molecules are ionized in a crossbeam ion source and accelerated in the quadrupole mass spectrometer, which either uses a Faraday cup or secondary electron multiplier (SEM) as detector with a mass resolution up to 2048 amu.

Multiple additional vacuum ports allow further extensions in the future.

Publications

1. KARTSOVNIK M.V., SIMONOV S., ANDRES D., BIBERACHER W., KUSHCH W., MÜLLER H., SHEIKIN I.,
   Incoherent versus coherent interlayer transport in layered conductors under an magnetic field
   J. Phys. IV France **131**, 265-268 (2006).
2. WAGENKNECHT M., EITEL H., NACHTRAB T., PHILIPP J.B., GROSS R., KLEINER R., KOELLE D.,
   Laser Microscopy of Tunneling Magnetoresistance in Manganite Grain-Boundary Junctions
   Phys. Rev. Lett. **96**, 047203 (2006).
3. HACKL R., TASSINI L., VENTURINI F., ERB A., HARTINGER CH., KIKUGAWA N., FUJITA T.,
   Raman study of ordering phenomena in copper-oxygen systems
   J. Phys. Chem. Sol. **67**, 289-293 (2006).
4. KARTSOVNIK M.V., ANDRES D., SIMONOV S.V., BIBERACHER W., SHEIKIN I., KUSHCH N.D., MÜLLER H.,
   Angle-Dependent Magnetoresistance in the Weakly Incoherent Interlayer Transport Regime in a Layered Organic Conductor
   Phys. Rev. Lett. **96**, 166601 (2006).
5. GEPRÄGS S., MAJEWSKI P., GROSS R., RITTER C., ALFF L.,
   Electron doping in the double perovskite $La_xA_{2-x}CrWO_6$ with A = Sr and Ca
   J. Appl. Phys. **99**, 08J102 (2006).
6. EINZEL D.,
   Superfluids
   Encyclopedia of Mathematical Physics, Elsevier Ltd. (2006).
7. LERF A., BUCHSTEINER A., PIEPER J., SCHÖTTL S., DEKANY I., SZABO T., BOEHM H.P.,
   Hydration behavior and dynamics of water molecules in graphite oxide
   J. Phys. Chem. Sol. **67**, 1106-1110 (2006).
8. UHLIG K., WANG C.,
   Cryogen-free dilution refrigerator precooled by a pulse-tube refrigerator with non-magnetic regenerator
   Cryogenics **51**, 939-945 (2006).
9. JAEGER C., BIHLER C., VALLAITIS T., GÖNNENWEIN S.T.B., OPEL M., GROSS R., BRANDT M.S.,
   Spin-glass-like behavior of Ge:Mn
   Phys. Rev. B **74**, 045330 (2006).
10. GROSS R.,
    Grain boundaries in high temperature superconductors: A retrospective view
    Physica C **432**, 105-115 (2006).
11. GROSS R.,
    Magnetic Tunnel Junctions Based on Half-Metallic Oxides
    in *Nanoscale Devices – Fundamentals and Applications*, R. Gross, A. Sidorenko, and L. Tagirov (eds.), Springer Verlag (2006), pp. 49-110.
12. HERMANN B.A., SCHERER L.J., HOUSECROFT C.E., CONSTABLE E.C.,
    Self-Organized Monolayers : A Route to Conformational Switching and Read-Out of Functional Supramolecular Assemblies by Scanning Probe Methods
    Adv. Funct. Mater. **16**, 221-235 (2006).
13. REDDY S. BHASKAR, KANT K. MOHAN, RAO K. PRASAD, OPEL M., GROSS R., RAO M.S. RAMACHANDRA,
    Ferroelectric and magnetic properties of Ho_2CuTiO_6 double perovskite
    Journal of Magnetism and Magnetic Materials **303**, e332-334 (2006).
14. HASAN R.A., KARTSOVNIK M.V., PESCHANSKY V.G.,
    Hall effect in organic layered conductors
    Condensed Matter Physics **9**, 145-150 (2006).
15. NIELSEN K., BAUER S., LÜBBE M., GÖNNENWEIN S.T.B., OPEL M., SIMON J., MADER W., GROSS R.,
    Ferromagnetism in epitaxial $Zn_{0.95}Co_{0.05}O$ films grown on ZnO and Al_2O_3
    phys. stat. sol. (a) **203**, 3581-3596 (2006).

16. BUCHSTEINER A., LERF A., PIEPER J.,
Water Dynamics in Graphite Oxide Investigated with Neutron Scattering
J. Phys. Chem. B **110**, 22328-22338 (2006).
17. EVTUSHINSKY D.V., KORDYUK A.A., BORISENKO S.V., ZABOLOTNYY V.B., KNUPFER M., FINK J., BÜCHNER B., PAN A.V., ERB A., LIN C.T., BERGER H.,
Unadulterated spectral function of low-energy quasiparticles in $Bi_2Sr_2CaCu_2O_{8+\delta}$
Phys. Rev. B **74**, 172509 (2006).
18. ZABOLOTNYY V.B., BORISENKO S.V., KORDYUK A.A., FINK J., GECK J., KOITZSCH A., KNUPFER M., BÜCHNER B., BERGER H., ERB A., LIN C.T., KEIMER B., FOLLATH R.,
Effect of Zn and Ni Impurities on the Quasiparticle Renormalization of Superconducting Bi-2212
Phys. Rev. Lett. **96**, 037003 (2006).
19. HERMANN B.A.,
Self-Assembled Monolayers
Encyclopedia of Supramolecular Chemistry, J.A. Atwood, J.W. Steed, Eds. **1**, 1-9 (2006).
20. HERMANN B.A.,
Scanning Probe Microscopy
Analytical Methods of Supramolecular Chemistry, C.A. Schalley, Ed. **1** , 337-390 (2006).
21. KEIZER R.S., GÖNNENWEIN S.T.B., KLAPWIJK T.M. MIAO G.-X., XIAO G., GUPTA A.,
A spin triplet supercurrent through the half-metallic ferromagnet CrO_2
Nature **439**, 825 (2006).
22. LIMMER W., GLUNK M., DÄUBLER J., HUMMEL T., SCHOCH W., SAUER R., BIHLER Ch., HÜBL H., BRANDT M.S., GÖNNENWEIN S.T.B.,
Angle-dependent magnetotransport in cubic and tetragonal ferromagnets: Application to (001)- and (113)A-oriented (Ga,Mn)As
Phys. Rev. B **74**, 205205 (2006).
23. BIHLER Ch., HÜBL H., BRANDT M.S., GÖNNENWEIN S.T.B., REINWALD M., WURSTBAUER U., DÖPPE M., WEISS D., WEGSCHEIDER W.,
Magnetic anisotropy of $Ga_{1-x}Mn_xAs$ thin films on GaAs (311)A probed by ferromagnetic resonance
Appl. Phys. Lett. **89**, 012507 (2006).
24. DEVEREAUX T.P., HACKL R.,
Inelastic Light Scattering from Correlated Electrons
Rev. Mod. Phys. **78**, 4 (2006).
25. AHLERS S., BOUGEARD D., SIRCAR N., ABSTREITER G., TRAMPERT A., OPEL M., GROSS R.,
Magnetic and structural properties of GeMn films: precipitation of intermetallic nanomagnets
Phys. Rev. B **74**, 214411 (2006).
26. GROSS R., MARX A., EINZEL D.,
From Flux Quantization to Superconducting Quantum Bits (dedicated to Prof. V.L. Ginzburg on the occasion of his 90th birthday)
J. Supercond. Novel Magn., DOI 10.1007/s10948-006-0167-6 (2006).
27. DIACONU, M., SCHMIDT, H., HOCHMUTH, H., LORENZ, M., BENNDORF, G., LENZNER, J., SPEMANN, D., SETZER, A., ESQUINAZI, P., PÖPPL, A., VON WENCKSTERN, H., NIELSEN, K.-W., GROSS, R., SCHMID, H., MADER, W., WAGNER, G., GRUNDMANN, M.,
Room-temperature ferromagnetic Mn-doped ZnO-films obtained by pulsed laser deposition
J. Magn. Magn. Mat. **307**, 212–221 (2006).
28. LU, YAFENG, KLEIN, J., HERBSTRITT, F., PHILIPP, J.B., MARX, A., GROSS, R.,
Effect of strain and tetragonal lattice distortion in doped perovskite manganites
Phys. Rev. **B 73**, 184406 (2006).
29. DOLL R., EINZEL D.,
Ginzburg-Landau Analysis of the Doll-Näbauer Experiment (dedicated to Prof. V.L. Ginzburg on the occasion of his 90th birthday)
J. Supercond. Novel Magn., accepted for publication (2006).
30. LERF A., ERB A., WAGNER F.E., POYATO J., PÉREZ-RODRIGUEZ J.L., PÉREZ-RODRIGUEZ L.A.,
Reduction reactions induced by heating in hydrazinium and ammonium vermiculites from

Andulusia (Spain)
Phys. Chem. Miner., submitted for publication (2006).

31. MADEK K., BEUTNER S., WILD G., PROBST CH., WEIDES M., KOHLSTEDT H., MARX A., GROSS R.,
Observation of Macroscopic Quantum Behavior in p Josephson Junctions with Ferromagnetic Interlayer
Phys. Rev. Lett., submitted for publication (2006).
32. GEPRÄGS S., OPEL M., GÖNNENWEIN S.T.B., GROSS R.,
Multiferroic Materials Based on Artificial Thin Film Heterostructures
Philosophical Magazine Letters, accepted for publication (2006).
33. MAJEWSKI P., BOGER A., GEPRÄGS S., SIMON J., YU W., MADER W., GÖNNENWEIN S.T.B., OPEL M., GROSS R.,
Magnetotransport in epitaxial Sr_2CrWO_6 thin films
European Physical Journal B, submitted for publication (2006).
34. SCHUBERTH E.A., KATH M., BAGO S.,
Pulsed NMR in the Nuclear Spin Ordered Phases of Solid ^{3}He in a Silver Sinter
Proc. LT24, Journal Low Temp. Physics, in press (2006).
35. KARTSOVNIK M.V., ANDRES D., BIBERACHER W., GRIGORIEV P.D., SCHUBERTH E.A., MÜLLER H.,
New Electronic Phase Transitions in α-(BEDT-TTF)$_2$KHg(SCN)$_4$
J. Phys. IV (Paris), submitted to publication (2006).
36. FLACHBART K., GABANI S., NEUMAIER K., PADERNO Y., PAVLIK V., SCHUBERTH E., SHITSEVALOVA N.,
Specific Heat of SmB_6 at very low temperatures
Physica B, in press (2006).
37. KARTSOVNIK M.V., ANDRES D., BIBERACHER W.,
Hierarchy of the density-wave states and superconductivity in the organic conductor α-(BEDT-TTF)$_2$KHg(SCN)$_4$
C.R. Chimie, in press (2006).
38. RAMA, N., SANKARANARAYANAN, V., OPEL, M., GROSS, R. RAMACHANDRA RAO, M.S.,
Influence of disorder on the low and high temperature magnetization and magnetoresistance in $Pr_{0.6}R_{0.1}Sr_{0.3}MnO_3$ (R = Tb, Y, Ho and Er) manganite
J. Alloys and Compounds , in press (2006).
39. CONSTABLE E.C. HÄUSSLER M., HERMANN B.A., HOUSECROFT C.E., NEUBURGER M., SCHAFFNER S., SCHERER L.,
Self-assembled monolayers as two-dimensional crystals: relationship to three-dimensional crystals
Cryst. Eng. Com., submitted to publication (2006).
40. GÖNNENWEIN S.T.B., KEIZER R.S., SCHINK S.W., VAN DIJK I., KLAPWIJK T.M., MIAO G.-X., XIAO G., GUPTA A.,
Planar Hall effect and magnetic anisotropy in epitaxially strained chromium dioxide thin films
Appl. Phys. Lett., submitted to publication (2006).
41. TASSINI L., PRESTEL W., ERB A., LAMBACHER M., HACKL R.,
Ordering versus superconductivity in CuO_2 compounds
Nature Physics, submitted to publication (2006).
42. GÖNNENWEIN, S.T.B., SCHINK, S.W., BRANDLMAIER, A., BOGER, A., OPEL, M., GROSS, R., KEIZER, R.S., KLAPWIJK, T.M., GUPTA, A., HUEBL, H., BIHLER, C., BRANDT, M.S.,
Electrically detected ferromagnetic resonance
Appl. Phys. Lett., submitted for publication (2006).
43. MARIANTONI, M., STORCZ, M.J., WILHELM, F.K., OLIVER, W.D., EMMERT, A., MARX, A., GROSS, R., CHRIST, H., SOLANO, E.,
On-Chip Microwave Fock States and Quantum Homodyne Measurements
Europhys. Lett., submitted for publication (2006).
44. STORCZ, M.J., MARIANTONI, M., CHRIST, H., EMMERT, A., MARX, A., OLIVER, W.D., GROSS, R., WILHELM, F.K., SOLANO, E.,
Orthogonally-Driven Superconducting Qubit in Circuit QED

Phys. Rev. Lett., submitted for publication (2006).

Theses, Appointments, Awards

Completed and ongoing Ph.D. Theses

1. **Magnetischer Austauschmechanismus und Magnetotransport in ferromagnetischen Doppelperowskiten $A_2BB'O_6$**
   Petra Majewski, Juli 2006.
2. **Symmetrie des Ordnungsparameters und Pseudogap-Verhalten in Hochtemperatur-Supraleitern**
   Bettina Welter, seit August 2000.
3. **Herstellung und Charakterisierung von supraleitenden Fluss-Quantenbits**
   Frank Deppe, seit April 2002.
4. **Raman scattering in materials with quantum phase transitions**
   Leonardo Tassini, seit April 2003.
5. **Supraleitende Quantenbits mit π-Josephson-Kontakten für die Quanteninformationsverarbeitung**
   Matteo Mariantoni, seit November 2003.
6. **Wachstum und Physik künstlicher magnetischer Heterostrukturen**
   Karl Nielsen, seit Dezember 2003.
7. **Magnetisierungsmessungen an festem ^{3}He bei ultratiefen Temperaturen**
   Matthias Kath, seit April 2004.
8. **Supraleitende Quantenbits mit Supraleiter-Ferromagnet-Supraleiter Josephson-Kontakten**
   Georg Wild, seit September 2004.
9. **Kristallzüchtung und Charakterisierung von elektronendotierten Hochtemperatur-Supraleitern**
   Michael Lambacher, seit September 2004.
10. **Spin-Engineering in funktionalen Schichtsystemen aus Übergangsmetalloxiden**
    Stephan Geprägs, seit Oktober 2004.
11. **Herstellung und Charakterisierung von supraleitenden Nanostrukturen für die Realisierung von supraleitenden Quantenbits**
    Tobias Heimbeck, seit November 2004.
12. **Untersuchung der Wechselwirkungspotenziale in Kupratsupraleitern durch quantitativen Vergleich spektroskopischer Resultate**
    Wolfgang Prestel, seit November 2004.
13. **Entwicklung von Verfahren zur Manipulation und zum Auslesen von supraleitenden Quantenbits**
    Karl Madek, seit März 2005.
14. **Tunnelkontakte und Spininjektoren auf der Basis von ferromagnetischen Übergangsmetalloxiden**
    Andrea Boger, seit März 2005.
15. **Kohärente Dynamik und Dekohärenz in supraleitenden Quantenbits**
    Edwin Menzel, seit Januar 2006.
16. **Quantenelektrodynamik mit supraleitenden Schaltkreisen**
    Thomas Niemczyk, seit Juli 2006.
17. **Multiferroisches Verhaltung und steuerbarer Magnetismus in oxidischen Heterostrukturen**
    Andreas Brandlmaier, seit Dezember 2006.

Completed and ongoing Diploma, Bachelor, Master Theses

1. **Makroskopisches Quantenverhalten von Josephson-Kontakten aus Hochtemperatur-Supraleitern**
   Renke Stolle, Januar 2006
2. **Magnetische und suprafluide Eigenschaften von ^{3}He**
   Simone Bago, Januar 2006.
3. **Circuit Quantum Electrodynamics (c-QED) with Superconducting Flux Qubits**
   Andreas Emmert, Februar 2006.
4. **Herstellung von π-Josephson-Kontakten mit Supraleiter/Ferromagnet/Supraleiter Schichtsystemen**
   Bernhard Huber, Februar 2006.
5. **Probing Quantum States of Josephson Junctions with Ferromagnetic Barriers by Microwaves**
   Sven Beutner, März 2006.
6. **Novel Room Temperature Ferromagnetic Semiconductors: Preparation and Characterization of Bulk Samples and Thin Films of Cu-doped ZnO**
   Amilcar Bedoya Pinto, April 2006.
7. **Superconducting Microwave Circuits for Quantum Experiments**
   Thomas Niemczyk, Mai 2006.
8. **Quantenelektronik mit supraleitenden Bauelementen – Herstellung und Charakterisierung von Fluss-Qubits**
   Martin Göppl, Mai 2006.
9. **Cell Curing**
   Christiane Reuter, Juni 2006.
10. **Raumtemperatur-Ferromagnetismus in Cobalt-dotiertem ZnO**
    Sebastian Bauer, Juli 2006.
11. **Magnetotransport Based Determination of the Magnetic Anisotropy in Materials for Spintronics**
    Sebastian Schink, September 2006.
12. **Magnetische Anisotropie in dünnen Schichten aus Magnetit**
    Andreas Brandlmaier, Oktober 2006.
13. **Characterization of Humidity Sensors for Application on the High Altitude Research Aircraft HALO**
    Ingmar Mayerbuch, Oktober 2006.
14. **Transport und Ramanstreuung in unkonventionellen Supraleitern**
    Ludwig Klam, Dezember 2006.
15. **Measurement of Phonon Linewidths in $YBa_2Cu_3O_{7-\delta}$ with Neutron Spin Echo**
    Markus Bröll, Dezember 2006.
16. **Spinabhängiger Transport in Magnetit**
    Wolfgang Kaiser, Dezember 2006.
17. **Superconducting Microwave Circuits for Quantum Experiments**
    Ferhat Katmis, Dezember 2006.
18. **Herstellung und Charakterisierung einer definierten elektromagnetischen Umgebung für supraleitende Fluss-Qubits**
    Sonja Dandl, Dezember 2006.
19. **STM und AFM Untersuchungen an großen Molekülen und biologischen Systemen**
    Carsten Rohr, seit Februar 2006.
20. **Magnetic Field Effects in the CDW Organic Superconductor α-(BEDT-TTF)$_2$MHg(SCN)$_4$**

Sebastian Jakob, seit März 2006.

21. **Design, Fabrication, and Characterization of Microwave Resonators for Circuit-QED**
    Susanne Hofmann, seit April 2006.
22. **Wechselwirkung zwischen ferromagnetischen und dielektrischen Eigenschaften dünner Filme**
    Franz Czeschka, seit April 2006.
23. **Magnetotransport in dünnen Schichten aus Übergangsmetall-dotiertem Zinkoxid**
    Konrad Senn, seit Juni 2006.
24. **Rastersondenmikroskopie-Untersuchungen an homogenen und heterogenen Molekülanordnungen auf Oberflächen**
    Kathrin Gruber, seit Juli 2006.
25. **Oberflächencharakterisierung mittels STM und AFM an oxidischen Materialien**
    Johannes Büttner, seit November 2006.
26. **Untersuchung von Y123 in der Umgebung des Einsatzpunktes der Supraleitung**
    Nathalie Munnikes, seit Dezember 2006.
27. **Magnetische Anisotropie und Verspannung in dünnen ferromagnetischen Schichten**
    Mathias Weiler, seit Dezember 2006.
28. **Magneto-galvanische Effekte und Verspannungen in dünnen ferromagnetischen Filmen**
    Matthias Althammer, seit Dezember 2006.
29. **Untersuchung von $La_{2-x}Sr_xCuO_4$ und $Re_{2-x}Ce_xCuO_4$ (Re=Nd, Pr) nahe des Einsatzpunktes der Supraleitung bei hoher Dotierung**
    Bernhard Muschler, seit Dezember 2006.

Research Projects and Cooperations

Many of our research projects are benefitting from the collaboration with external groups in joint research projects, as well as from individual collaborations, exchange programs and visitors. Several collaborations are based on joint projects, which are financially supported by different organizations (see list below). A large number of collaborations also exists with several universities and other research institutions without direct financial support. These are also listed below.

Funded Projects

Deutsche Forschungsgemeinschaft: Exzellenzinitiative

Cluster of Excellence "Nanosystems Initiative Munich"

1. Project Area A: Single Electron and Spin Systems
   R. Gross, S.T.B. Gönnenwein
2. Project Area C: Quantum Information Nanosystems
   R. Gross, A. Marx
3. Project Area F: Nanoanalytics and Enabling Techniques
   B.A. Hermann

Deutsche Forschungsgemeinschaft: Sonderforschungsbereiche

Sonderforschungsbereich 631: "Festkörperbasierte Quanteninformationsverarbeitung: Physikalische Konzepte und Materialaspekte"

1. Project A3/A4: *Supraleitende Bauelemente mit π-Kontakten als Grundelemente für Quanteninformationssysteme*
   R. Gross, A. Marx
2. Project C5: *Spinabhängiger Transport in nanostrukturierten Festkörpern*
   A. Marx, R. Gross, M. Opel
3. Project S: *Verwaltung des Sonderforschungsbereichs*
   R. Gross

Deutsche Forschungsgemeinschaft: Forschergruppen

Forschergruppe 538: "Dotierungsabhängigkeit von Phasenübergängen und Ordnungsphänomenen in Kupratsupraleitern"

1. Project: *Einkristallzüchtung von p- und n-dotierten Kupratsupraleitern*
   A. Erb, R. Gross

2. Project: *Raman-Untersuchungen zu konkurrierenden Ordnungsphänomennen in Kupraten*
   R. Hackl, R. Gross

3. Project: *Koordination der Forschergruppe*
   R. Hackl

Deutsche Forschungsgemeinschaft: Schwerpunktprogramme

1. Project: *Neue funktionale Schichtsysteme auf der Basis künstlicher heteroepitaktischer Mehrlagenstrukturen aus Übergangsmetalloxiden*
   im Rahmen des Schwerpunktprogramms 1157 *Integrierte elektrokeramische Funktionsstrukturen*
   R. Gross (Az. GR 1132/13-1 und 1132/13-2)

2. Project: *Spin injection, spin transport and controllable ferromagnetism in transition metal doped ZnO*
   im Rahmen des Schwerpunktprogramms 1285 *Halbleiter-Spinelektronik*
   R. Gross, S.B.T. Gönnenwein, M. Opel (Az. GR 1132/14-1)

Deutsche Forschungsgemeinschaft: Normalverfahren

1. Entwicklung eines hochgenauen Rotatiossensors mit superfluidem ^{3}He als Arbeitsmedium
   E. Schuberth (Az. Schu 450/4-1+2)

European Union

1. European Science Foundation Network *"Thin Films for Novel Oxide Devices: THIOX"*
   R. Gross; coordination by Prof. D. Blank, University of Twente, The Netherlands
   partners: several European Universities and research facilities.

2. Research and Training of Young Researchers on the *"Magnetic Properties of ^{3}He by Means of Neutron Diffraction"*
   E. Schuberth; coordination by Dr. Konrad Siemensmeyer, Hahn–Meitner Institute Berlin GmbH
   European Community, Contract No.: HPRN-CT-2000-00166
   Partners: Hahn–Meitner Institut, Berlin, Univ. of Florida, Royal Holloway College, London, Univ. Liverpool, CNRS, Grenoble and Univ. Paris, Saclay.

3. ERA-Chemistry-network: *Hierarchically organized chemical structures: from molecules to hybrid materials*, project: *Probing Hierarchical Self-Assemblies Relevant for Drug and Vaccine Design by Employing STM*
   B.A. Hermann (project number ERA HE 5162/1-1)

Alexander von Humboldt Stiftung

1. Humboldt Forschungsstipendium "Devereaux"
   R. Hackl (Förderkennzeichen IV-USA/109800 6 STP)

2. Humboldt Forschungspreis “Di Castro”
   R. Hackl (Förderkennzeichen IV-ITA/111548 6 GSA)

3. Humboldt Forschungspreis “Zawadowski” (Wiedereinladungsprogramm)
   R. Hackl (Förderkennzeichen 3-3-UNG/1052138)

4. Institutspartnerschaft “Kamaras-Hackl”
   R. Hackl (Förderkennzeichen 3-Fokoop-DEU/1009755)

Ministerio de Educacion y Ciencia, Spanien

1. Intercalación de minerales de la arcilla por medio de tratamiento con ultrasonidos y reacciones de transferencia de electrones. Producciòn de arcillas funcionalizadas con estructuras complejas jerarquizadas en el espacio interlaminar.
   J.L. Perez-Rodriguez, A. Lerf (Reference No. : MAT2005-04838)

IDK-NBT

1. STM on magnetic layers and self-organized magnetic molecules
   B.A. Hermann, coordination by C. Bräuchle and J. Rädler (IDK-NBT 1506-42501-1)

Research Equipment financed via HBFG

1. Helium Liquefaction System, Linde TCF 20
   R. Gross (reference No.: HBFG-163-957)

2. Reactive Ion Etching System
   R. Gross (reference No.: HBFG-163-1009)

Conferences and Workshops

The Walther-Meißner-Institute has organized/co-organized the following conferences and workshops in 2006:

1. **International Workshop on Solid-State Based Quantum Information (QIP 2006)**
   May 24 – 26, 2006, Herrsching, Germany.

International Workshop
on
Solid State Based
Quantum Information Processing
QIP 2006

May 24 – 26, 2006
Herrsching, Bavaria

SFB 631 Deutsche Forschungsgemeinschaft DFG

2. **Workshop des Arbeitskreises** *"Deposition und Integration"* **des DFG-Schwerpunktprogramms SPP 1157** ***"Integrierte Elektrokeramische Funktionsstrukturen"***
   February 12 – 13, 2006, Garching, Germany.

Collaborations

Other collaborations without direct project funding involve:

- University of Waterloo, Department of Physics, Ontario, Canada (Prof. Dr. T.P. Devereaux)
- NTT Basic Research Laboratories, Japan (Prof. Dr. H. Takayanagi)
- Instituto de Ciencia de Materiales de Sevilla, Spain (Prof. J. Poyato, Prof. J.L. Perez-Rodriguez)
- Research Institute for Solid State Physics and Optics, Hungarian Academy of Sciences, Budapest, Hungary (Prof. K. Kamaras and Prof. I. Tüttö)
- University of Rome "La Sapienza", Rome, Italy (Prof. S. Caprara, Prof. C. Di Castro and Prof. M. Grilli)
- Hungarian Academy of Sciences, Budapest University of Technology and Economics Budapest, Hungary (Dr. Attila Virosztek, Prof. Dr. A. Zawadowski)
- Central Research Institute of the Electric Power Industry, Tokyo, Japan (Dr. S. Ono and Dr. Y. Ando)
- University of Fribourg (Prof. C. Bernhard)
- University of Basel, Institute of Inorganic Chemistry, Switzerland (Prof. E. Constable, Prof. C. Housecroft)
- University of Basel, Institute of Physics, Switzerland (Prof. H.-J. Güntherodt)
- European Synchrotron Radiation Facility (ESRF), Grenoble (Dr. H. Müller, Dr. J. Criginski Cezar)
- LEPES, CNRS, Grenoble (Dr. J. Dumas and Prof. C. Schlenker)
- University of Florida, USA (Prof. D. Adams, Prof. Y. Takano)
- Materials Science Research Centre, IIT Madras, India (Prof. M.S. Ramachandra Rao)
- Trinity College, Physics Department, Dublin, Ireland (Prof. I.V. Shvets)
- Kungliga Tekniska Högskolan (KTH) Stockholm, Sweden (Dr. G. Vaitheeswaran, Dr. V. Kanchana)
- ETH-Zurich, Schweiz (Prof. P. Seeberger)
- Chalmers University of Technology, Gothenburg, Sweden (Prof. Dr. P. Delsing)
- Universidad del Pais Vasco, San Sebastian, Spain (Prof. A. Rubio)
- MINT Center, University of Alabama (Prof. A. Gupta)
- Materials Physics Laboratory, Helsinki University of Technology, Finland (Dr. Tero Heikkilä)
- Department of Condensed Matter Physics, The Weizmann Institute of Science, Israel (Dr. Moshe Schechter)
- Kavli Institute of NanoScience, Delft University of Technology, Delft, The Netherlands (Prof. T.M. Klapwijk)
- Institute for Experimental Physics, Slowakian Academy of Sciences, Kosice, Slovakia (Prof. K. Flachbart)
- High–Magnetic–Field Laboratory, Grenoble, France (Dr. I. Sheikin)
- B. Verkin Institute for Low Temperature Research and Engineering, Kharkov, Ukraine (Prof. V.G. Peschansky)
- Landau Institute for Theoretical Physics, Chernogolovka, Russia (Dr. P. Grigoriev)
- Royal Holloway University, London, UK (Prof. J. Saunders)

- University of Liverpool, UK (Dr. J. Goff)
- CNRS Grenoble, France (Prof. H. Godfrin)
- Vericold Technologies, Ismaning, Germany (Dr. J. Höhne, Dr. M. Bühler)
- University of Bonn, Germany (Prof. W. Mader)
- HMI Berlin, Germany (Dr. A. Buchsteiner, Dr. J. Pieper, Dr. K. Siemensmeyer)
- IFW Dresden, Germany (Prof. B. Büchner, Prof. J. Fink, Dr. S. V. Borisenko, Dr. M. Knupfer)
- Max-Planck-Institut für Festkörperforschung, Stuttgart (Prof. B. Keimer)
- University of Tübingen, Germany (Prof. R. Kleiner, Prof. D. Kölle)
- University of Würzburg, Germany (Prof. W. Hanke, Prof. L. Molenkamp)
- University of Augsburg, Germany (Prof. Dr. P. Hänggi)
- Brandenburgisch-Technische Universität Cottbus (Prof. D. Schmeißer)
- University of Hamburg, Germany (Dr. G. Meier)
- University of Ulm, Abt. Halbleiterphysik (Dr. W. Limmer)
- Walter-Schottky-Institut, Garching, Germany (Prof. G. Abstreiter, Prof. J. Finley, Dr. M. Brandt, Dr. D. Bougeard)
- Ludwig-Maximilians-University of Munich (Prof. J.P. Kotthaus, Prof. J. von Delft, Prof. E. Frey, Prof. T. Franosch, Prof. J. Rädler, Dr. B. Nickel)
- Physik Department der TUM, Lehrstuhl E10 (Prof. D. Grundler)
- Anorganic Chemistry, TU Munich, Germany (Prof. T. Fässler)

Stays abroad

Extended visits of members of the Walther-Meißner-Institute at foreign research laboratories:

1. **Mark Kartsovnik**
   High Magnetic Field Laboratory, Grenoble, France
   12. 03. – 19. 03. 2006
2. **Mark Kartsovnik, Sebastian Jakob, Werner Biberacher**
   High Magnetic Field Laboratory, Grenoble, France
   07. 05. – 14. 05. 2006
3. **Matthias Opel**
   European Synchrotron Radiation Facility (ESRF), Grenoble
   21. 04. – 28. 04. 2006
4. **Bianca Hermann**
   University of Basel, Institute of Physics (Prof. E.C. Constable and Prof. H.-J. Güntherodt) Basel, Switzerland
   28. 02. – 03. 03. 2006, 12. 04. – 13. 04. 2006, 28. 10. – 05. 11. 2006
5. **Rudolf Hackl**
   Hungarian Academy of Sciences, Research Institute for Solid State Physics and Optics (Prof. I. Tüttö) and Budapest University of Technology and Economics (Prof. A. Jánossy and Prof. Zawadowski)
   06. 04. – 12. 04. 2006

Conference Talks and Seminar Lectures

B.S. Chandrasekhar

1. **Low Temperature Physics and Physicists sixty years ago: Some Reminiscences**
   06. 09. 2006
   Max-Planck-Institut für Chemische Physik fester Stoffe, Dresden.
2. **Low Temperature Physics and Physicists six decades ago**
   19. 09. 2006
   New Cavendish Laboratory, University of Cambridge.
3. **Low Temperature Physics and Physicists Six Decades Ago**
   07. 12. 2006
   Nehru Centre for Advanced Scientific Research, Bangalore,India.

Dietrich Einzel

1. **Die Scherviskosität von suprafluidem ^{3}He in Aerogel**
   14. 01. 2006
   Kommissionssitzung Walther-Meißner-Institut.
2. **Was ist Licht? Antworten der Physik**
   20. 03. 2006
   Bayerische Akademie der Wissenschaften, Öffentlicher Vortrag im Rahmen der Vortragsreihe Licht der Sprecher der Wissenschaftler.
3. **The shear viscosity of superfluid ^{3}He in aerogel**
   15. 11. 2006
   Max-Planck-Institut für Festkörperforschung, Stuttgart.

Andreas Erb

1. **Crystal growth of the high temperature superconductors**
   25. – 30. 06. 2006
   C-MRS Meeting Beijing, China.
2. **Crystal growth of the high temperature superconductors**
   28. – 29. 09. 2006
   Workshop der Deutschen Gesellschaft für Kristallwachstum und Kristallzüchtung (DGKK), Garching.
3. **Crystal growth of the high temperature superconductors**
   24. 11. 2006
   Max-Planck-Institut für Festkörperforschung, Stuttgart.

Sebastian Gönnenwein

1. **Electronic Transport in Single Ferromagnetic Domains**
   14. 03. 2006
   Festkörperphysik-Seminar, Physikalisches Institut, Eberhard Karls Universität, Tübingen.
2. **Triplet supercurrent through a half-metallic ferromagnet**
   08. 05. 2006
   ESF Workshop on Trends in Future Electronics, Bordeaux, France.
3. **Emil Warburg - die Physik: Ferromagnetische Hysterese und magnetische Nanostrukturen**
   06. 10. 2006
   Physikalisch-Technische Bundesanstalt, Berlin.

Rudolf Gross

1. **Multifunctional Oxide Thin Films and Heterostructures**
   02. 06. 2006
   Kolloquium des Fachbereichs für Physik, Martin-Luther-Universität Halle-Wittenberg.

2. **Quantum Information Processing with Superconducting Flux Qubits**
   8^{th} International Conference on Materials and Mechanisms of Superconductivity and High Temperature Superconductors
   July 09–14, 2006, Dresden, Germany.

3. **Ferromagnetic Oxide Heterostructures for Spin Electronics**
   R. Gross
   E-MRS Fall Meeting 2006
   September 04 – 08, 2006, Warsaw, Poland.

4. **Superconducting Quantum Circuits: On the way to Solid-State Quantum Information Processing**
   17.–29. 09. 2006
   Ferienakademie der TU-München, der Universität Erlangen-Nürnberg und der Universität Stuttgart, Sarntal, Italien.

5. **Multifunctional Oxide Thin Films and Heterostructures for Spintronics**
   21. 11. 2006
   Kolloquium des Fachbereichs für Physik, Technische Universität Cottbus.

Rudolf Hackl

1. **Electron-phonon coupling in the cuprates: how relevant is it?**
   07. 04. 2006
   Colloquium on the occasion of A. Zawadowski's 70th birthday, Budapest, Hungary.

2. **Electronic properties of antiferromagnetic and strongly underdoped cuprates**
   27. 06. 2006
   Institut für Festkörper- und Werkstoffforschung, Dresden

3. **From a Mott insulator to a d-wave superconductor**
   13. 07. 2006
   8th International Conference on Materials and Mechanisms of Superconductivity and High Temperature Superconductors, Dresden, Germany.

4. **Carrier dynamics in the cuprates**
   13. 10. 2006
   University of Bristol, United Kingdom.

5. **Carrier dynamics in the cuprates**
   12. 12. 2006
   Universität Stuttgart

6. **Raman study at the onset of superconductivity: relation between ordering and pairing**
   18. – 22. 12. 2006
   International Conference "Stripes 2006", Rome, Italy.

Bianca Hermann

1. **With Dynamic and Static Self-Organization to Well -Defined Molecular Monolayers – a Scanning Tunneling Microscopy Investigation**
   20. 02. 2006
   Department of Physical Chemistry, Mainz.

2. **Little Changes - big effects: Molecular Self-Organization probed by Scanning Tunneling Microscopy**
   29. 03. 2006
   Frühjahrstagung der Deutschen Physikalischen Gesellschaft, Dresden.
3. **Tracing Molecules - Scanning Tunneling Microscopy (STM) Used for Molecular Characterization**
   29. 06. 2006
   Department of Physics, AG Prof. Weiss and Prof. Strunk, Regensburg.
4. **Einblicke in die Nanowelt mit modernen mikroskopischen Methoden**
   06. 10. 2006
   Tagung der Internationalen Studiengesellschaft (ISG), Munich.
5. **Tracing Molecules - a Scanning Tunneling Microscopy (STM) Investigation of Molecular Structure and Dynamics**
   11. 10. 2006
   International Conference on Engineering Physics (VSG9) in Hanoi, Vietnam.
6. **Management mal X**
   30. 11. 2006
   Physiker bei der Arbeit, Physik Department, Universität Regensburg.

Mark Kartsovnik

1. **Interlayer between the charge-density-wave and superconducting instabilities in a layered organic conductor**
   09. – 14. 07. 2006
   8th International Conference on Materials and Mechanisms of Superconductivity and High Temperature Superconductors, Dresden, Germany.
2. **Unconventional interlayer magnetotransport in the weakly incoherent regime**
   02. – 07. 07. 2006
   International Conference on Science and Technology of Synthetic Metals, ICSM 2006, Dublin, Ireland

Anton Lerf

1. **Fe^{3+} intercalation into vermiculite or deposition of iron oxyhydroxides? A Mößbauer spectroscopy investigation**
   18. - 22. 09. 2006
   Mid European Clay Conference 2006, Opatija.
2. **Von der Welt der vernachlässigten Dimensionen zur Nanowelt**
   09. - 10. 11. 2006
   Innovationsforum "Nanobasierte Umwelttechnik", Jena.

Karl Madek

1. **Observation of Macroscopic Quantum Behavior in Josephson Junctions with Ferromagnetic Interlayer**
   03. – 05. 10. 2006
   Tagung "Kryoelektronische Bauelemente 2006", Ilmenau.

Matteo Mariantoni

1. **Generation and detection of microwave single photons**
   23. 03. 2006
   Frühjahrstagung der Deutschen Physikalischen Gesellschaft, Dresden.

2. **Multi-mode circuit QED**
   23. 03. 2006
   Frühjahrstagung der Deutschen Physikalischen Gesellschaft, Dresden.
3. **Nonclassical states of the microwave radiation**
   24. 05. 2006
   International Workshop on Solid-State Quantum Information Processing, QIP 2006, Herrsching, Germany.
4. **Nonlinear circuit QED with superconducting flux qubits**
   22. 09. 2006
   Institute for Quantum Computation, University of Waterloo, Canada.

Matthias Opel

1. **Deposition of novel integrated electroceramic functional structures**
   13. 02. 2006
   Treffen des Arbeitskreises Deposition und Integration des DFG-Schwerpunktprogramms SPP 1157, Garching.
2. **Magnetische Charakterisierung mittels SQUID-Messungen**
   06. 03. 2006
   Treffen des Arbeitskreises TEM und Charakterisierung des DFG-Schwerpunktprogramms SPP 1157, Universität Bonn.
3. **Herstellung und Charakterisierung magnetischer Tunnelkontakte**
   14. 06. 2006
   Treffen des Arbeitskreises Technologie und Demonstration des DFG-Schwerpunktprogramms SPP 1157, Fraunhofer-Institut für Angewandte Optik und Feinmechanik, Jena.
4. **Pulsed Laser Deposition for the Fabrication of Magnetic Heterostructures**
   13. 11. 2006
   IFF-Seminar, Institut für Festkörper- und Werkstoffforschung, Dresden.

Erwin Schuberth

1. **NMR an den kernspingeordneten Phasen von festem ^{3}He**
   16. 11. 2006
   Max-Planck-Institut für Chemie und Physik fester Stoffe, Dresden.

Leonardo Tassini

1. **Charge and spin ordering phenomena in HTSC**
   26. – 31. 03. 2006
   Frühjahrstagung der Deutschen Physikalischen Gesellschaft, Dresden.
2. **Raman study of underdoped $(Y_{1-y}Ca_y)Ba_2Cu_3O_{6+x}$**
   05. – 07. 07. 2006
   International Conference on Low-energy excitations in high-T_c superconductors, Stuttgart, Germany.

Seminars, Courses, Lectures and other Scientific Activities

The WMI Seminars

The WMI Seminars

The Friday Seminar — Walther-Meißner-Seminar on Current Topics in Low Temperature Physics

1. **Positioning for the nanoworld**
   Dr. Christoph Bödefeld, Firma Attocube
   27. 01. 2006
2. **Adiabatic passage and Fock state generation in superconducting circuits**
   Dr. Jens Siewert, Universita di Catania and Universität Regensburg
   24. 02. 2006
3. **Superconducting microwave circuits for quantum experiments**
   Thomas Niemczyk, Walther-Meissner-Institut
   28. 04. 2006
4. **Tunneling through band gap or Mott insulators**
   Prof. Jürgen Halbritter, Institut für Materialforschung, Forschungszentrum Karlsruhe
   05. 05. 2006
5. **Infrared and phonon Raman measurements on organic metals close to charge ordering**
   Dr. Natalia Drichko, 1. Physikalisches Institut, Universität Stuttgart
   19. 05. 2006
6. **Experimental observation of bias-dependent no-local Andreev reflection**
   Dr. Saverio Russo, Delft University of Technology, The Netherlands
   02. 06. 2006
7. **Interactions between spin currents and domain walls**
   Dr. Mathias Klaeui, Universität Konstanz
   09. 06. 2006
8. **Organic molecules on insulating substrates investigated by noncontact atomic force microscopy**
   Dr. Christian Loppacher-Voirol, IAPP, Universität Dresden
   23. 06. 2006
9. **Vibrational spectra of fullerene-cubane compounds and functionalized nanotubes**
   Dr. Gyöngyi Klupp, Research Institute for Solid State Physics and Optics, Budapest, Hungary
   30. 06. 2006
10. **Einkristallzüchtung intermetallischer Verbindungen mit dem Zonenschmelzverfahren**
    Dr. Günter Behr, IFW Dresden
    07. 07. 2006
11. **The fused quartz thermal expansion cell and its application in the investigation of phase transitions and dimensionality in novel materials**
    Prof. John Neumeier, Physics Department, Montana State University, Bozeman, USA
    17. 07. 2006
12. **New perspectives for Molecular Beam Epitaxy of Complex Oxides**
    Dr. Gennadii Logvenov, Brookhaven National Laboratory, USA
    21. 07. 2006
13. **Nanoscale gap inhomogeneity in cuprate superconductors**
    Dr. Tamara Nunner, Institut für Theoretische Physik, Freie Universität Berlin
    28. 07. 2006
14. **Resonant x-ray scattering studies of multiferroic $TbMnO_3$ in applied magnetic fields**
    Dr. Daniel Mannix, ESRF Grenoble
    20. 10. 2006

15. **Harnessing BEDT-TTF Based Organic Conductors for Plastic Electronics and Nanowires Construction**
    Dr. E. Laukhina, Institut de Ciencia de Materials de Barcelona (CSIC), Spain and Institute of Problems of Chemical Physics, Chernogolovka, Russia
    17. 11. 2006
16. **Ultrafast dynamics in nanostructures - femtosecond x-ray diffraction experiments**
    Prof. M. Bargheer, Max-Planck-Institut für Kolloid- und Grenzflächenforschung, Potsdam und Max-Born-Institut, Berlin
    24. 11. 2006
17. **Adsorption at the Liquid-Solid Interface - Stabilization through Hydrogen-Bonds**
    Lorenz Kampschulte, Deutsches Museum, München
    08. 12. 2006

Topical Seminar on Advances in Solid State Physics – WS 2005/2006 and WS 2006/2007

1. **Makroskopische Quantensysteme: Konzept der makroskopischen Wellenfunktion**
   22. 11. 2005
   Susanne Hofmann
2. **Makroskopische Quanteninterferenz in Supraleitern: Supraleitende Quanteninterferometer (SQUIDs)**
   29. 11. 2005
   Marc Tippmann
3. **Makroskopisches Quantentunneln und makroskopische Quantenkohärenz: Josephson-Kontakte und rf-SQUIDs**
   06. 12. 2005
   Thomas Hell
4. **Makroskopisches Quantentunneln der Magnetisierung**
   13. 12. 2005
   Christoph Geißinger
5. **Quantisierung elektromagnetischer Schaltkreise: LC-Oszillator und supraleitende Ladungs-Fluss-Qubits**
   20. 12. 2005
   Matthias Weiler
6. **Quantenmechanische Zwei-Niveausysteme**
   10. 01. 2006
   Gunther Jegert
7. **Quantenmechanische Zwei-Niveausysteme in Resonatoren: cQED**
   17. 01. 2006
   Matthias Althammer
8. **Supraleitende Fluss/Phasen-Qubits**
   24. 01. 2006
   Hans-Martin Eiter
9. **Dekohärenz**
   31. 01. 2006
   Stefan Nimmrichter
10. **Quantenmechanischer Messprozess und Quantentomographie**
    07. 02. 2005
    Thorbjörn Buck
11. **Rauschmessungen**
    Achim Marx
    14. 11. 2006
12. **Mikrowellenspektroskopie und zeitaufgelöste Messungen an supraleitenden Fluss-Qubits**
    Frank Deppe
    21. 11. 2006

13. **Grundlagen der Raman-Streuung**
    Wolfgang Prestel
    28. 11. 2006
14. **Einführung in die Mikrowellenmesstechnik**
    Thomas Niemczyk
    05. 12. 2006
15. **Spin-Echo Neutronen-Spektroskopie**
    Markus Bröll
    12. 12. 2006
16. **Zirkularer magnetischer Röntgendichroismus (XMCD)**
    Karl Nielsen
    19. 12. 2006
17. **Hochauflösende Messung magnetischer Eigenschaften (SQUID- und Torque-Magnetometrie, VSM, etc.)**
    Toni Helm
    09. 01. 2007
18. **Messung der Magnetotransporteigenschaften von magnetischen Schichtsystemen**
    Wolfgang Kaiser
    16. 01. 2007
19. **Texturanalyse dünner Schichten mittels hochauflösender Röntgenstreuung**
    Andrea Boger
    23. 01. 2007
20. **Magnetische Resonanzverfahren (NMR, ESR, etc.)**
    Andreas Brandlmaier
    30. 01. 2007
21. **Magnetisierungs- und NMR-Messungen an festem ^{3}He**
    Matthias Kath
    06. 02. 2007

Lectures

A: Technical University of Munich

Dietrich Einzel

WS 2005/2006
- Mathematische Methoden der Physik I (Mathematical Methods of Physics I)
- Übungen zu Mathematische Methoden der Physik I (Mathematical Methods of Physics I, Problem Sessions)

SS 2006
- Mathematische Methoden der Physik II (Mathematical Methods of Physics II)
- Übungen zu Mathematische Methoden der Physik II (Mathematical Methods of Physics II, Problem Sessions)
- Supraleitung und Suprafluidität (Superconductivity and Superfluidity)

WS 2006/2007
- Mathematische Methoden der Physik I (Mathematical Methods of Physics I)
- Übungen zu Mathematische Methoden der Physik I (Mathematical Methods of Physics I, Problem Sessions)

Rudolf Gross

WS 2005/2006
- Angewandte Supraleitung (Applied Superconductivity)
- Festkörperkolloquium (Colloquium on Solid State Physics (with D. Einzel)
- WMI-Seminar über aktuelle Fragen der Tieftemperatur-Festkörperphysik (WMI Seminar on Current Topics of Low Temperature Solid State Physics) (with D. Einzel, S.B.T. Gönnenwein, A. Marx, M. Opel, R. Hackl)
- Seminar über Makroskopische Quantensysteme in Festkörpern (Seminar on Macroscopic Quantum Systems in Solids)

SS 2006
- Supraleitung und Tieftemperaturphysik II (Superconductivity and Low Temperature Physics II)
- Festkörperkolloquium (Colloquium on Solid State Physics (with D. Einzel)
- WMI-Seminar über aktuelle Fragen der Tieftemperatur-Festkörperphysik (WMI Seminar on Current Topics of Low Temperature Solid State Physics) (with D. Einzel, S.B.T. Gönnenwein, A. Marx, M. Opel, R. Hackl)
- Seminar: Magnetismus und Spinelektronik (Seminar on Magnetism and Spintronics)

WS 2006/2007
- Angewandte Supraleitung (Applied Superconductivity)
- Festkörperkolloquium (Colloquium on Solid State Physics (with D. Einzel)
- WMI-Seminar über aktuelle Fragen der Tieftemperatur-Festkörperphysik (WMI Seminar on Current Topics of Low Temperature Solid State Physics) (with D. Einzel, S.B.T. Gönnenwein, A. Marx, M. Opel, R. Hackl)

- Seminar: Physikalische und technische Grundlagen von modernen Messverfahren (Seminar on the Physical and Technological Foundations of Modern Measuring Techniques) (with S.T.B. Gönnenwein, A. Marx, M. Opel)

Sebastian T.B. Gönnenwein

WS 2005/2006
- Magnetismus (Magnetism)
- Seminar on Advances in Solid State Physics (with R. Gross, D. Einzel, A. Marx, M. Opel, R. Hackl)
- WMI-Seminar über aktuelle Fragen der Tieftemperatur-Festkörperphysik (WMI Seminar on Current Topics of Low Temperature Solid State Physics) (with R. Gross, D. Einzel, A. Marx, M. Opel, R. Hackl)

SS 2006
- Spinelektronik (Spin Electronics)
- Seminar on Advances in Solid State Physics (with R. Gross, D. Einzel, A. Marx, M. Opel, R. Hackl)
- WMI-Seminar über aktuelle Fragen der Tieftemperatur-Festkörperphysik (WMI Seminar on Current Topics of Low Temperature Solid State Physics) (with R. Gross, D. Einzel, A. Marx, M. Opel, R. Hackl)
- Seminar zu aktuellen Fragen der Magneto- und Spinelektronik (with M. Brandt, M. Opel)

WS 2006/2007
- Magnetismus (Magnetism)
- WMI-Seminar über aktuelle Fragen der Tieftemperatur-Festkörperphysik (WMI Seminar on Current Topics of Low Temperature Solid State Physics) (with R. Gross, D. Einzel, A. Marx, M. Opel, R. Hackl)
- Seminar: Physikalische und technische Grundlagen von modernen Messverfahren (Seminar on the Physical and Technological Foundations of Modern Measuring Techniques) (with R. Gross, A. Marx, M. Opel)
- Seminar zu aktuellen Fragen der Magneto- und Spinelektronik (with M. Brandt, M. Opel)

Rudi Hackl

WS 2005/2006
- Supraleitung und Tieftemperaturphysik I (Superconductivity and Low Temperature Physics I) (with D. Einzel)

SS 2006
- Seminar on Superfluids and Superconductivity (with D. Einzel, Chr. Pfleiderer and W. Zwerger)

WS 2006/2007
- Supraleitung und Tieftemperaturphysik I (Superconductivity and Low Temperature Physics I) (with D. Einzel)

Anton Lerf

WS 2005/2006	• Angewandte Anorganische Chemie II: Feste Stoffe (Applied Inorganic Chemistry II: Solids)
SS 2006	• Moderne Aspekte der Chemie für Physiker II (Modern Aspects of Chemistry for Physicists II) • Nanostrukturierte Materie (Nanostructured Matter)
WS 2006/2007	• Stoffströme in Natur und Technik (zusammen mit Prof. K. Köhler)

Erwin Schuberth

WS 2005/2006	• Höhere Physik I (Advanced Physics I) • Übungen zur Höheren Physik I (Exercises to Advanced Physics I)
SS 2006	• Höhere Physik II (Advanced Physics II) • Übungen zur Höheren Physik II (Exercises to Advanced Physics II)
WS 2006/2007	• Höhere Physik I (Advanced Physics I) • Übungen zur Höheren Physik I (Exercises to Advanced Physics I)

B: Ludwig-Maximilians University of Munich

Bianca Hermann

WS 2005/2006	• Hauptseminar: Tiefkalte Quantenphänomene • Erstkontakt mit der Programmiersprache LabVIEW (First contact with the programming language LabVIEW) • Seminar über die aktuelle Literatur im Bereich Molekularer Selbstorganisation • Seminar über spezielle Fragen der Rastertunnelmikroskopie
SS 2006	• Rastertunnelmikroskopie (A-Vorlesung) • Seminar: Dissertationen und Diplomarbeiten schreiben • Seminar über die aktuelle Literatur im Bereich Selbst-Organisierende Moleküle • Seminar über spezielle Fragen der Rastertunnelmikroskopie
WS 2006/2007	• Selbst-organisierende Moleküle (A-Vorlesung) • Seminar über die aktuelle Literatur im Bereich Molekularer Selbstorganisation • Seminar über spezielle Fragen der Rastertunnelmikroskopie

Staff of the Walther-Meißner-Institute

Director
Prof. Dr. Rudolf Gross

Deputy Director
Dr. Werner Biberacher

Technical Director
Dr. Achim Marx

Head of the Scanning Probe Division
Prof. Dr. Bianca Hermann

Administration/Secretary's Office
Jutta Laaser
Emel Dönertas
Tina Pinkert

Scientific Staff
Dr. Werner Biberacher
Dr. habil. Dietrich Einzel
Dr. habil. Andreas Erb
Dr. Sebastian Gönnenwein
Dr. habil. Rudolf Hackl
Dr. Mark Kartsovnik
Prof. Dr. Anton Lerf
Dr. Achim Marx
Dr. Matthias Opel
Prof. Dr. Erwin Schuberth
Dr. Kurt Uhlig
Dipl.-Phys. Andrea Boger
Dipl.-Phys. Stephan Geprägs
Dipl.-Phys. Wolfgang Prestel
Dipl.-Phys. Michael Lambacher
Dipl.-Phys. Karl Madek
Dipl.-Phys. Georg Wild
Dipl.-Phys. Markus Schmeißner
Dipl.-Phys. Matthias Kath
Dipl.-Phys. Petra Majewski
Dipl.-Phys. Edwin Menzel
Dipl.-Phys. Frank Deppe
Dipl.-Phys. Thomas Niemczyk
Dipl.-Phys. Matteo Mariantoni
Dipl.-Phys. Karl-Wilhelm Nielsen
Dipl.-Phys. Leonardo Tassini
Dipl.-Phys. Tobias Heimbeck

Technical Staff
Thomas Brenninger
Joachim Geismann
Gabrielle Görblich
Ulrich Guggenberger
Dieter Guratzsch
Josef Höss
Julius Klaus
Robert Müller
Jan Naundorf
Georg Nitschke
Walter Nitschke
Christian Reichlmeier
Harald Schwaiger
Helmut Thies
Siegfried Wanninger

Assistants
Sybilla Plöderl
Brigitte Steinberg

Permanent Guests
Prof. Dr. B. S. Chandrasekhar
Dr. Robert Doll
Dr. Karl Neumaier
Dr. Christian Probst
Prof. Dr. Schöllhorn

Guest Researchers

1. Prof. Dr. B.S. Chandrasekhar
   permanent guest
2. Dr. Robert Doll
   permanent guest
3. Dr. Karl Neumaier
   permanent guest
4. Dr. Christian Probst
   permanent guest
5. Prof. Dr. Schöllhorn
   permanent guest
6. Prof. Dr. Juan Poyato Ferrera, Instituto de Ciencia de Materiales, Sevilla, Spain
   17. 07. – 14. 08. 2006
7. Verónica Ramirez del Valle, Instituto de Ciencia de Materiales, Sevilla, Spain
   14. 09. – 22. 12. 2006
8. Dr. Nataliya D. Kushch, Institute of Problems of Chemical Physics, Chernogolovka, Russia
   22. 11. – 12. 12. 2006
9. Prof. Dr. Jose Luis Pérez-Rodriguez, Instituto de Ciencia de Materiales de Sevilla, Spain
   12. 12. – 19. 12. 2006
10. Prof. Dr. Pavla Capkova, Institute of Materials Chemistry, Technical University, Ostrava, Tschechien
    25. 09. – 29. 09. 2006
11. Dr. G. Vaitheeswaran and Dr. V. Kanchana, Material Science and Engineering, Kungliga Tekniska Högskolan (KTH), Stockholm, Sweden
    06. 07. – 09. 07. 2006
12. Dr. Lukas Scherer, Universität Basel
    01. 07. – 04. 08. 2006
13. Dr. Michael Malarek, Universität Basel
    22. 02. – 25. 02. 2006
14. Gwenael Hervé, Universite de Rennes 1, France
    01. 04. – 31. 07. 2006
15. Dr. Gyöngyi Pergerné Klupp, Hungarian Academy of Sciences, Research Institute for Solid State Physics and Optics, Budapest, Hungary
    10. 01. – 02. 09. 2006
16. Prof. Thomas P. Devereaux, University of Waterloo, Canada
    14. 07. – 16. 07. 2006
17. Prof. Alfred Zawadowski, Budapest University of Technology and Economics, Budapest, Hungary
    02. 11. – 03. 12. 2006

Commission for Low Temperature Physics

Members of the Commission for Low Temperature Research of the Bavarian Academy of Sciences:

Kaiser, Wolfgang, Leiter (Technische Universität München)
Abstreiter, Gerhard (Technische Universität München)
Brenig, Wilhelm, stellv. Leiter (Technische Universität München)
Gross, Rudolf (Walther-Meißner-Institut)
Landwehr, Gottfried (Universität Würzburg)
Hänsch, Theodor (Max-Planck-Institut für Quantenoptik, Garching)
Kotthaus, Jörg Peter (Ludwig-Maximilians-Universität München)
Schwoerer, Markus (Universität Bayreuth)
Vollhardt, Dieter (Universität Augsburg)

Prof. Dr. Karl Friedrich Renk, University of Regensburg, has retired in 2006 and left the Commission for Low Temperature Research.